THE UNIVERSITY OF CHICAGO

A SEARCH FOR DIRECT CP VIOLATION IN THE 2π DECAY MODES OF NEUTRAL KAONS

A DISSERTATION SUBMITTED TO
THE FACULTY OF THE DIVISION OF THE PHYSICAL SCIENCES
IN CANDIDACY FOR THE DEGREE OF
DOCTOR OF PHILOSOPHY

DEPARTMENT OF PHYSICS

BY

MICHAEL B. WOODS

CHICAGO, ILLINOIS

JUNE, 1988

Acknowledgements

I want first to thank my thesis sponsor, Bruce Winstein, who has guided this experiment and who has introduced me to the fascinating subject of CP violation. I have learned and appreciated much from his enthusiasm and from his ability to see through to the heart of a problem.

It was a great pleasure to do my studies and participate in the atmosphere at the University of Chicago and with the High Energy group in the Department of Physics. I wish especially to thank my colleagues J. R. Patterson, Y. Wah, and H. Yamamoto for their efforts and many contributions to our experiment and to the analysis reported here; I also thank K. Nishikawa who made important contributions to the early stages of the experiment. Many thanks go to the Engineering Services group headed by D. Armstrong and to the Electronic Services group headed by H. Sanders, which provided much technical expertise necessary to building the experiment and especially for the Drift Chamber project. The chamber project also benefited greatly from the contributions of M. Asner, D. Burkeen, D. Cinabro, L. Gibbons and G. Wright.

It was a pleasure to work with our collaborators from Chicago (R. Winston); from Elmhurst (E. C. Swallow); from Fermilab (G. J. Bock, R. Coleman, Y. B. Hsuing, K. Stanfield, R. Stefanski, T. Yamanaka); from Princeton (G. D. Gollin, G. L. Grazer, J. K. Okamitsu); and from Saclay (R. Daudin, P. Debu, P. Jarry, B. Peyaud, R. Turlay). It has also been a pleasure to work with the new members of the group—from Chicago, L. Gibbons and V. Papadimitriou; from Princeton, G. Blair and M. Karlsson; and from Saclay, B. Vallage.

I would like to thank the Natural Sciences and Engineering Research Council (NSERC) of Canada and the Grainger Foundation in Chicago for support during the last six years.

Preparing this manuscript required much patience and effort, and I wish to thank T. Nguyen of Fermilab for her much appreciated help.

Lastly, I would like to thank my many friends at Chicago for the enjoyable years spent here: softball, late-night hockey, an occasional poker game (and a passion for physics). My 'little brother' Larry has been a good friend and I shall miss our Sunday outings that provided an important escape from the world of particle physics. I have come to feel at home in Chicago, largely due to my housemates Vivian, Per, Jim, John, 'Auntie', Eva and Sashie; their friendship, support and varied viewpoints on social and political issues I will greatly miss.

Contents

Acknowledgements ii
List of Figures vii
List of Tables xiii
Abstract xv

Chapter

1 Introduction 1
1.1 Symmetries (C, P, T) 2
1.2 Neutral Kaon Phenomenology 4
1.3 Experimental Status of CP Violation 9
1.4 CP Violation in the Standard Model 10
1.5 CP Violation from Other Sources 17
1.6 Objectives of this Experiment 17

2 The Experiment 19
2.1 Principles of the Measurement 19
2.2 Beamline and Detector 20
2.2.1 Beamline 21
2.2.2 The Regenerator and Decay Region 24
2.2.3 The Charged Particle Spectrometer 26
2.2.4 The Electromagnetic Calorimeter 29
2.2.5 The Background Rejection Systems 31
2.3 The Double Beam Technique 36

3 The Drift Chambers 42
3.1 Hardware and Construction 42
3.1.1 Features of the Design 42
3.1.2 Operation and Readout 46

3.2 Performance 46
3.2.1 Conversion of Drift times to Distances 46
3.2.2 Charged Particle Trajectories from Reconstruction of Tracks 47
3.2.3 Resolution and Efficiency 49
3.2.4 Momentum Determination 51

4 The Lead Glass **53**
4.1 Hardware and Operation 53
4.2 Energy and Position Measurements 56
4.3 Calibration 58
4.3.1 Electron Calibration Runs 59
4.3.2 Gains for Neutral Mode Data 60

5 Data Collection **64**
5.1 Running Conditions 64
5.2 Trigger Logic 64
5.3 Electronic Readout 66
5.4 Data Acquisition 68

6 Charged Mode Data **70**
6.1 Trigger 70
6.2 Event Reconstruction 71
6.3 Event Selection 75
6.3.1 Aperture Cuts 77
6.3.2 $K\mu_3$ Rejection 77
6.3.3 Lambda Rejection 78
6.3.4 Inelastic K_S Rejection 78
6.3.5 Kinematic Cuts on q^2 and m_K 79
6.4 Data Sets 81
6.5 Data Summary Tapes 81

7 Neutral Mode Data **83**
7.1 Trigger 83
7.2 Event Reconstruction 85
7.2.1 Electron And Photon Measurements 86
7.2.2 Decay Kinematics 88
7.3 Event Selection 89
7.3.1 Aperture Cuts 93
7.3.2 Hadron Rejection 93

7.3.3 Inelastic K_S Rejection 93
7.3.4 Eliminating Accidental Clusters 93
7.3.5 Fusion Recognition for Electron Clusters 94
7.3.6 Fusion Recognition for Photon Clusters 94
7.3.7 Photon Vetoes 95
7.3.8 Charged Particle Vetoes 96
7.3.9 e^+e^-, γ Energies 96
7.3.10 Longitudinal Decay Vertex 96
7.3.11 Kinematic Cuts on χ^2, q^2, and m_K 98
7.4 Data Summary Tapes 98
7.4.1 First Level DST's 100
7.4.2 Second and Third Level DST's 101

8 Background Subtractions 103
8.1 Diffractive and Inelastic Backgrounds 103
8.2 Semileptonic and Neutron Background 109
8.3 Background from $K_L \to 3\pi^0$ 114

9 Acceptance Corrections 119
9.1 Detector Simulation 119
9.2 Monte Carlo Event Generation 120
9.3 Data and Monte Carlo Comparisons 124
9.3.1 $K_{L(S)} \to \pi^+\pi^-$ Modes 125
9.3.2 $K_{L(S)} \to \pi^0\pi^0$ Modes 126
9.3.3 $K_L \to 3\pi^0$ Mode 129
9.4 What are the Acceptances? 133

10 The Determination of $|\epsilon'/\epsilon|$ 141
10.1 Determining $|\epsilon'/\epsilon|$ from the 2π Rates 141
10.2 Extracting $|\epsilon'/\epsilon|$ from the Data 145

11 Systematic Errors and Systematic Checks 153
11.1 Systematic Errors 153
11.1.1 Uncertainties Associated with Accidentals and Differences Between the Upper and Lower Beams 154
11.1.2 Uncertainties Associated with Energy Calibration . . . 157
11.1.3 Uncertainties Associated with the Background Subtractions and Acceptance Corrections 158
11.2 Systematic Checks 164

12 Conclusions 166

Appendix

Regeneration **171**
A.1 Coherent Regeneration 171
A.2 Diffractive and Inelastic Regeneration 173

List of Figures

1 Box diagrams for K^0–$\overline{K^0}$ mixing in the Standard Model . . . 11
2 Diagrams for the 2π decay of neutral kaons in the Standard Model: a) 'Spectator' diagram; b) 'Exchange' diagram; c) 'Penguin' diagram 12
3 quark-quark-W vertex 13
4 Three generations of quarks in the Standard Model 13

5 Meson Center Beamline for E731 at Fermilab 22
6 The E731 Detector 23
7 Side view of Regenerator 25
8 Configuration of HDRA Counters. a) Beam's view of counters; b) Side view of V, T and Pb Converter 27
9 Cell geometry for drift chamber wires 28
10 Beam's view of A Bank 28
11 Beam's view of B Bank 29
12 Lead Glass array and stand 30
13 Side view cross-section of a VA plane 32
14 Beam's view of VA1, VA2, VA3, and VA4 photon veto counters 33
15 Beam's view of MA and LGA photon veto counters 34
16 a) Beam's view of Collar Anti, b) Side view of Collar Anti . . 35
17 Exploded view of a Back Anti unit 36

18 Isometric drawing of the upper right corner of a chamber (viewed from upstream). 43
19 Schematic drawing of a 'pacman' 45
20 Measured drift time distribution for hits on tracks in an x plane of Chamber 2 47

21 Track finding procedure: a straight line is drawn between two hit wires in the outer planes, and candidate hits within a 1.5cm road of this line are searched for in the other planes. Different initial planes are tried so as not to miss tracks due to wire inefficiencies. 48
22 Sum of distances for paired hits—the chamber resolution of 150μm/wire was determined from this. 50
23 Offset distribution for an x plane in Chamber 2. The offset is with respect to the coordinate system defined by Chambers 1 and 4. 50
24 Distribution of P_M for π^+, π^- in charged mode running 51
25 (p, π) invariant mass distribution for identified lambda decays 52

26 Ratio of flasher responses for tenth and first flashes into the spill for data with LED's off. 54
27 Ratio of flasher responses for tenth and first flashes into the spill for data with LED's on. 55
28 Electromagnetic energy deposit in the Lead Glass for a $2\pi^0$ event. 57
29 E/p distribution from calibration data for electrons and positrons. The mean is tuned to be 1.0 and the FWHM is 8%. 61
30 E/p distribution of data and Monte Carlo for $K_S \rightarrow 2\pi^0$ events. (The solid circles are Monte Carlo.) 61
31 E/p distribution of data and Monte Carlo for $K_L \rightarrow 3\pi^0$ events. (The solid circles are Monte Carlo.) 62
32 (γ, γ) mass for identified sheet π^0 events. 63

33 Data taking modes for the 1985 run 65
34 Trigger logic diagram 67

35 Neutral kaon decaying to $\pi^+\pi^-$ 72
36 The kaon momentum vector is projected to the plane of the Regenerator to determine the beam of the parent particle. . . . 73
37 A kaon scatters at the Regenerator; the quantity q^2 measures the square of the transverse momentum transfer. 74
38 Reconstructed transverse location of kaons at the regenerator plane for identified $K \rightarrow \pi^+\pi^-$ events from the regenerator beam. 75
39 Invariant (π, π) mass of candidate $K \rightarrow \pi^+\pi^-$ events from the vacuum beam 76

40 Invariant (π, π) mass of candidate $K \rightarrow \pi^+\pi^-$ events from the regenerator beam 76
41 Lambda energy distribution for identified lambda decays in the vacuum beam 78
42 q^2 distribution of identified $K \rightarrow \pi^+\pi^-$ events from the vacuum beam. 79
43 q^2 distribution of identified $K \rightarrow \pi^+\pi^-$ events from the regenerator beam. 80
44 Invariant (π, π) mass of identified $K \rightarrow \pi^+\pi^-$ events from the vacuum beam. 80
45 Invariant (π, π) mass of identified $K \rightarrow \pi^+\pi^-$ events from the regenerator beam. 81

46 A kaon decays to two neutral pions, which subsequently decay to two photons. One photon converts at the Pb plane in the HDRA to an electron-positron pair; this pair is 'opened up' by the Separator Magnet and reconverged at the Lead Glass with the Analysis Magnet. 84
47 There are three possibilities for pairing photons to determine the longitudinal decay vertex in a $K \rightarrow 2\pi^0$ event. The pairing that gives the most consistent Z determines the pairing. 90
48 Transverse location of kaons at the Regenerator for identified $2\pi^0$ events from the regenerator beam 91
49 Invariant mass of candidate $K \rightarrow 2\pi^0$ events from the vacuum beam 91
50 Invariant mass of candidate $K \rightarrow 2\pi^0$ events from the regenerator beam 92
51 $SEP2$ distribution for identified $K \rightarrow 2\pi^0$ events from the regenerator beam 94
52 A plot of the block energies (in GeV) in one section of the Lead Glass. The fusion of two photons here is recognized as one cluster by the cluster finder. It can be identified as a fusion, however, because a corner block (in a 3x3 cluster about the block with maximum energy) has greater energy than its side block neighbours. 95
53 Reconstructed longitudinal decay vertex of identified $K \rightarrow 2\pi^0$ events from the vacuum beam 97
54 Reconstructed longitudinal decay vertex of identified $K \rightarrow 2\pi^0$ events from the regenerator beam 97

55 χ^2 distribution for identified $K \to 2\pi^0$ events from the regenerator beam 98
56 q^2 distribution for identified $K \to 2\pi^0$ events from the regenerator beam 99
57 Invariant mass of identified $K \to 2\pi^0$ events from the vacuum beam 99
58 Invariant mass of identified $K \to 2\pi^0$ events from the regenerator beam 100

59 Simulated q^2 distribution for single scatters in the Regenerator. The contributions from the Lead and B_4C are also shown separately. 105
60 Simulated q^2 distribution for scattering (single and multiple) in the Regenerator. A fit to two exponentials is shown superimposed. 106
61 q^2 distribution from $\pi^+\pi^-$ regenerated beam data with background fit superimposed 107
62 Same plot as Figure 61 in bin sizes of 1000 $(\mathrm{MeV/c})^2$ for q^2 . . 108
63 q^2 distribution for neutral mode regenerator beam data with fit to background superimposed. The dashed line shows the diffraction contribution to the background. 110
64 q^2 Distribution for identified $K\mu_3$ events from data 112
65 q^2 distribution for identified Ke_3 events from data 112
66 q^2 distribution for identified neutron events from data 113
67 q^2 distribution for identified $K\mu_3$ events from Monte Carlo . . 113
68 Longitudinal decay vertex distribution for vacuum beam $\pi^+\pi^-$ candidates with 5000 $(\mathrm{MeV/c})^2 < q^2 < 10000$ $(\mathrm{MeV/c})^2$. 114
69 q^2 distribution for identified $K_L \to \pi^+\pi^-$ events from data . . 115
70 The m_K distribution of $3\pi^0$ events which fake $2\pi^0$ events as determined by Monte Carlo for a) events with no photon fusions, b) events with one photon fusion, and c) events with two photon fusions. 117
71 The data m_K distribution for vacuum events with the $3\pi^0$ background overlayed 118

72 Definition of r and θ for creating table of fractional energy deposit 123
73 (center block energy) / (3x3 energy) for photons. (Solid circles are Monte Carlo.) 124

74 (3x3 energy) / (5x5 energy) for photons. (The long tail is due to nearby clusters. Solid circles are Monte Carlo.) 125
75 Illumination of π^+ and π^- at the B Bank, x view. (Solid circles are Monte Carlo.) 126
76 Illumination of π^+ and π^- at the B Bank, y view. (Solid circles are Monte Carlo.) 126
77 Kaon energy distribution for charged mode vacuum events. (Solid circles are Monte Carlo.) 127
78 Kaon energy distribution for charged mode regenerator events (with correction applied to Monte Carlo spectrum. Solid circles are Monte Carlo). 127
79 Longitudinal decay vertex distribution for charged mode vacuum events. (Solid circles are Monte Carlo.) 128
80 Longitudinal decay vertex distribution for charged mode regenerator events. (Solid circles are Monte Carlo.) 128
81 Illumination of electrons and positrons at the Lead Glass; x view. (Solid circles are Monte Carlo.) 129
82 Illumination of electrons and positrons at the Lead Glass; y view. (Solid circles are Monte Carlo.) 130
83 Illumination of photons at the Lead Glass; x view (Column corresponds to a column of Lead Glass blocks. The solid circles are Monte Carlo.) 130
84 Illumination of photons at the Lead Glass; y view (Row corresponds to a row of Lead Glass blocks. The solid circles are Monte Carlo.) 131
85 Distribution of number of overlapping clusters for $K_S \rightarrow 2\pi^0$ events. (Solid circles are Monte Carlo.) 131
86 Distribution of number of clusters neighboring the beam pipes for $K_S \rightarrow 2\pi^0$ events. (Solid circles are Monte Carlo.) 132
87 Distribution of number of clusters on the array's outer edge for $K_S \rightarrow 2\pi^0$ events. (Solid circles are Monte Carlo.) 132
88 Kaon energy distribution for $\pi^0\pi^0$ events from the vacuum beam. (Solid circles are Monte Carlo.) 136
89 Kaon energy distribution for $\pi^0\pi^0$ events from the regenerator beam. (Solid circles are Monte Carlo.) 136
90 Longitudinal decay vertex for $\pi^0\pi^0$ events from the vacuum beam. (Solid circles are Monte Carlo.) 137
91 Longitudinal decay vertex for $\pi^0\pi^0$ events from the regenerator beam. (Solid circles are Monte Carlo.) 137

92 $SEP2$ distribution for $3\pi^0$ events. (Solid circles are Monte Carlo.) 138
93 χ^2 distribution for $3\pi^0$ events. (Solid circles are Monte Carlo.) 138
94 q^2 distribution for $3\pi^0$ events. (Solid circles are Monte Carlo.) 139
95 Kaon energy distribution for $3\pi^0$ events. (Solid circles are Monte Carlo.) 139
96 Energy distribution of photons for $3\pi^0$ events. (Solid circles are Monte Carlo.) 140
97 Energy distribution of electrons and positrons for $3\pi^0$ events. (Solid circles are Monte Carlo.) 140

98 Energy dependence of the regeneration amplitude for B_4C . . 148
99 Energy dependence of $|\epsilon'/\epsilon|$ 149
100 Energy dependence of the regeneration amplitude for B_4C as determined by neutral mode data only 150
101 Energy dependence of the regeneration amplitude for B_4C as determined by charged mode data only 151

102 The longitudinal decay vertex distribution for $K_L \rightarrow 3\pi^0$ events for kaon energies between 50 and 60 GeV. (The solid circles are Monte Carlo.) 160
103 The same plot as 102 for kaon energies between 70 and 80 GeV. 160
104 The same plot as 102 for kaon energies between 90 and 100 GeV.161
105 The same plot as 102 for kaon energies between 110 and 120 GeV. 161
106 The ratio of data to Monte Carlo from Figure 102. 162
107 The ratio of data to Monte Carlo from Figure 103. 162
108 The ratio of data to Monte Carlo from Figure 104. 163
109 The ratio of data to Monte Carlo from Figure 105. 163
110 Energy dependence to the effective acceptance error per meter as determined from straight line fits to plots in Figures 106–109. 164

111 Measurements of $|\epsilon'/\epsilon|$ 167

112 Schematic representation of the q^2 dependence to the 2π rate downstream of a regenerator. 174

List of Tables

1 Results of experiments testing CPT invariance [8] 4
2 Parameters governing the time-evolution of neutral kaons [8] . 10

3 Positions and dimensions of detector elements 37
4 Positions and dimensions of detector elements 38
5 Radiation and interaction lengths of detector elements 39

6 Coefficients describing the nonlinear Lead Glass response to electromagnetic showers 60

7 Charged mode signal losses due to reconstruction criteria . . . 77

8 Neutral mode signal losses due to reconstruction criteria . . . 92

9 Energy dependence to diffractive and inelastic backgrounds for the regenerator beam $K \to \pi^0\pi^0$ data 109
10 Photon veto planes and their efficiencies used in the Monte Carlo 116
11 Energy dependence of the $3\pi^0$ background with and without the photon fusion cut. 116
12 Summary of background subtractions and their associated uncertainties 117

13 Constants in Malensek particle energy spectrum 120
14 Acceptances for the $2\pi^0$ data 134
15 Acceptances for the $\pi^+\pi^-$ data 134
16 Ratio of vacuum and regenerator beam acceptances downstream of the Lead Mask 135

17 Weighting factor that reflects the relative contribution of the kaon beam's primary K_S component to the vacuum 2π rate . . 143
18 Event totals in each energy bin for the neutral data after background subtractions 145

19 Event totals in each energy bin for charged data after background subtractions 146
20 Constants used in the fitting procedure 146
21 Summary of results from fits for $(f - \overline{f})/k$ and $|\epsilon'/\epsilon|$ 152

22 Summary of systematic uncertainties 165

Chapter 1

Introduction

This experiment searches for 'direct' CP violation in the decays of neutral kaons. The operator CP represents the action of taking the mirror image of a process (P) and then changing all particles to anti-particles (C) in that mirror image. A process conserves CP if the observed rate for the process and the observed rate for the CP transformed process are identical. No experimental evidence has been found for violation of the CP symmetry in strong or electromagnetic interactions; however in 1964, the experiment of Christenson, Cronin, Fitch and Turlay [1] found evidence for a small amount of CP violation in the weak interaction. This they detected by observing approximately 45 events of $K_L \rightarrow \pi^+\pi^-$, a decay mode that is forbidden if CP is a good symmetry.

CP violation can manifest itself in two ways in the process $K_L \rightarrow \pi^+\pi^-$. First, the K_L particle may not be an eigenstate of CP, and the parameter ϵ is used to describe the relative amount of admixture of the wrong CP state. Second, the decay amplitude may have a CP violating component (direct CP violation) and this is described by the parameter ϵ'. To date, CP violation has only been observed in the neutral kaon system and the experimental status is summarized by:

$$|\epsilon| = (2.275 \pm 0.021) \cdot 10^{-3} \tag{1.1}$$

$$|\epsilon'/\epsilon| = (-3 \pm 4) \cdot 10^{-3} \tag{1.2}$$

All CP violation can therefore be accounted for by the single parameter ϵ, which was first measured in 1964.

Our experiment seeks to measure $|\epsilon'/\epsilon|$ with a precision of better than 10^{-3} and hopes to observe evidence for direct CP violation. CP violation arises 'naturally' in the 6-quark Standard Model if the Yukawa couplings of quarks to charged W's are complex. Standard Model predictions for $|\epsilon'/\epsilon|$ are in the

range $0.001 < |\epsilon'/\epsilon| < 0.01$, so that a measurement of this quantity with 0.001 precision has a good chance to observe a significant signal and at the same time such a measurement presents a good test of the model.

In this chapter we discuss the nature of symmetries in physics (in particular the discrete symmetries C, P, and T) and the role they play in our understanding of the physical universe. CP violation is discussed for neutral kaons and the current status of CP violation, both from experiment and from theory, is given. Finally, the objectives of this experiment and its approach to searching for direct CP violation are presented.

1.1 Symmetries (C, P, T)

Symmetries can be viewed as being responsible for generating interactions in gauge theories—for example, invariance of the Lagrangian under local phase rotations of the quantum mechanical wavefunction generates electromagnetic interactions [2]. A second and more familiar role of symmetries in physical theories relates to conservation laws. The Lagrangian and its associated equations of motion are typically invariant with respect to certain transformations of the quantities on which they depend. This invariance corresponds to a symmetry of the Lagrangian and generally leads to a conservation law via Noether's theorem [3]. The most familiar example is that of Lorentz invariance, which states that the Lagrangian should be invariant under translations, rotations and (velocity) boosts of the chosen coordinate system. Lorentz invariance follows from Einstein's theory of special relativity and is generally believed to be a necessary component of all physical theories. Translation invariance with respect to space and time leads to the laws of conservation of momentum and energy; rotational invariance results in the law of angular momentum conservation; and (velocity) boost invariance yields conserved quantities such as the invariant mass of a particle.

Translations, rotations, and boosts are continuous transformations, which means that a finite translation is comprised of a succession of infinitesimal translations, and similarly for rotations and boosts. Discrete transformations also exist, and the symmetries with which this thesis is concerned are of this nature. The C and P transformations have been described earlier and it is evident that there are no infinitesimal transformations associated with these.

While the principle of Lorentz invariance has a strong theoretical basis (special relativity), there is no similar theoretical motivation for C or P invariance; but why should nature choose not to respect these symmetries? The notions of C and P invariance for all interactions were firmly ingrained into

the thinking of physicists until about 1956. In that year Lee and Yang were motivated by the τ–θ paradox to propose that P was violated by the weak interaction [4]. τ and θ referred to two particles, later realized to be the same and now called the K^+, which were measured to have the same mass and lifetime yet decayed to final states of opposite parity. For two different particles to have the same mass and lifetime seemed too great a coincidence, but the alternative was to postulate P violation. Lee and Yang then proposed the famous ^{60}Co radioactive decay experiment, which was carried out by Wu et. al. [5]. The result of this experiment, and subsequent others, firmly established violation of both the C and P symmetries in weak decay processes. It was realized at this time, however, that the product CP remained a good symmetry and it was thus believed that weak interactions were CP invariant.

There is one other discrete transformation of importance to this discussion, and that is the time reversal operator, T. T interchanges initial and final states in an interaction, and reverses the momenta of all particles. Similarly to C and P violation, T violation occurs if the rate for a process and the rate for the time-reversed process are different. In the macroscopic world T appears to be violated in the sense that there is an "arrow of time" associated with increasing entropy [6]. This violation, however, results from the statistics of possible initial conditions and does not imply T violation in interactions. It is T violation on the microscopic scale of interactions that concerns us here, and we note that there has been no direct experimental observation of T violation (as of 1988).[1]

If one takes the combined product of operators CPT (in any order), it has been shown by Luders and Pauli that this should be a good symmetry for any field theory [7]. This result is very general and is based on assumptions of local Lorentz invariance and hermiticity of operators, where hermiticity follows from conservation of probability (unitarity). Two consequences of CPT invariance are that particle and antiparticle should have the same mass and lifetime, and this has been found to be true to very high precision as is shown in Table 1 [8]. There is currently no reason to doubt the validity of CPT symmetry, though it is very important to test this experimentally. Any CPT violation found would have far-reaching consequences for theories of the physical universe.

By the late 1950's, though P and C had been found to no longer be exact symmetries of nature, CP remained a good symmetry as did T and CPT. Given the CPT theorem any CP violation would have implied also a violation of T. Though the time coordinate becomes intimately connected with spatial

[1]There is, however, indirect evidence of T violation from measurements on the neutral kaon system—a good review of this, both with and without assumptions of CPT invariance, can be found in reference [6].

Table 1: Results of experiments testing CPT invariance [8]

Particle Pair	$\delta M/M$	$\delta\Gamma/\Gamma$
$K^0 - \overline{K^0}$	$< 6 \cdot 10^{-19}$	
$K^+ - K^-$	$(-0.6 \pm 1.8) \cdot 10^{-4}$	$(1.1 \pm 0.9) \cdot 10^{-3}$
$p - \overline{p}$	$(0.7 \pm 0.4) \cdot 10^{-4}$	
$\pi^+ - \pi^-$	$(0.2 \pm 0.5) \cdot 10^{-3}$	$(5 \pm 7) \cdot 10^{-4}$
$\mu^+ - \mu^-$		$(3 \pm 8) \cdot 10^{-5}$

coordinates in special relativity, it retains a special character as is noted by the concept of causality and the conceptually different nature of time-like and space-like intervals in the space-time continuum. Thus T has been viewed as a more fundamental symmetry than C or P, and it was expected that T, CP and CPT would all be good symmetries. Of course, one must test these hypotheses with experiment and in 1964 CP was also found to be violated. Its violation was not maximal as was the case with P and C, but appeared at the level of approximately two parts in a thousand with respect to the normal CP conserving weak interaction. Before addressing possible theories that could explain the origin of this CP violation, let us first examine the phenomenology associated with neutral kaons.[2]

1.2 Neutral Kaon Phenomenology

There are two neutral kaons, which are the K^0 and its antiparticle $\overline{K^0}$. The relative phase of the $\overline{K^0}$ wavefunction with respect to that of the K^0 is arbitrary, but it is useful to define it such that

$$CP|K^0\rangle = |\overline{K^0}\rangle$$

We consider first the quantum mechanics associated with a two state quantum system, which in this case is the K^0–$\overline{K^0}$ system. The Hamiltonian is given by

$$H = H_{\rm S} + H_{\rm em} + H_{\rm W}$$

where $H_{\rm S}$, $H_{\rm em}$, and $H_{\rm W}$ are respectively the strong, electromagnetic and weak interaction Hamiltonians. The strangeness quantum number, S, is known to

[2]For a more comprehensive treatment of the phenomenology, consult references [6,9,10,11,12,13]. The treatment given here assumes CPT symmetry to hold; for discussions without this assumption, the reader is referred to [6,10,11].

be conserved by H_s and H_{em}, and so K^0 and $\overline{K^0}$ are defined to be states with definite strangeness—K^0 is defined to have S=+1 and $\overline{K^0}$ is defined to have S=-1. It is these states which are produced in particle collisions via the strong interaction. Choosing $|K^0\rangle$ and $|\overline{K^0}\rangle$ to form the basis vectors $\begin{pmatrix} 1 \\ 0 \end{pmatrix}$ and $\begin{pmatrix} 0 \\ 1 \end{pmatrix}$, the time evolution of a neutral kaon state is given by [14]

$$i\frac{\mathrm{d}}{\mathrm{dt}}\begin{pmatrix} a \\ \bar{a} \end{pmatrix} = H\begin{pmatrix} a \\ \bar{a} \end{pmatrix} \tag{1.3}$$

$$= \left(M - i\frac{\Gamma}{2}\right)\begin{pmatrix} a \\ \bar{a} \end{pmatrix} \tag{1.4}$$

where $|\Psi\rangle = \begin{pmatrix} a \\ \bar{a} \end{pmatrix}$ is a state vector with a and $\bar{a}$ denoting the respective amounts of $|K^0\rangle$ and $|\overline{K^0}\rangle$, and M and Γ are hermitian matrices (as required by unitarity), termed the mass and decay matrices. The presence of Γ follows from the observation that neutral kaons decay.

Treating H_W as a small perturbation to $H_s + H_{em}$, the matrix elements M_{ij} and Γ_{ij} are given from a perturbation expansion: [12]

$$M_{ij} = m_i\delta_{ij} + \langle i|H_W|j\rangle + \sum_n \frac{\langle i|H_W|n\rangle\langle n|H_W|j\rangle}{m_i - m_n} + \ldots \tag{1.5}$$

$$\Gamma_{ij} = 2\pi\sum_f \rho_f\langle i|H_W|f\rangle\langle f|H_W|j\rangle + \ldots \tag{1.6}$$

where:

m_i is the K^0 or $\overline{K^0}$ mass,

m_n is the invariant mass of the intermediate state,

the states $|n\rangle$ are all possible intermediate virtual states,

and the states $|f\rangle$ are all possible real final states with density ρ_f to which K^0 and $\overline{K^0}$ can decay

The terms $\langle\overline{K^0}|H_W|K^0\rangle$ and $\langle K^0|H_W|\overline{K^0}\rangle$ which appear in Equation 1.5 turn out to be zero since weak interactions require $\Delta S \leq 1$ in lowest order. Requiring CPT to be a good symmetry, which shall be assumed for the rest of this discussion, one obtains $M_{11} = M_{22}$ and $\Gamma_{11} = \Gamma_{22}$ (ie. K^0 and $\overline{K^0}$ have the same mass and lifetime).

The physical particles with definite masses and lifetimes are the eigenstates associated with Equation 1.3. We denote these particles by $|K_L\rangle$ and $|K_S\rangle$, where L and S signify Long(-lived) and Short(-lived) and the reason for this will become clear shortly. The eigenvalue problem we wish to solve is

$$i\frac{\mathrm{d}}{\mathrm{dt}}|K_{L(S)}\rangle = M_{L(S)}|K_{L(S)}\rangle \tag{1.7}$$

where $M_{L(S)} = m_{L(S)} - i\Gamma_{L(S)}/2$ and $m_{L(S)}$ is the $K_{L(S)}$ mass and $\Gamma_{L(S)}$ its decay width. After some algebra, solving Equation 1.7 yields (assuming CPT invariance):

$$\begin{aligned}
|K_L\rangle &= \frac{1}{\sqrt{2(1+|\epsilon|^2)}}[(1+\epsilon)|K^0\rangle - (1-\epsilon)|\overline{K^0}\rangle] \\
&= \frac{1}{\sqrt{1+|\epsilon|^2}}(|K_2\rangle + \epsilon|K_1\rangle) \\
|K_S\rangle &= \frac{1}{\sqrt{2(1+|\epsilon|^2)}}[(1+\epsilon)|K^0\rangle + (1-\epsilon)|\overline{K^0}\rangle] \\
&= \frac{1}{\sqrt{1+|\epsilon|^2}}(|K_1\rangle + \epsilon|K_2\rangle)
\end{aligned}$$

where

$$\begin{aligned}
\epsilon &= \frac{\mathrm{Im}(M_{12}) - i\mathrm{Im}(\Gamma_{12}/2)}{i(m_L - m_S) - (\Gamma_S - \Gamma_L)/2} \\
|K_1\rangle &= \frac{1}{\sqrt{2}}(|K^0\rangle + |\overline{K^0}\rangle) \qquad (CP = +1) \\
|K_2\rangle &= \frac{1}{\sqrt{2}}(|K^0\rangle - |\overline{K^0}\rangle) \qquad (CP = -1)
\end{aligned}$$

The states $|K_1\rangle$ and $|K_2\rangle$ are the CP eigenstates and ϵ is the CP violation parameter that describes the asymmetry in mixing of K^0 and $\overline{K^0}$. ϵ has contributions from both the mass and decay matrices, but one can show from experimental measurements that the contribution from the decay matrix is negligible [10]. Given this and given that $\Gamma_S >> \Gamma_L$ (see Table 2), the phase of ϵ is given by $\arctan(2\Delta m/\Gamma_S) = (43.8 \pm 0.2)^0$, where $\Delta m = m_L - m_S$.

The dominant decay channels for neutral kaons are to 2π ($\pi^+\pi^-$ or $\pi^0\pi^0$) and 3π ($\pi^+\pi^-\pi^0$ or $\pi^0\pi^0\pi^0$) final states. Bose symmetry of the pion requires that the total wavefunction for these states be symmetric. For the 2π final states, because the kaon and pion both have spin 0, angular momentum conservation requires that the two pions be in a relative S state. Pions have

intrinsic $P = -1$ and $C = +1$, so that the overall wavefunction has $CP = +1$. The pions in the 3π final states are predominantly in a relative S-state, so that their total wavefunction has $CP = -1$. Thus if CP were an exact symmetry one would expect $\epsilon = 0$, the K_S should decay to 2π and the K_L should decay to 3π. In addition, the K_S lifetime should be much shorter than that for the K_L due to the greater phase space available in the decay. Experimentally, one observes $|\epsilon|$ as given in Equation 1.1 and the values for the lifetimes as given in Table 2. The value for $|\epsilon|$ given in Equation 1.1 is determined from the observed ratio $\Gamma(K_L \to 2\pi)/\Gamma(K_S \to 2\pi)$ and assuming that $K_2 \to 2\pi$ does not occur. But there may be CP violation in the decay amplitudes as well as CP violation in the mixing phenomenon. To examine this possibility, we need to consider the dynamics of the 2π decay mode.

Let us define η_{+-} and η_{00} to be the following ratio of transition amplitudes:

$$\begin{aligned}
\eta_{+-} &= \frac{\langle\pi^+\pi^-|T|K_L\rangle}{\langle\pi^+\pi^-|T|K_S\rangle} \\
&= \frac{\langle\pi^+\pi^-|T|K_2\rangle + \epsilon\langle\pi^+\pi^-|T|K_1\rangle}{\epsilon\langle\pi^+\pi^-|T|K_2\rangle + \langle\pi^+\pi^-|T|K_1\rangle} \qquad (1.8) \\
\eta_{00} &= \frac{\langle\pi^0\pi^0|T|K_L\rangle}{\langle\pi^0\pi^0|T|K_S\rangle} \\
&= \frac{\langle\pi^0\pi^0|T|K_2\rangle + \epsilon\langle\pi^0\pi^0|T|K_1\rangle}{\epsilon\langle\pi^0\pi^0|T|K_2\rangle + \langle\pi^0\pi^0|T|K_1\rangle} \qquad (1.9)
\end{aligned}$$

We note that if $K_2 \to 2\pi$ does not occur, then $\eta_{+-} = \eta_{00} = \epsilon$. The $\pi\pi$ final state can have I=0 or I=2, where the isospin states $\langle 0|$ and $\langle 2|$ are related to the physical 2π states by:

$$\begin{aligned}
\langle 0| &= \frac{1}{\sqrt{3}}\langle\pi^-\pi^+| - \frac{1}{\sqrt{3}}\langle\pi^0\pi^0| + \frac{1}{\sqrt{3}}\langle\pi^+\pi^-| \\
\langle 2| &= \frac{1}{\sqrt{6}}\langle\pi^-\pi^+| + \frac{2}{\sqrt{3}}\langle\pi^0\pi^0| + \frac{1}{\sqrt{6}}\langle\pi^+\pi^-|
\end{aligned}$$

Following Kleinknecht [13], we define

$$\begin{aligned}
\epsilon_0 &= \frac{\langle 0|T|K_S\rangle}{\langle 0|T|K_S\rangle} \\
\epsilon_2 &= \frac{1}{\sqrt{2}}\frac{\langle 2|T|K_L\rangle}{\langle 0|T|K_S\rangle} \\
\omega &= \frac{\langle 2|T|K_S\rangle}{\langle 0|T|K_S\rangle}
\end{aligned}$$

One then finds that

$$\begin{aligned}\eta_{+-} &= \frac{\epsilon_0 + \epsilon_2}{1 + \omega/\sqrt{2}} \\ \eta_{00} &= \frac{\epsilon_0 - 2\epsilon_2}{1 - \sqrt{2}\omega}\end{aligned}$$

Experimentally, $\Delta I = 3/2$ amplitudes are suppressed with respect to $\Delta I = 1/2$ amplitudes by a factor 1/20, so that $\omega << 1$. Neglecting the ω terms then yields

$$\begin{aligned}\eta_{+-} &= \epsilon_0 + \epsilon_2 \\ \eta_{00} &= \epsilon_0 - 2\epsilon_2\end{aligned}$$

The transition amplitudes for $K^0(\overline{K^0})$ decays to 2π final states can be defined by

$$\begin{aligned}\langle 0|T|K^0\rangle &= A_0 e^{i\delta_0} \\ \langle 2|T|K^0\rangle &= A_2 e^{i\delta_2} \\ \langle 0|T|\overline{K^0}\rangle &= \overline{A_0} e^{i\delta_0} \\ \langle 2|T|\overline{K^0}\rangle &= \overline{A_2} e^{i\delta_2}\end{aligned}$$

where δ_0 and δ_2 are the $\pi\pi$ phase shifts from final state interactions. Further, CPT invariance requires that $A_I = \overline{A_I}^*$ [10]. There is one arbitrary phase which can be fixed by requiring A_0 to be real. We then obtain

$$\begin{aligned}\epsilon_0 &= \epsilon \\ \epsilon_2 &= \frac{i}{\sqrt{2}} \frac{\mathrm{Im}(A_2)}{A_0} e^{i(\delta_2 - \delta_0)}(1 + \epsilon) \\ &\approx \frac{i}{\sqrt{2}} \frac{\mathrm{Im}(A_2)}{A_0} e^{i(\delta_2 - \delta_0)} \\ &\equiv \epsilon'\end{aligned}$$

Thus, η_{+-} and η_{00} may be expressed as

$$\begin{aligned}\eta_{+-} &= \epsilon + \epsilon' \\ \eta_{00} &= \epsilon - 2\epsilon'\end{aligned}$$

The parameter ϵ' measures the difference of η_{+-} from η_{00} and therefore is a signal for direct CP violation (ie. $K_2 \rightarrow 2\pi$) if it is non-zero. It will in general be non-zero if there is a relative phase between the I=0 and I=2 decay

amplitudes, though it is small due to the $\Delta I = 1/2$ rule. Its phase is given by $(\pi/2 + \delta_2 - \delta_0)$; $\delta_2 - \delta_0$ is measured from nuclear scattering experiments to be $(-41.4 \pm 8.1)^0$, so that the phase of ϵ' is $(48.6 \pm 8.1)^0$.[3] This is very nearly the phase of ϵ so that to good approximation

$$\left|\frac{\eta_{00}}{\eta_{+-}}\right| = 1 - 3\left|\frac{\epsilon'}{\epsilon}\right| \tag{1.10}$$

1.3 Experimental Status of CP Violation

The original observation of $K_L \to \pi^+\pi^-$ by Christenson et. al. was very strong evidence for CP violation; but it was necessary, in order to unambiguously prove CP violation, to show that K_L and K_S were coherent states of the same quantum system. This was demonstrated by the experiment of Fitch et. al. [16] in 1965, which observed interference between the decays of K_L and K_S to $\pi^+\pi^-$. Since 1964 CP violation has only been observed with neutral kaons,[4] and the experimental measurements give [8]

$$\begin{aligned}
\eta_{+-} &= (2.275 \pm 0.021) \cdot 10^{-3} e^{i(44.6 \pm 1.2)^0} \\
\eta_{00} &= (2.299 \pm 0.036) \cdot 10^{-3} e^{i(54 \pm 5)^0} \\
\left|\frac{\eta_{00}}{\eta_{+-}}\right| &= 1.009 \pm 0.012
\end{aligned}$$

Another measurement demonstrating CP violation with neutral kaons is the charge asymmetry δ_l,

$$\delta_l = \frac{\Gamma(K_L \to \pi^- l^+ \nu) - \Gamma(K_L \to \pi^+ l^- \nu)}{\Gamma(K_L \to \pi^- l^+ \nu) + \Gamma(K_L \to \pi^+ l^- \nu)}$$

where l is either an electron or a muon. The charge asymmetry can be expressed in terms of ϵ as

$$\delta_l = \frac{1 - |x|^2}{|1 - x|^2} 2\mathrm{Re}\epsilon$$

where x is the ratio of the $\Delta Q = -\Delta S$ to $\Delta Q = +\Delta S$ amplitudes. In the quark model, one expects only $\Delta Q = +\Delta S$ and hence $\delta_l = 2\mathrm{Re}\epsilon$. The experimental measurement is [8]

$$\delta_l = (3.30 \pm 0.12) \cdot 10^{-3}$$

[3] The value for $\delta_2 - \delta_0$ is taken from the review article of Devlin and Dickey [15].

[4] There is evidence for CP violation from lack of observations of antimatter in our region of the universe [2]. If one accepts the big bang scenario for the origin of the universe, then any baryon asymmetry would presumably require CP violation. The connection of this to CP violation in the neutral kaon system remains unclear.

Table 2: Parameters governing the time-evolution of neutral kaons [8]

Parameter	Value
$m_L - m_S$	$(3.521 \pm 0.014) \cdot 10^{-12}$ MeV/c^2
τ_L	$(5.183 \pm 0.040) \cdot 10^{-8}$s
τ_S	$(0.8923 \pm 0.0022) \cdot 10^{-10}$s

which implies $|\epsilon| = (2.33 \pm 0.08) \cdot 10^{-3}$ (assuming ϵ has the same phase as η_{+-}) in good agreement with $|\epsilon|$ determined from η_{+-} and η_{00}. The values for the K_L–K_S mass difference, Δm, as well as the K_L and K_S lifetimes, τ_L and τ_S, have also been well measured in the many neutral kaon experiments and their values are given in Table 2.

1.4 *CP* Violation in the Standard Model

The Standard Model of electroweak interactions provides a framework for accommodating CP violation. The phenomena of K^0–$\overline{K^0}$ mixing and the decay of a neutral kaon to two pions are described in this model by the Feynman diagrams in Figures 1 and 2. Each vertex in these diagrams (Figure 3) contributes the following amplitude [17]

$$\mathcal{A} \propto -i\frac{g}{\sqrt{2}} U_{ij}\gamma_\mu \left(\frac{1-\gamma_5}{2}\right)$$

where

i, j label the two quarks,

U_{ij} are the 'quark mixing angles' that transform the strong quark eigenstates to the weak quark eigenstates, and

γ_μ, γ_5 are the gamma matrices

The Standard Model has 3 generations of up-like quarks of charge +2/3 and down-like quarks of charge -1/3 (Figure 4). By convention, mixing is confined to the down-like quarks so that the down-like weak eigenstates are related to the down-like quark eigenstates by: [18]

$$\begin{pmatrix} d' \\ s' \\ b' \end{pmatrix} = \begin{pmatrix} U_{ud} & U_{us} & U_{ub} \\ U_{cd} & U_{cs} & U_{cb} \\ U_{td} & U_{ts} & U_{tb} \end{pmatrix} \begin{pmatrix} d \\ s \\ b \end{pmatrix} \tag{1.11}$$

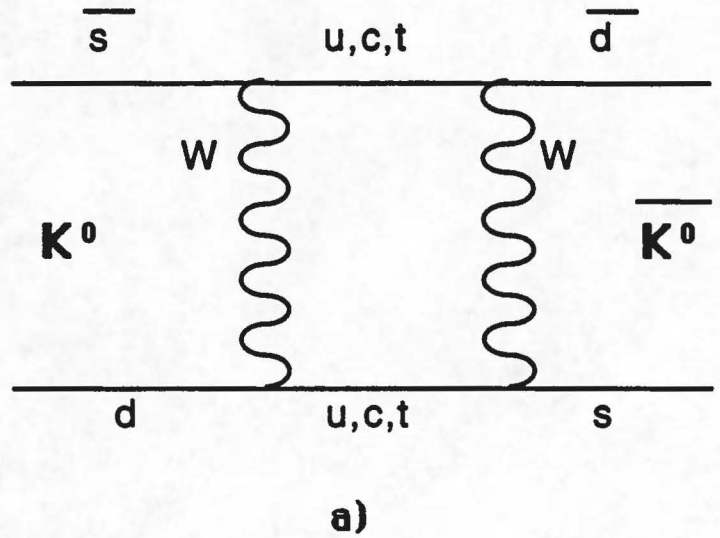

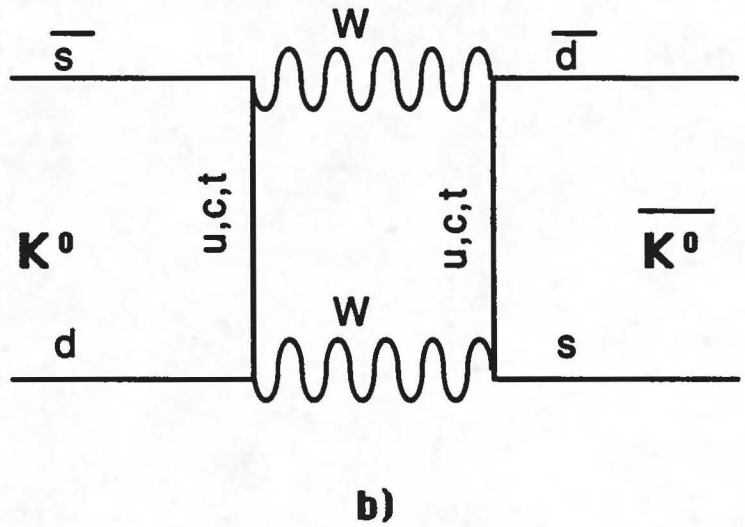

Figure 1: Box diagrams for K^0–$\overline{K^0}$ mixing in the Standard Model

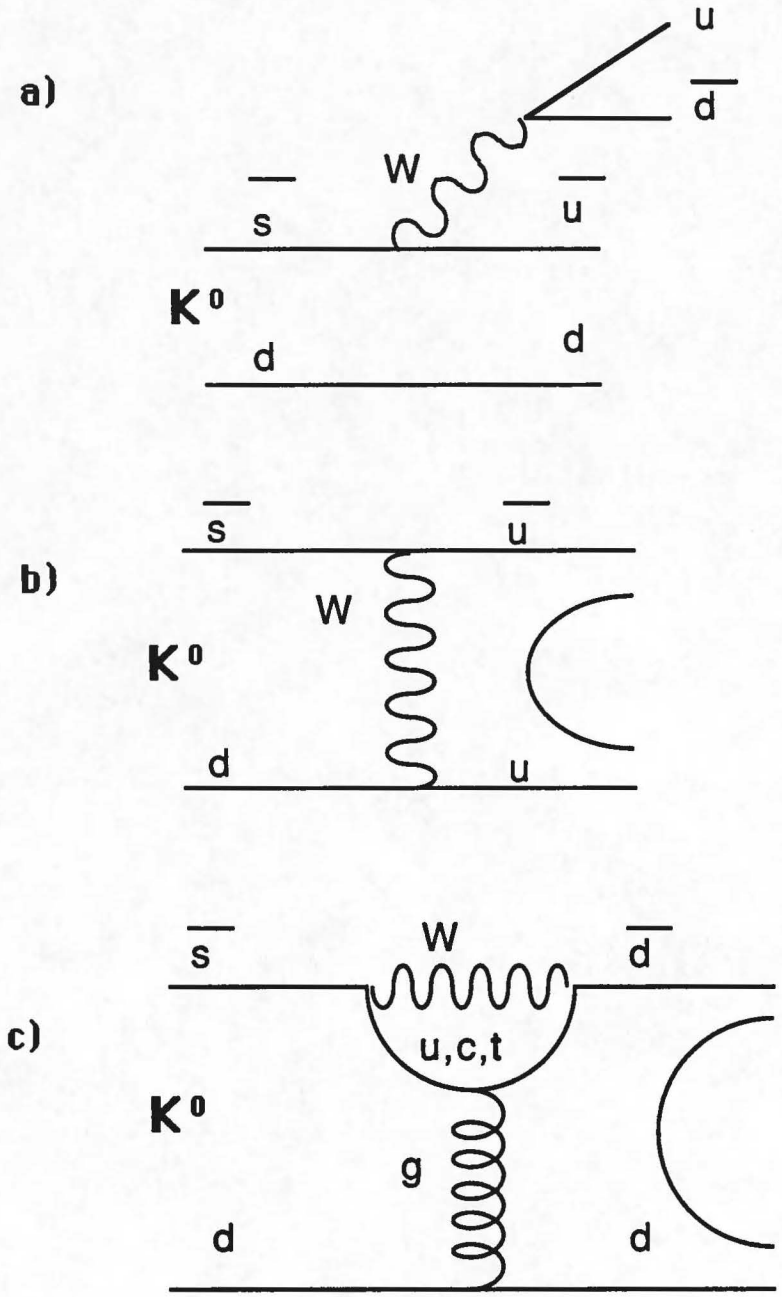

Figure 2: Diagrams for the 2π decay of neutral kaons in the Standard Model: a) 'Spectator' diagram; b) 'Exchange' diagram; c) 'Penguin' diagram

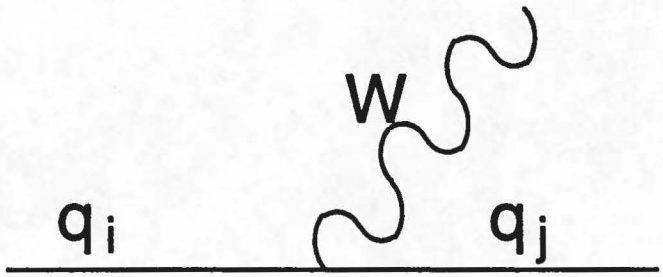

Figure 3: quark-quark-W vertex

			Charge
$\begin{pmatrix} u \\ d \end{pmatrix}$	$\begin{pmatrix} c \\ s \end{pmatrix}$	$\begin{pmatrix} t \\ b \end{pmatrix}$	$+2/3$ $-1/3$

Figure 4: Three generations of quarks in the Standard Model

The Kobayashi-Maskawa (K–M) matrix, U_{ij}, is a 3x3 unitary matrix with four free parameters—3 Cabibbo-like angles and 1 phase. The phase, if non-zero, allows for CP and T violation. In this model, one cannot have CP violation with only two generations (4 quarks) since then there is only 1 free parameter which is the Cabibbo angle. The desire to accommodate CP violation in the Standard Model was the motivating factor for Kobayashi and Maskawa to consider the possibility of 3 generations and propose the matrix U, prior to the discovery of even a fourth quark.

Five quarks have so far been discovered (the top quark remains elusive) and our knowledge of the K–M matrix, assuming unitarity and 3 generations, is summarized by the following 90% confidence limits for the magnitudes of the elements U_{ij}: [8]

$$\begin{pmatrix} 0.9742 - 0.9756 & 0.219 - 0.225 & 0. - 0.008 \\ 0.219 - 0.225 & 0.973 - 0.975 & 0.037 - 0.053 \\ 0.002 - 0.018 & 0.036 - 0.052 & 0.9986 - 0.9993 \end{pmatrix} \tag{1.12}$$

Recently, the Argus experiment has reported [19] evidence for $b \rightarrow u$ transitions that would imply $|U_{ub}/U_{cb}| > 0.07$. This is important, because if any of the U_{ij} were to be identically 0, the phase would have to be 0 and there would be no CP violation. Unitarity for 3 generations requires that the sum of the squares of the K–M matrix elements in any row or column be equal to 1. Since the top quark has not been found yet, the elements in the third row given above have been derived from this condition.

Given these values, Wolfenstein has suggested a phase convention with the following form for the matrix U [9]:

$$U = \begin{pmatrix} 1 - \lambda^2/2 & \lambda & A\lambda^3(\rho - i\eta) \\ -\lambda & 1 - \lambda^2/2 & A\lambda^2 \\ A\lambda^3(1 - \rho - i\eta) & -A\lambda^2 & 1 \end{pmatrix} \tag{1.13}$$

Equations 1.12 and 1.13 then give

$$\lambda = 0.220 \pm 0.002 \tag{1.14}$$

$$A = 1.0 \pm 0.2 \tag{1.15}$$

$$\rho^2 + \eta^2 \leq 1.3 \tag{1.16}$$

To determine ϵ requires evaluating the box diagrams of Figure 1. This involves the difficult calculation of the matrix element

$$\mathcal{M} = \langle \overline{K^0} | \bar{s}\gamma_\mu(1 - \gamma_5) d \bar{s}\gamma^\mu(1 - \gamma_5) d | K^0 \rangle$$

where $\bar{s}$ and d are quark field operators. One approach is to insert the vacuum state between the quark operators $d\bar{s}$, which splits $\mathcal{M}$ into two matrix elements that can be calculated. One then defines the parameter B such that

$$\langle\overline{K^0}|\bar{s}\gamma_\mu(1-\gamma_5)d\bar{s}\gamma^\mu(1-\gamma_5)d|K^0\rangle = B\langle\overline{K^0}|\bar{s}\gamma_\mu(1-\gamma_5)d|0\rangle\langle 0|\bar{s}\gamma^\mu(1-\gamma_5)d|K^0\rangle$$

The uncertainties in B are large—most calculations give values for B on the order of 1/3, but this is uncertain to a factor of 2 [9]. Wolfenstein has arrived at the following form for $|\epsilon|$ that results from the box diagram calculation of M_{12} and uses the experimental value for Δm: [9]

$$|\epsilon| = 0.6\lambda^4 A^2\eta B[-n_1 + n_2\ln(m_t^2/m_c^2) + n_3\lambda^4 A^2(1-\rho)(m_t^2/m_c^2)] \quad (1.17)$$

where n_i are QCD correction factors: $n_1 = 0.7, n_2 = 0.4, n_3 = 0.6$ for $\Lambda_{QCD}^2 = 0.01$ GeV^2; and the n_3 term is an approximation for $m_t << m_W$. For m_t in the range 35 GeV/c^2 to 60 GeV/c^2, Wolfenstein claims a good approximation for $|\epsilon|$ is

$$|\epsilon| = (3.1\cdot 10^{-3})A^2\eta B[1 + \frac{1}{2}A^2(1-\rho)(m_t/42\mathrm{GeV}/c^2)^2] \quad (1.18)$$

The experimental value for $|\epsilon|$ can be accommodated, but it favours values for B and m_t closer to the upper limits of the ranges stated. If m_t is greater than 60 GeV/c^2, $|\epsilon|$ is more easily accommodated.

The contribution to ϵ' in the Standard Model is believed to mainly arise from the Penguin diagram of Figure 2c. The spectator and exchange diagrams of Figures 2a and 2b do not contribute since they do not not involve all three generations of quarks, and the K–M phase therefore does not enter. Calculation of the Penguin diagram also involves a difficult calculation of a matrix element of a 4 quark operator. This time the uncertainty gets absorbed into a factor P, where P is defined by

$$P = \frac{\langle\pi^+\pi^-|\mathcal{O}_5|K^0\rangle}{0.43\mathrm{GeV}^3} \quad (1.19)$$

and $\mathcal{O}_5$ is the relevant 4 quark operator. Donoghue et. al. [20] find $0.7 < P < 2.6$, and Wolfenstein gives

$$|\epsilon'| = 1.27\cdot 10^{-6}A^2\eta P\ln(m_t^2/m_c^2) \quad (1.20)$$

Taking the experimental value for $|\epsilon|$ and the constraint that places on η, Wolfenstein then determines $|\epsilon'/\epsilon|$ to be in the range 0.001 to 0.007. The sign is most likely positive, though this is not completely certain. A recent

calculation by Donoghue et. al. [20] has also included contributions from an electromagnetic Penguin, where the gluon in Figure 2c is replaced by a photon. The effect of this is to add an additional 30% uncertainty to ϵ' calculated solely from the penguin diagram, and the authors give $0.002 < |\epsilon'/\epsilon| < 0.01$. They point out that heavier top quark masses ($m_t > 60$ GeV/c^2) imply smaller values for $|\epsilon'/\epsilon|$, as is apparent from the ratio of Equations 1.20 and 1.18.

A recent paper by Buras and Gérard [21] claims to accurately calculate the hadronic matrix elements associated with the box and penguin diagrams using a $1/N$ approach, where N is the number of quark colors. They obtain $B \approx 2/3$ and give the following result for $|\epsilon'/\epsilon|$,

$$|\epsilon'/\epsilon| = 2.1 \cdot 10^{-3}[150\text{MeV}/m_s(1\text{GeV})]^2(M_W/m_t)^{4/3}[\beta^{4/5}/(1 + 8/3\sqrt{\overline{R}})]$$

where

m_s (1GeV) is the strange quark mass,[5]

M_W is the W mass,

m_t is the top quark mass,

β is related to the b quark lifetime: $\tau_b = \beta \cdot 10^{-12}$s, and

$\overline{R}$ is the relative branching ration of $b \to u$ to $b \to c$, $\overline{R} = \text{B}(b \to ue\nu)/\text{B}(b \to ce\nu)$

For $0.01 \leq \overline{R} \leq 0.1$, $\tau(B) = 1.1 \cdot 10^{-12}$s, and 55 GeV/c$^2 \leq m_t \leq 130$ GeV/c^2, this gives

$$|\epsilon'/\epsilon| = (1.7 \pm 1.0) \cdot 10^{-3}[150\text{MeV}/m_s(1\text{GeV})]^2$$

The authors do not include contributions from the electromagnetic penguin diagram, and they only calculate the hadronic matrix elements to lowest order in $1/N$. Since $N = 3$ is not very large, one has to worry about higher order effects; but this Standard Model prediction is a strong statement, and hopefully other precise predictions (at the level of ± 0.001 in $|\epsilon'/\epsilon|$) will soon be forthcoming.

The Standard Model predictions for the CP violating parameters ϵ and ϵ' are therefore in good agreement with the data, though the predictions currently have large uncertainties. CP violation and all other measured phenomena still do not require any new physics beyond the minimal theory.

[5]This is the current algebra mass that appears in the QCD Lagrangian; it runs with energy as does the strong coupling constant. A review of quark masses may be found in reference [22], which gives m_s (1GeV) $= 180 \pm 50$ (MeV/c^2).

1.5 CP Violation from Other Sources

In the Standard Model, CP violation arises from complex couplings of quarks to charged W's. Some extensions of the Standard Model have similar sources of CP violation[6]. A fourth generation of quarks would introduce 3 new angles and 2 new phases into the K–M matrix and these extra parameters would facilitate accommodating the experimental measurements. In left-right symmetric models there can be complex couplings of quarks to right-handed W's so that CP violation could arise even for two generations of quarks. If there are extra Higgs bosons in the theory, there could also be CP violating effects from complex Yukawa couplings of quarks to charged Higgs. Also, more than one Higgs boson would allow for a physical relative phase between vacuum expectation values of a given pair of Higgs bosons; this spontaneous symmetry breaking mechanism would then generate CP violation.

In Equation 1.5 the term $\langle \overline{K^0} | H_w | K^0 \rangle$ was argued to be 0 since there is no $\Delta S = 2$ weak interaction in lowest order. Wolfenstein proposed in 1964 a new 'superweak' interaction that would have $\Delta S = 2$ in lowest order and a strength of order 10^{-9} with respect to the weak interaction [23]. The parameter $|\epsilon|$ sets this strength and one would expect $|\epsilon'/\epsilon|$=0 (no $\Delta S = 1$ amplitudes in lowest order). This model can not yet be ruled out.

Gauge theories of electroweak interactions allow for CP violation as described above and do not allow for CP violation in purely electromagnetic interactions (ie. processes with no W's, Z's or Higgs). In gauge theories of strong interactions one can have a CP violating term in the Lagrangian of the form $\theta/16\pi(G^*_{\mu\nu}G^{\mu\nu})$, where $G^{\mu\nu}$ is the gluon field strength tensor and θ is a new parameter in the theory. The θ term violates P and T invariance and is similar in nature to P and C violation in weak interactions; one might therefore expect it to be large. However, experimental limits on the electric dipole moment of the neutron[7] require $\theta < O(10^{-9})$, and this is too small to produce the observed CP violation in the kaon system. Why the θ term is so small has come to be known as the strong CP problem[8], and it may be due to a symmetry mechanism suggested by Peccei and Quinn [26].

1.6 Objectives of this Experiment

This experiment has set out to search for direct CP violation and to determine $|\epsilon'/\epsilon|$ to a precision of 0.001. From Equation 1.10, $|\epsilon'/\epsilon|$ can be determined from

[6]See [9] and references therein.

[7]The best limit comes from reference [24], $|d_n| < 2.6 \cdot 10^{-25}$ e-cm at 95% confidence level.

[8]For a recent review of the strong CP problem, see reference [25].

measurements of the relative decay rates of K_L and K_S to charged and neutral pions. Chapter 2 gives a detailed discussion of the experimental techniques and apparatus we have used to make these measurements. Particular attention is paid to systematic effects, since this experiment is required to look for a small asymmetry and one therefore needs a careful understanding of effects that could give a false signal. The technique used for the measurements is one that has evolved from an earlier experiment at Fermilab (E617), and the experience gained there has greatly influenced the design of the current experiment.

This thesis reports results for $|\epsilon'/\epsilon|$ from a first run of the new experiment, FNAL E731. The data collection for this run took place during July and August of 1985 and enough data were taken to make a measurement of $|\epsilon'/\epsilon|$ with a sensitivity of 0.003 (combined statistical and systematic error). The data collection for a second run has just been completed (February 1988) with a significant increase in statistics over the 1985 run, and a statistical error of 0.0005 for $|\epsilon'/\epsilon|$ is expected from this. As with E617, much was learned from the first run of E731 and this thesis shall give a careful and detailed description of this experiment and the $|\epsilon'/\epsilon|$ analysis. Much attention is focused on systematic effects and systematic checks of the analysis, since these will have a critical bearing on results from the second run, especially if that data indicate that direct CP violation does indeed exist.

Chapter 2

The Experiment

We have shown that one can search for direct CP violation by measuring the deviation of $|\eta_{00}/\eta_{+-}|^2$ from unity. Our experiment simultaneously measures K_L and K_S decays to 2π final states ($\pi^0\pi^0$ or $\pi^+\pi^-$) using a double beam technique. Decays are observed from two nearly parallel kaon beams far downstream of the production target, so that the initial K_S component of the beam has decayed away. One of these beams has material in it (the Regenerator) to produce K_S, while the other beam has only a K_L component. $K \rightarrow 2\pi$ decays are observed in a 14m Decay Region downstream of the Regenerator, where nearly all of the regenerated K_S decay. The relative 2π rates from the two beams are then determined for both $\pi^0\pi^0$ and $\pi^+\pi^-$ final states, and these rates are compared to extract $|\eta_{00}/\eta_{+-}|^2$. This chapter discusses the principles of this measurement and the detector which was built to perform the measurement.

2.1 Principles of the Measurement

The precise details of how $|\epsilon'/\epsilon|$ is extracted from the 2π rates are given in Chapter 10. For a quick and approximate derivation, however, ignore for the moment CP violating decays in the regenerator beam. The relative number of K_S in the regenerator beam to K_L in the vacuum beam is given by $|\rho|^2$ where ρ is the amplitude for $K_L X \rightarrow K_S X$ and X is our Regenerator. The experiment is run in two separate modes—one in which $K_{L(S)} \rightarrow \pi^0\pi^0$ events are detected (neutral mode), and one in which $K_{L(S)} \rightarrow \pi^+\pi^-$ events are detected (charged mode). For a given mode and for a given kaon energy, the ratio of the 2π rate in the regenerator beam to the 2π rate in the vacuum beam is determined. This ratio is proportional to $|\rho/\eta|^2$, and a comparison of the charged and neutral

ratios gives the double ratio

$$\begin{aligned}\mathcal{R} &= \frac{|\rho/\eta_{+-}|^2}{|\rho/\eta_{00}|^2} \\ &\equiv \frac{R^{+-}}{R^{00}}\end{aligned}$$

Because the same Regenerator is used for charged and neutral modes, the $|\rho|^2$ factors cancel and one obtains

$$\mathcal{R} = \left|\frac{\eta_{00}}{\eta_{+-}}\right|^2$$

from which $|\epsilon'/\epsilon|$ can be extracted using Equation 1.10.

We are attempting to search for direct CP violation by measuring the deviation of $\mathcal{R}$ from unity, and it is expected from theory and past experiments that the deviation will be at most 3–5%. The goal of this experiment, as stated in Chapter 1, is to measure $|\epsilon'/\epsilon|$ with a sensitivity of 0.001, which corresponds to a sensitivity of 0.6% for $\mathcal{R}$. To do this requires high statistics—detection and full reconstruction of at least 50,000 events of each of the following decay modes:

$$\begin{aligned}K_L &\rightarrow \pi^0\pi^0 \\ K_S &\rightarrow \pi^0\pi^0 \\ K_L &\rightarrow \pi^+\pi^- \\ K_S &\rightarrow \pi^+\pi^-\end{aligned}$$

In addition, controls of possible systematic errors are very important. One wants a detector with very good resolution and background rejection to achieve a good signal to noise ratio. One also wants a well understood detector acceptance for each of the decay modes, since determining the 2π rates results from correcting for acceptance the observed number of 2π events. The next section shall describe the E731 detector which was designed to achieve these goals.

2.2 Beamline and Detector

A new beamline and detector were constructed for this experiment, and these were optimized for studying $K \rightarrow 2\pi$ decays. The beamline was designed to provide a high flux kaon beam with a good kaon to neutron ratio. The detector was designed to achieve good resolution, operate at high rates, and

provide good background rejection. The mean detected kaon energy was approximately 70 GeV, with kaons in the energy range 30–160 GeV being used in the analysis.

For measuring energies and positions of photons and electrons, a Lead Glass electromagnetic calorimeter was used. This is the same calorimeter that was used in E617, but it was reconfigured from a rectangular array to a circular array for this experiment. A Drift Chamber spectrometer was used for measuring trajectories and momenta of charged particles. For reducing background from $K_L \rightarrow 3\pi^0$ events, where one or two photons miss the Lead Glass so as to fake $K_L \rightarrow 2\pi^0$ events, a large number of photon veto planes were employed to detect extra photons. For reducing background from inelastic processes in the Regenerator, the Regenerator was longitudinally segmented into four sections with an *RA* (Regenerator Anti) scintillator plane at the end of each section. The beamline and detector elements for E731 are shown in Figures 5 and 6, and we will now discuss the key features of these.

2.2.1 Beamline

The experiment was run in the M Center beamline at Fermilab. The 800 GeV proton beam struck a one interaction length Be target at a targeting angle of 4.8 mrad in the horizontal plane. This targeting angle was chosen as a compromise between getting a high kaon flux (greatest at 0^0), and achieving a good kaon to neutron ratio (best at large angles). There were typically 10^{12} protons per spill incident on our target, and the Tevatron delivered one 20s spill of protons every minute; the 20s spill had an rf substructure of 2ns 'buckets' of protons every 18.8ns. The duty factor for the machine was approximately 35%, which represents a factor 5 improvement over the 400 GeV pre-Tevatron era, where the spill structure was 850ms of beam every 12s. This improvement greatly aided the experiment's ability to produce and detect a large sample of kaons, with reasonable background rates in the detector components.

Immediately downstream of the target were sweeping magnets to eliminate charged particles, and this was followed by a two-hole collimator, which also served as the beam dump. This collimator was 5.8m of water-cooled Cu with two tapered precision machined holes, each 1.0cm x 1.0cm in cross-section (at the downstream end of the collimator), having their centers spaced 1.8cm apart. The solid angle of the beams defined by the two-hole collimator was roughly twice as large as the final beam sizes defined by CH1, CV1 and the second slab collimator (Figure 5).

To convert photons, 7.5cm of Pb was placed in the beams and more sweeping magnets downstream of this swept away the resulting electron-positron

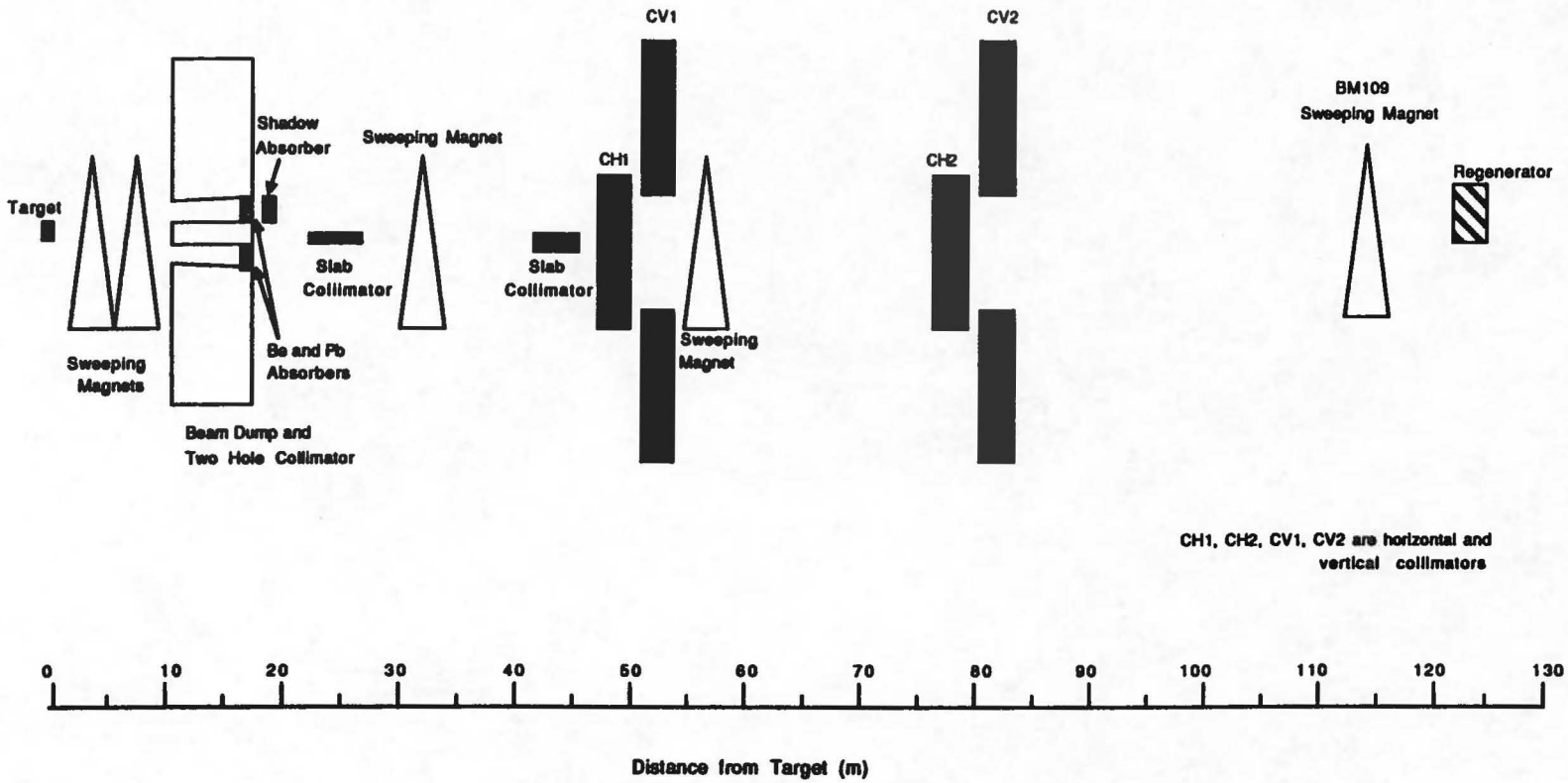

Figure 5: Meson Center Beamline for E731 at Fermilab

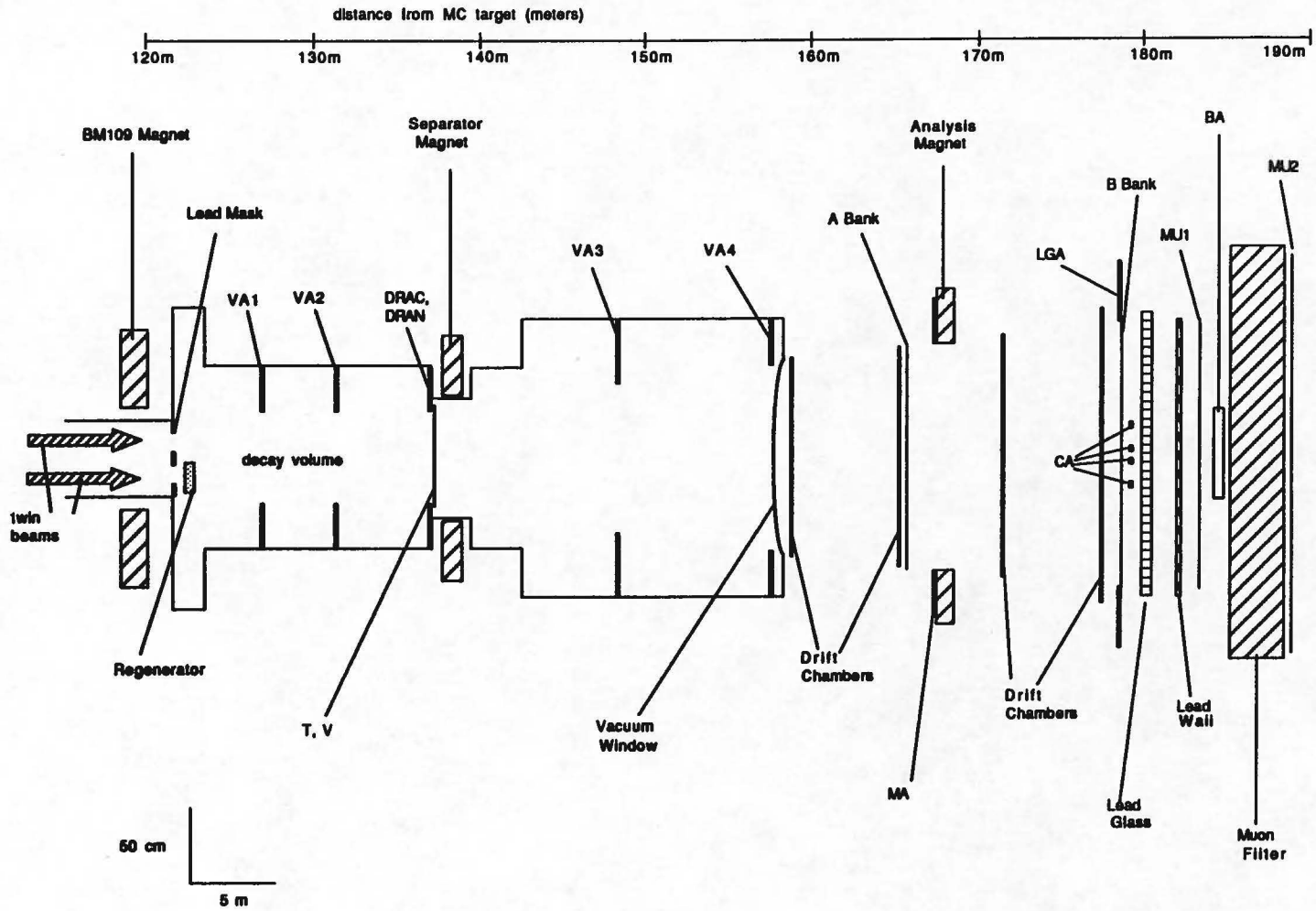

Figure 6: E731 Detector

pairs. To further enhance the kaon to neutron ratio, 54cm of Be was placed in each beam, and the resulting neutron to kaon ratio was less than 2:1. This represents nearly a factor 10 improvement with respect to E617, and largely resulted from reducing secondary neutrons produced in the walls of the first collimator. For E617 the first collimator was much closer to the target and the solid angle of the collimator walls was many times larger than that of the beam.

Following the Pb and Be absorbers which were common to both beams, there was an additional 45.7cm of Be (the Shadow Absorber) placed in the same beam as the Regenerator. The Shadow Absorber and Regenerator alternated between the two beams once every machine cycle (60s). This absorber reduced the kaon intensity by a factor of 3.5 to make more comparable the observed number of 2π decays between the beams, and to reduce the instantaneous rates in the detector components (in particular the RA counters). With the absorber, approximately three times as many 2π events are observed from the regenerator beam as from the vacuum beam.

The beams entered vacuum after the Shadow Absorber, and this vacuum continued to the Vacuum Window just upstream of Chamber 1. The beam sizes were defined by the slab collimator 50m downstream of the target and the first set of horizontal and vertical collimators, CH1 and CV1, shown in Figure 5. A second set of collimators, CH2 and CV2, were downstream of this, but were set at a wider aperture. More sweeping of charged particles was achieved with magnets at 60m and 115m.

2.2.2 The Regenerator and Decay Region

The Regenerator configuration is shown in Figure 7. It consisted of four 19cm B_4C blocks, each of which was followed by 1.27cm of Pb and 0.635cm of scintillator. The phenomenon of regeneration is discussed in Appendix A, and it is noted there that three components to the regenerated K_S signal exist. Coherent regeneration is the process $K_L\ X \rightarrow K_S\ X$ and the K_S is produced along the initial direction of the K_L. The regeneration amplitude, ρ, for this process is proportional to the difference in forward scattering amplitudes of K^0 and $\overline{K^0}$. A K_S can also be regenerated at a finite angle with respect to the K_L, in which case there is a scattering process involving a nucleus recoiling (diffractive regeneration) or a nucleus breaking up (inelastic regeneration). Our measurement uses only the coherent signal, so the diffractive and inelastic signals are treated as backgrounds. The Regenerator composition and length were chosen to maximize the coherent signal and minimize the diffractive signal as discussed in the Appendix. The RA (Regenerator Anti) scintillator counters

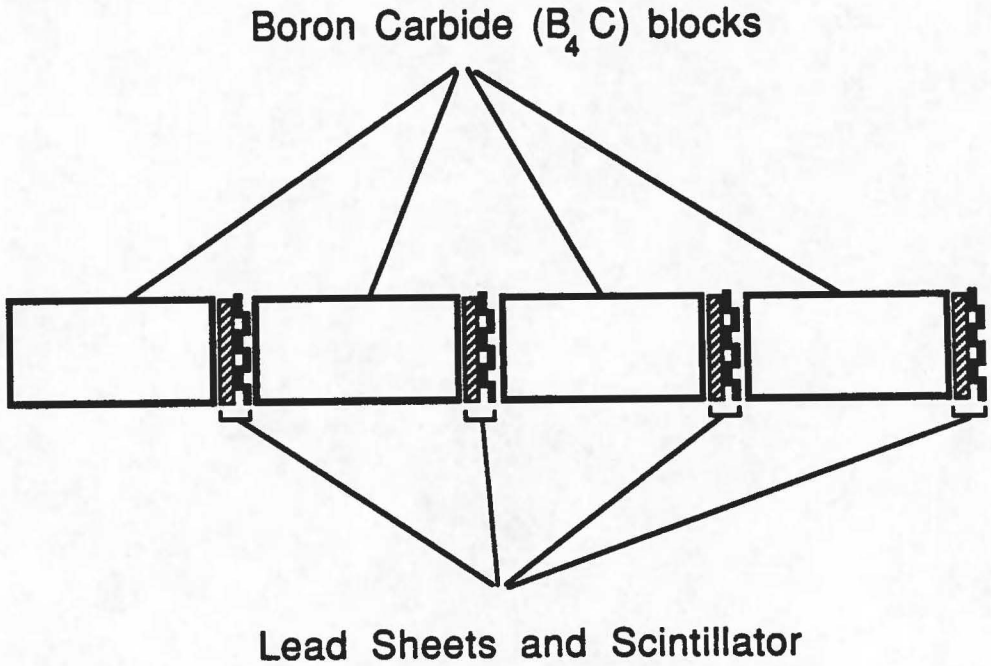

Figure 7: Side view of Regenerator

detected inelastic processes that produced charged particles and rejected such events. The purpose of the Pb was to convert photons from π^0 decays. The RA counters served a second function, which was to give a well defined edge to the start of the Decay Region for the regenerator beam by vetoing events with a charged particle upstream of the fourth layer of RA counters (RA4). Note that this does veto upstream $K \rightarrow 2\pi^0$ events since the π^0's decay to two photons which then produce electromagnetic showers in the B_4C and Pb which are detected by the RA counters.

For the vacuum beam there was no similar hard edge to define the start of the Decay Region. The upstream acceptance for 2π decays in the vacuum beam was determined by the Lead Mask aperture located just upstream of the Regenerator. This Mask was 5.1cm thick and had two 10.16cmx10.16cm holes for the beams to pass.

The downstream end of the Decay Region was defined by the V and T scintillator planes in the HDRA (Figure 8). A signal in V was required for charged mode events, thereby requiring decays to be upstream of it. For the neutral mode an 0.1 radiation length Pb converter was placed between the V and T planes and neutral events were required to have no signal in V accompanied by a signal in T. This signified a photon conversion (to an

electron-positron pair) in the Pb, and therefore required decays to be upstream of this plane. The photon conversion requirement served two purposes. First, it allowed the downstream end of the Decay Region to be well-defined by hardware. If there were no hardware determination of this, one would have had to make a software requirement instead which could have caused a significant bias if the energy scale of the Lead Glass calibration had an uncertainty at the level of 0.1%. Second, tracking information of the electron-positron pair allowed a precise determination of the transverse decay vertex, which was very useful for background rejection. The V and T planes were surrounded by the DRAC (Decay Region Anti Charged) and DRAN (Decay Region Anti Neutral) veto counters, which converted any photons hitting in that region. Thus, $K \rightarrow 2\pi$ events with a photon outside the aperture defined by V and T were eliminated.

2.2.3 The Charged Particle Spectrometer

Charged particles were tracked and momentum analyzed with the Drift Chamber spectrometer. There were four Drift Chambers, each having 2 x planes and $2y$ planes with 0.635cm sense wire spacing. The cell geometry is shown in Figure 9. The chambers were designed to have good resolution, perform at high rates, and contain a minimum of material to reduce multiple scattering of charged particles. They achieved a position resolution of 150μm/wire and an efficiency of 98%/wire. Details of the design, construction and performance are given in Chapter 3. The Analysis Magnet between chambers 2 and 3 had a 1.47m gap between pole faces and gave a transverse momentum kick of ± 200 MeV/c (± 100 MeV/c) to the π^+ and π^- (e^+ and e^-) in charged (neutral) mode running. A second magnet (Separator Magnet) immediately downstream of the HDRA was used in neutral mode to give an opening angle to the electron-positron pair. The Separator Magnet gave a 28 MeV/c transverse momentum kick, of opposite polarity with respect to the Analysis Magnet, so as to result in reconvergence of the pair at the Lead Glass array. This gave a good topology for triggering with the A and B scintillator banks and for pattern recognition in the Lead Glass.

Figures 10 and 11 show the segmentation of the A and B banks; these counters were used in both charged and neutral modes to trigger on two track topologies. The A bank was made of thin (2mm) scintillator to reduce multiple scattering, while the B Bank scintillator was 1cm thick.

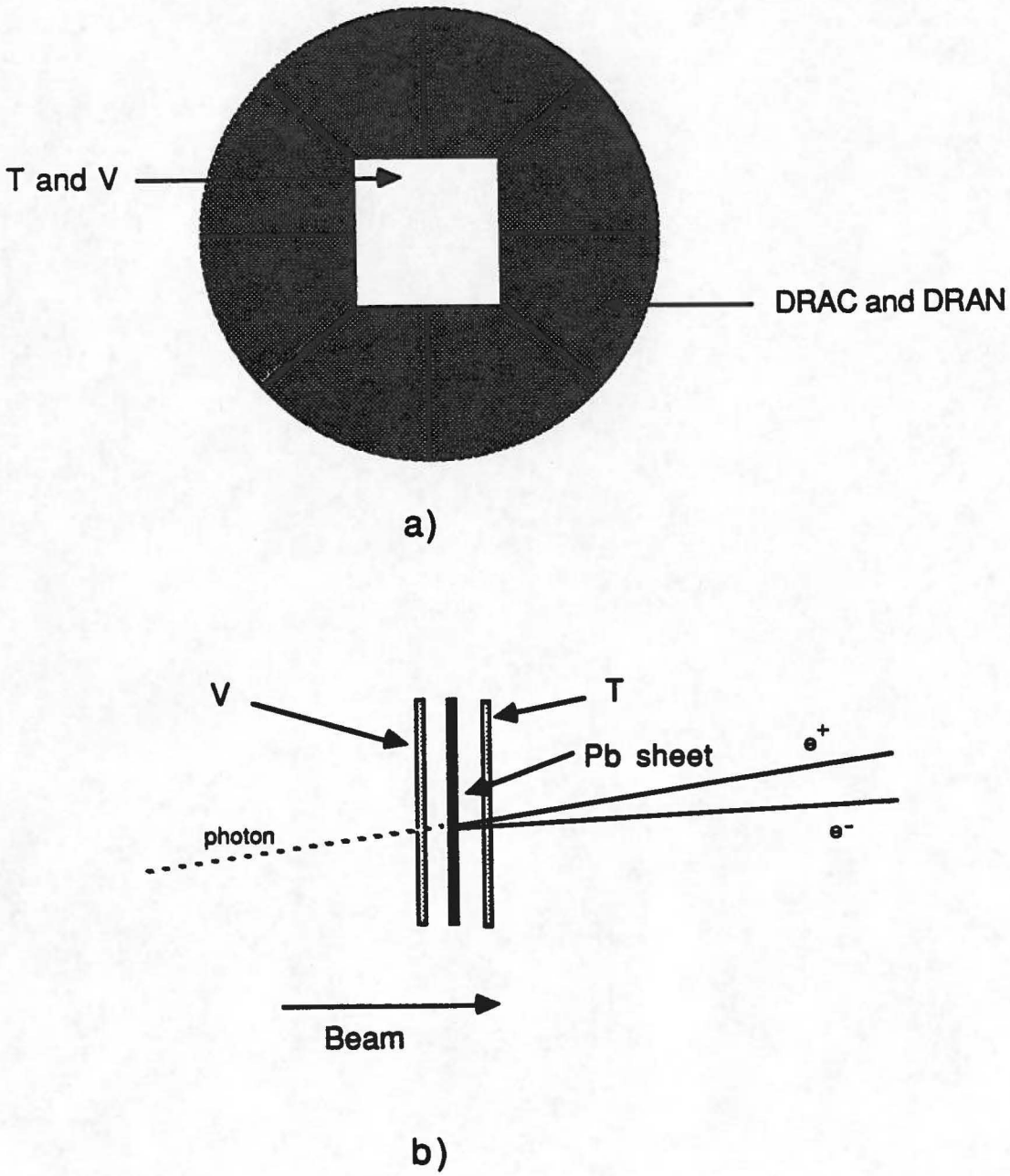

Figure 8: Configuration of HDRA Counters. a) Beam's view of counters; b) Side view of V, T and Pb Converter

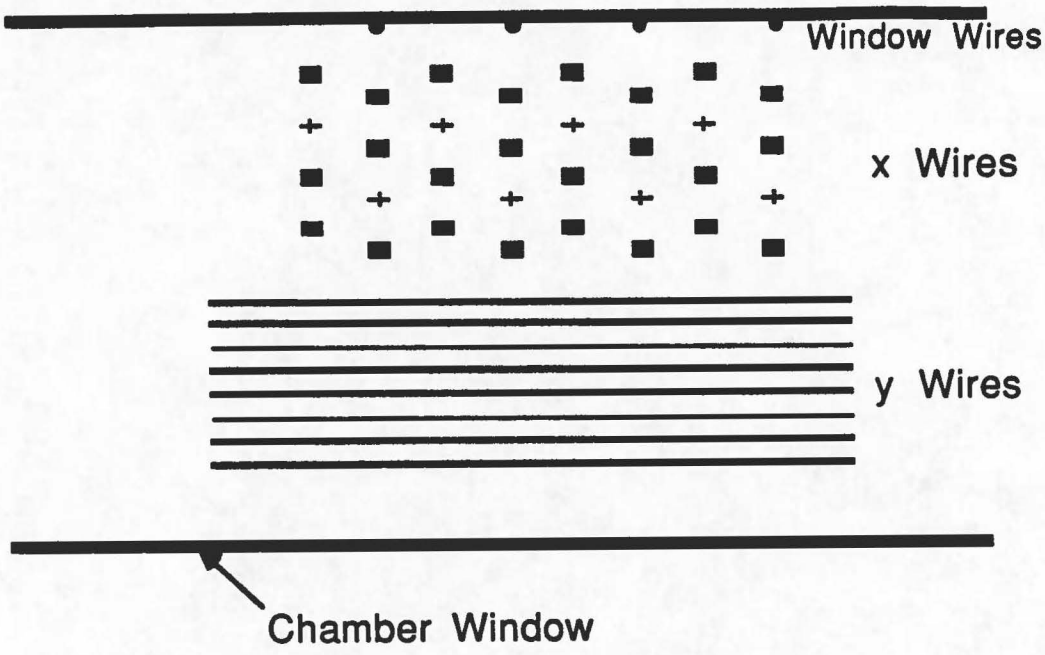

Figure 9: Cell geometry for drift chamber wires

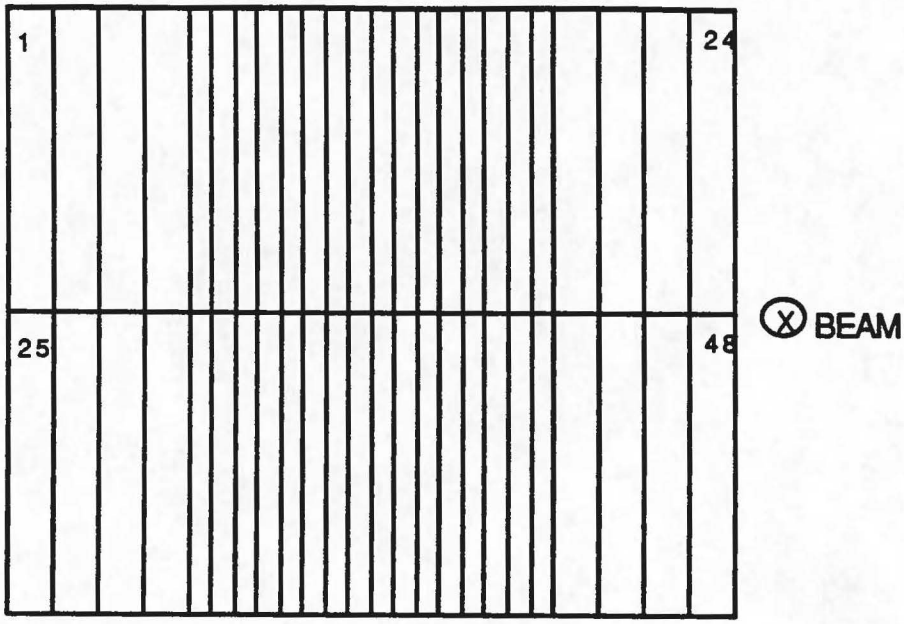

Figure 10: Beam's view of A Bank

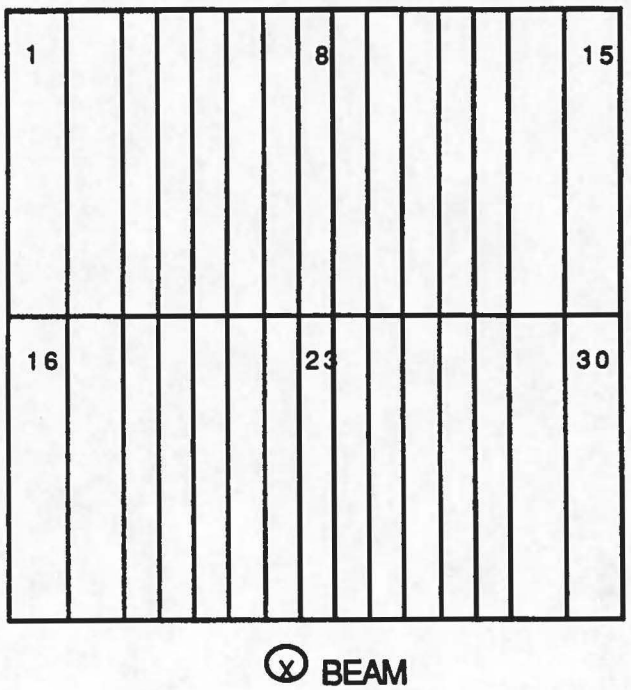

Figure 11: Beam's view of B Bank

2.2.4 The Electromagnetic Calorimeter

Position and energy measurements of electrons and photons were made with an 804 element Lead Glass Array. Each block of Lead Glass measured 5.81cm x 5.81cm x 60.96cm, giving a depth of 20 radiation lengths. The characteristics of this Lead Glass are described in reference [27], and in Chapter 4 the details of its calibration, resolution and use in the analysis are described. The stacking arrangement of the array is shown in Figure 12—two beam holes, each approximately 11.6cm x 11.6cm, allow the beams to pass. There is a large loss in acceptance due to these two holes (on the order of a factor two), but it was not possible to have a precision calorimeter in the intense kaon and neutron beam. There were no corresponding holes in the Drift Chambers or A and B Banks which were comprised of little material and could withstand the high rates. Typical rates over an entire plane such as the A Bank were approximately 1 MHz. (One of the improvements over E617 was eliminating the beam pipe that went from the Vacuum Window through the Lead Glass.)

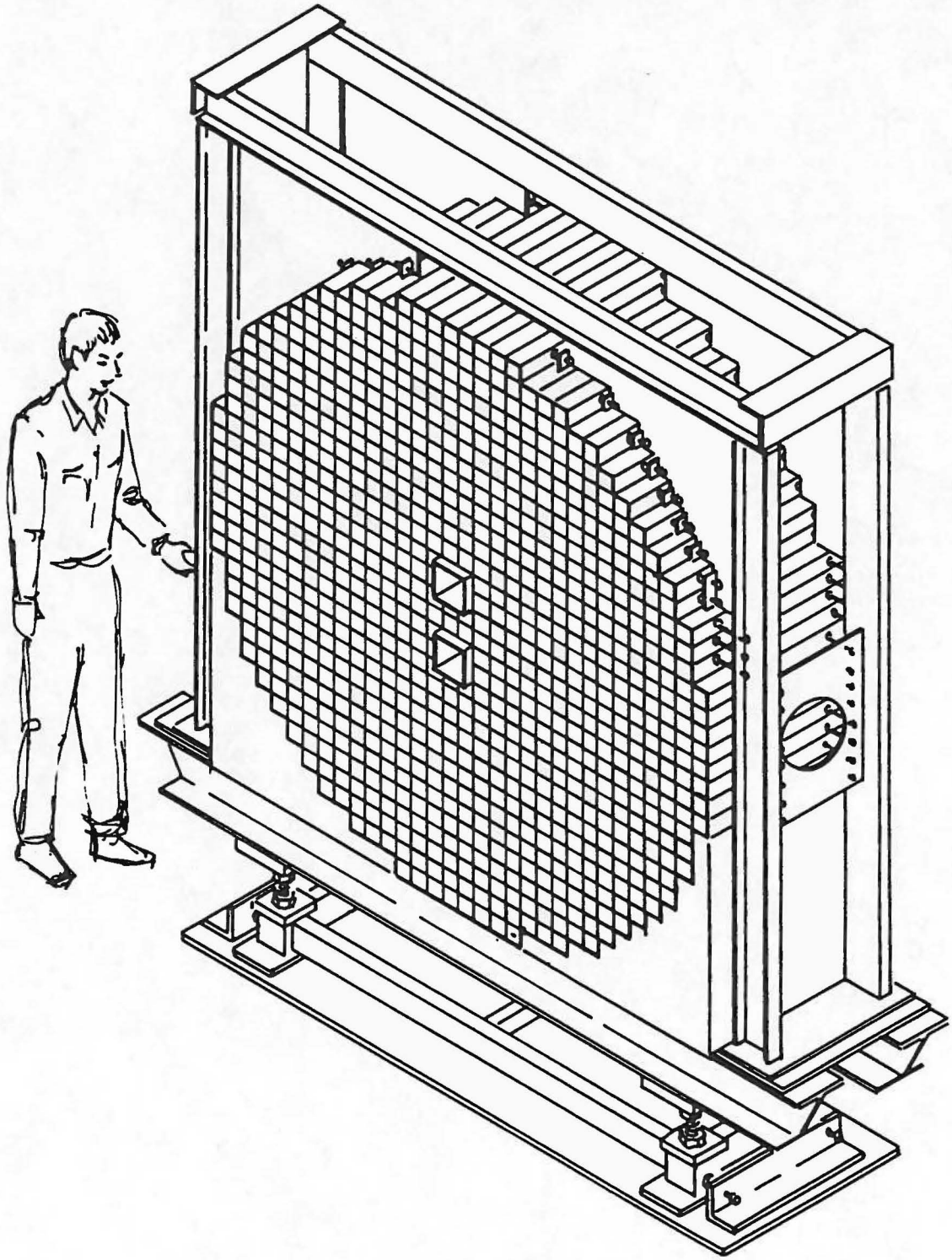

Figure 12: Lead Glass array and stand

2.2.5 The Background Rejection Systems

The major sources of background were diffractive and inelastic regeneration for the $K_S \rightarrow 2\pi$ modes, semileptonic K_L decays and neutron interactions for the $K_L \rightarrow \pi^+\pi^-$ mode, and $K_L \rightarrow 3\pi^0$ decays for the $K_L \rightarrow 2\pi^0$ mode. The RA counters provided rejection for the inelastic source of regeneration as described earlier. Segmenting the Regenerator into four sections improved the rejection of inelastics by a factor of 5 compared to having only one set of RA counters at the downstream end, as was done in E617.

The semileptonic decays, Ke_3 and $K\mu_3$, were rejected with electron identification at the B Bank and muon identification at the MU2 bank. For charged mode running a 1.27cm (2 radiation length) Pb Curtain was inserted in front of the B Bank to initiate electromagnetic showers from electrons and photons. These showers were recognized as having a large pulse height in the B counters. A 3.2m steel filter downstream of the Lead Glass filtered out all charged particles except muons, which were then detected by the MU2 counter bank.

To reject $3\pi^0$ events in which photons miss the Lead Glass, 9 planes of photon vetoes were employed. DRAN, which was mentioned earlier, consisted of a lead-scintillator sandwich. This veto plane and four others, VA1–VA4 (VA is Vacuum Anti), were in vacuum and Figure 13 gives a cutaway view of a VA plane. A VA unit contained a plane of scintillator for charged particle identification, and two layers of lead-lucite sandwiches for identifying photons. MA (Magnet Anti) and LGA (Lead Glass Anti) were of similar construction to the VA's; the VA's, MA and LGA are shown schematically in Figures 14 and 15. Photons passing through or close to the beam holes in the Lead Glass were identified by the CA (Collar Anti) and BA (Back Anti). A diagram of CA is given in Figure 16. It formed a collar around the beam holes and detected electrons and photons within 1/2 block of these. It gave a well defined edge to the acceptance of particles in the central region— electrons and photons more than 1/2-block from an edge typically lost less than 1.5% of their energy down the holes and were well reconstructed. The BA was centered on the beams two meters behind the Lead Glass array, and was comprised of a lead-lucite sandwich. It was highly segmented, both longitudinally and transversely, to be able to withstand high rates and to distinguish between neutrons and photons. One unit of BA is shown in Figure 17, and 8 of these units stacked longitudinally made up one layer. Light pipes from each set of 8 longitudinally spaced lucite counters were attached to a single phototube, so that there were 8 vertical and 16 horizontal phototubes reading out signals in each layer. Three layers made up the BA, and ratios of signals in the layers gave longitudinal information about showers.

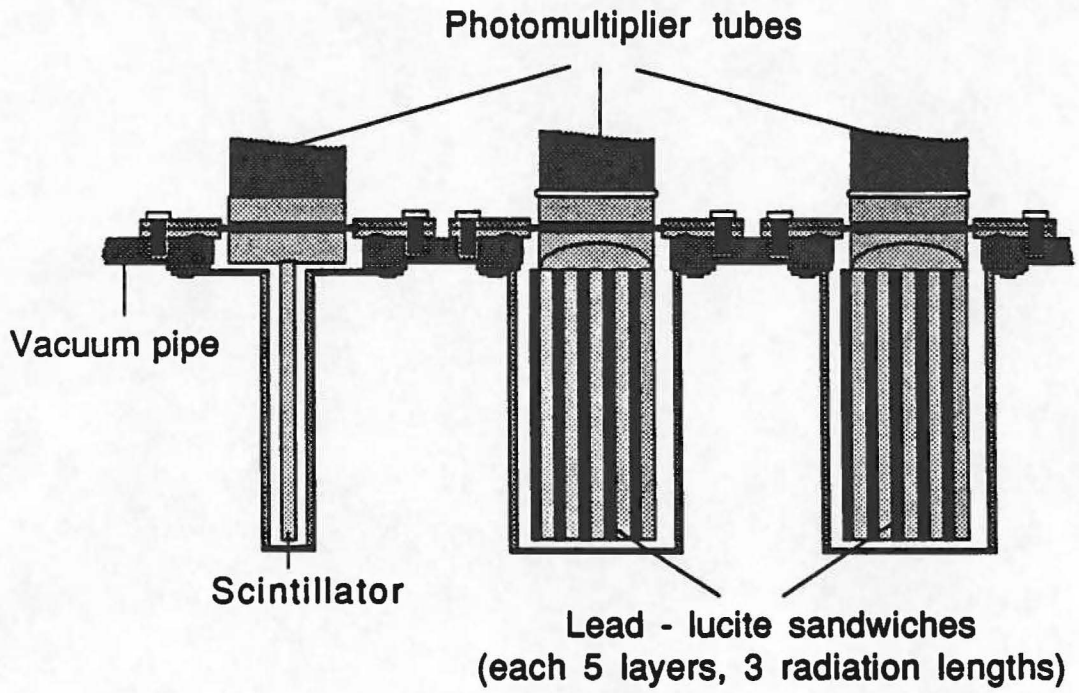

Figure 13: Side view cross-section of a VA plane

Events with wide angle charged particles were identified and vetoed with scintillator planes at PA (Pinching Anti) and DRAC. There were also scintillators at VA1–VA4, MA and LGA providing charged particle identification.

To reduce the neutral mode trigger rate, the MU1 counters behind the Lead Glass array were used to reject hadronic events. The Lead Glass and a Lead Wall 12cm thick behind the Glass contained 41 radiation lengths and 3 interaction lengths of material. Electromagnetic showers were therefore completely contained in these, while hadronic showers were not and typically gave a large pulse height in MU1. There was a single hole in this bank allowing both beams to pass.

A summary of the locations and sizes of most Detector Elements can be found in Tables 3 and 4. Table 5 gives the number of radiation lengths and (proton) interaction lengths for some of the elements. Two inactive but important elements which we have not so far discussed are the Vacuum Window and Helium Bags. It was important for obtaining good resolution of charged track trajectories and momenta to minimize multiple scattering. This required minimizing the amount of material in the T and V counters, the Vacuum Window, the Drift Chambers and the spaces between them, and the A Bank. Helium Bags were used between each of the Drift Chambers with thin 140μm my-

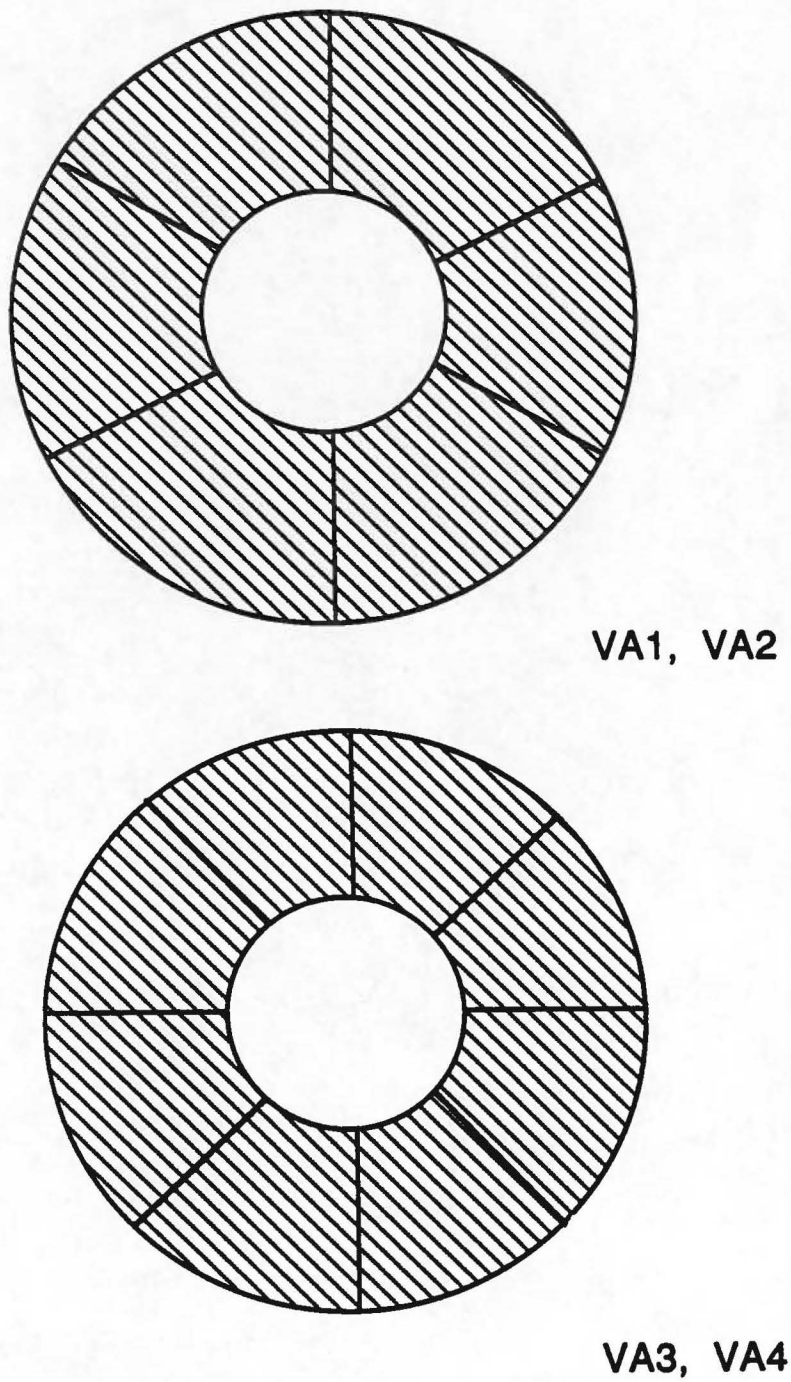

Figure 14: Beam's view of VA1, VA2, VA3, and VA4 photon veto counters

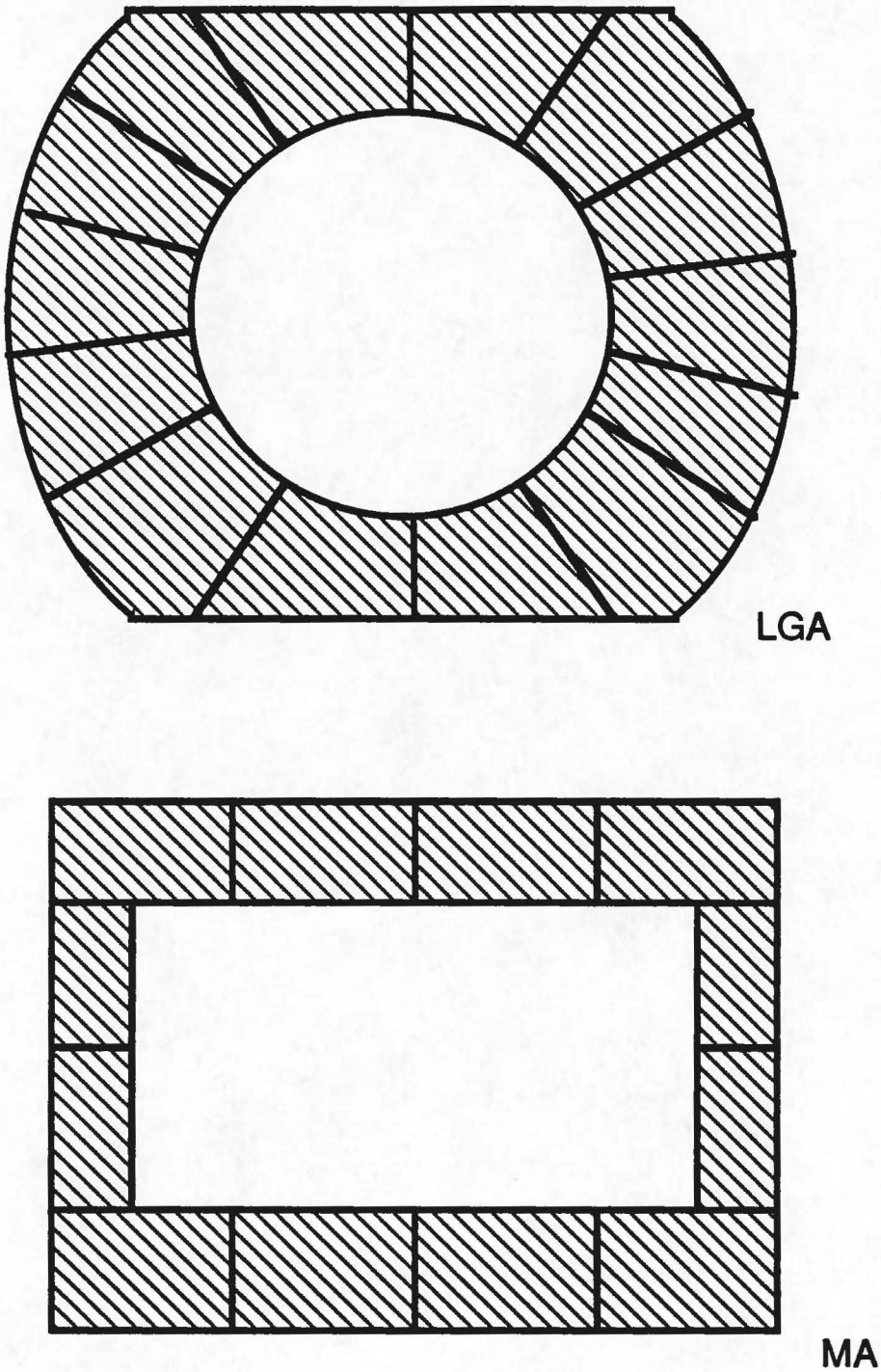

Figure 15: Beam's view of MA and LGA photon veto counters

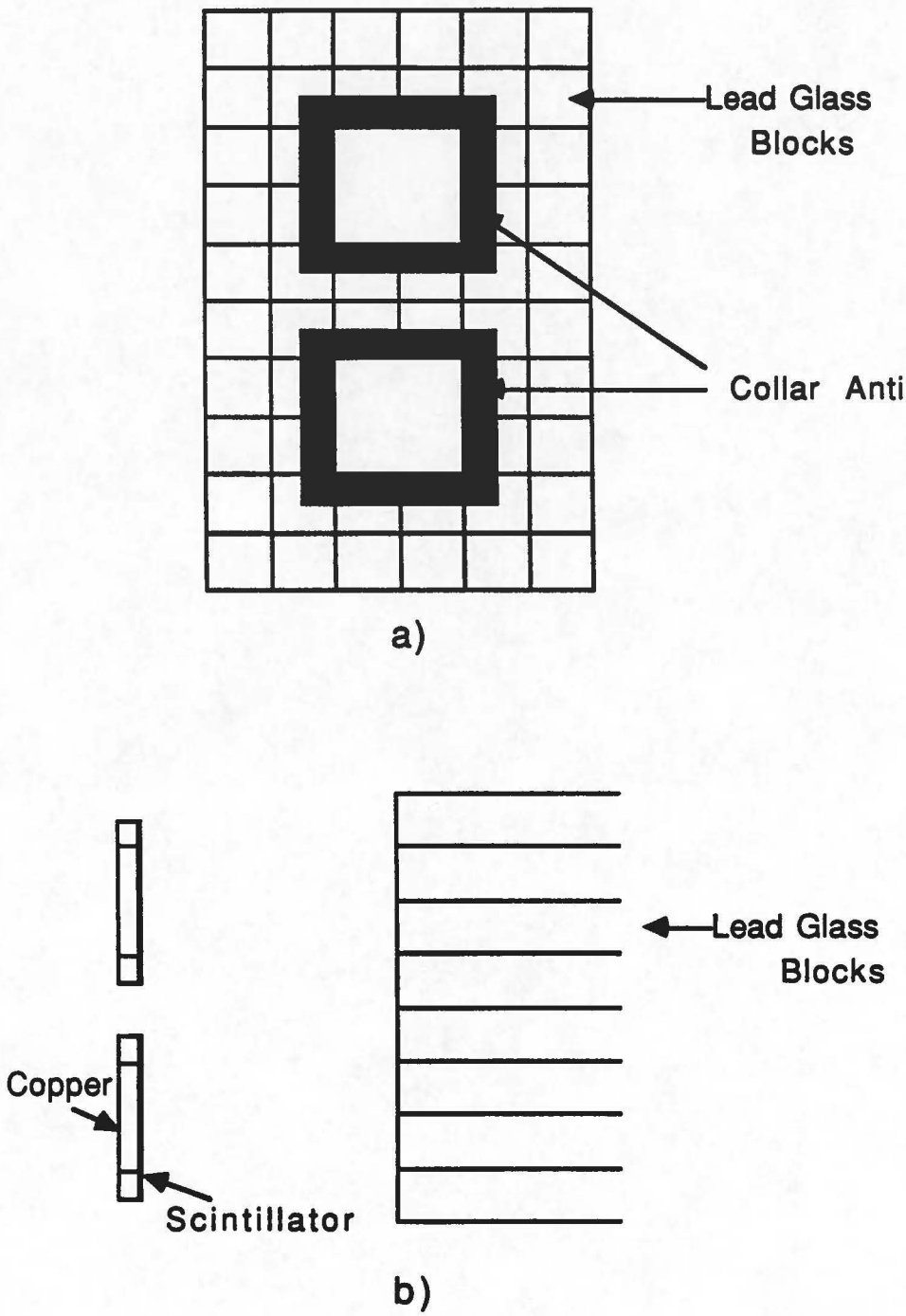

Figure 16: a) Beam's view of Collar Anti, b) Side view of Collar Anti

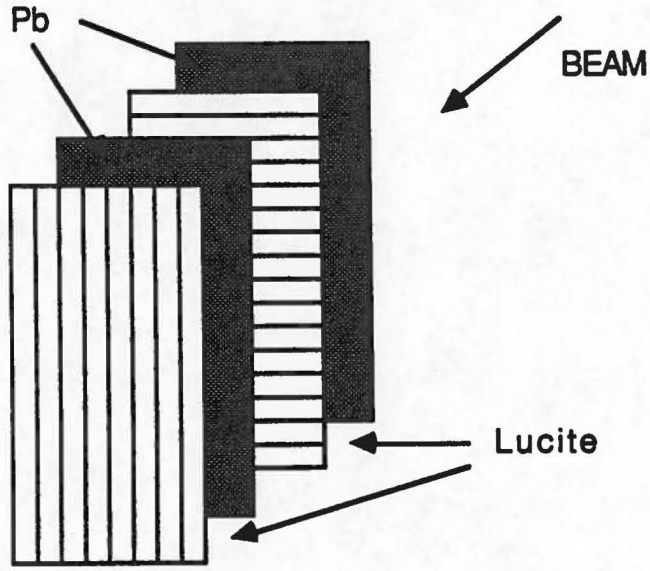

Figure 17: Exploded view of a Back Anti unit

lar windows, while the Vacuum Window was made of 0.584mm of Kevlar 29 glued onto 127μm of mylar. A steel o-ring was used for clamping the window between two steel flanges to provide the mechanical stability. This window deflected approximately 10.8cm at one atmosphere of pressure.

2.3 The Double Beam Technique

The detector assembled for this experiment is a complex one with thousands of components and channels of electronics. This complexity is typical of high energy experiments and demands careful monitoring of the system components to optimize the detector performance. Unlike most high energy experiments, however, ours is attempting a precision measurement and we therefore have to assess carefully effects due to detector stability. In addition, the beam stability must also be considered. We have noted that this experiment measures K_L and K_S decays simultaneously and the primary reason for this is to make negligible, effects associated with detector and beam stability. Consider the following three effects: i) changes in accidental activity, ii) electronic drifts, and iii) changes in detector resolution.

The instantaneous rate in a detector channel determines its accidental ac-

Table 3: Positions and dimensions of detector elements

Detector Element	Z Location (wrt target)	Transverse Dimensions (width x height)
Lead Mask	122.242m	40.64cmx50.8cm with two 10.16cmx10.16cm holes for the beams
Regenerator	123.598m (at downstream end)	4 sections; each 8.89cmx8.89cm
VA1	127.857m	inner edge has radius 28.2cm; outer edge has radius 57.4cm
VA2	132.813m	inner edge has radius 28.2cm; outer edge has radius 57.4cm
V	137.803m	50cm x 62cm
T	137.810m	50cm x 62cm
DRAC, DRAN	137.803m	inner edge is 50cm x 62cm; outer edge has radius 60.5cm
Separator Magnet	139.0m	
VA3	149.326m	inner edge has radius 54.4cm; outer edge has radius 80.7cm
VA4	158.307m	inner edge has radius 64.0cm; outer edge has radius 92.3cm
Vacuum Window	158.981m	Radius of 61cm
Chamber 1 Plane 1	159.257m	1.27m x 1.27m
2	159.268m	
3	159.289m	
4	159.300m	
Chamber 2 Plane 1	165.839m	1.42m x 1.57m
2	165.850m	
3	165.871m	
4	165.882m	
A Bank	166.133m	1.60m x 1.40m
MA	166.133m	inner edge is 1.82m x 1.49m; outer edge is 2.09m x 2.13m

Table 4: Positions and dimensions of detector elements

Detector Element	Z Location (wrt target)	Transverse Dimensions (width x height)
Analysis Magnet	168.858m (at center)	
Chamber 3 Plane 1	171.864m	1.57m x 1.73m
2	171.875m	
3	171.896m	
4	171.907m	
Chamber 4 Plane 1	178.016m	1.78m x 1.78m
2	178.027m	
3	178.048m	
4	178.059m	
LGA	178.707m	inner edge has diameter 1.80m; outer edge has 2.64m diameter clipped at a height of 2.11m
B Bank	179.526m	1.78m x 1.78m
CA	179.800m	
Lead Glass	180.884m (at upstream face)	approximate radius is 0.91m
MU1 Bank	183.783m	
BA	185.378m	20.32cm x 40.64cm
MU2	189.822m	2.4m x 2.4m

Table 5: Radiation and interaction lengths of detector elements

Detector Element	Number of Radiation Lengths	Number of Interaction Lengths
HDRA T	0.0051	
HDRA V	0.0037	
HDRA Pb	0.1003	
Vacuum Window	0.0025	
Chamber 1	0.0033	
Chamber 2	0.0030	
A Bank	0.0075	
Chamber 3	0.0036	
Chamber 4	0.0021	
Sense Wire	0.00643	
Field Wire	0.0057	
Lead Glass	19.9	2.2
Lead Wall	21.4	0.7
CA copper	3.0	
BA	28.1	1.3

tivity. As an example, consider the first plane of RA counters which saw the highest rate of any counter in this experiment because of beam interactions in the Regenerator. This RA plane typically counted 10^6 charged particles per second, so that in any 25ns time period (this time corresponded to the gate width for the latches) they would fire 2.5% of the time. So for each recorded event in which a kaon decay was observed, there was a 2.5% chance that an RA counter would fire and veto the event (RA was used to reject inelastically regenerated events). This accidental activity in RA depended directly on beam intensity, so that a 10% change in beam intensity would have changed the total reconstruction efficiency by 0.2% just due to using RA in veto. Now it was common for the beam intensity to change by more than 10%, not only over periods of hours and days, but also pulse to pulse (there was one 20 second pulse of beam every minute). Further, there were large bucket to bucket variations in beam intensity (recall the beam's rf microstructure of one 2ns bucket of beam every 18.8 ns), and the 'superbucket' phenomenon, where one can get a factor of 10 more particles than normal in a given bucket, is not uncommon at Fermilab. To put the accidental question in perspective, recall that the systematic error in the measurement of the relative rates of K_L and K_S to 2π must be less than 0.5%. If K_L and K_S decays had been measured separately a 10% difference in beam intensity between K_L and K_S running would have induced an 0.2% systematic effect in the measured relative rates due to RA alone. Many other detector elements were also sensitive to accidentals, in particular the Lead Glass where accidental activity resulted in the loss of approximately 10% of otherwise good events. Simultaneous measurement of K_L and K_S decays ensured that accidentals losses would be the same for both and would therefore cancel in the ratios R^{+-} and R^{00}. (There is a further discussion of accidentals in Section 11.1.1)

Because of accidentals, any detector element used for background rejection also rejects signal events at some level. The level of this accidental rejection changes if the level of accidentals changes, and it can also change due to electronic drifts associated with the detector element and its electronics. As an example, consider the MU1 signals which were used in the neutral mode trigger to veto events with hadronic showers in the Lead Glass. The signals from each MU1 counter were added in a linear sum, which was then discriminated at twice the pulse height for a minimum ionizing particle. It does happen that the dc level in the linear sum drifts from its nominal setting of 0mV, thereby changing the veto threshold. This in turn changes the accidental loss. But by simultaneously measuring K_L and K_S decays with the same detector and the same trigger logic, the accidental loss cancels explicitly in the ratios R^{+-} and R^{00}.

Changes in the detector resolution change the acceptance due to requirements on kinematic quantities such as the reconstructed K^0 mass. Worse resolution results in more signal being lost with a given cut and changes in the resolution therefore cause changes in the signal acceptance. But again, simultaneous measurement of K_L and K_S decays ensures that these acceptance changes are the same since the detector resolution is the same for both.

Thus, the double beam technique is a very important control on certain systematic errors. The acceptance, which is the probability for an event to be accepted by the trigger and pass all reconstruction criteria, is sensitive to changes in beam and detector performance. Essentially every trigger and reconstruction requirement (and there are many of these) are affected by stability questions, but the double beam technique eliminates possible systematic errors associated with this.

Chapter 3

The Drift Chambers

The Drift Chambers accurately measured trajectories and momenta of charged particles. In charged mode all reconstructed kinematic information for an event was obtained from them; and in neutral mode their measurements of the electron-positron pair determined the transverse coordinates of the decay vertex, the longitudinal vertex being determined from the Lead Glass information. The first part of this chapter details many of the characteristics of the chambers—their design, materials, assembly and operation. The latter part of the chapter describes their performance in this experiment, including details of the drift time to distance calibration, track reconstruction, and momentum calibration.

3.1 Hardware and Construction

3.1.1 Features of the Design

The Drift Chambers were designed for good resolution, operation at high rates, and low material to reduce multiple scattering. A hexagonal cell geometry was decided upon as was shown in Figure 9, resulting in three field-shaping wires for every sense wire. Each chamber had two x planes and two y planes, and the total chamber gas thickness was only three inches. The sense wires in each view were offset by one-half cell between planes to resolve the left-right ambiguity. An isometric drawing of a chamber corner is presented in Figure 18.

The sense wires were 25μm diameter gold-plated W, and the field wires were 100μm diameter gold-plated BeCu. There was an additional set of BeCu field-shaping wires attached to the inside of the chamber windows. Three independent high voltage settings were possible for the window wires, the

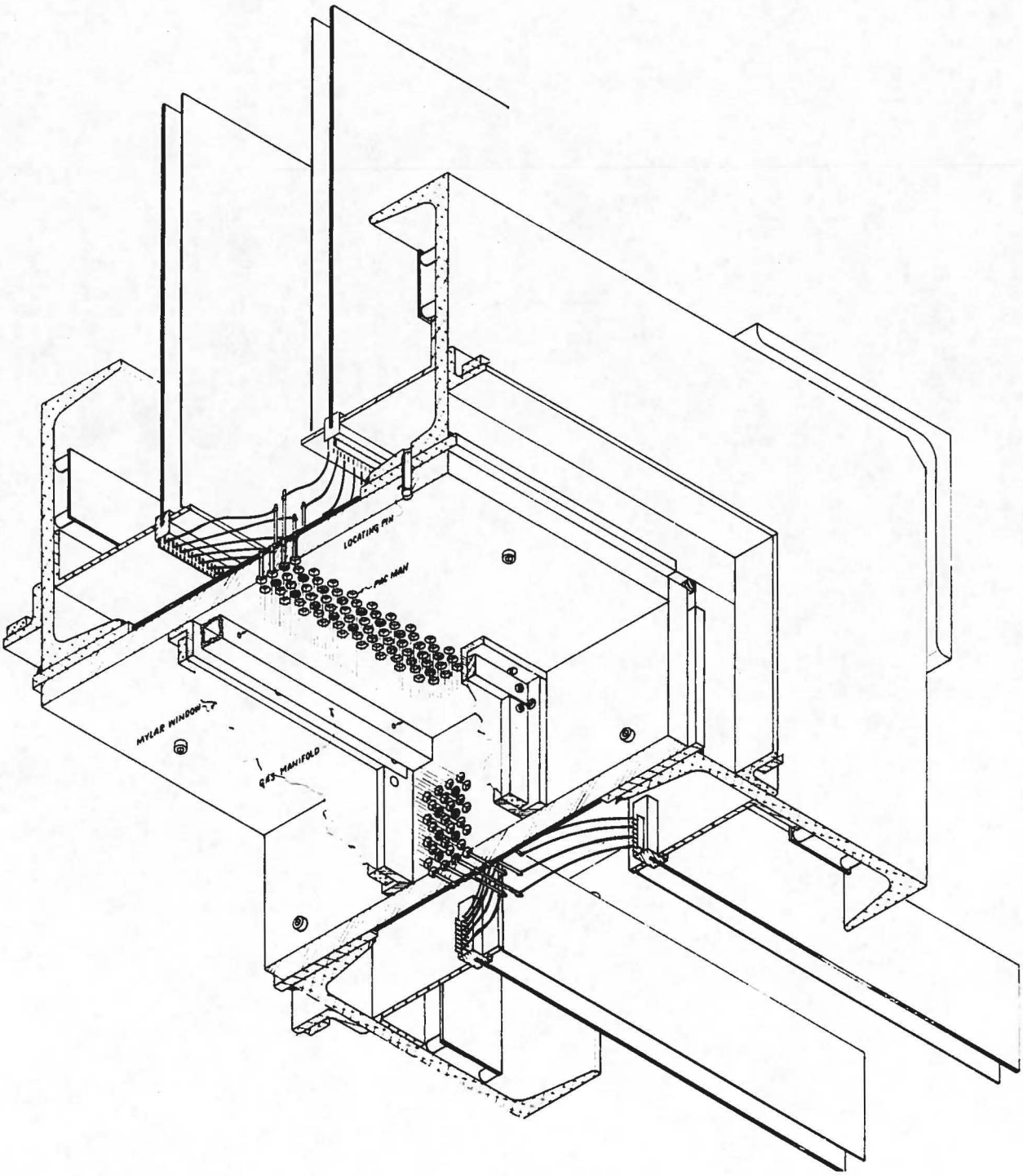

Figure 18: Isometric drawing of the upper right corner of a chamber (viewed from upstream).

outer layer of field wires, and the other five field wire layers in a given view. In practice, optimal performance was achieved using the same voltage for all of these. In retrospect, a ground plane should have been added between the x-view wires and y-view wires, in which case the window wires would have operated at ground potential. This added ground plane and corresponding ground voltage for the window wires would have improved the electrostatic symmetry between the inner and outer planes, and eliminated a low field region between the x and y wire planes. This region caused some inefficiency in the two inner wire planes in each chamber due to electrons produced in the low field region drifting into a cell late and canceling a real hit.

The sense wires were tensioned with 65g weights, and the field wires were tensioned with 420g weights; these tensions were chosen so that the gravitational sag of the wires (approximately 75μm at the center of a 2m wire) would be the same. The wires were located by the vertex of accurately spaced 'pacmen' (Figure 19) with a precision of approximately 25μm. The pacman that positions the wire is a molded plastic disc with a slice missing, so that it resembles the famous video game character. Each of the roughly 16,000 pacmen used in the four chambers were examined under a microscope for a precise and well-formed groove for locating the wires (approximately one-half of the produced pacmen were acceptable). The pacmen were epoxied into recessed holes in 1.27cm G10 boards. These holes were located and drilled with a numerically controlled milling machine to better than 25μm precision. Wires were anchored by soldering them to 0.32cm long brass eyelets in 0.24cm G10 boards. These boards were epoxied to the 1.27cm G10 with the epoxy forming a gas seal. Glyptol over the solder joints provided another gas seal.

The solder used for the sense wires was 95/5 Ag/Sn, while 60/40 Pb/Sn was used for the field wires. The length of the solder joint proved adequate to anchor the wires, though better anchoring (longer eyelets or additional epoxy) would have been preferable. The strain supported by the joint is roughly 640 psi for the BeCu wires tensioned at 420g and this is in the region of the limit for creep resistance [28]. There have been almost no problems with sense wires breaking after stringing (out of nearly 2000 total), while one field wire breaks every 3 or 4 weeks. In each case where a field wire has broken, it has pulled out of the solder joint. (Wires have not broken along their lengths or snapped at the solder joints—their tensions are substantially less than the breaking points, which have been measured at 110g for the sense wires and 700g for the field wires.)

The chamber gas was 50/50 argon-ethane with approximately 0.5% ethanol, which was added by bubbling the gas through a container of ethanol at 0°C. The gas was distributed to the chamber volumes by manifolds, which were

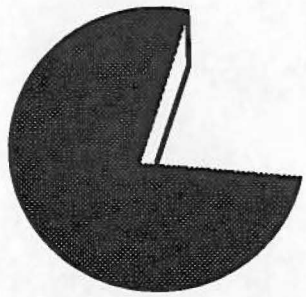

Figure 19: Schematic drawing of a 'pacman'

hollow lucite pipes 1.27cm x 1.27cm in cross-section. Manifolds were epoxied to the top and bottom 1.27cm G10 boards in each chamber, and each manifold had 0.16cm diameter holes spaced every 6cm. Since argon-ethane is heavier than air, the top manifold was used as the inlet and the bottom one was used as the outlet to optimize the gas flow and speed of purging (going from air or N_2 in the chamber to argon-ethane).

The chamber windows were 25μm thick aclar,[1] that had a thin coating of saran to reduce the permeability for water vapor. These windows had a 2.5cm seam in the middle, with the two halves being joined by 50μm isotac[2] adhesive. They were stretched and attached (with isotac) onto an aluminum bar frame. Copper-clad G10 strips, 2.5cm wide, were attached (again with isotac) to the outer edges of the windows and the window wires were strung and soldered onto these strips. A transfer plate supported the window frame during this process and during the installation of the windows on the chambers' G10 angle frames. A gasket of 0.48cm neoprene was used between the G10 angles and the windows for a gas seal, and additional epoxy and two-component RTV provided gas seals at the window corners.

[1] Aclar is a thin film (similar to mylar) made by Allied Chemical Corporation.
[2] Isotac is a 3M product.

The chamber frames were made of aluminum channel 27cm wide, and the 1.27cm G10 boards were epoxied and bolted onto these. Two pins were used to locate each board onto the frames, and these determined the orthogonality of the x and y view wires.

3.1.2 Operation and Readout

The chambers were operated at atmospheric pressure, and gas flow rates were such that the chamber gas was renewed every 12 hours. The operating high voltage for the field wires was 2.6kV, and this was ramped down between beam spills to 2.1kV. Sense wire signals were amplified and discriminated at the chambers and ECL logic signals were sent over 100 feet of twisted pair cable to LeCroy 4291B TDC's.

Sense and field wires were terminated at one end only. The field wires were connected through 100kΩ resistors to high voltage and also had 2200pF capacitors to ground. The sense wires were connected to boards which used LeCroy HIL440 chips to amplify and discriminate their signals. The output signals from the HIL440's went through one-shots that gave fixed-width signals of 50ns duration.

The double pulse resolution for the chamber/discriminator/TDC system was 250ns, and this was determined by the TDC's. This was reasonably well matched to the observed pulse shapes from single particles. The average drift velocity for electrons was approximately 50μm/ns and the longest drift times were of the order of 150ns. Sense wire pulses for single particles were observed to have as many as two or three peaks from different primary electrons (300μm is the mean path length for a charged particle to produce a primary electron), with the total pulse width being as much as 150ns. With the TDC's operating in common stop mode and the chamber signals giving the start signals, it was advantageous that the TDC's did not restart on the secondary peaks in the pulse shape.

3.2 Performance

3.2.1 Conversion of Drift times to Distances

The observed drift time distribution is shown in Figure 20. The edge at 230ns corresponds to particles passing very close to the sense wires, while the tail at short times corresponds to particles passing near the edge of a cell. Assuming that the illumination of tracks across the cell is uniform the distance, d, from

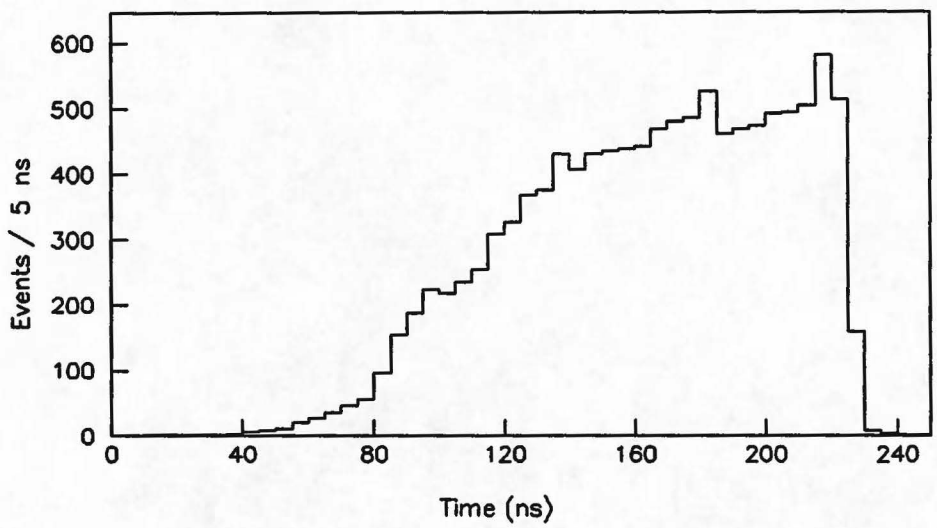

Figure 20: Measured drift time distribution for hits on tracks in an x plane of Chamber 2

the sense wire is related to the measured time, t, according to

$$\frac{d}{0.635\text{cm}} = \frac{\int_{240}^{t} \mathcal{D}(t')\mathrm{d}t'}{\int_{240}^{0} \mathcal{D}(t')\mathrm{d}t'} \tag{3.1}$$

where:

0.635cm is the maximum drift distance (equal to the cell width), and

$\mathcal{D}(t')$ is the observed drift time distribution (t' is in ns)

The drift time distribution was measured for each of the 16 wire planes (4 planes in each of 4 chambers), and a conversion table was calculated for each via Equation 3.1. These tables were updated throughout the running period to track slow changes in the distributions.

3.2.2 Charged Particle Trajectories from Reconstruction of Tracks

Hit wires with drift times between 10ns and 250ns were considered for hits along possible tracks. The track finding procedure used hits in two chosen planes (for a given view) for a candidate track. A straight line was drawn between the two wire centers and hit wires within a road of 1.5cm in other planes were searched for (Figure 21). A y-view track was required to have 5 or more hits out of a possible 8 for the 4 chambers. The tracks were bent by the Analysis Magnet in the x-view, and so track segments in this view were found

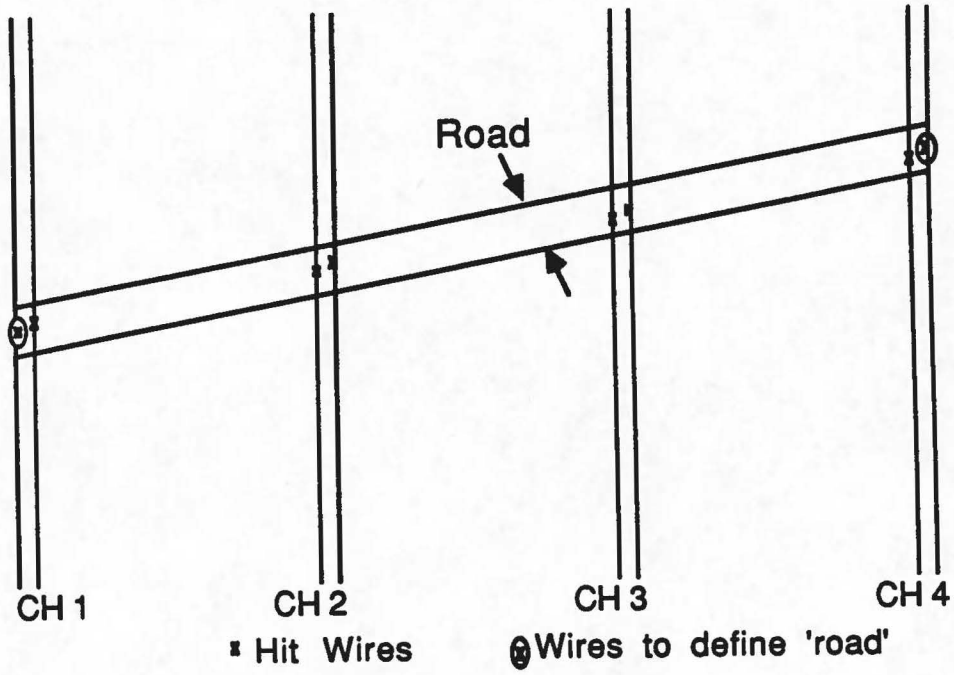

Figure 21: Track finding procedure: a straight line is drawn between two hit wires in the outer planes, and candidate hits within a 1.5cm road of this line are searched for in the other planes. Different initial planes are tried so as not to miss tracks due to wire inefficiencies.

for the upstream and downstream chambers separately. These track segments were required to have at least 3 of a possible 4 hits.

In a given chamber there could be 1 or 2 hits on a track (x or y); if there were 2 hits, the left-right ambiguity (for which side of the wire the particle went by) was resolved, and the drift time information was utilized to obtain a more precise determination of the track position. For cases with only 1 hit in a chamber, the drift times were implemented to generate 2 tracks—one on each side of the hit wire.

The track finding procedure generated redundant tracks which were squeezed out. In general tracks were not allowed to share hits, and if two tracks did so the track with a better χ^2 was chosen (χ^2 was the sum of the square of residuals of hit positions with respect to fitted track positions). In the x-view, upstream track segments were required to match downstream track segments within a road of 1.5cm at the Analysis Magnet center to form a complete track.

Both x-view and y-view tracks were required to project within 5cm of the T and V planes at the HDRA, and to project within an aperture of 2m x 2m at the Lead Glass.

Two x-tracks and two y-tracks were required from the above procedure for $\pi^+\pi^-$ candidates; e^+e^- candidates were required to have two x-tracks and one or two y-tracks. Variations to the track finding procedure peculiar to these two modes are given in Chapters 6 and 7, where the correlation of the x- and y-views of tracks is also presented. Corrections to the track hit positions resulting from signal transit times in the chamber wires and in the B Bank scintillator (this scintillator bank defined the trigger timing) were applied after track views were correlated; the tracks were then refit. Track parameters were also determined for upstream and downstream segments of y-view tracks at this stage. It was found that the y-view track segments gave more accurate track trajectories than the complete y-track, due to a small amount of track bending in this view from the Analysis Magnet.

3.2.3 Resolution and Efficiency

The Drift Chamber resolution was measured to be 150μm from the sum of distances distribution for paired hits in a chamber. Recall that a track should have two hits in adjacent planes, with the two hit wires being offset by one-half cell, or 0.635cm. The drift times determine the drift distances from the wires and the sum of these distances should equal 0.635cm for paired hits. Figure 22 gives a typical plot of this distribution. One also measures the resolution by examining the distribution of the difference between hit positions and fitted track positions at individual chamber planes. The transverse offsets of Chambers 2 and 3 with respect to Chambers 1 and 4, which defined the coordinate system for this experiment, were determined from these distributions during muon alignment runs with the Analysis Magnet off. Such alignment runs were done two or three times a day during the run, and Figure 23 shows the offset distribution for an x-plane in Chamber 2.

The wire plane efficiencies were measured from the probability for a track to have a hit in a given plane. It was found that the inner 2 planes in a chamber had an average efficiency of 96%, while the outer 2 planes had an average efficiency of 99.5%. Only 5 wires (out of nearly 2000 total) had measured efficiencies below 90%. The lower efficiency for the inner planes resulted from electrons produced in the low field region between the x and y views drifting in late and replacing a good hit.

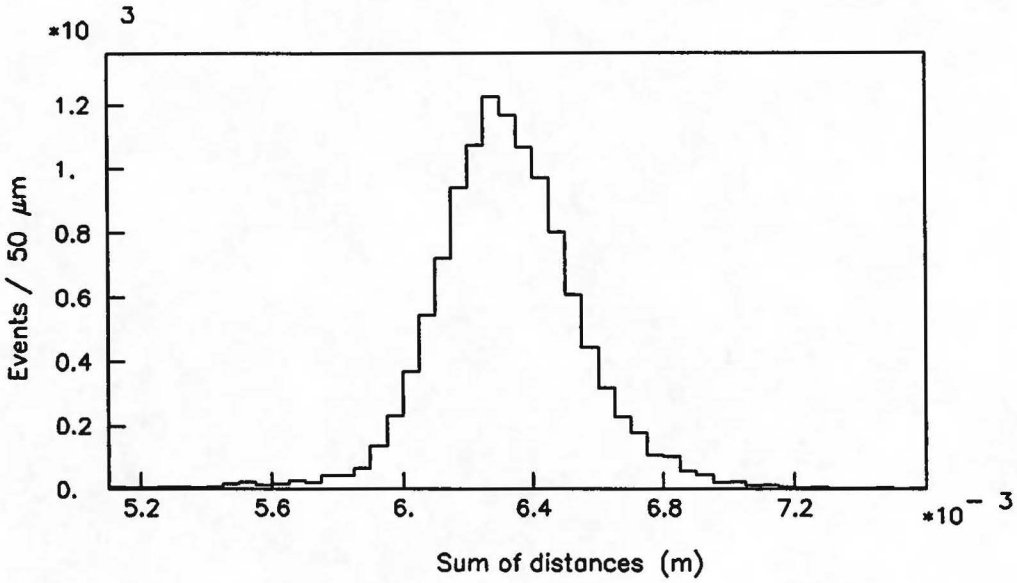

Figure 22: Sum of distances for paired hits—the chamber resolution of 150μm/wire was determined from this.

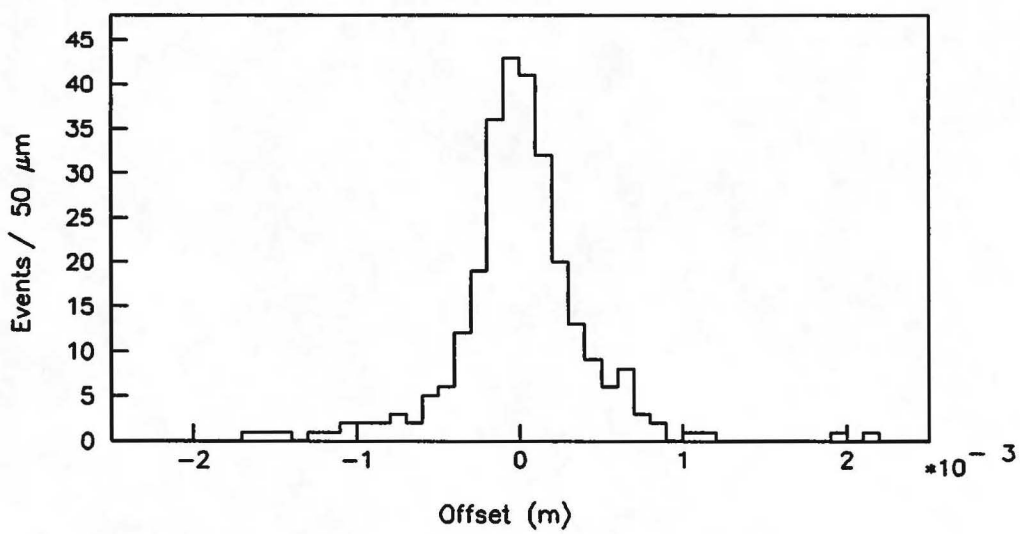

Figure 23: Offset distribution for an x plane in Chamber 2. The offset is with respect to the coordinate system defined by Chambers 1 and 4.

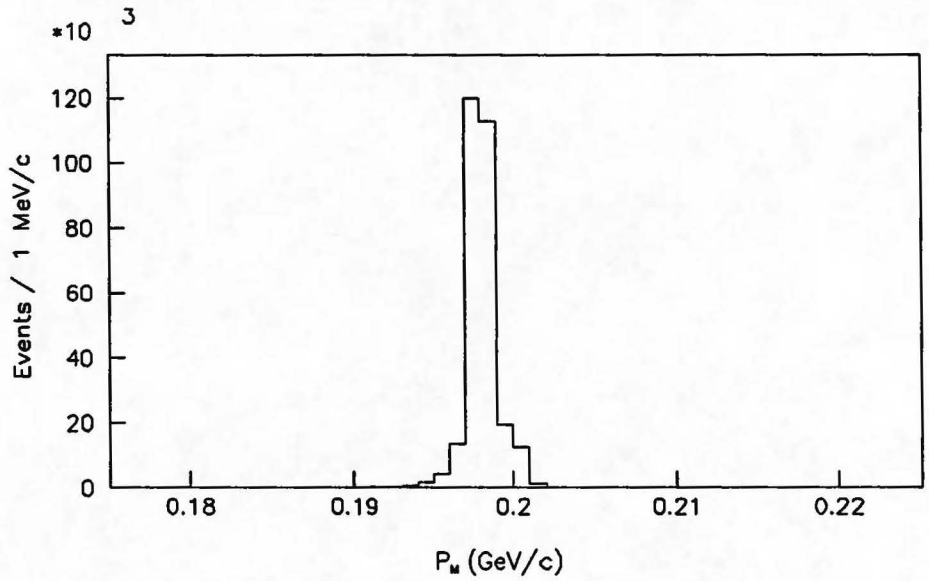

Figure 24: Distribution of P_M for π^+, π^- in charged mode running

3.2.4 Momentum Determination

The momentum of a track was determined from the bend angle between its upstream and downstream track segments. For a transverse momentum kick, P_M, in the $\hat{x}$ direction, the track momentum, P, can be calculated from conservation of momentum. Let $\vec{p_u}$ ($\vec{p_d}$) be the momentum vector of the upstream (downstream) track segment, and let it have modulus p. One obtains

$$\vec{p_u} \cdot \hat{x} + P_M = \vec{p_d} \cdot \hat{x}$$

Hence,

$$p = P_M \left[\frac{\theta_{x_D}}{\sqrt{\theta_{x_D}^2 + \theta_{y_D}^2 + 1}} - \frac{\theta_{x_U}}{\sqrt{\theta_{x_U}^2 + \theta_{y_U}^2 + 1}} \right]^{-1} \tag{3.2}$$

where

$\theta_{x_{U(D)}}$ is the track direction tangent for the upstream (downstream) track segment; similarly for $\theta_{y_{U(D)}}$

P_M had small variations across the aperture of the Analysis Magnet, which were determined from a field map done prior to the experiment. The distribution in P_M is shown in Figure 24 for tracks in identified $K \to \pi^+\pi^-$ events. The overall normalization for P_M, which set the charged mode energy scale, was determined from the known K^0 mass. Recall that the invariant mass of a

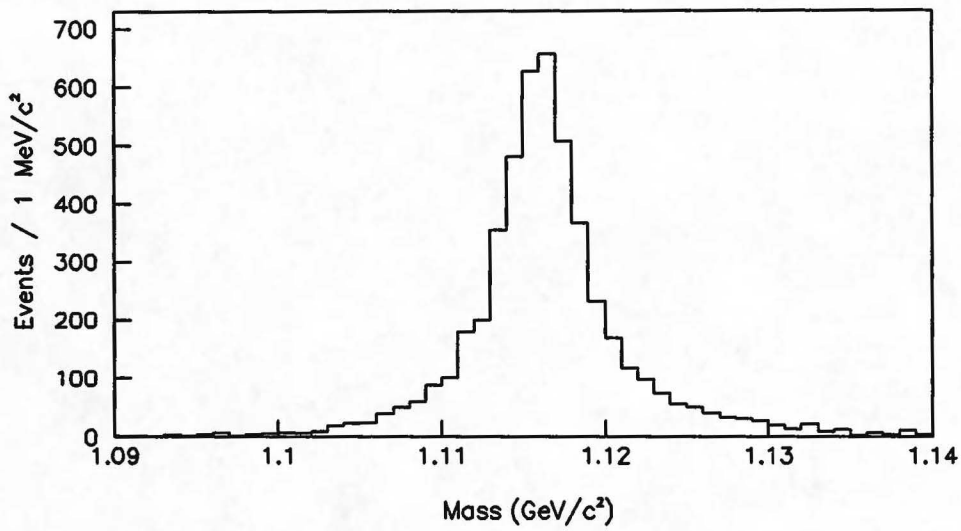

Figure 25: (p, π) invariant mass distribution for identified lambda decays

particle which decays into two daughter particles is given by $m^2 = (\tilde{p_1} + \tilde{p_2})^2$, where $\tilde{p_1}$ and $\tilde{p_2}$ are the 4-momenta of the daughter particles. As a check on the energy scale, the experiment detected a large number of $\Lambda \rightarrow p\pi^-$ events and Figure 25 shows the reconstructed (p, π) mass for these, which is in good agreement with the Particle Data Book (PDB) value of 1115.6 MeV/c^2 [8]. The known K^0 and Λ masses determined the charged mode energy scale to better than 0.1%.

Chapter 4

The Lead Glass

Energies and positions of photons and electrons were measured with the Lead Glass array. Much care and effort was directed towards obtaining optimal performance of this calorimeter, since good resolution aided in distinguishing signal from background and enabled understanding of the characteristics of electromagnetic showers. Accurate energy calibration was also required, so that charged mode and neutral mode data would be compared at the same energy. We will first discuss the hardware associated with the array and its operation. This will be followed by a discussion of the algorithms for finding clusters of electromagnetic energy and determining the energies and positions of electrons and photons from them. Lastly, the procedure for determining the 'gains' that convert ADC counts to energies will be given.

4.1 Hardware and Operation

The Lead Glass used in this experiment was Schott Optical Glass Type F2. The array consisted of 804 blocks in a circular array as depicted in Figure 12. Each block was viewed by a single phototube, and signals were sent over 275 feet of cable to the ADC's. A detailed description of the properties of this Lead Glass and the characteristics of the Lead Glass/phototube/ADC system can be found in reference [27]. The only changes in this system for the current experiment pertained to the mode of operation of the ADC's, and this is discussed in Chapter 5. As well, prior to the experiment, tests were done on the ADC channels to measure their gains and linearities. Gains were required to be uniform within $\pm 10\%$, and responses were required to have a deviation of less than 4 counts from a straight line fit over the range 0 counts to 16000 counts. A 20 GeV energy deposit in a block corresponded to roughly 6000 counts—20 GeV was a typical photon energy.

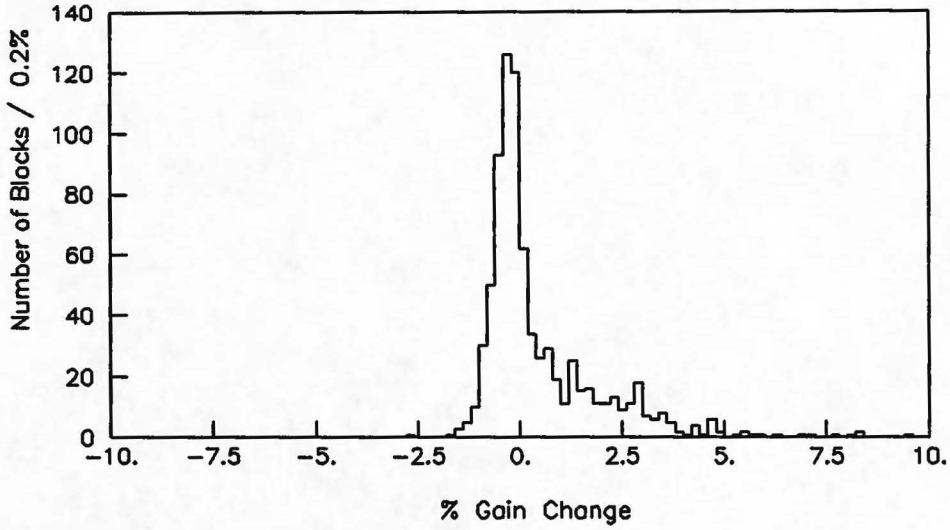

Figure 26: Ratio of flasher responses for tenth and first flashes into the spill for data with LED's off.

The array was contained in a light-tight house, with temperature control of better than 1^0F at the phototube bases for gain stability. To improve gain stability as a function of beam intensity a low level of dc light, supplied by LED's, was shone on the front faces of the blocks. Stability was monitored by a Xenon flasher system—the flasher was triggered at 1Hz during the 20s beam spill and the flasher light was transmitted to each of the 804 blocks and two reference tubes with fiber optics. The light pulse from the Xenon flash lamp was stable to 5% and each flash gave a 1% measurement of each block's gain, allowing short-term monitoring of stability. The improvement made by the LED's was measured with flasher data and is shown in Figures 26 and 27. The percentage change in gain between the first and tenth flash into the spill is plotted for LED's off and LED's on. The improvement is dramatic, but unfortunately only the last third of the data taking was with this configuration. The resolution obtained was not that much degraded during the LED-off period, however, since most of the gain change occurred during the first second of the spill and the spill duration was 20s.

The Lead Glass signals were an important ingredient of the neutral mode trigger. Analog sums of signals from mini-arrays of 7–9 blocks were formed to make 92 'Adder' signals, the total sum of which measured the total energy seen by the Lead Glass for an event. The Adder signals were also used by a fast processor, the 'Mass Box', to form the second moment of the energy distribution with respect to the array center, and calculate the product of this with the total energy. This product is related to the kaon mass; consider a

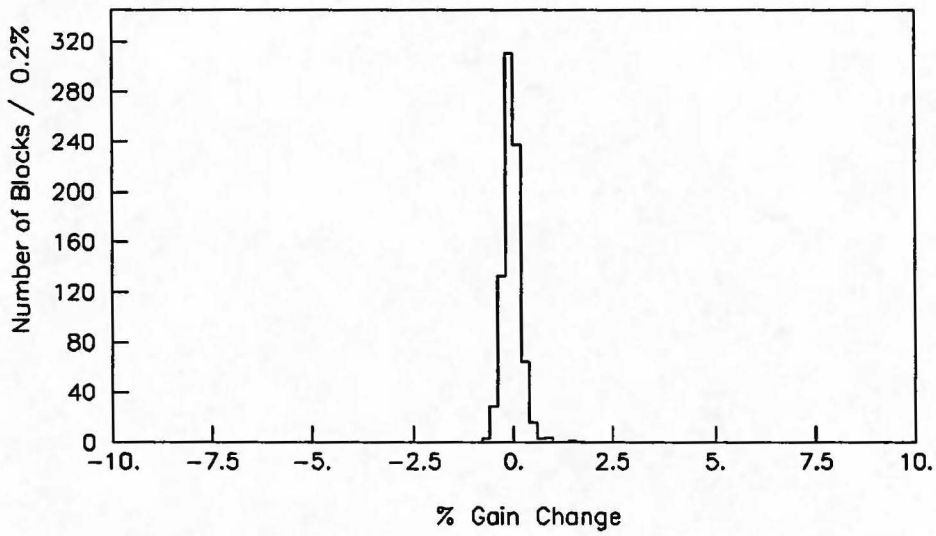

Figure 27: Ratio of flasher responses for tenth and first flashes into the spill for data with LED's on.

beam particle decaying to a final state consisting only of photons at a distance Z meters from the Lead Glass. The invariant mass of the parent particle is given to good approximation by

$$m^2 = \frac{E_T E_2}{Z^2} \tag{4.1}$$

where E_T is the particle energy and E_2 is the second moment of the energy distribution ($E_T = \sum_i E_i$ and $E_2 = \sum_i E_i r_i^2$, where i represents each photon or each group of 9 blocks that form an Adder, and r measures the distance from the center of the Lead Glass array). Both E_T and $E_T E_2$ were used in the neutral mode trigger.

Let us give here a short derivation of the relation $m^2 = E_T E_2 / Z^2$.
Let

m - mass of decaying particle,

$\tilde{p_i}$ - 4-momentum of photon i,

E_i - energy of photon i,

p_i - momentum of photon i,

θ_{ij} - angle between photons i and j,

r_{ij} - distance between photons i and j at the Lead Glass,

(x_i, y_i) - transverse coordinates of photon i at the Lead Glass, and

Z - distance from the decay vertex to the Lead Glass

From conservation of the 4-momentum,

$$\begin{aligned} m^2 &= (\sum_i \widetilde{p_i}) \cdot (\sum_i \widetilde{p_i}) \\ &= \sum_{ij} \widetilde{p_i} \cdot \widetilde{p_j} \\ &= \sum_{ij} (E_i E_j - E_i E_j cos\theta_{ij}) \end{aligned}$$

If we assume θ_{ij} is small, then

$$\begin{aligned} m^2 &= \sum_{ij} E_i E_j - E_i E_j (1 - \frac{\theta_{ij}^2}{2}) \\ &= \frac{1}{2} \sum_{ij} \frac{E_i E_j r_{ij}^2}{Z^2} \\ &= \frac{1}{2} \sum_{ij} \frac{E_i E_j (r_i^2 + r_j^2 - 2x_i x_j - 2y_i y_j)}{Z^2} \end{aligned}$$

Ignoring the small terms involving $\sum_i E_i x_i$, $\sum_i E_i y_i$ (these terms vanish for a kaon pointing at the center of the Lead Glass), one has

$$\begin{aligned} m^2 &= \frac{1}{2} \sum_{ij} \frac{E_i E_j (r_i^2 + r_j^2)}{Z^2} \\ &= \frac{E_T E_2}{Z^2} \end{aligned}$$

4.2 Energy and Position Measurements

The radiation length of Schott F2 glass is 3.06cm, so that each block measures roughly 2x2x20 radiation lengths. The energy leakage out the back of the array has a logarithmic dependence on energy and is of the order of 0.5–3% for electron and photon energies below 80 GeV. Transversely, 90% of the energy is typically contained within a cylinder of one radiation length radius. 3x3 'clusters' of blocks were used for measuring energies and positions of electromagnetic showers. A $K_{L(S)} \rightarrow 2\pi^0$ event has four clusters of energy corresponding to three showers from photons and one somewhat fatter shower from the electron-positron pair. A typical event is shown in Figure 28.

The cluster reconstruction algorithm searched for local maxima of block energies. A 3x3 cluster was found if its center block (the maximum) had an

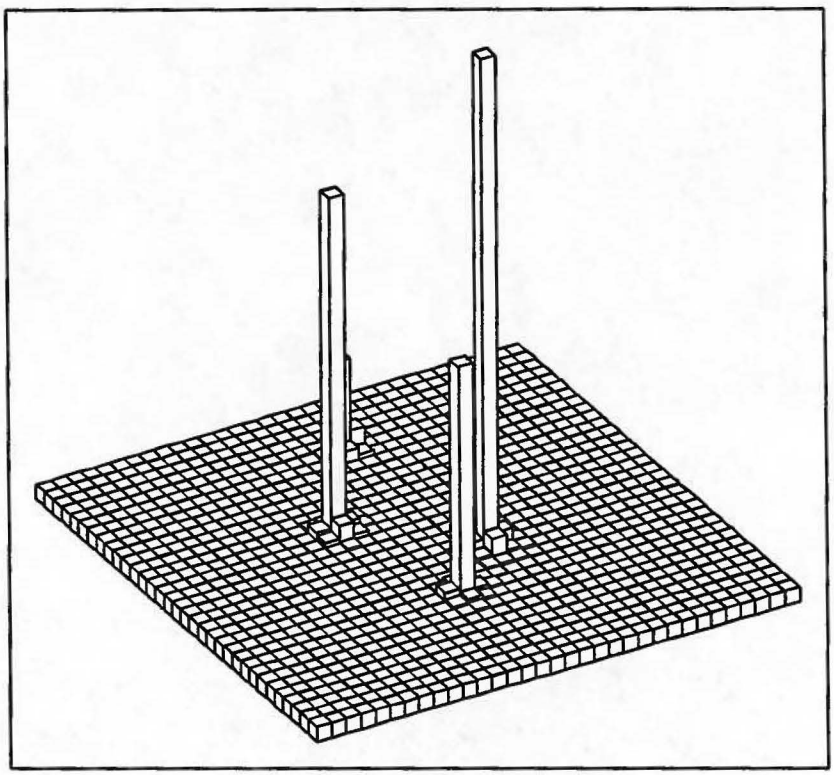

Figure 28: Electromagnetic energy deposit in the Lead Glass for a $2\pi^0$ event.

energy greater than 0.25 GeV and if its 3x3 energy sum was greater than 0.5 GeV. Clusters were distinct if there was an energy minimum between their cluster centers.

Cluster energies were obtained from the sum of nine block energies, and cluster positions were determined from the ratio of columns or rows of energy. Each cluster had 3 columns (3 rows) and the ratio of the greater side column (row) energy to center column energy determined the cluster's x (y) position. Converting the ratio to a position involved doing an inversion equivalent to the procedure for converting times to distances with the Drift Chambers (Section 3.2). Average position resolutions of 3mm were achieved, with better resolution achieved for clusters centered near block edges.

4.3 Calibration

A Lead Glass ADC measures the integrated charge in a phototube signal, and this is proportional to the number of Čerenkov (and scintillation) photons seen by the phototube. Ideally, the number of photons from an electromagnetic shower seen by the phototubes in a cluster would be proportional to the cluster energy. This would be true if the showers were completely contained and if there was no attenuation of photons going through lead glass. The showers are not completely contained, however, as was mentioned earlier. Even more significant, is the attenuation which is roughly 2% per radiation length. (This is the attenuation for wavelengths above 420nm—optical filters between the phototubes and lead glass blocks cut out wavelengths below this.) This attenuation, coupled with the energy dependence to 'shower max' (the shower depth with the greatest number of electrons and positrons), results in a nonlinear lead glass response; hence, a single number, the gain, cannot describe the conversion of ADC counts to energy. Additionally, an electron-photon response difference arises because the photon converts at some depth in the glass, causing its shower max to be deeper into the block than the electron's. Let us consider the nature of an electromagnetic shower in lead glass and the attenuation of the resulting photons. Photon production can be modeled by assuming that the photons originate solely from shower max. The energy dependence to shower max for electrons has been found by others [29] to be

$$S = c_1 + c_2 \ln E$$

where

S is shower max measured in radiation lengths,

E is the energy of the showering particle in GeV, and

c_1, c_2 are constants (reference [29] gives $c_1 = 4.28$ radiation lengths and $c_2 = 1.16$ radiation lengths)

For photons traveling through R radiation lengths of lead glass, which has an attenuation coefficient α, the transmission is given by $T = e^{-\alpha R}$. R is equal to $(N - S)$, where N is the length of the lead glass blocks (in radiation lengths), so that the energy (E_m) seen by the phototubes is given by

$$\begin{aligned} E_m &= Ee^{-\alpha(N-S)} \\ &= Ee^{-\alpha N} e^{\alpha c_1} e^{\alpha c_2 \ln E} \\ &= e^{-\alpha N + \alpha c_1} E^{1+\alpha c_2} \\ &= a_1 E^{a_2} \end{aligned}$$

Thus, the lead glass response has a power law dependence on the particle energy in this model. The power depends only on the attenuation coefficient, α, and the shower development coefficient, c_2, so that it is the same for all blocks of similar transmission properties. The coefficient a_1 gets coupled with the phototube and ADC gains to form an overall gain for each block. This gain is different for electrons and photons, however, since c_1 is greater for photons.

4.3.1 Electron Calibration Runs

From electron calibration data, the Lead Glass response was studied in detail in the energy range 2–20 GeV. Special calibration runs were taken with a photon beam that produced electron-positron pairs from a thin sheet of copper inserted into the beam. The electron and positron momenta (p) were measured with the Drift Chamber spectrometer thereby determining the true particle energies. The nonlinearity of the Lead Glass response was studied by measuring E_m/p for a range of energies in each block. A power law was found to describe the response very well, and Table 6 summarizes the results for the power a_2 determined from each calibration run. Blocks next to the beam pipes were found to have greater nonlinearity and were therefore considered separately. These blocks experienced measurable radiation damage that caused yellowing of the blocks and loss of light transmission. This loss worsened by 10–20% for pipe blocks during the run and the greater attenuation increased the nonlinearity. The change in observed nonlinearities during the run was not large, and so no time dependence was used in the analysis. Given the nonlinearities, the normalized gains at 1 GeV for each block in the array were determined. This was done by measuring E/p for each block and iterating to choose gains

Table 6: Coefficients describing the nonlinear Lead Glass response to electromagnetic showers

Calibration Run	Nonlinearity Coefficient ($1/a_2$) for non-pipe blocks	Nonlinearity Coefficient ($1/a_2$) for pipe blocks
1	0.9806	0.9751
2	0.9791	0.9726
3	0.9801	0.9720
4	0.9804	0.9720
5	0.9808	0.9708
<>	0.9804	0.9722

such that all blocks had $< E/p >= 1$. (E was obtained from E_m by applying the nonlinearity correction.) Three or four iterations were usually required for convergence. Figure 29 shows a typical E/p distribution from calibration data (all blocks) after fitting for the gains. The full width at half maximum (FWHM) is 8%, with the mean electron energy being 5 GeV; after correcting for momentum resolution (due to chamber resolution and multiple scattering), the Lead Glass was found to have an energy resolution of approximately $1.5\% + 5.5\%/\sqrt{E}$ for electrons, where the two terms are added in quadrature. The constant term results from shower fluctuations and energy leakage, while the $1/\sqrt{E}$ term is due to photostatistics.

4.3.2 Gains for Neutral Mode Data

The above procedure described the Lead Glass response during calibration mode running, which was done at low beam intensity. The neutral mode data taking was with substantially different beam conditions and it was found that a gain correction was required to account for this. Note that this effect is similar to the time into the spill gain variation mentioned earlier. The E/p distributions from electron-positron pairs in $2\pi^0$ and $3\pi^0$ events were studied for each block and corrections were applied to make these distributions match with equivalent distributions produced by Monte Carlo. The corrections were generally less than 1%, and Figures 30 and 31 present the E/p distributions of data and Monte Carlo for $K_S \to 2\pi^0$ and $K_L \to 3\pi^0$ events. These distributions have a high-side tail resulting from Bremsstrahlung photons produced in the lead converter. This tail is well understood and well simulated with the Monte Carlo.

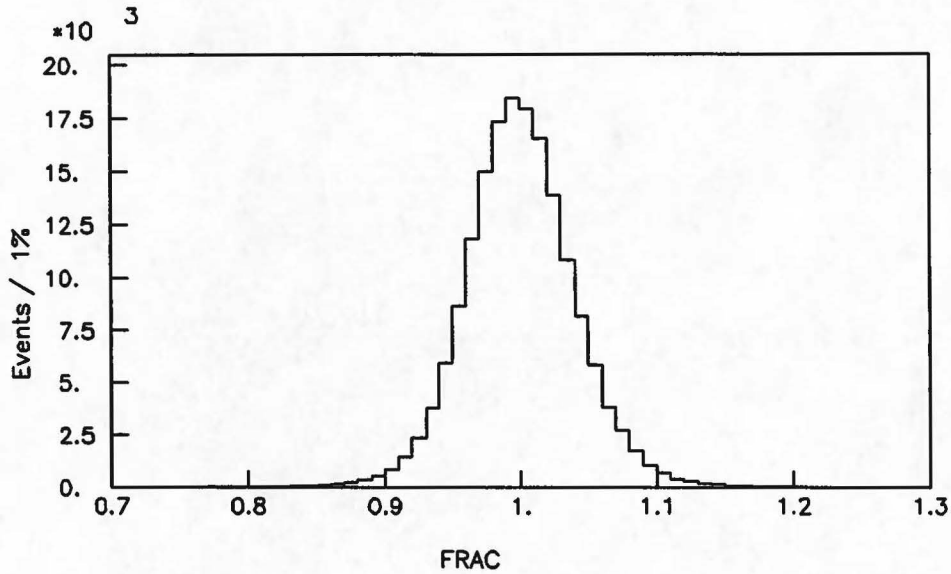

Figure 29: E/p distribution from calibration data for electrons and positrons. The mean is tuned to be 1.0 and the FWHM is 8%.

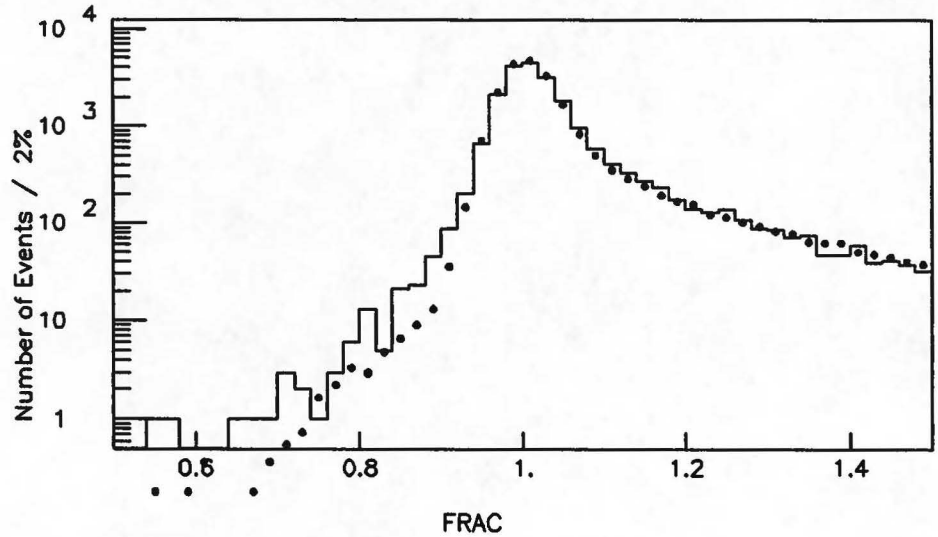

Figure 30: E/p distribution of data and Monte Carlo for $K_S \rightarrow 2\pi^0$ events. (The solid circles are Monte Carlo.)

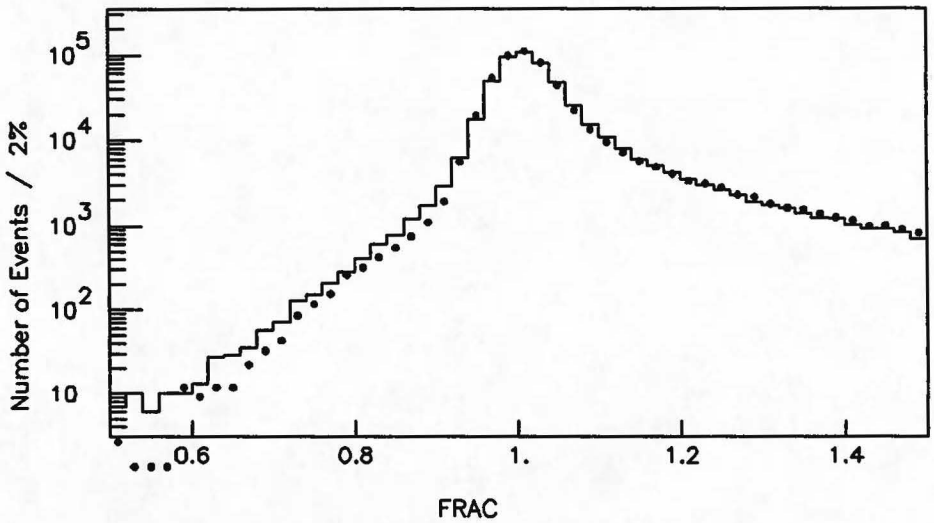

Figure 31: E/p distribution of data and Monte Carlo for $K_L \rightarrow 3\pi^0$ events. (The solid circles are Monte Carlo.)

The photon nonlinearities were the same as for electrons, but the electron-photon gain difference had to be determined. This was done with $2\pi^0$ events by tuning the photon gains such that the upstream edge of the longitudinal decay vertex (Z) distribution in the regenerator beam matched between Monte Carlo and data, and with $3\pi^0$ events for the downstream edge of the Z distribution. Recall that the energy scale and Z determination are coupled via Equation 4.1. From these studies, the electron-photon difference was found to be 1.8%. Checks of this were done by comparing reconstructed π^0 masses with and without the electron-positron pair in both $2\pi^0$ and $3\pi^0$ events. Also, there was a large sample of π^0's produced in the lead converter at the HDRA. These 'sheet' π^0's satisfied a neutral mode trigger if they were accompanied by two charged tracks and proved very useful as a check on the neutral mode energy scale since they were produced at a known Z. Figure 32 shows the (γ,γ) mass of identified sheet π^0 events using gains as determined above.

Thus, there were many ways of calibrating the neutral mode energy scale—for the electrons, E/p distributions were studied for calibration, $2\pi^0$ and $3\pi^0$ data; and for photons, Z distributions were studied for $2\pi^0$ and $3\pi^0$ data and the π^0 mass distribution was studied for sheet π^0 events. Each of these methods was capable of tuning the energy scale to agree with expectations to better than 0.1%. The actual energy scale uncertainty was determined to be less than 0.2% from consistency between the different methods. There were five electron calibration runs taken, and each produced a set of block gains which were then corrected by using E/p measurements obtained with neutral

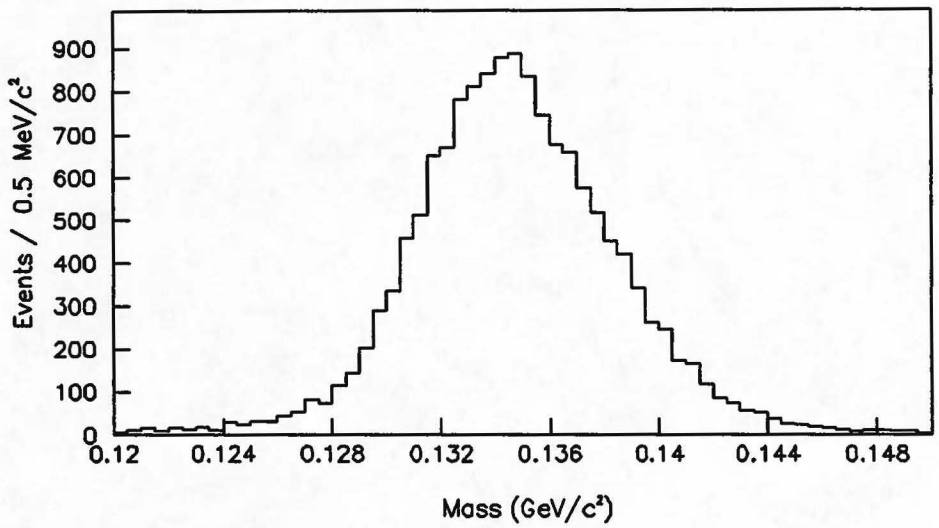

Figure 32: (γ, γ) mass for identified sheet π^0 events.

mode data. Between these runs, block gains were monitored with flasher data, and in general were found to change slowly and smoothly with time. A linear extrapolation of block gains between calibration runs was therefore used, except for blocks which were observed to have unusual changes (mostly due to high voltage changes or phototube replacements). The gains of such blocks were tracked with flasher data. The resulting average energy resolution for the Lead Glass from neutral mode data was approximately $2\% + 6\%/\sqrt{E}$ for electrons. The photon resolution was somewhat worse due to fluctuations of the conversion point.

Chapter 5

Data Collection

The data described in this thesis were taken during the last eight weeks of the 1985 fixed target run at the Fermilab Tevatron. The first few months of the run were used for completing the installation of the detector, bringing up the detector components and putting together the trigger logic, electronic readout, and data acquisition systems. This chapter discusses these systems after first describing the modes in which the experiment was run.

5.1 Running Conditions

The running conditions for the data taking are summarized in Figure 33. Most of the time was dedicated to measuring the $K_{L(S)} \rightarrow 2\pi^0$ modes (neutral mode running), and this was interspersed with measuring the $K_{L(S)} \rightarrow \pi^+\pi^-$ modes (charged mode running) and taking special runs to calibrate the Lead Glass. For charged and neutral data taking there were typically 10^{12} protons per spill on our Be target. For calibration running (see Section 4.3) the beam intensity was lowered to 2 x 10^{11} protons per spill on a 1/3 interaction length Cu target; the normal absorbers were removed and replaced with 1.2m of Be; and 1mm of Cu was inserted into the neutral beams (essentially pure photon beams) 70m downstream of the target to convert photons to electron-positron pairs.

5.2 Trigger Logic

To detect a large number of CP violating decays, the detector had to run at high rates and a good trigger was needed to distinguish signal from background. Fast scintillator signals from PA, RA4, V, T, DRAC, A, B, MU1 and MU2 were discriminated to form NIM logic signals with which to form the

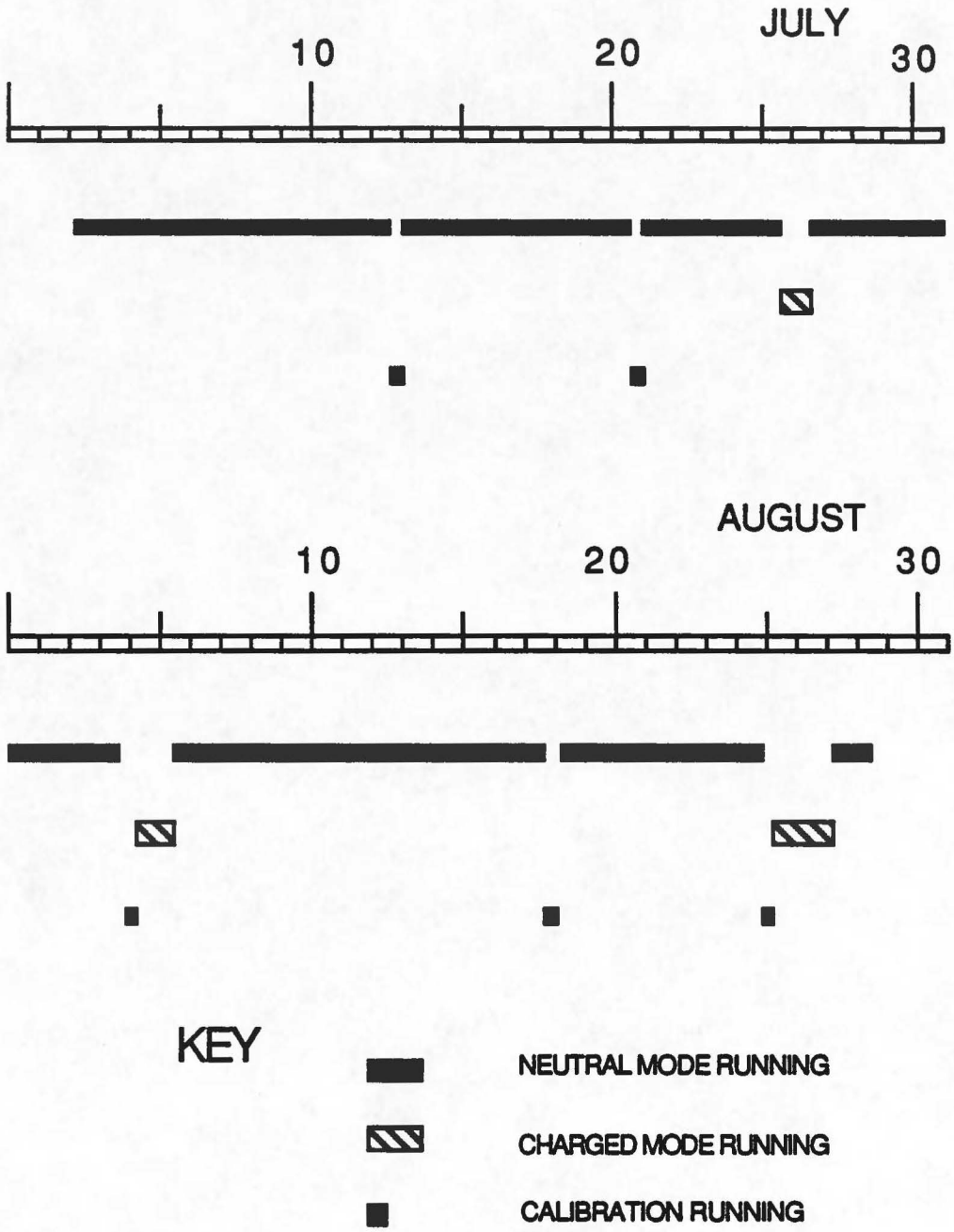

Figure 33: Data taking modes for the 1985 run

logic circuits (coincidence elements had logic signals 10ns wide, while veto elements had signals 20ns wide). For PA, RA4, V, T, DRAC, and MU2 we asked only whether any counter in these banks had a pulse height above that due to a minimum ionizing particle (MIP). For MU1, an analog sum was made of all its counter pulse heights and this was discriminated at 2x MIP; this counter bank was used to distinguish electromagnetic showers from hadronic showers in the Lead Glass. For the A and B banks the number of charged particles passing through them was determined from the number of counters hit, and the logic elements 1A, 2A etc. were formed, which were true if the indicated number of counters (or more) were hit. In addition to these scintillator signals, the total energy in the Lead Glass (E_T) and the product of the total energy with the second moment of the energy distribution ($E_T E_2$) were also used in the trigger logic.

The final trigger, which was formed from combinations of the logic elements described above, had its timing defined by the B Bank scintillator signals. (It was decided not to use the Tevatron rf signal for timing due to some difficulties experienced with this in earlier experiments. For the 1987-88 run, however, the experiment did use the rf signal to define the timing of all triggers.) For charged mode running, $2B$ defined the trigger timing while for neutral mode running, it was defined by $1B$. The timing therefore had variations with respect to the time of a particle traversing the B Bank due to the propagation speed of signals in scintillator. Corrections for this were made when converting time to distance in the Drift Chamber response and when converting charge to energy in the Lead Glass response.

There were two levels of trigger logic. Level 1 was denoted by either Charged Trigger or Neutral Trigger; Level 2 was an abort trigger and was denoted by either Charged Abort or Neutral Abort. The Level 1 trigger was formed approximately 300ns after a particle passed through the B Bank scintillator, and it initiated the readout sequence. The Level 2 Abort came later and was used to abort the readout and reinitialize everything to be ready for the next event. The logic diagrams for the Charged, Neutral, and $B \cdot MU2$ triggers, with approximate timing of signals indicated, are shown in Figure 34. Details of the trigger and abort elements are left for Chapters 6 and 7, where the charged and neutral data samples are discussed.

5.3 Electronic Readout

The electronic readout of the detector components consisted of time to digital converters (TDC's), analog to digital converters (ADC's), latches and scalers.

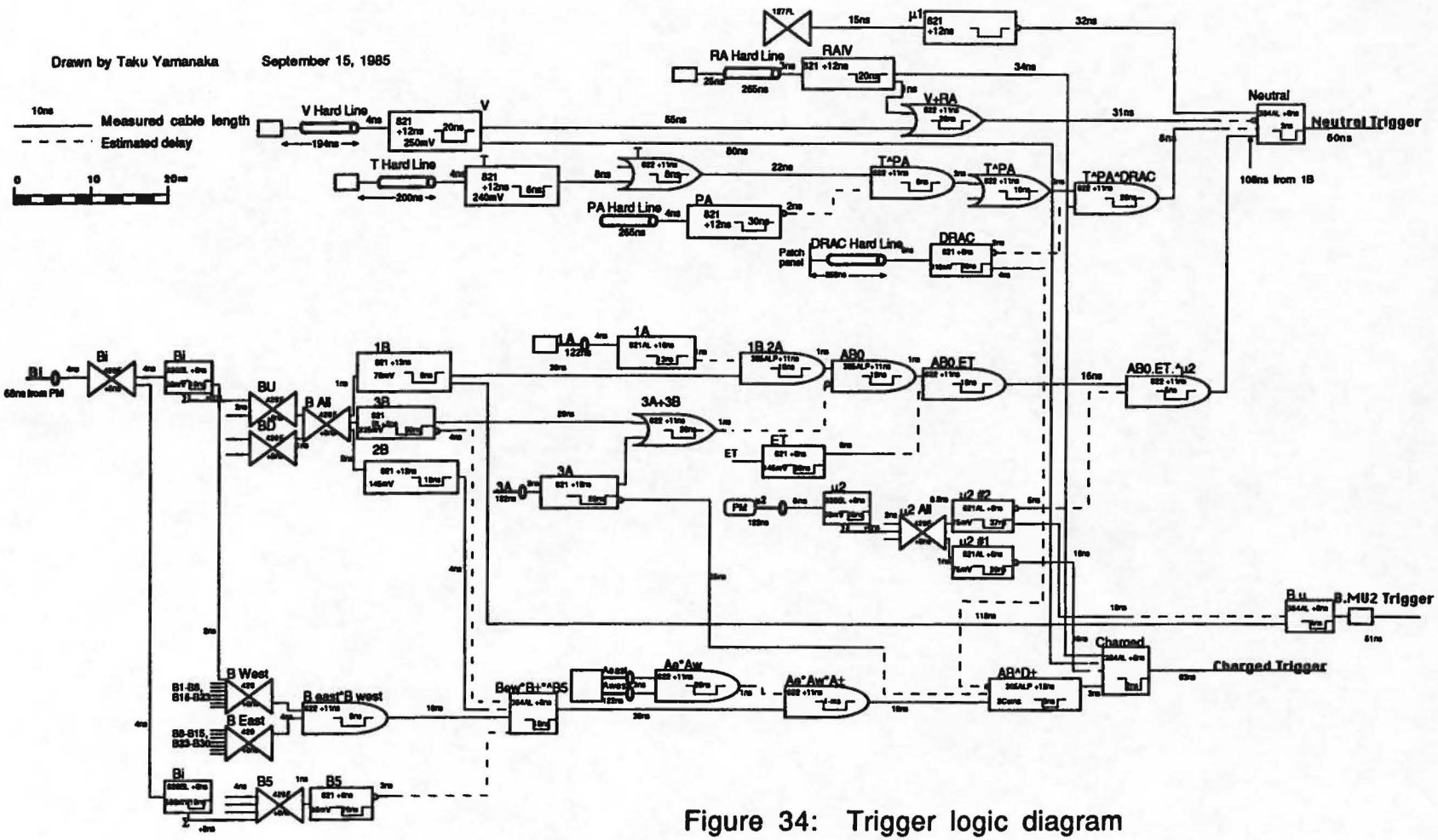

Figure 34: Trigger logic diagram

The Drift Chambers used the LeCroy 4290 TDC system as discussed in Section 3.1.2. LeCroy 2228 TDC's were used to measure the timing of 1A, 1B, V, and T with respect to the trigger. To measure the energy deposited in the VA's, MA, LGA, DRAC, DRAN, and MU1, LeCroy 2249 ADC's were used with a 25ns gate derived from the trigger. The LeCroy 2280 ADC system was used to measure signals from the BA, the Adders and the Mass Box. A 100ns gate was used for these signals and the ADC's were operated in 12-bit mode. For the Lead Glass and the CA, the 2280 system was also used but in 15-bit mode and with a 250ns gate. All ADC channels were read out in this experiment and no pedestal subtraction was done online. The status of all counters (either on or off) was recorded with latches, where a counter was considered 'on' if it had a pulse height above MIP in a 25ns or 50ns gate formed from the trigger. (A 25ns gate was used for A, B, V, T, and MU2 signals; a 50ns gate was used for all others.) There was also a trigger latch word that recorded which type of event triggered the apparatus—eg. a charged event or a neutral event.

The TDC's, ADC's, and latches were read out for every event. The scalers, which recorded the number of times a given logic element was true for an entire spill, were read out with the End of Spill (EOS) Pedestal events. So far only events due to Charged and Neutral triggers have been mentioned, but there were also Pedestal, Flasher, and $B \cdot MU2$ triggers. Pedestal events were recorded between every spill, with a quiet detector (no beam), so that the pedestal (dc-value) of each ADC channel was measured. During the spill, Xenon flasher events measured and monitored the Lead Glass gains. Also during the spill a set fraction of $B \cdot MU2$ (prescaled $B \cdot MU2$) triggers were recorded. This was a very loose muon trigger that was useful for monitoring performances of detector components.

The digitization and readout of the detector signals required approximately 5ms for neutral mode and 2.5 ms for charged mode, the difference resulting from not reading out any ADC's in charged mode. During this 'dead time' the detector was insensitive to any new triggers. For neutral mode running the trigger rate was $\sim 1900/10^{12}$ protons on target and the resulting dead time was about 50%. The charged mode had a similar dead time, but the trigger rate was much higher—$\sim 6000/10^{12}$ protons on target.

5.4 Data Acquisition

A PDP-11 was used for the data acquisition computer and data was written onto 6250 bpi 9-track magnetic tapes. The Fermilab version of the Multi

Data Acquisition package was used to control readout from the Camac[1] crates and interface it with the PDP-11. Multi also provided the online monitoring program, which was used to monitor counter rates and many distributions for the detector components—including hit Drift Chamber wires, hit Counters, Lead Glass Pedestals and Lead Glass Flasher responses.

[1]Camac is a standard architecture with its own protocol for organizing modules (such as TDC's) and formatting the readout of these modules.

Chapter 6

Charged Mode Data

This chapter discusses the measurements of $K_{L(S)} \rightarrow \pi^+\pi^-$. The organization of the chapter follows the logical sequence of how the data was taken and then analyzed to isolate the signal. We start by discussing the hardware trigger that selected which events were recorded. The reconstruction of candidate $K_{L(S)} \rightarrow \pi^+\pi^-$ events is then discussed, followed by a detailed look at the cuts employed to isolate the signal from the background. Finally, for completeness, the processing of the data to form Data Summary Tapes is presented.

Before beginning, it is important to emphasize here that at all stages of the experiment, from the hardware trigger to the final event selection, the K_L and K_S events were treated equally and at the same time. This was true for the charged mode data sample treated here, and for the neutral mode data sample treated in Chapter 7. In Section 2.3 we outlined the reasons for simultaneously measuring K_L and K_S decays, and as one follows the discussion of the event sample and analysis, the importance of this should become clear. If we had not made a simultaneous measurement, each trigger requirement and each event selection criteria could have introduced a systematic error.

6.1 Trigger

A characteristic of a $K_{L(S)}$ decaying to $\pi^+\pi^-$ is that at the decay vertex a neutral particle disappears and two charged particles appear. The trigger was designed to select events with two charged tracks originating in the Decay Region, and Figure 35 shows such an event. The dashed line is the neutral kaon and at the vertex two charged pions appear from the vacuum. The scintillator planes at the HDRA, A and B Banks were used to trigger on a two charged track topology. In addition events with final state muons, electrons, or photons were suppressed. We give below a complete specification

of the elements employed in the charged trigger, followed by a discussion of the individual elements and their purpose.

$$\begin{aligned} Charged\ Trigger &= V \cdot (AE \cdot AW \cdot \overline{3A}) \cdot (2B \cdot BE \cdot BW \cdot \overline{3B}) \cdot \\ &\quad \overline{RA4} \cdot \overline{B5} \cdot \overline{MU2} \cdot \overline{DRAC} \\ Charged\ Abort &= PA + VA3 + VA4 \end{aligned}$$

Events were required to have a charged particle entering the V counter at HDRA (V), thereby defining the end of the Decay Region. For $K_L \rightarrow \pi^+\pi^-$ and coherent $K_S \rightarrow \pi^+\pi^-$ one expects in general to have 2 A Bank counters fire. In addition, because of momentum conservation, these two counters should be on opposite sides of the beam from which the decay occurred. One counter from the east half of the A Bank and one counter from the west half were therefore required ($AE \cdot AW \cdot \overline{3A}$). One also expects, again from momentum conservation, the signal to have in general one hit B counter on the east and one hit B counter on the west. The central B counters, B8 and B23, were shared by both east and west, and the trigger required an east-west topology ($2B \cdot BE \cdot BW \cdot \overline{3B}$).

To reject inelastically regenerated events with extra charged particle production, the fourth layer of the RA counters was used in veto ($\overline{RA4}$) as discussed in Section 2.2.2. This requirement also defined the start of the Decay Region for the regenerator beam. (The other three layers of RA counters were used in veto offline.)

To reject triggers from Ke_3 ($K_L \rightarrow \pi^\pm e^\mp \nu$) and $K\pi_3$ ($K_L \rightarrow \pi^+\pi^-\pi^0$; $\pi^0 \rightarrow \gamma\gamma$) we placed the Lead Curtain in front of the B Bank and looked for electromagnetic showers in the Lead. Events with signals greater than 5x minimum ionizing in a single B counter ($\overline{B5}$) were vetoed. To reject $K\mu_3$ ($K_L \rightarrow \pi^\pm \mu^\mp \nu$) triggers, events with any counter in MU2 firing ($\overline{MU2}$) were vetoed. Signals from the scintillator planes PA, DRAC, VA3 and VA4 were used to veto events ($\overline{PA + DRAC + VA3 + VA4}$) with a charged track outside the acceptance of the detector.

6.2 Event Reconstruction

We want to determine the 4-momentum and invariant mass of a two track event, the decay vertex, and the beam from which the parent particle originated. The 4-momentum and invariant mass, assuming both tracks are pions, are given by:

$$\widetilde{P_K} = \widetilde{p_1} + \widetilde{p_2} \tag{6.1}$$

$$m_K^2 = (\widetilde{p_1} + \widetilde{p_2})^2 \tag{6.2}$$

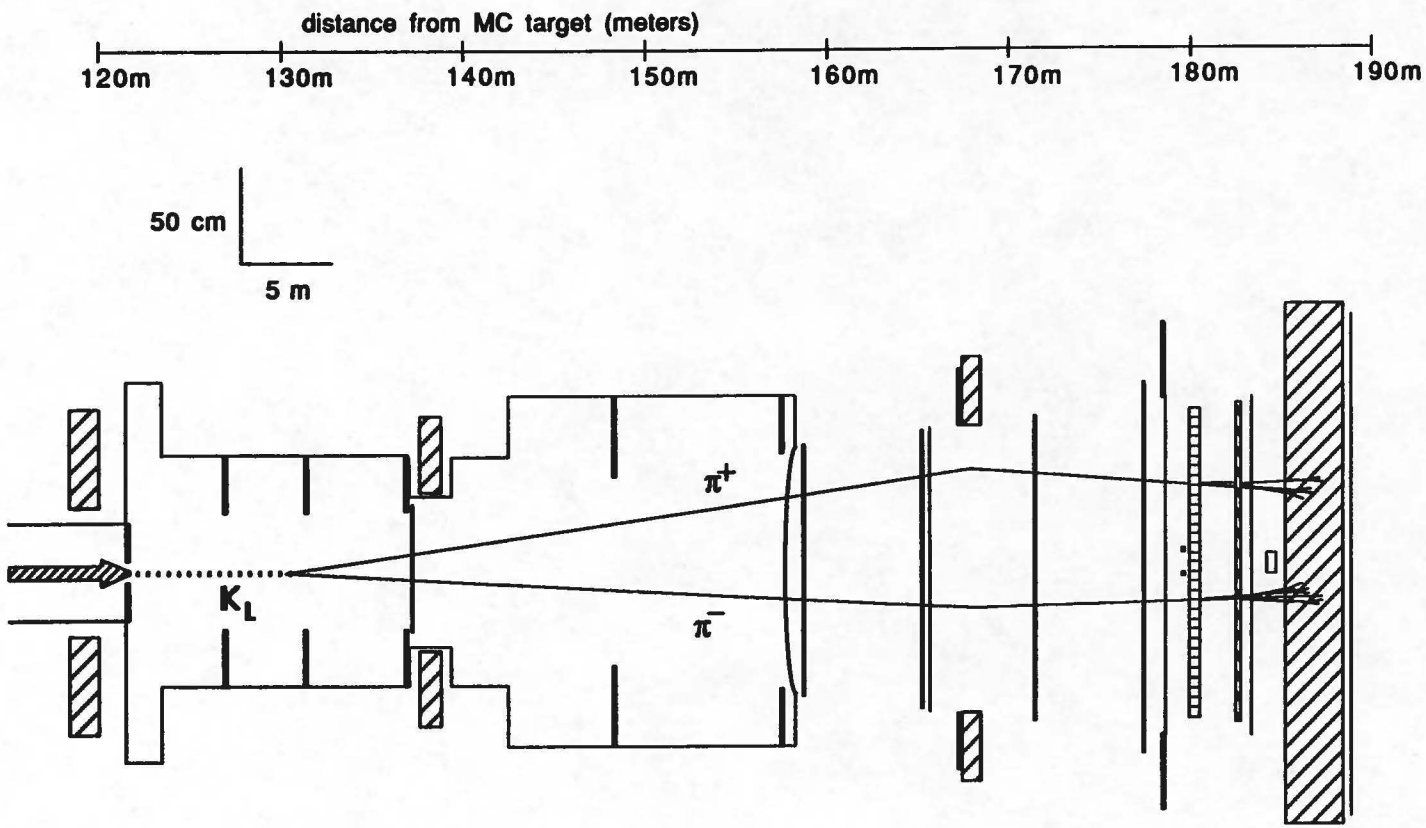

Figure 35: Neutral kaon decaying to $\pi^+\pi^-$

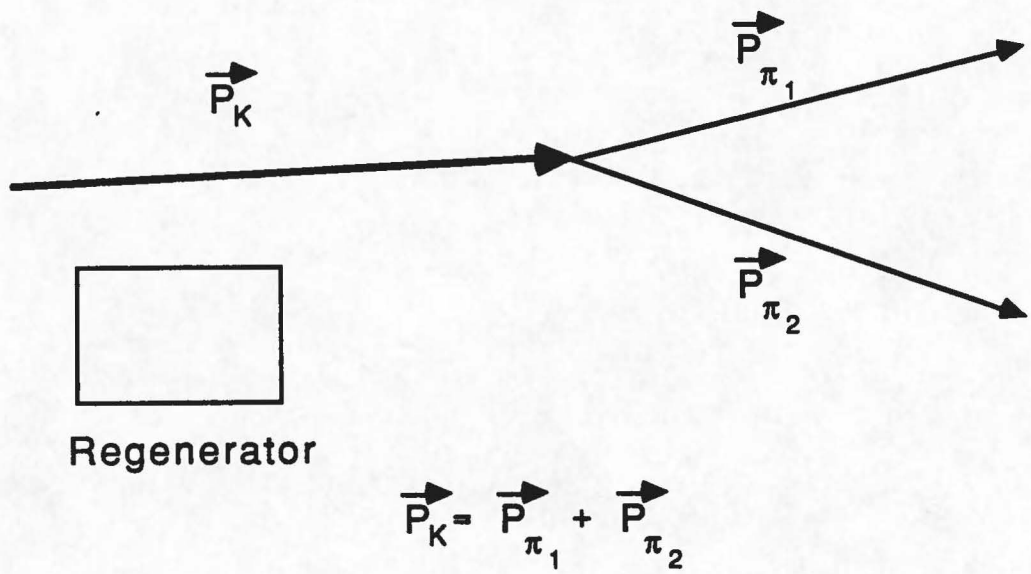

Figure 36: The kaon momentum vector is projected to the plane of the Regenerator to determine the beam of the parent particle.

where $\widetilde{p_1}, \widetilde{p_2}$ are the 4-momenta of the charged tracks. The decay vertex is determined from the intersection of the upstream track segments, and the determination of the beam of the parent particle is illustrated in Figure 36. The kaon momentum vector is projected to the plane of the Regenerator and the sign of the kaon's y position there determines the beam (vacuum or regenerator).

Charged mode events were reconstructed from the Drift Chamber information. The track requirements were that there be two and only two x tracks, two and only two y tracks, and that there be no shared hits on tracks in either the x or y views. Before we discuss matching of the x and y views of tracks (there are two possible pairings), consider the scattering of a kaon at the Regenerator as illustrated in Figure 37. The quantity $q^2 = P^2 \sin^2\theta$, measures the square of the transverse momentum transfer in the scattering process. For kaons in the vacuum beam and for coherently regenerated kaons in the regenerator beam, q^2 is zero. Miscorrelating the x and y views has the effect of introducing a finite q^2, and so the pairing with the smallest q^2 was chosen.

The track momenta are determined from the bend angles of the tracks at the Analysis Magnet using Equation 3.2. Given the tracks and their momenta,

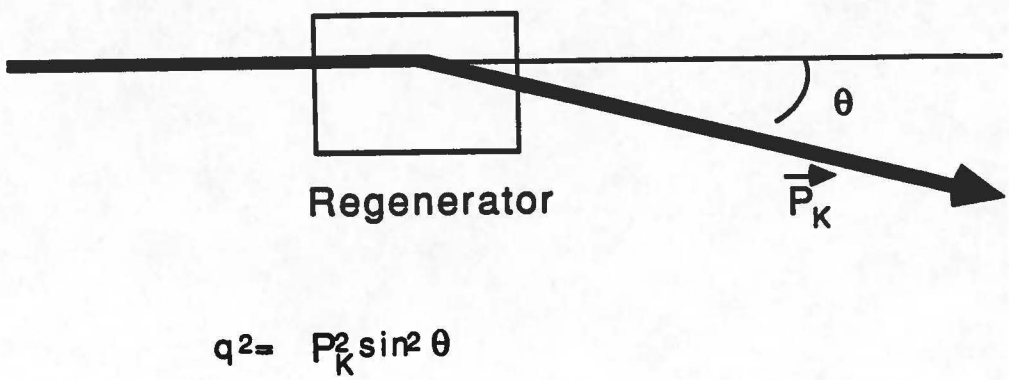

Figure 37: A kaon scatters at the Regenerator; the quantity q^2 measures the square of the transverse momentum transfer.

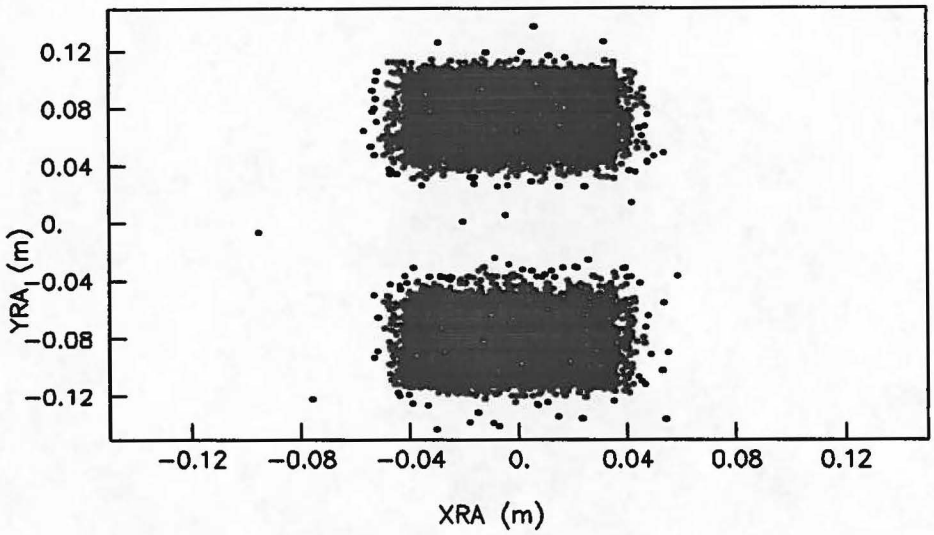

Figure 38: Reconstructed transverse location of kaons at the regenerator plane for identified $K \rightarrow \pi^+\pi^-$ events from the regenerator beam.

the invariant mass, m_K, can be reconstructed using Equation 6.2. From the track information the closest approach vector of the upstream track segments can be calculated, and the midpoint of this vector is taken to be the decay vertex. The kaon momentum vector, as calculated by Equation 6.1, can be projected through the decay vertex to the plane of the Regenerator to determine which beam the kaon came from. For identified $K \rightarrow \pi^+\pi^-$ events from the regenerator beam the kaon x, y position at the regenerator plane is shown in Figure 38. The crosstalk between beams is seen to be negligible.

6.3 Event Selection

Figure 39 shows the raw mass distribution for candidate $K_L \rightarrow \pi^+\pi^-$ decays. This is the invariant (π, π) mass of reconstructed 2-track events which come from the vacuum beam. Figure 40 shows a similar plot for 2-track events which come from the regenerator beam. Note that there is very little background for the regenerator events, while there is substantial background for the vacuum events. In fact, most of the triggers in the vacuum beam are due to background processes. The broad distribution below the K^0 mass peak is due to Ke_3, $K\mu_3$, and $K\pi_3$, and there is some additional background due to lambda decays as well as neutron interactions in the Lead Mask and the V counter. The edge at 360 MeV in Figure 39 is from kinematics of $K_L \rightarrow \pi^+\pi^-\pi^0$ decays (360 MeV $\approx K^0$ mass - π^0 mass).

To isolate the $K \rightarrow \pi^+\pi^-$ signal from the background a number of cuts were

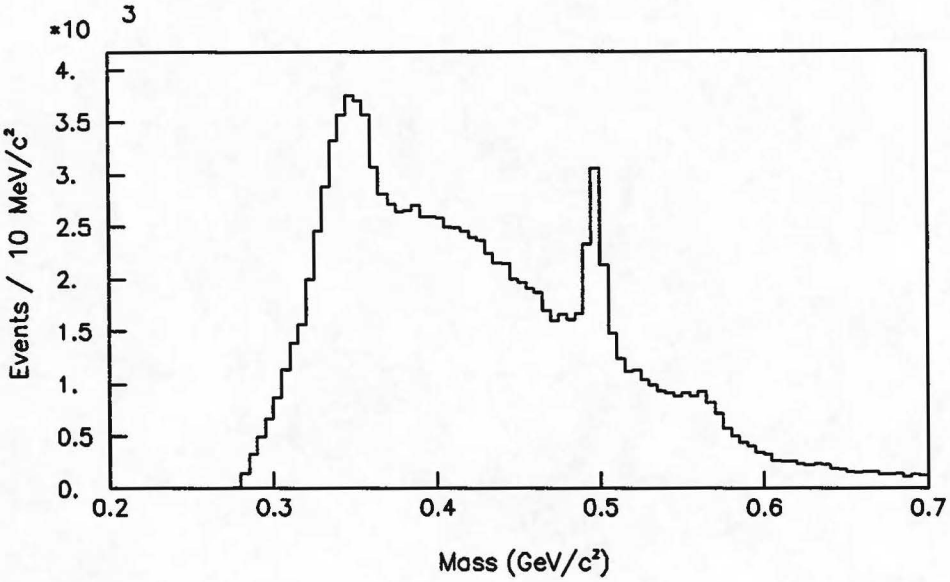

Figure 39: Invariant (π, π) mass of candidate $K \rightarrow \pi^+\pi^-$ events from the vacuum beam

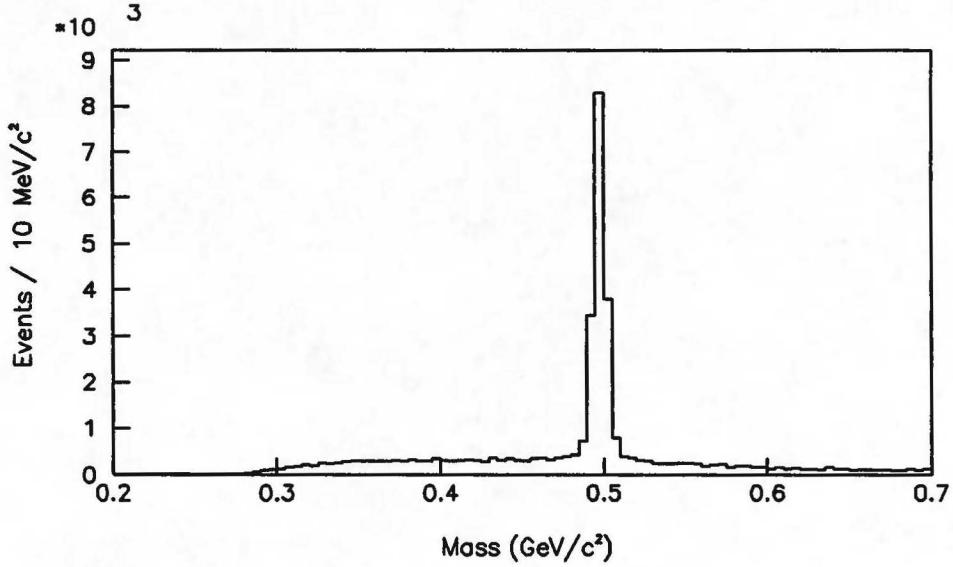

Figure 40: Invariant (π, π) mass of candidate $K \rightarrow \pi^+\pi^-$ events from the regenerator beam

Table 7: Charged mode signal losses due to reconstruction criteria

Charged Mode Cut	Signal Loss
Λ Rejection	0.2%
Scattering Angle of Kaon at Regenerator (q^2)	0.1%
K^0 Mass	1.0%

made. These cuts are described below and Table 7 shows the resulting signal losses as determined by Monte Carlo. (Losses due to geometrical acceptance and accidentals are not included.)

6.3.1 Aperture Cuts

There were aperture cuts made at five planes. The first was the Pb Curtain in front of the B Bank, which had two holes cut in it for the beams to pass. There was no electron identification in the region of the holes, and so a software cut requiring tracks to project within an aperture 1cm larger than the size of the holes was made to reduce background from Ke_3 decays. Also, we would have had to understand the effect of charged pions showering in lead if we had allowed tracks in the hole region. The MU2 counter bank had an aperture of 2.4m x 2.4m, but a software cut of $|x| < 0.80$m, $|y| < 1.10$m was made for the charged tracks projected to this plane to reduce background from $K\mu_3$ decays. In addition, for assuring an understanding of the geometrical acceptance of the detector with the Monte Carlo, a software requirement was made that the tracks be 1cm inside of the following apertures: Vacuum Window, A Bank, and LGA.

6.3.2 $K\mu_3$ Rejection

Each track energy was required to be greater than 10 GeV. This reduced background from $K\mu_3$ decays where the muon had low energy and ranged out in the muon filter (3.2m of iron). Even though MU2 was in veto in the trigger it was found that the background could be significantly reduced by cutting on MU2 latches offline. This was due to a looser timing for the latches than for the trigger logic.

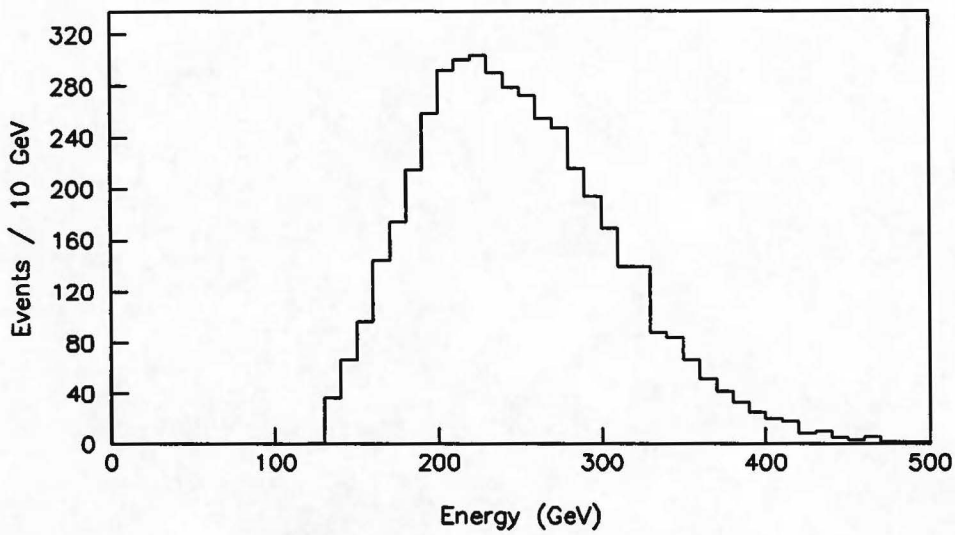

Figure 41: Lambda energy distribution for identified lambda decays in the vacuum beam

6.3.3 Lambda Rejection

Lambdas were produced at the production target and at the Regenerator, and their decays, $\Lambda \rightarrow p\pi^-(\overline{\Lambda} \rightarrow \overline{p}\pi^+)$, were a potential source of background. The lambdas produced at the Regenerator did not pose a problem; in fact, no significant number of them (<< 0.1% of signal) could be identified from this source after applying all cuts. The lambdas produced at the target mostly decayed upstream ($c\tau$ = 7.9cm) and only very high energy lambdas survived as far as the Decay Region. For these lambdas the proton assumes most of the energy in the lab frame. To eliminate them the higher momentum track was assigned to be a proton, and events were cut if both the (p,π) invariant mass was within 10 MeV/c^2 of the lambda mass and the lambda energy was greater than 130 GeV. Figure 41 shows the lambda energy distribution for identified lambda decays in the vacuum beam.

6.3.4 Inelastic K_S Rejection

As described in Section 2.2.2 the Regenerator was segmented longitudinally and had four planes of scintillator for identifying charged particles. Only the fourth layer was employed in the trigger to reject inelastically regenerated K_S events. A further factor of 5 reduction was achieved in the inelastic background by cutting events when any RA scintillator fired.

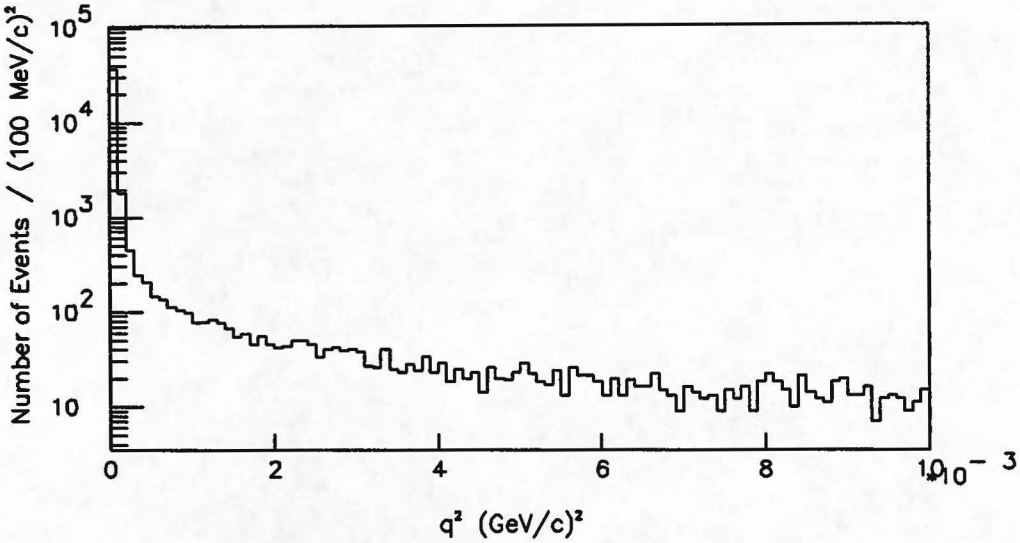

Figure 42: q^2 distribution of identified $K \rightarrow \pi^+\pi^-$ events from the vacuum beam.

6.3.5 Kinematic Cuts on q^2 and m_K

The kinematic quantities which were used to make a final identification of $K_{L(S)} \rightarrow \pi^+\pi^-$ events were q^2 and m_K. Figure 42 shows the q^2 distribution for vacuum events after all other cuts, and Figure 43 shows the same distribution for regenerator events. We cut at 250 (MeV/c)^2 in this variable. Figure 44 shows the reconstructed K^0 mass for identified K$\rightarrow \pi^+\pi^-$ events from the vacuum beam, and Figure 45 shows a similar plot for events from the regenerator beam. A cut was made at $\pm$ 14 MeV/c^2 about the K^0 mass.

It is useful to make a few remarks on resolution at this point. Note that in the limit of perfect chamber resolution and no multiple scattering of the charged pions, one expects a delta function in the mass distribution at the K^0 mass and a delta function in the q^2 distribution at 0. The resolutions actually measured were σ = 3.6 MeV in m_K and σ = 40 (MeV/c)^2 in q^2. These had roughly equal contributions from chamber resolution and multiple scattering (scattering in the V counter and in the A Bank in particular). The cuts on q^2 and m_K were therefore quite loose, but were sufficient to reduce the backgrounds to a manageable level. With these cuts the background in the vacuum beam was approximately 1.2% (due to residual $K\mu_3$ and neutron interactions), and approximately 0.3% in the regenerator beam (due to diffractive and inelastic regeneration) . The shapes of the background distributions and the background subtractions will be treated in detail in Chapter 8.

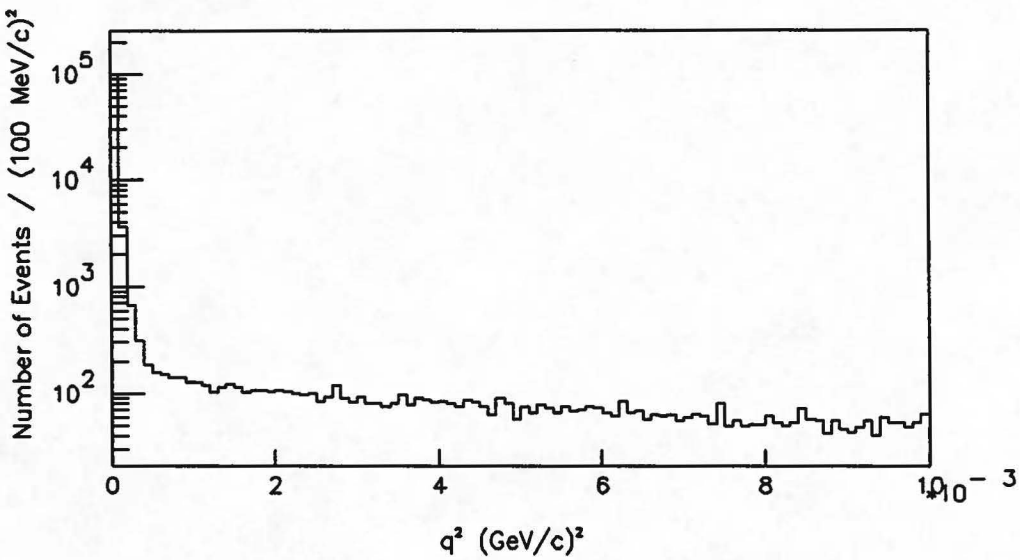

Figure 43: q^2 distribution of identified $K \to \pi^+\pi^-$ events from the regenerator beam.

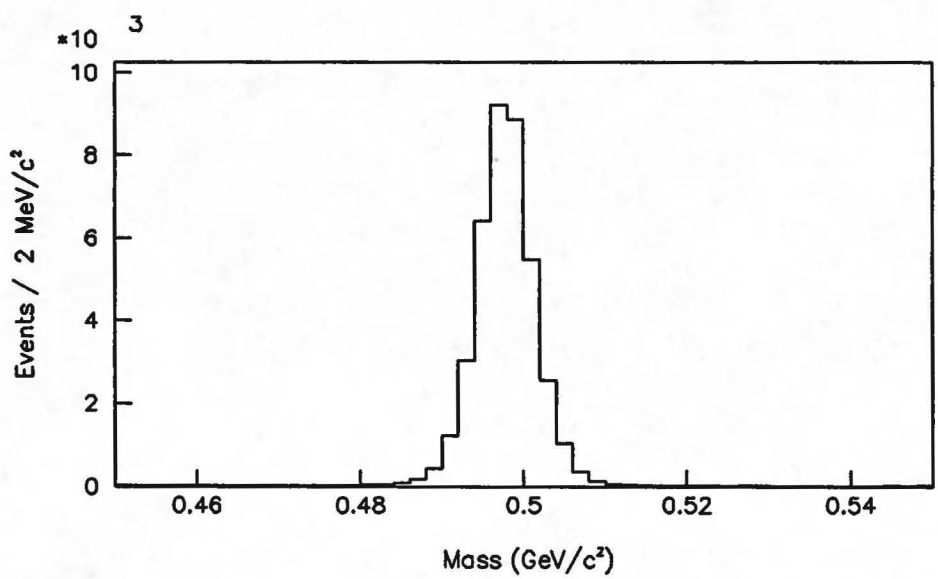

Figure 44: Invariant (π, π) mass of identified $K \to \pi^+\pi^-$ events from the vacuum beam.

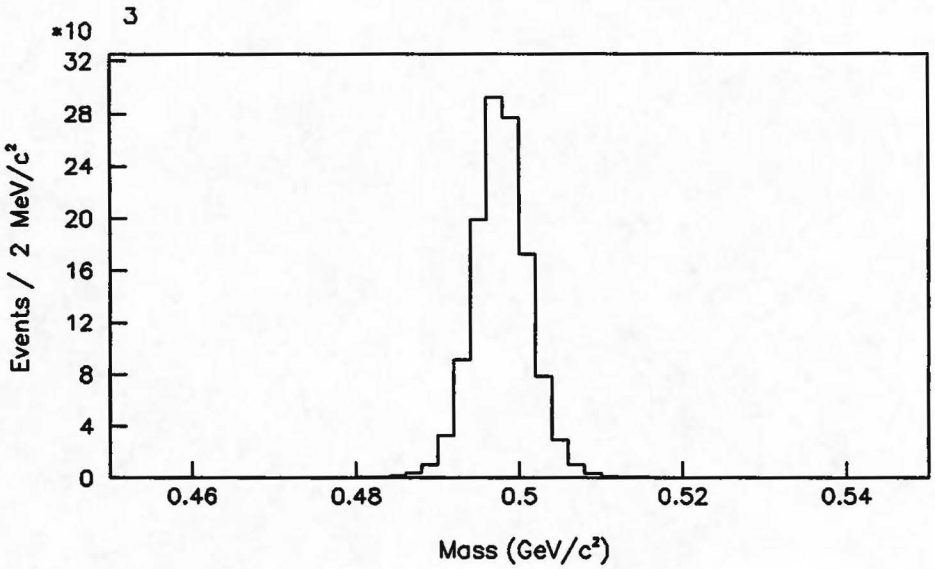

Figure 45: Invariant (π, π) mass of identified $K \rightarrow \pi^+\pi^-$ events from the regenerator beam.

6.4 Data Sets

This analysis used 3 charged data sets, each consisting of approximately 1 day's running time and spaced throughout the neutral running period as shown in Figure 33. The first data set was taken with the BM109 bending magnet[1] on, limiting us to only consider data downstream of the Pb Mask for this data set. The last two data sets were taken with the BM109 off which allowed use of decays upstream of the Pb Mask.

6.5 Data Summary Tapes

The three charged mode data sets consisted of 40 data tapes, and two levels of DST's were made from these. The first level preserved the raw data format while making the following cuts:

- Regenerator and Absorber in same beam
- No RA counters firing
- 2 and only 2 x tracks; 2 and only 2 y tracks.
- Track energies greater than 5 GeV

[1]This is the magnet at $Z = 115$m in Figure 5.

- longitudinal decay vertex between 90 and 150m from the target
- K energy between 15 and 200 GeV
- (π, π) mass between 400 and 600 MeV/c^2

This achieved a compression of $\sim$ 7:1. The second level of DST's had a compressed data format and made the following additional cuts:

- Track energies greater than 10 GeV
- Aperture Cuts as described above
- Lambda cut as described above
- No MU2 counters firing

For each event the following information was written out:

- run number
- Regenerator position
- hit A, B counters
- fitted track parameters
- for Monte Carlo events—true (generated) kaon energy and decay vertex, and absorber scattering

The additional Monte Carlo information was added to understand resolutions and reconstruction biases. (The Monte Carlo is described in detail in Chapter 9.) With respect to absorber scattering, in approximately 10% of events which pass all cuts the kaon has scattered once in the upstream absorbers. To understand this effect we kept track in Monte Carlo events of whether the kaon scattered in any of the three absorbers.

The second level DST's allowed each of the 3 charged data sets to be contained in a single disk file. Monte Carlo events went only through the second level DST process.

Chapter 7

Neutral Mode Data

This chapter discusses the measurements of $K_{L(S)} \rightarrow \pi^0\pi^0$. The design and implementation of the trigger is discussed followed by a detailed treatment of the event reconstruction. This reconstruction is significantly more complicated than in charged mode and there are many subtleties in extracting and optimizing information from the Lead Glass to aid in identifying clean samples of $K_{L(S)} \rightarrow \pi^0\pi^0$. The cuts imposed on the data to eliminate background sources are discussed, and finally a summary of how the data was processed to form Data Summary Tapes is given.

7.1 Trigger

The neutral mode trigger was designed to select K $\rightarrow \pi^0\pi^0$ decays, where the final state consisted of 3 photons and an e^+e^- pair (the pair having resulted from a photon conversion in the Lead Converter at the HDRA). The topology for a typical event is shown in Figure 46.

The electrons and photons deposited all their energy in the Lead Glass so that the total energy measured by the Glass, E_T, measured the kaon energy. The trigger required E_T greater than 30 GeV (E_T).

Events with hadrons or muons were suppressed by using the MU1 and MU2 counter banks. Muon rejection was achieved by vetoing events when any MU2 counter fired ($\overline{MU2}$). Hadron rejection was achieved by using an analog sum of the MU1 counter pulse heights to distinguish events with only electrons and photons from those with hadrons. Events with greater than twice minimum ionizing pulse height in MU1 ($\overline{MU1}$) were vetoed. (This trigger requirement was not used in the early part of the run and was implemented after studies showed it would reduce the trigger rate by 30% with no loss of signal.)

A powerful part of the trigger required a two-track topology consistent

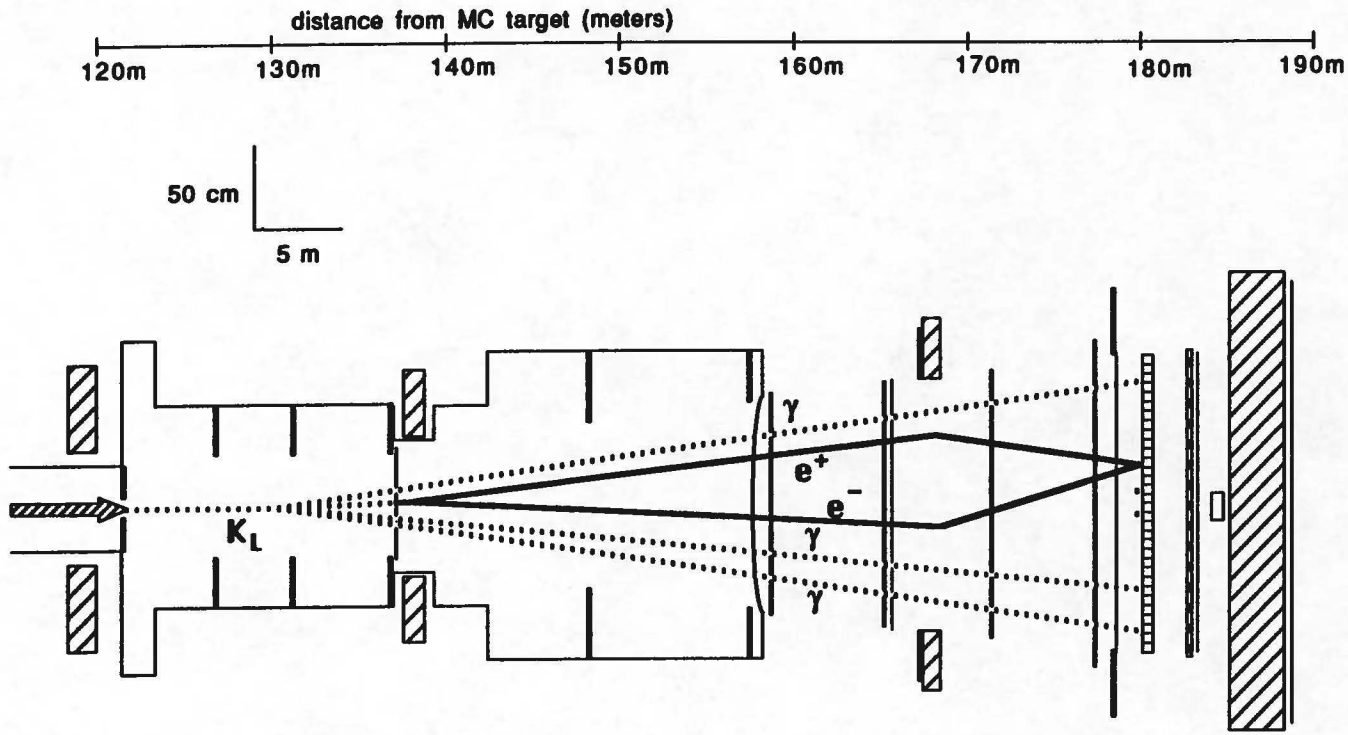

Figure 46: A kaon decays to two neutral pions, which subsequently decay to two photons. One photon converts at the Pb plane in the HDRA to an electron-positron pair; this pair is opened up by the Separator Magnet and reconverged at the Lead Glass with the Analysis Magnet.

with a photon conversion at the HDRA. No signal in the V counter together with a signal in the T counter ($\overline{V} \cdot T$) was the signature for the appearance of a charged particle at the Lead Converter between these two scintillator planes. This trigger requirement also defined the end of the Decay Region. The electron and positron were produced at very small angles with respect to the initial photon direction. They received equal and opposite P_T kicks from the Separator Magnet producing two well separated tracks at the A Bank, where two A counters were required to fire ($2A \cdot \overline{3A}$). The Analysis Magnet reconverged the e^+e^- pair at the Lead Glass, so that at the B Bank there were two reconverging tracks. One or two B counters were demanded in the trigger ($1B \cdot \overline{3B}$).

To reject inelastically regenerated events RA4 was used in veto ($\overline{RA4}$) as was done in charged mode, and again this defined the start of the Decay Region for the regenerator beam. PA and DRAC scintillators were used to reject events with charged particles from upstream of the HDRA ($\overline{PA} \cdot \overline{DRAC}$).

The final trigger requirement, but an important one which reduced the trigger rate from 3000/spill to 1900/spill, was a fast mass calculation performed by the Mass Box. The Adder signals were used as input to the Mass Box which did a fast calculation of $E_T E_2$, and an event was aborted if $E_T E_2 <$ 375 GeV^{2}m^2. Recall from Equation 4.1 that the invariant mass of a particle decaying into photons is given by

$$m^2 = \frac{E_T E_2}{Z^2}$$

At the end of the Decay Region $Z \approx 43m$ and the abort corresponded to a mass cut of 450 MeV/c^2. For decays further upstream, the mass cut was lower.

This completes the discussion of the elements of the neutral mode trigger, which can be summarized as follows:

$$\begin{aligned} \textit{Neutral Trigger} &= (\overline{V} \cdot T) \cdot (2A \cdot \overline{3A}) \cdot (1B \cdot \overline{3B}) \cdot E_T \cdot \\ &\quad \overline{PA} \cdot \overline{RA4} \cdot \overline{DRAC} \cdot \overline{MU2} \cdot \overline{MU1} \\ \textit{Neutral Abort} &= E_T E_2 \end{aligned}$$

7.2 Event Reconstruction

The topology for a $K \rightarrow 2\pi^0$ event consists of 5 particles —3 photons and an electron-positron pair—depositing all of their energy in the Lead Glass. Reconstructing an event involves determining the invariant mass, m_K, of the decay products as well as the decay vertex and the beam from which the kaon

originates. To do this requires first obtaining the energies and positions of the electrons and photons. From these measurements the decay kinematics can then be reconstructed.

7.2.1 Electron And Photon Measurements

The electron energies, photon energies and photon positions were measured from the Lead Glass information, while the electron positions were determined from the Drift Chambers. This section discusses in detail the reconstruction of these quantities and some of the early stages of the event selection.

The first stage of reconstructing an event was to find clusters of energy in the Lead Glass and to determine the energies and positions of these clusters (see Section 4.2). For the $2\pi^0$ analysis, events with fewer than 4 clusters were rejected at this stage. Tracks in the Drift Chambers were then reconstructed and a two track topology was required. Single tracks were allowed in the y-view, however, since the tracks were only separated in this view due to multiple scattering. Distinct tracks were not allowed to share hits except for y-view hits in Chambers 1 and 2 (tracks with little separation) and x-view hits in Chamber 4 (reconverging tracks). Events with more than 4 x tracks or more than 9 y tracks were eliminated at this stage. Some extra tracks were allowed due to the procedure of allowing shared hits and to not reject events with an accidental track. Events with more than two x tracks or more than one y track were carefully analyzed to choose the tracks that were best candidates for an e^+e^- pair. If more than two x tracks were found, the two x tracks which converged best at the Lead Glass were chosen. If more than one y track was found, y tracks were required to project within 5cm of clusters that also had x tracks projecting within 5cm of them. Tracks not projecting to clusters but consistent with going down a beam hole were allowed at this stage. If greater than 2 y tracks still remained, the 2 y tracks which had the smallest separation at the Lead Glass were chosen.

The next stage of the analysis was to correlate the x and y views of the tracks and to associate tracks with clusters. All combinations of track correlations were tried (either 2 or 4) and a track was said to match a cluster if it projected within 5cm of the center of a cluster. If there were 2 y tracks, the correlation was decided by which one had the greater number of matched clusters. If this did not work, the one which had the smallest residual of (track projection - cluster center) was chosen. Once the track correlation was complete, the clusters were identified as either electron or photon candidates. Candidate electron clusters were required to match with 1 or 2 tracks, and the number of such clusters was assigned to the variable NGCLUS. Candidate

photon clusters were required to not match any tracks and to have an energy greater than 2 GeV. The number of such photon clusters was assigned to the variable NEXCL. Only events with NGCLUS=1 or 2 (2 clusters were allowed so as to keep events with an imperfectly reconverged e^+e^- pair) and NEXCL=3 were kept for further $2\pi^0$ analysis. In addition, events were rejected if a track did not match a cluster and was consistent with going through one of the Lead Glass holes.

At this stage energy corrections were applied to the electrons and photons because of i) cluster overlaps, ii) overlapping electrons on NGCLUS=1 events, iii) missing blocks in clusters iv) trigger timing variations and v) nonlinear response of the Lead Glass.

i) Since clusters consist of a 3x3 array of Lead Glass blocks, it can happen that 2 clusters overlap by 1, 2 or 3 blocks. Recall that 2 clusters must have a minimum between them and so cannot overlap by more than 3 blocks. The energy of a cluster is the sum of its 3x3 array and so blocks which are shared by two clusters have their energy double counted. A procedure was therefore applied to correct this and partition an overlapping block's energy between the two competing clusters. The procedure was to partition it according to the relative energies of the clusters when not including the overlapping blocks. The cluster centers were then recomputed.

ii) For NGCLUS=1 events, a 5x5 sum was used rather than 3x3 to get a better measurement of the e^+e^- cluster. If any of the outer 16 blocks overlapped another cluster they were not included. This electron cluster was 'fatter' than a normal cluster since there were two electrons which were not perfectly converged. Additionally, there could be a bremsstrahlung photon (produced in the Lead Converter) of significant energy present as well. The 5x5 energy sum was then scaled down by 2% to reflect that the energy calibration of the Glass was done using 3x3 clusters, which contained 98% (on average) of the shower energy.

iii) Clusters which were centered on pipe blocks or were on the outer edge of the array had missing blocks and therefore required energy corrections for this. For pipe block clusters, the correction was 0.54% if one block was missing and 1.67% if two blocks were missing.

iv) The Lead Glass response had an 0.4%/ns signal energy dependence on the trailing edge of the ADC gate. The neutral mode trigger timing was defined by the 1B timing and hence by the track nearest to a B Bank phototube. A propagation speed of 20cm/ns for light signals was assumed in the B Bank scintillator to calculate the trigger timing correction to the Lead Glass response.

v) The nature of the nonlinear Lead Glass response for electrons and pho-

tons was discussed earlier in Section 4.3. The nonlinearity correction applied was given by $E = E_m^B$, where E_m is the measured energy using the Glass gains at 1 GeV and assuming a linear response, and E takes into account the nonlinearity. This correction was described in detail in Section 4.3 and a description of the exponent B can be found there. For NGCLUS=1 events, the electron energy correction was applied to the individual electron energies rather than their sum.

One final correction was made before reconstructing the decay kinematics and that was to take the position of the electron cluster from the track information rather than from the Lead Glass information. Each track gave an independent estimate of the impact point of the pseudophoton trajectory—the pseudophoton being that photon which converted to an e^+e^- pair. The positions from each track were weighted proportionate to their (momentum)^2 which is the optimal weighting if one considers the multiple scattering effects.

7.2.2 Decay Kinematics

Given the energies and positions of the electrons and photons, one can reconstruct the decay vertex, mass and q^2 for $K \rightarrow 2\pi^0$ or $K \rightarrow 3\pi^0$ events. Each of the π^0's from these events undergoes a fast electromagnetic decay to 2 photons, and it was shown in Section 4.1 that for a particle of mass m decaying to n photons,

$$m^2 = \frac{1}{2} \sum_{i,j=1}^{n} \frac{E_i E_j r_{ij}^2}{Z^2} \tag{7.1}$$

This relation was used for the π^0 decay to determine the longitudinal decay vertex, Z, in meters from the Lead Glass. For a $2\pi^0$ decay there are 4 clusters in the Lead Glass and 3 possibilities for pairing the clusters such that each cluster is associated with a π^0 (there are 15 distinct ways to pair clusters in a $3\pi^0$ event). This is illustrated in Figure 47. For each pairing Z was calculated using Equation 7.1 and the uncertainty in Z (σ_Z) was determined by propagating the rms uncertainties in the energy and position measurements. Each pairing possibility gave two Z measurements from which a weighted average (AVZ) was taken:

$$AVZ = \frac{Z_1/\sigma_{Z_1}^2 + Z_2/\sigma_{Z_2}^2}{1/\sigma_{Z_1}^2 + 1/\sigma_{Z_2}^2}$$

The consistency of the pairing correctly describing a $K \rightarrow 2\pi^0$ decay was measured by χ^2, where

$$\chi^2 = \frac{(AVZ - Z_1)^2}{\sigma_{Z_1}^2} + \frac{(AVZ - Z_2)^2}{\sigma_{Z_2}^2}$$

The correct pairing was chosen to be that with the lowest χ^2 and this determined Z. The transverse vertex of the decay was found with the aid of tracking information for the e^+e^- pair. The center of energy of the pair was calculated at Chambers 1 and 4, and these two points formed a vector which was projected to the Z of the decay, thereby determining the x and y decay vertices. Typical resolutions for the decay vertex were 1.1m in Z, 7mm in x and 10mm in y.

Given Z, the mass of the parent particle was computed using all 4 clusters,

$$m_K^2 = \frac{1}{2}\sum_{i,j=1}^{4}\frac{E_iE_jr_{ij}^2}{Z^2}$$

The kaon trajectory was given by the vector that joined the decay vertex and the center of energy in the Lead Glass, where the center of energy is calculated from weighting the cluster positions by their energies:

$$x_{CE} = \frac{\sum_i x_iE_i}{\sum_i E_i}$$
$$y_{CE} = \frac{\sum_i y_iE_i}{\sum_i E_i}$$

As in charged mode, the kaon momentum vector was projected to the plane of the Regenerator to determine which beam the parent came from. Figure 48 shows the reconstructed transverse position at the regenerator plane for $K_S \rightarrow 2\pi^0$ events after all cuts. The q^2 calculation was again done the same as in charged mode by measuring the angle of the momentum vector of the kaon to the vector formed by the target and decay vertex.

7.3 Event Selection

Figure 49 shows the invariant mass distribution for candidate $K \rightarrow 2\pi^0$ decays from the vacuum beam. Included in this sample are events satisfying NGCLUS=1 or 2, NEXCL=3, 2 x tracks, 1 or 2 y tracks, and decay vertex in the vacuum beam. Figure 50 shows a similar distribution for events reconstructing in the regenerator beam. As in the charged mode, the regenerator beam events are quite free of background while there is considerable background for the vacuum events. Here the principle source of background comes from $K_L \rightarrow 3\pi^0$ decays where two photons either miss the Lead Glass or fuse there with other photons. To isolate the $K^0 \rightarrow 2\pi^0$ signal from the background a number of cuts were made which are described below. Table 8 shows how much signal was lost by these cuts as determined by Monte Carlo. Losses due to geometrical acceptance and accidentals are not included.

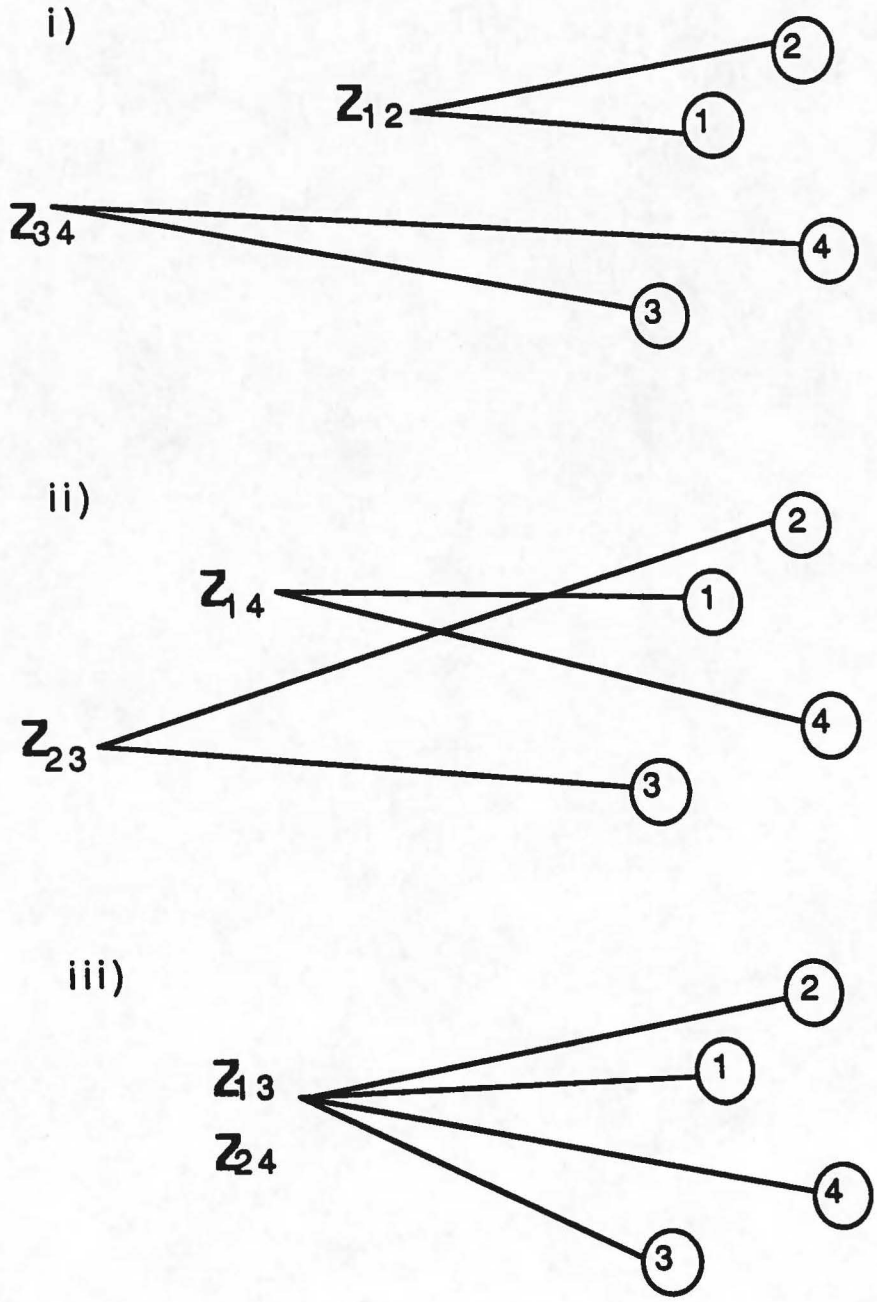

Figure 47: There are three possibilities for pairing photons to determine the longitudinal decay vertex in a $K \rightarrow 2\pi^0$ event. The pairing that gives the most consistent Z determines the pairing.

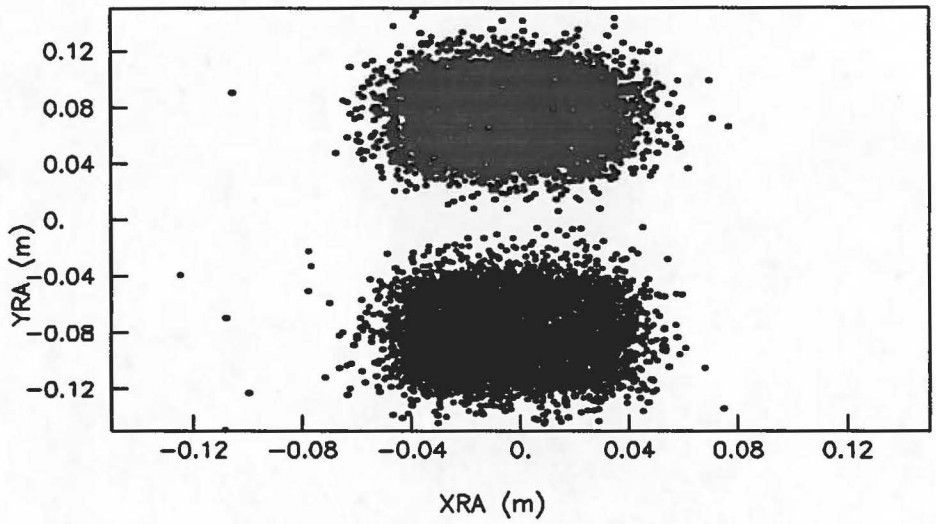

Figure 48: Transverse location of kaons at the Regenerator for identified $2\pi^0$ events from the regenerator beam

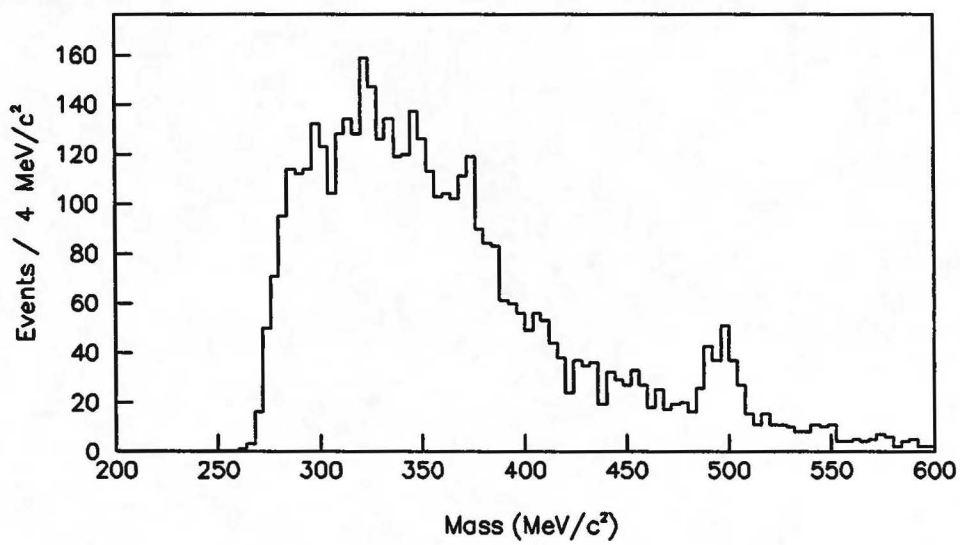

Figure 49: Invariant mass of candidate $K \rightarrow 2\pi^0$ events from the vacuum beam

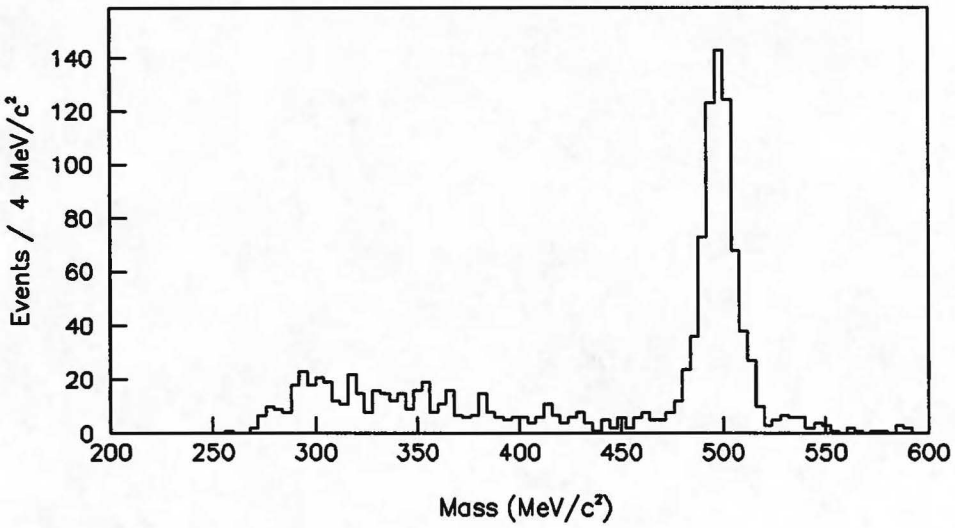

Figure 50: Invariant mass of candidate $K \rightarrow 2\pi^0$ events from the regenerator beam

Table 8: Neutral mode signal losses due to reconstruction criteria

Neutral Mode Cut	Amount of Signal Lost
Hadron Rejection (SEP2)	2.5%
Fusion Rejection for Electrons	2.5%
Fusion Rejection for Photons	0.1%
$\chi^2 < 4$	3.7%
$q^2 < 4000$ (MeV/c)^2	9.6%
$480 < m_K < 520$ MeV/c^2	2.1%

7.3.1 Aperture Cuts

For assuring an understanding of the geometrical acceptance of the charged tracks with the Monte Carlo, a software requirement was made that the charged tracks be 1cm inside of the following apertures: vacuum window, A Bank, and B Bank. One other important aperture cut concerned the holes in the Lead Glass. This was a crucial region in which to understand the acceptance and use was made of the Collar Anti to facilitate this (see Section 2.2.5 and CA diagram in Figure 16). Events which had greater than a 5x minimum ionizing signal in any CA counter were rejected. This effectively vetoed all electrons hitting the CA and all photons which converted in its 3 radiation lengths of copper.

7.3.2 Hadron Rejection

A measure of how well the tracks reconverge at the Lead Glass is given by the variable $SEP2$,

$$SEP2 = \frac{(x_1 - x_2)^2 + (y_1 - y_2)^2}{1/p_1^2 + 1/p_2^2}$$

where (x,y) are the coordinates of a track at the Lead Glass. Note that tracks associated with hadrons are not expected to converge at the Lead Glass and therefore have a large $SEP2$. The $SEP2$ distribution for $K_S \rightarrow 2\pi^0$ decays is shown in Figure 51, and the analysis required $SEP2 < 0.2$.

7.3.3 Inelastic K_S Rejection

Similar to charged mode running, RA4 was the only regenerator plane employed as a veto in the trigger to reduce inelastically regenerated K_S events. Thus we made a software requirement that no RA counter in any of the four layers fired to further reduce this background.

7.3.4 Eliminating Accidental Clusters

The ADC gate for the Adders was 100ns compared to 250ns for the Lead Glass, so that Adders were less sensitive to accidentals. Adders were therefore required to see at least 80% of the energy of clusters whose center was in that Adder. Only cluster blocks who were in the appropriate Adder were included for this calculation of the cluster energy. This helped save events with an extra out of time cluster.

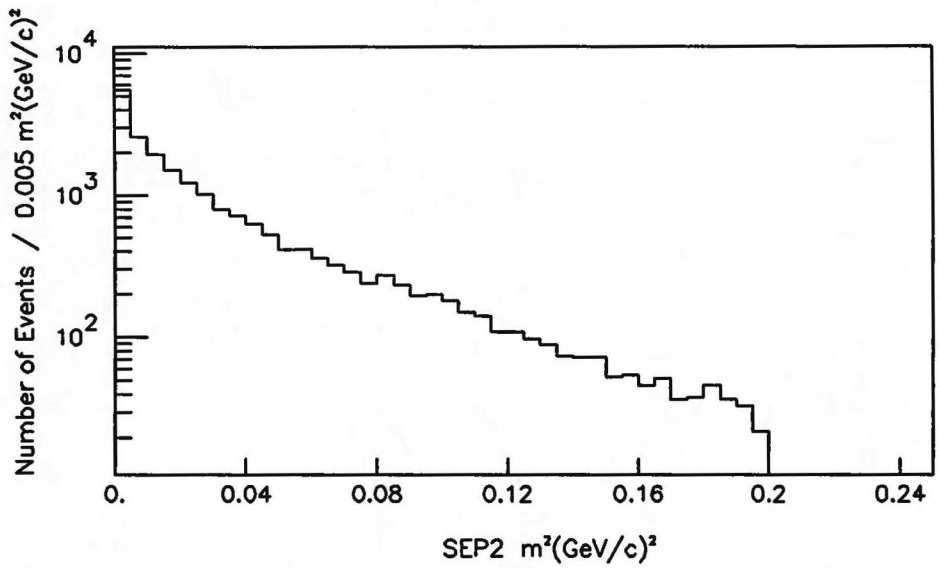

Figure 51: $SEP2$ distribution for identified $K \rightarrow 2\pi^0$ events from the regenerator beam

7.3.5 Fusion Recognition for Electron Clusters

$FRAC$ was defined to be the ratio E/P for the e^+e^- pair, where E was the energy measured by the Lead Glass and P was the sum of track momenta measured by the Drift Chambers. The $FRAC$ distribution for $K_S \rightarrow 2\pi^0$ events was shown earlier in Figure 30. The high side tail is due to events with a large energy bremsstrahlung photon produced at the Lead Converter in the HDRA. Because the e^+e^- pair was reconverged on top of the impact point of the pseudophoton at the Lead Glass, the Lead Glass also measured the energy of brem photons which were not seen by the chambers. A large $FRAC$ also occurred if a photon fused (ie. landed close enough to the electron cluster so as to be unresolved by the cluster finder) with the electron cluster. $FRAC$ was therefore a useful variable in identifying background from $K_L \rightarrow 3\pi^0$ events where there was a fusion of 1 photon with the e^+e^- cluster. A cut requiring $FRAC$ less than 1.5 was made.

7.3.6 Fusion Recognition for Photon Clusters

To reduce background from $K_L \rightarrow 3\pi^0$ decays where 2 photons fused into 1 photon cluster, we made a cut to eliminate 'diagonal clusters'. Figure 52 below illustrates a typical example. The cut applied was the following: if

	.2	.2	.5	.2	
	.2	.6	14.1	.5	
	.6	14.7	.3	.2	
	.1	.3	.1	.1	

Figure 52: A plot of the block energies (in GeV) in one section of the Lead Glass. The fusion of two photons here is recognized as one cluster by the cluster finder. It can be identified as a fusion, however, because a corner block (in a 3x3 cluster about the block with maximum energy) has greater energy than its side block neighbours.

- a corner block had greater energy than each of its neighboring side blocks, and
- this corner block energy was greater than 1 GeV, and
- this corner block was not an overlapping block between 2 clusters

then the event was cut.

7.3.7 Photon Vetoes

The detector had a large number of counters whose purpose was to recognize photons that missed the Lead Glass array, and thereby reduce background from $3\pi^0$ events. The following planes were found to be useful in distinguishing the signal from the background and were used in the analysis: CA, BA, VA3 and DRAN.

The Collar Anti was previously mentioned as being very important for understanding the acceptance. Additionally, it served as an important photon veto. The BA had 3 longitudinal layers with horizontal and vertical counters in each layer, and was useful for vetoing photons with energy greater than 5 GeV. The sum of the ADC signals from the vertical counters was used to form EBA_I, EBA_{II}, EBA_{III} for each layer. We defined EBA = $EBA_I + EBA_{II}$ and EBAR = EBA_{III}/EBA. Events that had EBA>5 GeV and EBAR<0.2 were cut, where EBAR was used to distinguish electromagnetic energy in BA from hadronic energy so as not to veto events with an accidental neutron interaction. For VA3 and DRAN, events were rejected when any counter in these two banks had an ADC signal larger than 0.8x minimum ionizing.

7.3.8 Charged Particle Vetoes

Events in which a scintillator fired in VA2 or VA4 were cut. These scintillators were for charged particle identification, yet cutting on them improved the signal to background for the vacuum events. Whether this was due to charged particles from wide angle photons converting upstream was not clear.

7.3.9 e^+e^-,γ Energies

The final stage of analysis required the e^+e^- energy as measured by the Lead Glass to be greater than 1 GeV. Also, photon energies were required to be greater than 2.5 GeV. These cuts were imposed to reduce the sensitivity to using preliminary calibration constants at early stages of the analysis. Recall that 0.5 GeV had been required for electron clusters and 2 GeV for photon clusters.

7.3.10 Longitudinal Decay Vertex

The Z distribution for identified $K \rightarrow 2\pi^0$ events from the vacuum beam is shown in Figure 53, and a similar distribution for events from the regenerator beam is shown in Figure 54. We required $Z < 141$m, which is more than 3m downstream of the HDRA (the resolution on Z was 1.1m). No upstream Z cut was made—the acceptance there was choked off quickly by the Lead Mask. Since the Z for $3\pi^0$ events misreconstructing as $2\pi^0$ events is shifted downstream due to missing energy, this cut helped reduce the $3\pi^0$ background.

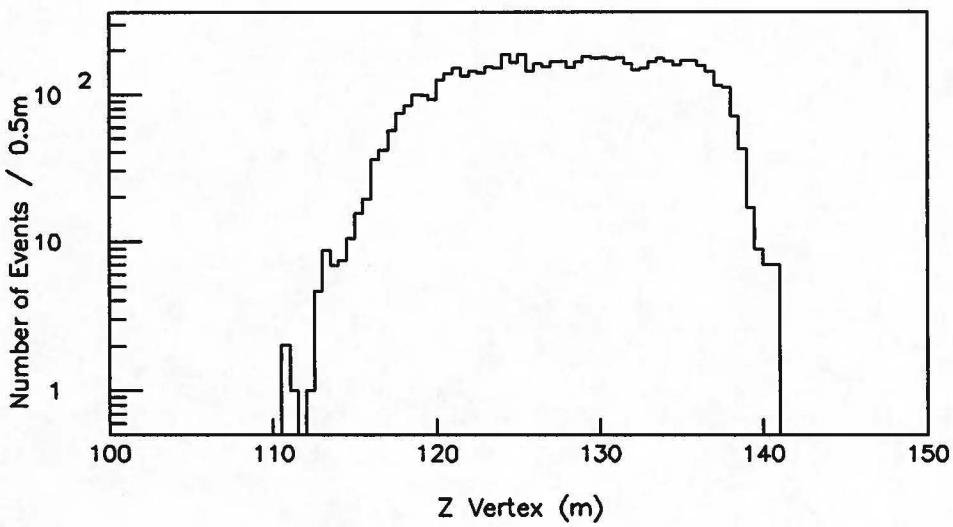

Figure 53: Reconstructed longitudinal decay vertex of identified $K \rightarrow 2\pi^0$ events from the vacuum beam

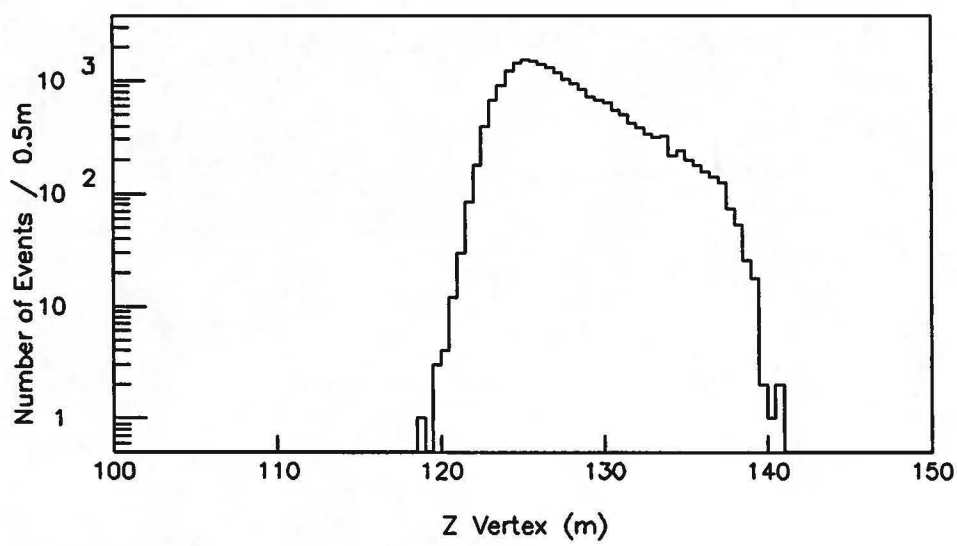

Figure 54: Reconstructed longitudinal decay vertex of identified $K \rightarrow 2\pi^0$ events from the regenerator beam

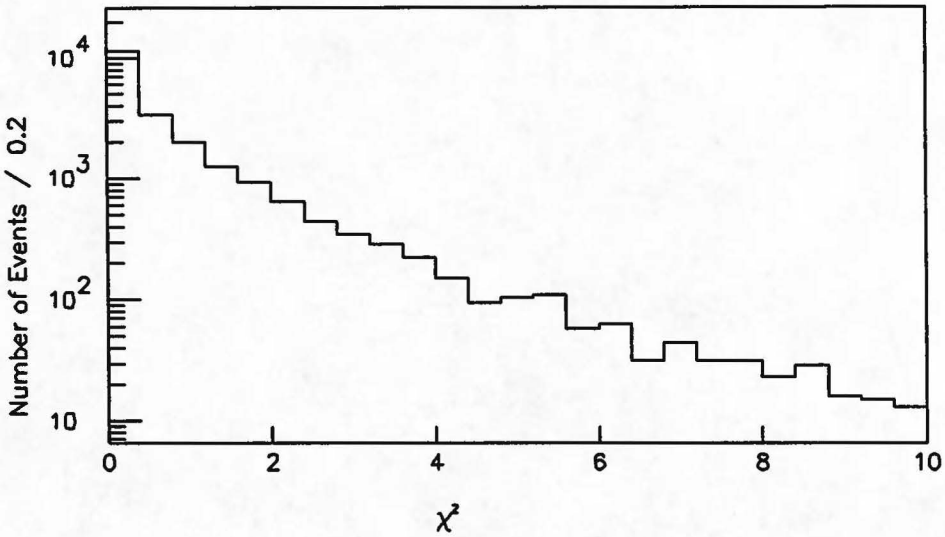

Figure 55: χ^2 distribution for identified $K \rightarrow 2\pi^0$ events from the regenerator beam

7.3.11 Kinematic Cuts on χ^2, q^2, and m_K

Finally, cuts were imposed on the kinematic quantities χ^2, q^2, and m_K to isolate the signal. The χ^2 and q^2 distributions for identified $K \rightarrow 2\pi^0$ events from the regenerator beam are shown in Figures 55 and 56. The cuts applied were $\chi^2 < 4$ and $q^2 < 4000$ MeV^2. Note that the q^2 resolution was much worse than in charged mode and a much looser cut was made. The inelastic and diffractive backgrounds were therefore much worse—approximately 3% compared to 0.3% in charged mode. The $K \rightarrow 2\pi^0$ mass plot for vacuum events is shown in Figure 57 after all cuts. A similar plot for regenerator beam events is shown in Figure 58. We cut at ± 20 MeV (3.3 sigma) about the K^0 mass, leaving a background subtraction of 1.5% to make for the K_L mode. The background shapes and background subtractions will be discussed in Chapter 8.

7.4 Data Summary Tapes

Approximately 500 data tapes were analyzed to obtain the neutral mode data sample. For candidate $2\pi^0$ events three levels of DST's were produced. DST's were also produced for candidate $K_L \rightarrow 3\pi^0, K_L \rightarrow \gamma\gamma$ and sheet π^0 events.[1]

[1]Sheet π^0 events are described in Section 4.3.

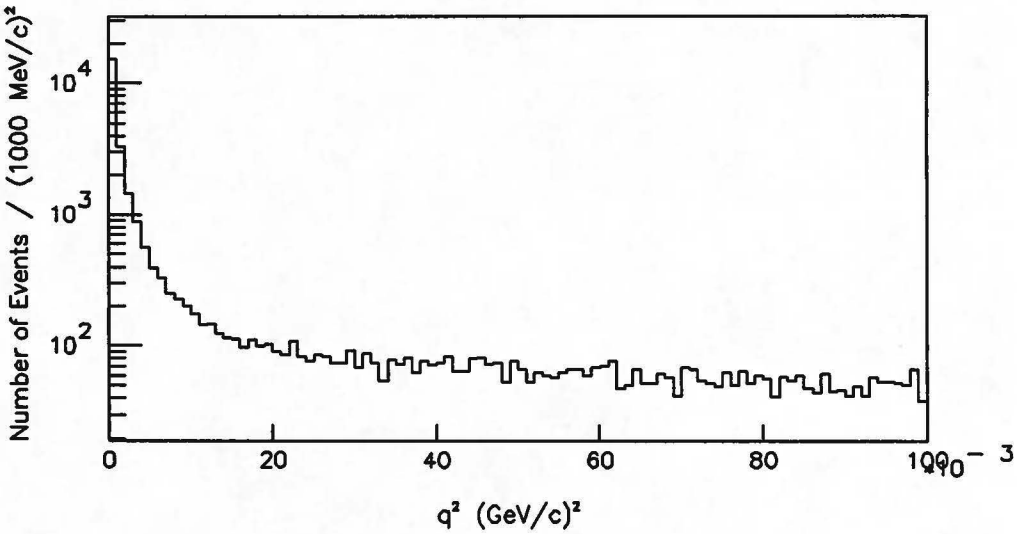

Figure 56: q^2 distribution for identified $K \rightarrow 2\pi^0$ events from the regenerator beam

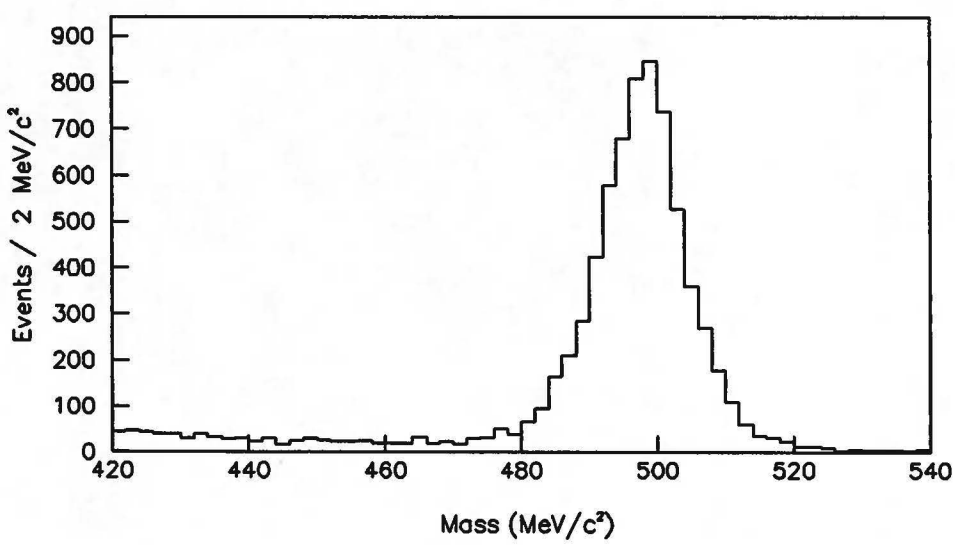

Figure 57: Invariant mass of identified $K \rightarrow 2\pi^0$ events from the vacuum beam

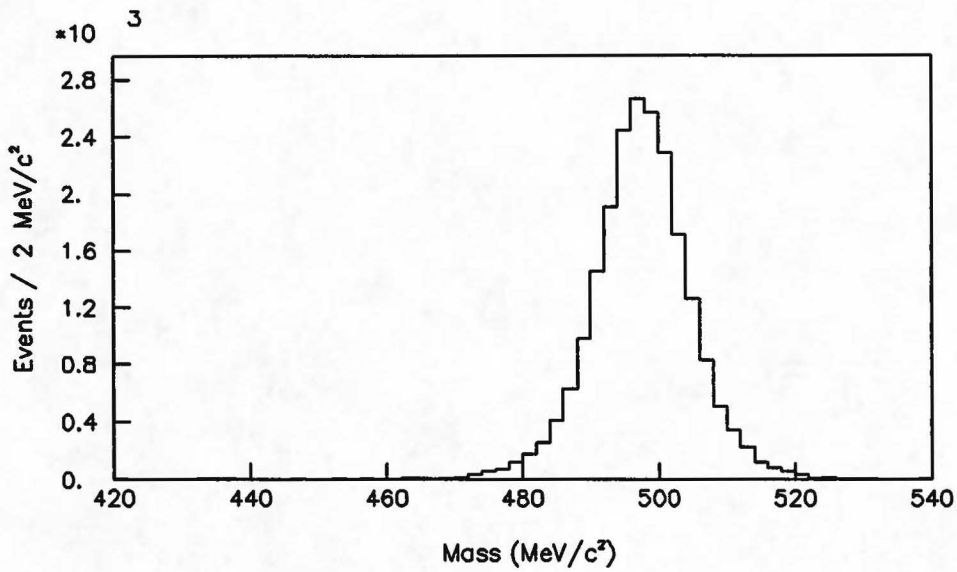

Figure 58: Invariant mass of identified $K \rightarrow 2\pi^0$ events from the regenerator beam

7.4.1 First Level DST's

The first level of summary tapes produced separate DST's for $K^0 \rightarrow 2\pi^0$ and $K^0 \rightarrow 3\pi^0$ candidates. A third type of DST was produced for candidate $K^0 \rightarrow \gamma\gamma$ and sheet π^0 events. The following cuts were made for the $K^0 \rightarrow 2\pi^0$ sample:

- Regenerator and Absorber in same beam
- BA cut as described above
- Adder ratio cut as described above to eliminate accidental clusters
- 2 x tracks and 1 or 2 y tracks
- SEP2 < 0.2
- no tracks down beam hole in Lead Glass
- NGCLUS = 1 or 2
- NEXCL = 3

For the $K^0 \rightarrow 3\pi^0$ sample, the same cuts were applied except:

- NEXCL = 5

- no BA cut was applied

The candidate $K^0 \rightarrow \gamma\gamma$ events had the same cuts as the $3\pi^0$ candidates, except NEXCL=1 was required. The candidate sheet π^0 events passed the following cuts:

- Regenerator and Absorber in same beam
- Adder ratio cut as described above to eliminate accidental clusters
- 2 x and 1 or 2 y tracks
- $SEP2 > 0.2$
- NGCLUS=2
- NEXCL=2

In addition to the above cuts, the data was compressed in the following manner. A sparse readout of the Lead Glass and Adders was done. The Adders were required to have more than 10 counts above pedestal. All Glass blocks in a 5x5 array around the center of each of (NGCLUS + NEXCL) clusters were saved. Information from the ADC's of VA1, VA2, VA3, VA4, DRAN, MA, LGA, and BA was compressed and converted to an energy signal for each counter. Adder and MU1 ADC's had their pedestals subtracted. All raw latch information, TDC information and Drift Chamber information was written out. One Lead Glass pedestal per spill was written out. It was an average of all good pedestals in that spill and was computed to 0.1 counts ($\approx$ 0.3 MeV).

The above cuts and data compression yielded 10 $K^0 \rightarrow 2\pi^0$ DST's, 12 $K^0 \rightarrow 3\pi^0$ DST's, and 10 $K^0 \rightarrow \gamma\gamma$, sheet π^0 DST's. (One DST was a 2400 foot 6250 bpi tape.)

7.4.2 Second and Third Level DST's

Second level DST's were produced for the $2\pi^0$ and $3\pi^0$ data samples. A more compressed data format was used and the following additional cuts were made:

- BA, VA3 and DRAN photon veto cuts
- VA2 and VA4 charged particle cuts
- RA latch cut for rejecting inelastics

The information saved for the second level DST's consisted of:

- run number
- Regenerator position
- NGCLUS, NEXCL
- EBA, EBAR
- latches
- maximum energy in a CA counter
- diagonal cluster information for photon fusion identification
- fitted track parameters
- cluster energies and positions
- for Monte Carlo—true K energy and decay vertex, absorber scattering

This produced 12 $3\pi^0$ files and 10 $2\pi^0$ files. For the $2\pi^0$ sample a final set of cuts produced 1 disk file having the same format as the second level DST's. This third level DST required $\chi^2 < 10$ and reconstructed K^0 mass between 420 and 540 MeV/c^2.

Monte Carlo events were generated with the same cuts and data format as the first level DST's. They subsequently went through the same analysis as data events.

Chapter 8

Background Subtractions

The previous two chapters have discussed in detail the data samples and the criteria for identifying $K_{L(S)} \rightarrow 2\pi$ events. Two corrections need to be made before extracting $|\epsilon'/\epsilon|$—the remnant background in each mode must be determined and subtracted, and a correction must be made for the relative acceptance differences between vacuum and regenerator events. This chapter shall discuss the backgrounds for each mode—the sources of background and their kinematic distributions, and the resulting uncertainties in the background subtractions.

We shall first discuss the backgrounds for the regenerator events for both charged and neutral modes, where the common source of background is from diffractive and inelastic regeneration. The semileptonic and neutron backgrounds will then be treated for the $K_L \rightarrow \pi^+\pi^-$ mode. Finally, we shall discuss the background to the $K_L \rightarrow 2\pi^0$ data sample, where a good understanding of the nature of $3\pi^0$ events which fake $2\pi^0$ events is required.

8.1 Diffractive and Inelastic Backgrounds

The characteristics of regeneration are described in the Appendix. Here we want to determine the relative amounts of the coherent, diffractive and inelastic signals that are present in the regenerator beam data. The diffractive and inelastic signals are treated as background to the coherent signal, which is used for the $|\epsilon'/\epsilon|$ calculation. These signals are most easily understood in the distribution of the variable q^2, and the charged mode is examined first since its q^2 resolution (40 (MeV/c)^2 rms) is excellent. Recall the q^2 distribution for the regenerator beam events shown in Figure 43. The coherent peak at $q^2 = 0$ is clear. Above 20,000 (MeV/c)^2 the data is dominated by inelastics, while below that there is a mixture of diffractive and inelastic data. Before proceeding, we

point out that with the requirement of $q^2 < 250$ (MeV/c)^2 the background is only 0.3%. It was therefore not necessary to do any more than draw a smooth line through the q^2 data points above 700 (MeV/c)^2 and extrapolate this to lower q^2 to obtain an adequate background determination. The neutral mode, however, due to its worse resolution demanded a good understanding of the q^2 distribution.

The inelastics are quite uniformly distributed in q^2; one expects the distribution to be that for scattering from a single nucleon with the probability for scattering proportional to $\exp(-6q^2)$ (see Appendix). The measured distribution is slightly different from this, resulting from the q^2 dependence of the acceptance. The distribution for diffractive scattering is more complicated and required a careful study to understand it.

Single diffractive scattering is described by Equation A.1 where the 3 scattering processes are i) a K_L scatters regenerating a K_S, ii) a K_L coherently regenerates a K_S and scatters elastically, and iii) a K_L scatters elastically. (The Appendix points out that the sum of processes i) and ii) is strongly suppressed by the choice of a 2 interaction length regenerator.) These 3 processes are coherent, since the scattering centers and scattering angles are the same, and it is important for understanding the q^2 distribution of single scattered events to include the interference effects. For a regenerator of finite length multiple scattering is also important and for a given order of scattering one should again include the interference effects, though they become less important for a large number of scatters.

We simulated diffractive scattering in the Regenerator [30] and properly included the interference effects described above for both single and multiple scatters. The input to this simulation were the geometry, density and atomic number for each material in the Regenerator, and the scattering amplitudes of K^0 and $\overline{K^0}$ as a function of q^2 for these.

The results of the scattering simulation are shown in Figures 59 and 60. The distribution in Figure 60 has been fit to two exponentials in the region $0 < q^2 < 50,000$ (MeV/c)^2. The resulting fit is superimposed on this plot and has the following form,

$$\frac{dN}{dq^2} \propto 0.648e^{-184.7q^2} + 0.352e^{-26.17q^2}$$

Consider again the q^2 distribution for the $\pi^+\pi^-$ data sample from the regenerator beam. This is shown in Figures 61 and 62 with the following fit to the background superimposed:

$$\frac{dN}{dq^2} = [p_1(0.648e^{-184.7t} + 0.352e^{-26.17t}) + p_2e^{-6t}]e^{-p_3t} \tag{8.1}$$

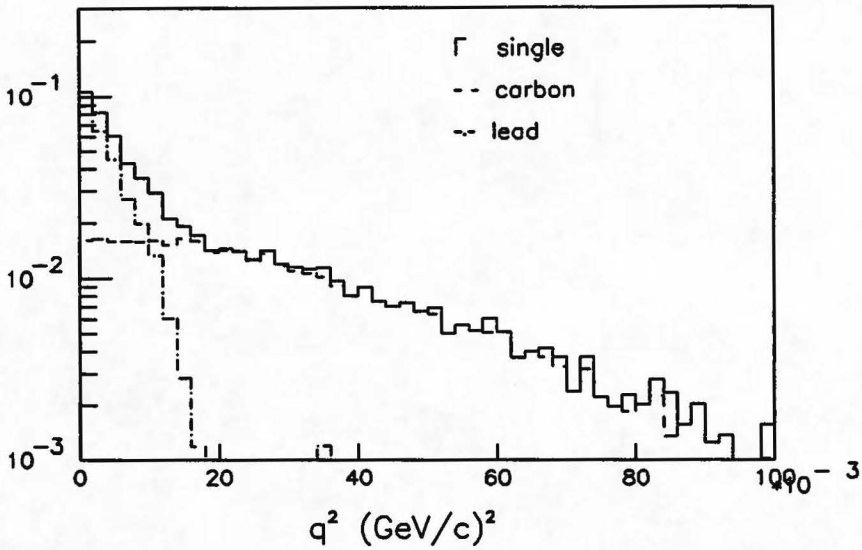

Figure 59: Simulated q^2 distribution for single scatters in the Regenerator. The contributions from the Lead and B_4C are also shown separately.

Here p_1 and p_2 give the relative amounts of the diffractive and inelastic components and $e^{-p_3 t}$ describes the q^2 dependence of the acceptance. This function has been fit, in the region 2000 (MeV/c)^2 $< q^2 <$ 100,000 (MeV/c)^2, to the data in 10 GeV energy bins. We found $p_2/p_1 = 0.312$ and for the requirement of $q^2 <$ 250 (MeV/c)^2 the background to the coherent signal was found to be 0.31%. The systematic uncertainty in this was determined to be 0.04% from the rms errors in the fit parameters and from studies of fitting to different regions of q^2. (A large component of the background was due to diffractive scattering and in particular due to single scatters in the 1.27cm Pb pieces at the end of each of the four regenerator sections. One upgrade for the 1987-88 running of this experiment was to remove the first three pieces of Pb leaving only the Pb in front of the RA4 scintillators. Preliminary analysis of this data indeed shows a reduction in the diffractive component in agreement with our calculations.)

The background to the coherent regenerator signal in the neutral mode, where the q^2 resolution is a factor 25 worse, was determined next. This worse resolution made it difficult to unfold the coherent and diffractive signals, and so the charged mode determination of the relative amounts of these was used. (The ratio of the coherent and diffractive signals does not depend on which final state the kaon decays to.) With this constraint, the neutral q^2 distribution was fit, in the region 20,000 $< q^2 <$ 100,000 (MeV/c)^2, to the functional form in Equation 8.1; the results are presented in Table 9, and Figure 63 shows the data

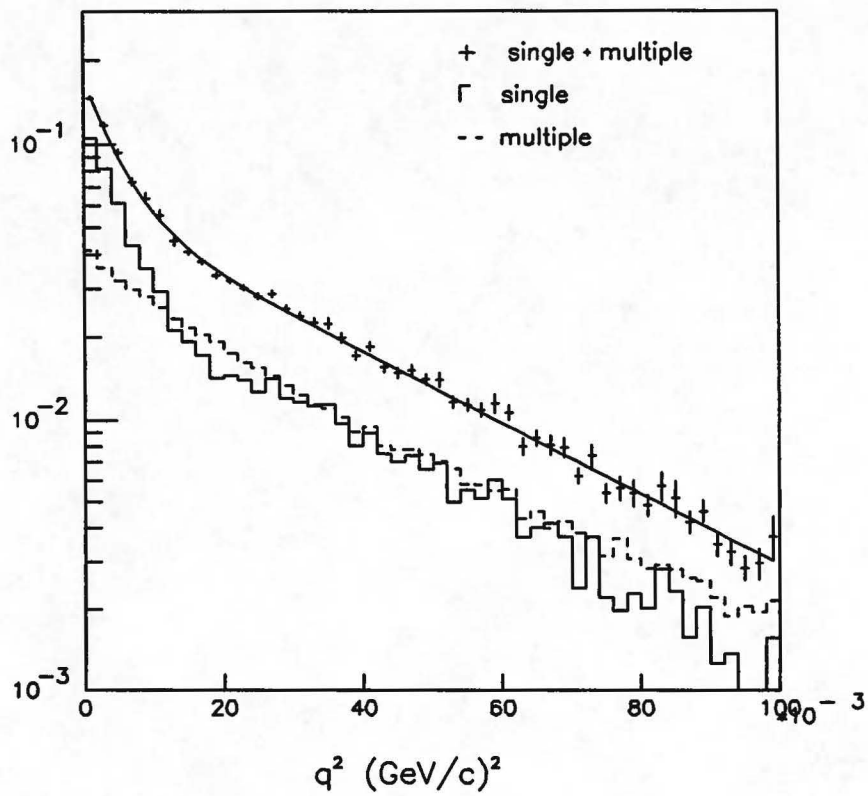

Figure 60: Simulated q^2 distribution for scattering (single and multiple) in the Regenerator. A fit to two exponentials is shown superimposed.

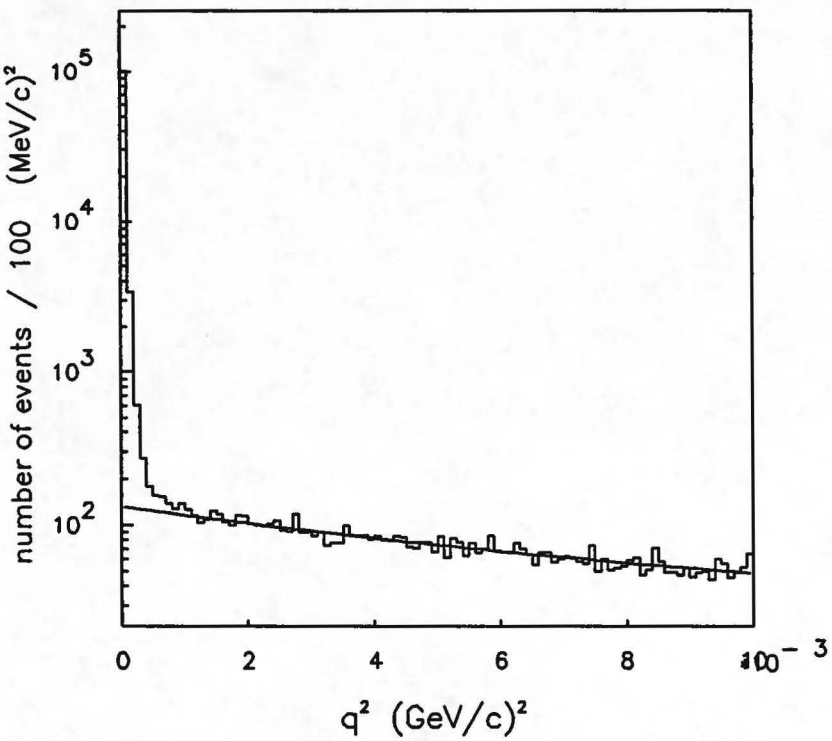

Figure 61: q^2 distribution from $\pi^+\pi^-$ regenerated beam data with background fit superimposed

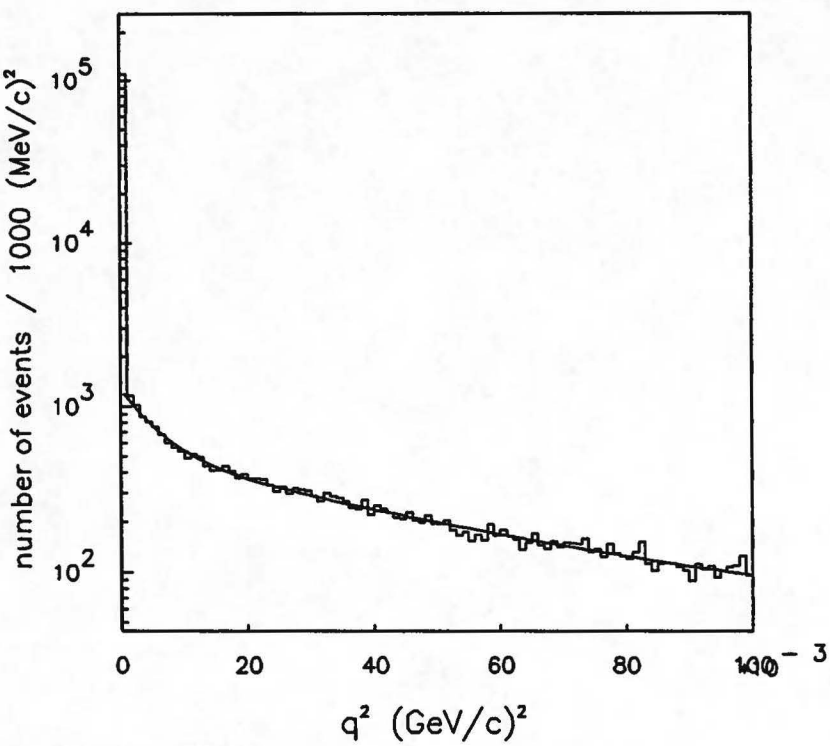

Figure 62: Same plot as Figure 61 in bin sizes of 1000 (MeV/c)^2 for q^2

Table 9: Energy dependence to diffractive and inelastic backgrounds for the regenerator beam $K \rightarrow \pi^0\pi^0$ data

Kaon Energy (GeV)	% Diffractive and Inelastic Background
40–50	3.20
50–60	2.90
60–70	2.80
70–80	2.70
80–100	3.07
100–120	2.90
120–160	2.52

with the background fit superimposed. There were two important corrections to Equation 8.1 in arriving at these backgrounds. First, there was leakage of the signal into the region $q^2 > 20,000$ (MeV/c)^2 where the fit was done, and second, the shape of the diffractive component was affected by resolution smearing. Without these two corrections the background was determined to be 3.42%. The signal leakage correction reduced this by $(0.30 \pm 0.10)\%$ and the resolution smearing for the diffracted events reduced this by a further $(0.18 \pm 0.06)\%$. The final background was determined to be $(2.94 \pm 0.16)\%$, where the systematic error was dominated by uncertainties in these corrections. (There were smaller contributions from the rms errors of the fit parameters and from fitting to different regions of q^2.) As a consistency check the charged mode background, with a $q^2 < 4000$ (MeV/c)^2 requirement, was also determined and it was found to be $(2.79 \pm 0.08)\%$, in good agreement with the neutral mode. Note that one expects slight differences due to loss of signal in the neutral mode from resolution effects (thereby increasing the background) and use of more veto planes in neutral mode (thereby reducing the inelastic background).

8.2 Semileptonic and Neutron Background

The background in the $K_L \rightarrow \pi^+\pi^-$ mode was due to residual semileptonic decays and neutron interactions in the Lead Mask and the V counter. Neutrons and kaons which scattered in the absorbers could hit the Lead Mask, and these neutrons produced a small but visible background which was calculated together with neutron background produced at the V plane. Kaon regeneration in the Lead Mask was also visible but at a very small level and no correction was

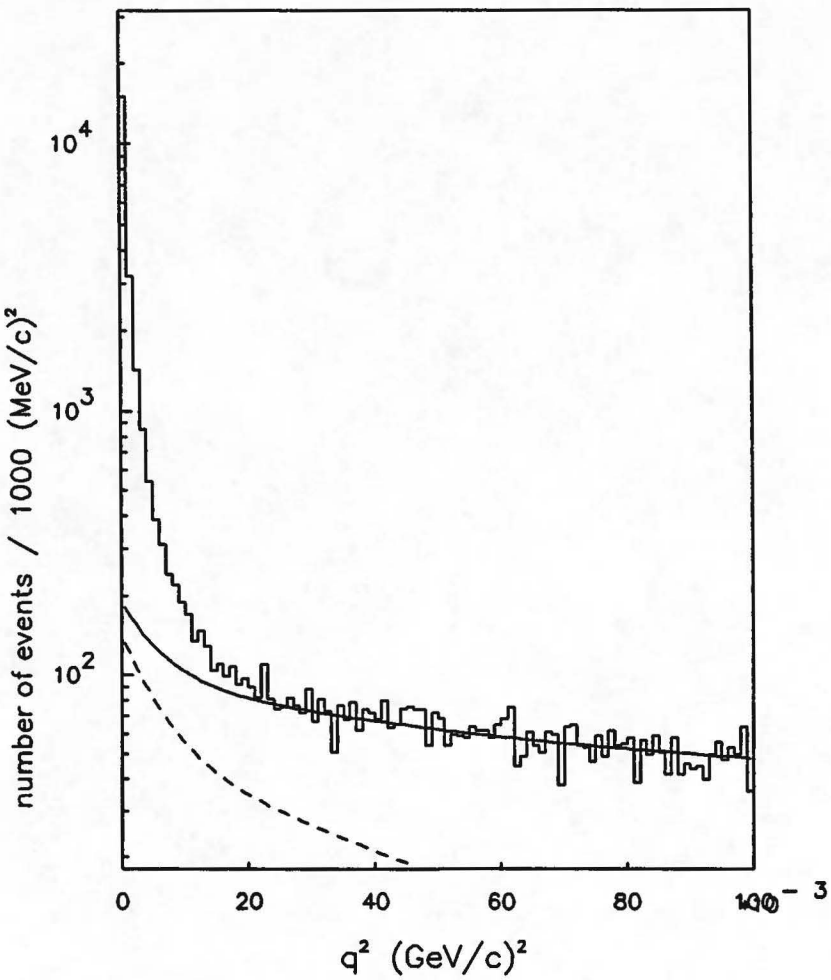

Figure 63: q^2 distribution for neutral mode regenerator beam data with fit to background superimposed. The dashed line shows the diffraction contribution to the background.

applied. In the neutral mode with the requirement of $q^2 < 4000$ (MeV/c)^2 this contribution was less than 0.1% of the vacuum signal. Nor was a correction applied for the even smaller effect that some of the scattered kaons[1] in the regenerator beam could miss the Regenerator.

The background sources were most easily understood by their distributions in the reconstructed quantity, q^2. There were identified samples of $K\mu_3$, Ke_3, and neutron interactions from our data taking and their q^2 distributions are shown in Figures 64, 65 and 66. The Ke_3 sample was taken from running without the Lead Curtain in front of the B Bank and requiring the same cuts as for the $\pi^+\pi^-$ sample. An additional requirement was made that one track have $E/P > 0.8$, consistent with being an electron, where E was the track energy measured with the Adders and P was the track momentum measured with the Drift Chambers. The $K\mu_3$ sample was also taken from running without the Lead Curtain and requiring all the normal cuts, except that the MU2 Bank was required to have at least one hit counter. The neutron sample was taken from the regular data sample with the usual cuts, except we required i) m_K between 520 and 600 MeV/c^2 and ii) longitudinal decay vertex within 0.25m of the Lead Mask. In addition to these data samples a $K\mu_3$ Monte Carlo was also generated, and the q^2 distribution for this is shown in Figure 67. The dominant source of background was from $K\mu_3$ and the agreement between the Monte Carlo and data for this gave us additional confidence in the background determination.

The q^2 distributions for neutron and Ke_3 events were similar enough to cause confusion in untangling their relative contributions to the vacuum data background. To resolve this, the Z distribution for the vacuum data with the requirement 5000 (MeV/c)^2 $< q^2 <$ 10000(MeV/c)^2 was studied and is shown in Figure 68. Most events are seen to come from the Lead Mask and the HDRA, indicating that the neutron background is larger than the Ke_3 background.

To determine the overall amount of background in the $K_L \rightarrow \pi^+\pi^-$ sample, the q^2 distribution was fit to two exponentials in the region 700 (MeV/c)^2 $< q^2 <$ 10000 (MeV/c)^2, where the exponentials corresponded to the $K\mu_3$ and neutron background sources. The steeper exponential was fixed to e^{-1000q^2}, consistent with the distribution for the identified $K\mu_3$ sample, while the shallow exponential slope was fitted for along with the relative amounts of each. The result of this is shown in Figure 69 where the data is shown overlayed

[1]Sections 9.2 and 10.1 discuss kaon scattering in the upstream absorbers.

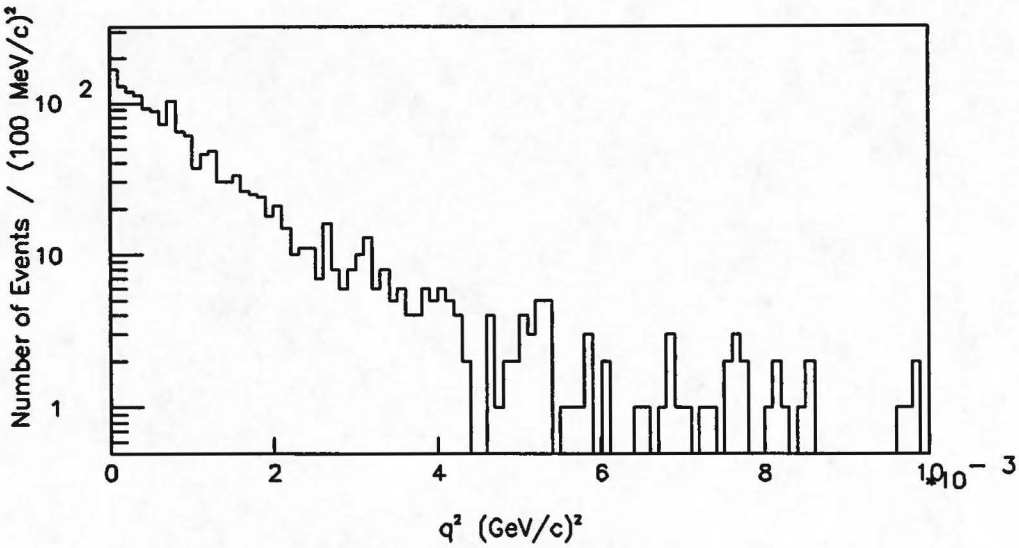

Figure 64: q^2 Distribution for identified $K\mu_3$ events from data

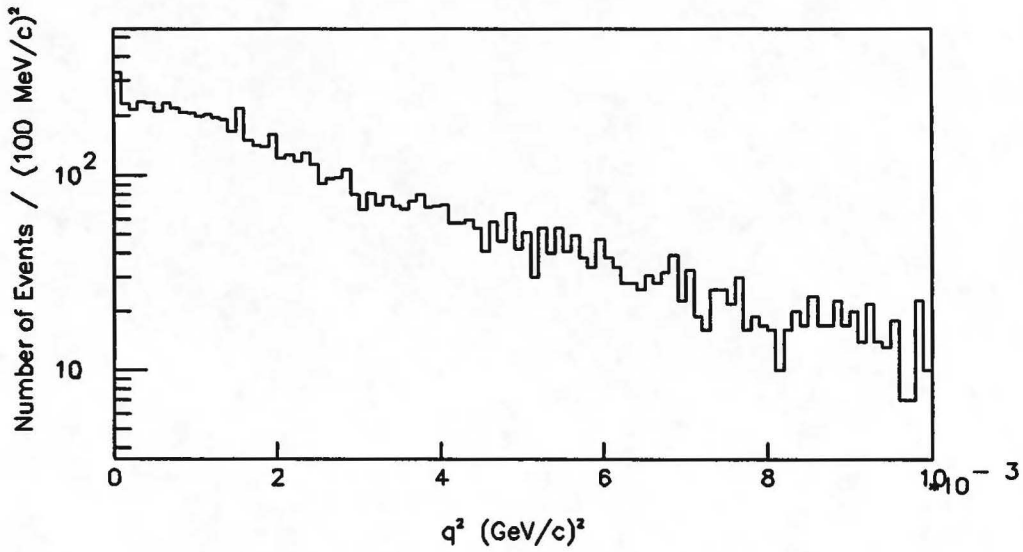

Figure 65: q^2 distribution for identified Ke_3 events from data

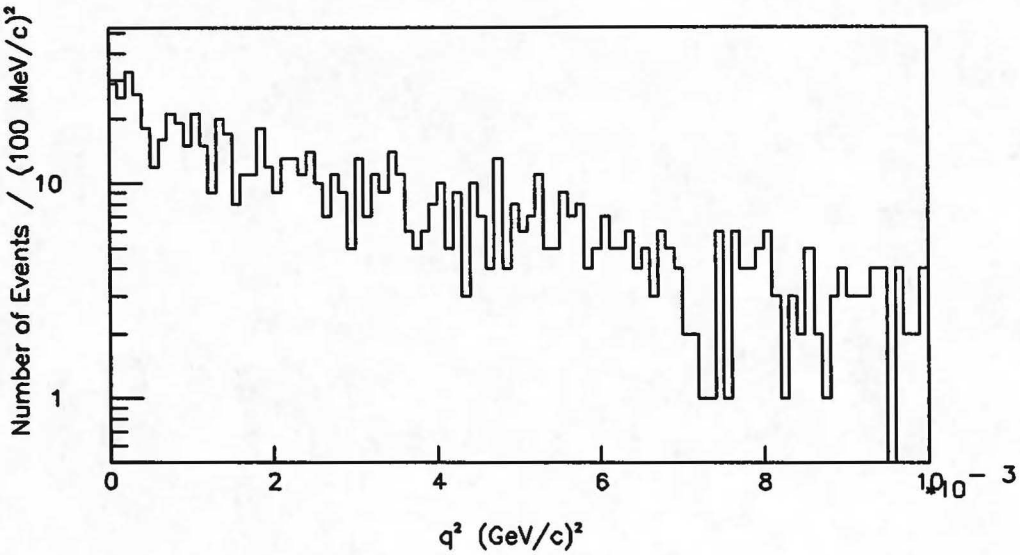

Figure 66: q^2 distribution for identified neutron events from data

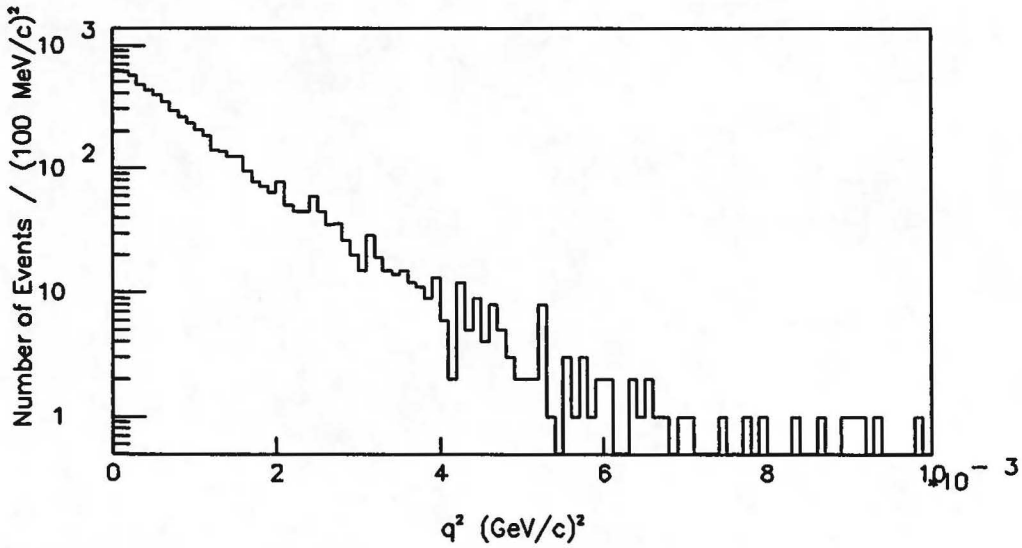

Figure 67: q^2 distribution for identified $K\mu_3$ events from Monte Carlo

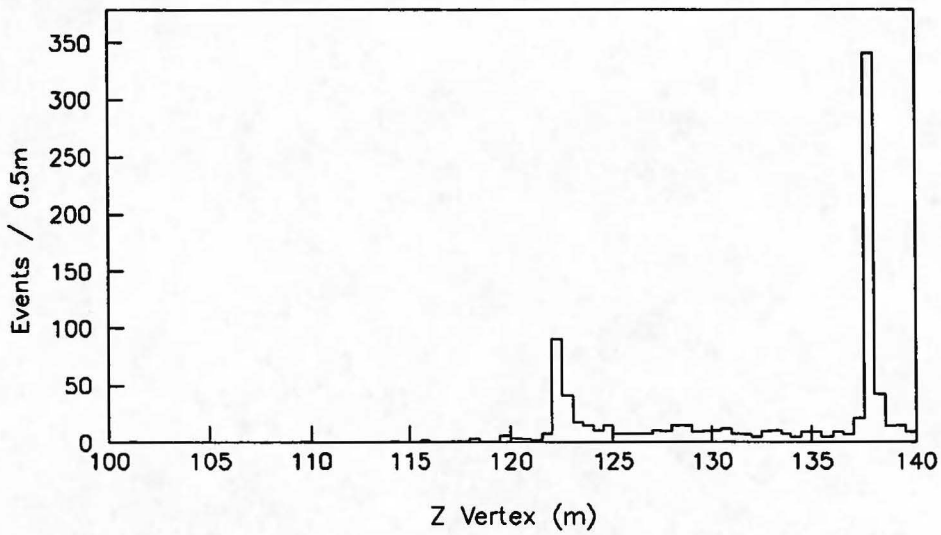

Figure 68: Longitudinal decay vertex distribution for vacuum beam $\pi^+\pi^-$ candidates with 5000 $(\mathrm{MeV/c})^2 < q^2 < 10000$ $(\mathrm{MeV/c})^2$.

with the following background fit:

$$\frac{dN}{dq^2} = 164e^{-1000q^2} + 33.3e^{-113q^2}$$

We find the backgrounds to be 1.05% from $K\mu_3$, 0.18% from neutron interactions and less than 0.1% from Ke_3 for the requirement $q^2 < 250$ $(\mathrm{MeV/c})^2$. The total background is therefore 1.23% and the uncertainty has been estimated to be 0.18%. This uncertainty was determined from the errors associated with the parameters in the fit and by fitting the background in different regions of q^2.

8.3 Background from $K_L \to 3\pi^0$

The only observable source of background for the $K_L \to 2\pi^0$ data sample was from $K_L \to 3\pi^0$ decays where two photons missed the Lead Glass or fused there with other photons. Understanding of this background was achieved through a detailed study of the m_K distribution—comparing the observed data with results from a Monte Carlo that was specifically engineered for looking at $3\pi^0$ events which faked $2\pi^0$ events. One has to generate many $3\pi^0$ decays to get enough statistics to study those which fake $2\pi^0$ decays, and so a simplified version of the Monte Carlo used for understanding the 2π acceptances was used. In particular, this Monte Carlo did not generate clusters in the Lead Glass and it did not generate digitized hits in the Drift

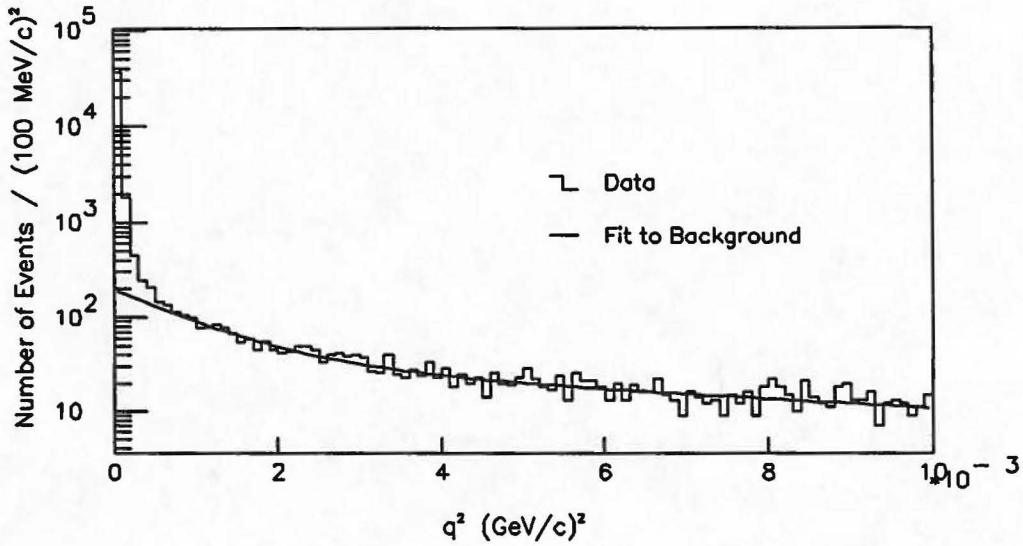

Figure 69: q^2 distribution for identified $K_L \rightarrow \pi^+\pi^-$ events from data

Chambers. Instead, energies and positions of photons were smeared according to the measured resolutions, and generated track information was used since no track reconstruction was done. Roughly 120 million $3\pi^0$ events were generated to obtain 600 events (passing all cuts) under the mass peak (480–520 MeV/c^2); the uncertainty in the background due to Monte Carlo statistics was less than 5% of the actual background.

The shape of the background in the variable m_K was sensitive to the number of photon fusions and this in turn depended on which photon veto planes were used and what their efficiencies were. The planes used in the analysis and their efficiencies used by the Monte Carlo are given in Table 10. The Lead Mask is also included here, though it had no scintillator, since charged particles produced in the electromagnetic shower of a photon hitting the Mask could hit other veto planes such as RA, V and VA2 scintillators. In Figure 70 the m_K distribution of Monte Carlo background $3\pi^0$ events is shown for 0,1 and 2 fusions. The overall background to the data is a linear combination of these and Figure 71 shows the data distribution for m_K with the best fit from the Monte Carlo background distribution superimposed. (The background was normalized to the data in the region 420–450 MeV/c^2. A check of this normalization was done by comparing the 2π signal to the 3π background measured by the data to that determined solely by the Monte Carlo. The two results for this ratio were consistent at the 10% level.) The resulting background from this fit is 0.19% due to 0 fusions, 0.66% due to 1 fusion and 0.71% due to 2 fusions for a total background of 1.56%. The systematic uncertainty in this was

Table 10: Photon veto planes and their efficiencies used in the Monte Carlo

Photon Veto Plane	Efficiency
Lead Mask	50% above 100 MeV photon energy
Regenerator	95% above 100 MeV photon energy
VA3	95% above 100 MeV photon energy
DRAN	95% above 100 MeV photon energy
CA	90% above 100 MeV photon energy
BA	100% above 5 GeV photon energy

Table 11: Energy dependence of the $3\pi^0$ background with and without the photon fusion cut.

Kaon Energy (GeV)	% Background (with photon fusion cut)	%Background (without photon fusion cut)
40–50	1.18	1.58
50–60	0.73	1.07
60–70	0.87	1.28
70–80	1.04	1.84
80–100	1.60	2.75
100–120	2.83	4.65
120–160	3.24	5.54

0.31% and resulted from uncertainties in the relative contributions of the 0,1 and 2 fusion classes, which were determined by the efficiencies of the photon vetoes. (For example, using no Lead Mask cut for photons in the Monte Carlo resulted in a background determination of 1.78%, though this did not fit the data as well.) The energy dependence to the background is shown in Table 11, where the determined backgrounds when no photon fusion cut is made are also listed. Analysis of the data with and without this fusion cut provided a systematic check of this background subtraction. Finally, Table 12 gives a summary of the background subtractions and the systematic uncertainties in each.

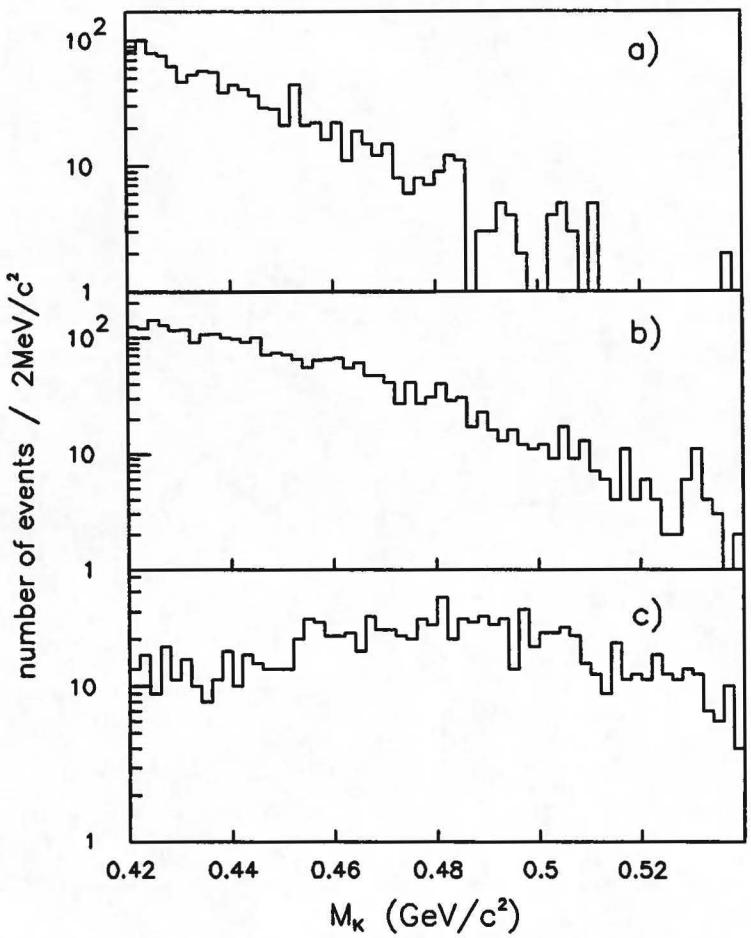

Figure 70: The m_K distribution of $3\pi^0$ events which fake $2\pi^0$ events as determined by Monte Carlo for a) events with no photon fusions, b) events with one photon fusion, and c) events with two photon fusions.

Table 12: Summary of background subtractions and their associated uncertainties

Mode	Background	Systematic uncertainty
$K_L \to \pi^+\pi^-$	1.23%	0.18%
$K_S \to \pi^+\pi^-$	0.31%	0.04%
$K_L \to \pi^0\pi^0$	1.56%	0.31%
$K_S \to \pi^0\pi^0$	2.94%	0.16%

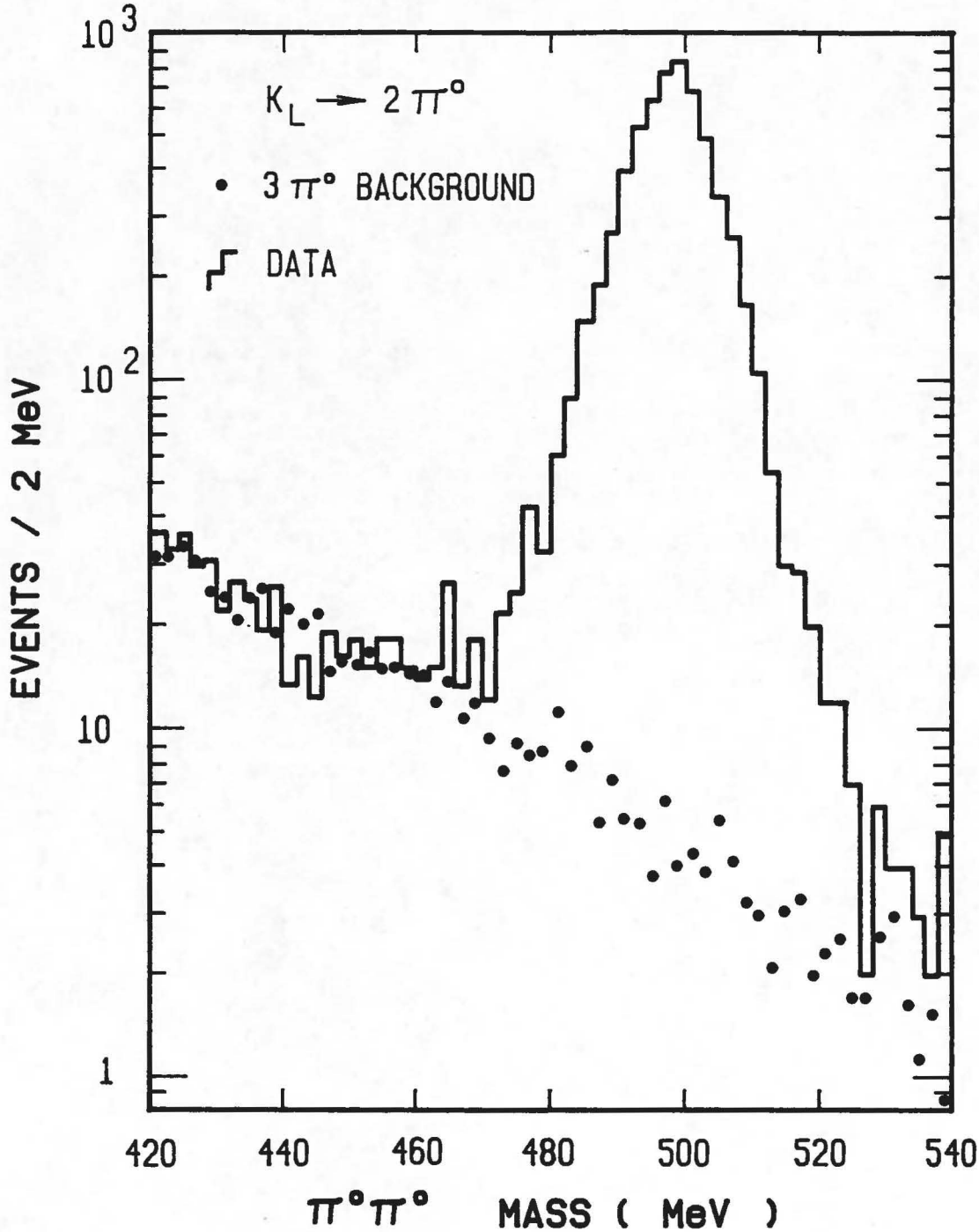

Figure 71: The data m_K distribution for vacuum events with the $3\pi^0$ background overlayed

Chapter 9

Acceptance Corrections

Before extracting $|\epsilon'/\epsilon|$ from the ratio of observed vacuum events to observed regenerator events, one has first to correct for the relative acceptances of these. An acceptance difference exists because the longitudinal decay distributions are different and the acceptance depends on the decay vertex. A Monte Carlo was used to determine the corrections, and this chapter shall describe the Monte Carlo and the nature of the corrections.

We shall first discuss the simulation of the detector and this will be followed by a discussion of how events were generated. The analysis of Monte Carlo events will be treated and we will compare Monte Carlo with data and demonstrate their agreement, showing our understanding of the detector and the important physics processes. This agreement provides a good check of the experiment, and gives us confidence in the acceptance corrections. We shall give the magnitude of these corrections, but the calculation of systematic uncertainties associated with the acceptance will be left for Chapter 11.

9.1 Detector Simulation

Many features of the E731 beamline and detector influenced the kinematic distributions of kaons in the Decay Region—beam and target size; target location; collimator sizes and locations; absorber materials, sizes and locations; regenerator materials, sizes and locations. All these were accurately determined and implemented in the Monte Carlo to ensure an understanding of the kaon energy spectra, longitudinal decay distributions, and beam profiles. The crucial apertures for the acceptance were the Lead Mask, the HDRA, and the Lead Glass; the positions and dimensions of these were carefully measured. Positions of other parts of the apparatus were also important and the reader can refer to Tables 3 and 4 as well as Figure 6, for the locations and sizes of

Table 13: Constants in Malensek particle energy spectrum

	A	B	M^2	D
K^+	2.924	14.15	1.164	19.89
K^-	6.107	12.33	1.098	17.78

beamline and detector elements. The essential features of all these were put in the Monte Carlo. The radiation lengths of all materials contributing to the scattering of charged particles were determined and put in the Monte Carlo also. These radiation lengths are summarized in Table 5. Small gaps between counters in the A and B Banks were measured and implemented in the Monte Carlo. Drift Chamber efficiencies and resolutions were treated as were details of cluster generation in the Lead Glass and the resolution of the Lead Glass.

9.2 Monte Carlo Event Generation

The first stage of event generation required choosing the energy and trajectory of the kaon. Malensek [31] has fit data by Atherton et. al. [32][1] to determine the following functional form for particle production by a proton beam on a Beryllium target:

$$\frac{d^2N}{dPd\Omega} = \frac{B}{400}\frac{(1-X)^A(1+5e^{-DX})}{(1+\frac{P_T^2}{M^2})^4}$$

where:

P is the particle energy,

X is particle energy / beam energy,

P_T is the transverse particle energy with respect to the beam direction,

$dN/d\Omega$ is the number of produced particles per unit solid angle, and

A, B, M^2, D are constants given in Table 13

We used this function and made the plausible assumption that $K^0(\overline{K^0})$ production was the same as that for $K^+(K^-)$. The K_L energy spectrum was

[1]This experiment was a study of particle production with a 400 GeV proton beam incident on a one interaction length Be target.

taken to be:

$$\frac{d^2N_L}{dPd\Omega} = \frac{1}{2}\left(\frac{d^2N^0}{dPd\Omega} + \frac{d^2\overline{N^0}}{dPd\Omega}\right)$$

Given this spectrum and using the 2-hole collimator at $Z = 15m$ (Figure 5) to define the two beams at a targeting angle of approximately 4.8mrad, the kaon energy and trajectory were generated. As will be seen later, this spectrum agrees well with our data below 120 GeV but predicts too much particle production above that energy.

The longitudinal decay vertex, Z, for the vacuum beam was chosen to be between 100m (downstream of the target) and the HDRA plane, according to its decay distribution, $P_V(Z) = e^{-Z/\Lambda_L}$, where $\Lambda_L = (P/m_K)c\tau_L$. For the regenerator beam we chose Z according to the distribution which is that describing the 2π rate downstream of the Regenerator as described in Section 10.1. The generated P and Z distributions at this stage constituted the generated numbers used in defining the acceptance.

Before propagating the kaon through the collimators, the kaon was allowed to elastically scatter in the absorbers. Recall that the absorbers consisted of 3" Pb and 20" Be common to both beams and an extra 18" Shadow Absorber for the regenerator beam (see Section 2.2.1). Only single elastic scatters were considered in a given absorber and the elastic scattering cross-sections were assumed to be of the form:

$$\frac{d\sigma}{dt} \propto \exp(-Bt)$$

where t is the square of the transverse momentum transfer ($t = q^2$), and we used $B = 55GeV^{-2}(400GeV^{-2})$ for Be (Pb). The ratio of single elastic scatters to no interaction for the kaons was taken to be 17.8% for the Pb absorber, 8.6% for the Be absorber and 7.8% for the Shadow Absorber.[2] (After full reconstruction and event selection, approximately 10% of events have scattered in the absorbers.)

The kaon was then propagated to the defining collimators, using the new trajectory if it scattered, and required to be within their apertures. If the kaon passed this stage, its decay kinematics for a given mode were generated and the decay particles were traced through the apparatus. In the neutral mode, one photon was randomly chosen to convert at the HDRA resulting in 3 photons and an e^+e^- pair. Charged particles for both modes underwent multiple scattering at the HDRA, the vacuum window, each of the 4 Drift chambers, and the A and B Banks.

[2]These were determined from cross-section measurements for kaons given in reference [33] .

Events were required to pass all the hardware trigger requirements which were described in Sections 6.1 and 7.1. Additionally, all photons in the neutral mode were required to hit the Lead Glass. At this point the charged particle trajectories were used to calculate which Drift Chamber wires were hit; the drift distances were calculated and smeared according to the measured 150 μm resolution. For the charged mode Monte Carlo first level summary tapes were then made. The neutral mode required generating clusters in the Lead Glass and computing the energy deposited in each block. No attempt was made to simulate the Lead Glass response for charged mode, since it was not used in that analysis.

The first step in modeling the Lead Glass response to electrons and photons was to simulate the nonlinearity and the electron-photon difference (a discussion of these was given in Section 4.3). The photons were allowed to convert in the Lead Glass to an e^+e^- pair, whose energy distributions are given by the Bethe-Heitler formula [34]. The conversion point in the Lead Glass was generated according to an exponential distribution,

$$P(l) \propto \exp\left(-\frac{l}{9/7X_0}\right)$$

where

$P(l)$ is the probability for a conversion a distance l into the Lead Glass, and

X_0 is an electron's radiation length in Lead Glass

From this conversion depth, a light attenuation correction factor was calculated and applied to the photon energy. A nonlinearity correction was applied for electrons, positrons and photons to simulate the Lead Glass response (Section 4.3). The reconstruction analysis of course 'undoes' the nonlinearity and electron-photon difference effects as described in Section 7.2; but this undoing is only in an average sense, and the modeling of these effects was to reflect the underlying physics and thereby get the actual energy distribution, complete with non-gaussian tail, of electrons and photons correct.

For simulating the transverse shape of electromagnetic showers in the Lead Glass, we used the following functional form for the fractional energy deposit per unit area,[3]

$$\frac{df(r)}{da} = 0.0285e^{-r/1.0921} + 0.00294e^{-r/5.7358} + \frac{0.0000316}{(1+(r/30)^2)^{3/2}}$$

[3]This formula is based on work done by D. Carlsmith with E617 data, where the same Lead Glass was used.

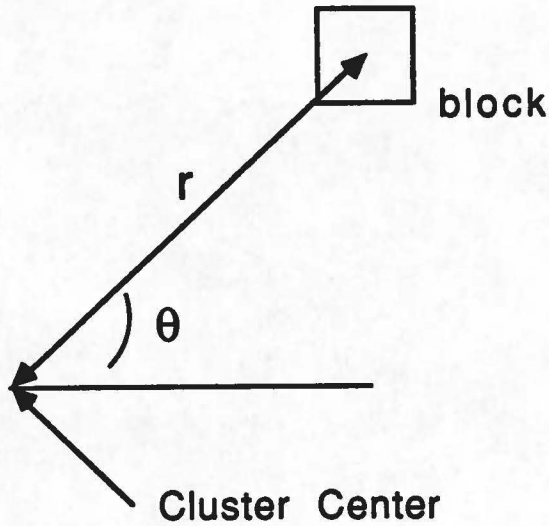

Figure 72: Definition of r and θ for creating table of fractional energy deposit

where

f is the fractional energy deposit per unit area at a distance r from the cluster center,

r is the distance from the cluster center in mm, and

a is the area in mm^2

A block's energy is given by integrating this function over the area of the block. A table was constructed for this integral as a function of r and θ, where r and θ measure the center of the block with respect to the cluster center (see Figure 72). Two hundred 1mm bins were used for r and ten $\pi/40$ rad bins were used for θ, and the integrals were evaluated by numerical integration. For each electromagnetic shower, the energies in each of the 5x5 array of blocks about the cluster center were calculated from this. The energies of the outer 16 blocks were fluctuated individually with a $15\%/\sqrt{E}$ (rms) smearing, followed by a normalization to conserve energy. A 2.0% (rms) common smearing was done for all blocks to simulate shower fluctuations, and finally individual blocks had their energies smeared independently by $6\%/\sqrt{E_{block}}$ (rms) to simulate photostatistics. This procedure gave an energy resolution of $2\% + 6\%/\sqrt{E}$

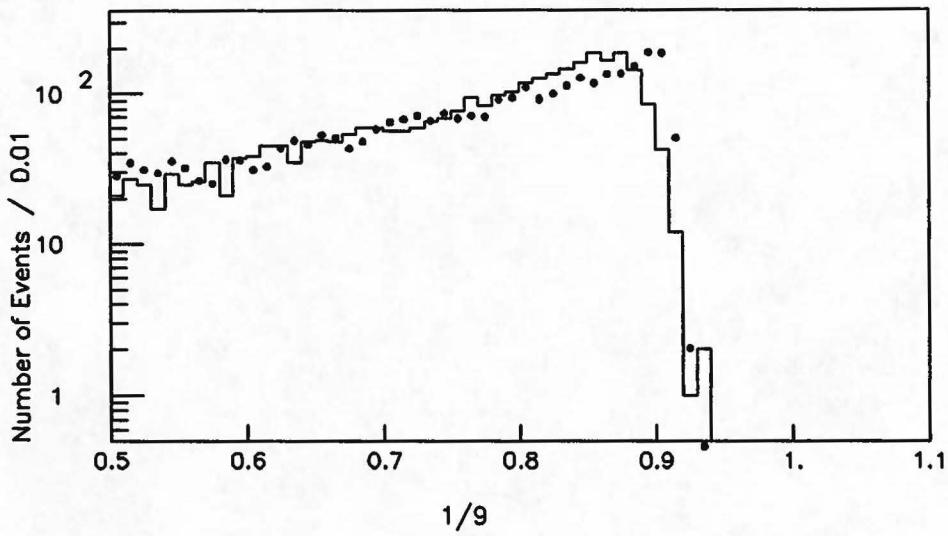

Figure 73: (center block energy) / (3x3 energy) for photons. (Solid circles are Monte Carlo.)

(added in quadrature) which agreed with the data, and gave a shower shape that also agreed with the data. The shower shape was studied by looking at distributions of i) (center block energy) / (3x3 energy), and ii) (3x3 energy) / (5x5 energy). These distributions are shown in Figures 73 and 74 for data and Monte Carlo, and demonstrate that the procedure for generating the shapes of clusters is quite good. We wanted a good simulation of the cluster shape so that we would accurately account for the effects of clusters overlapping and fusing together.

9.3 Data and Monte Carlo Comparisons

For both charged and neutral modes, the first level Monte Carlo tapes were equivalent to the first level DST's. They subsequently went through the same analysis and were required to pass the same reconstruction criteria and the same cuts. The same trackfinder and clusterfinder were used for data and Monte Carlo, so that any subtle biases in the reconstruction techniques would affect both equally. For the final data samples which passed all cuts, detailed comparisons were made between Monte Carlo and data for track and photon illuminations at various planes, and for kinematic quantities. The most important distribution to understand and obtain agreement between Monte Carlo and data for, was the longitudinal decay vertex (or Z) distribution, since the acceptance depended on this and it was different for the K_L and K_S samples. The Monte Carlo and data comparisons for charged and neutral events will

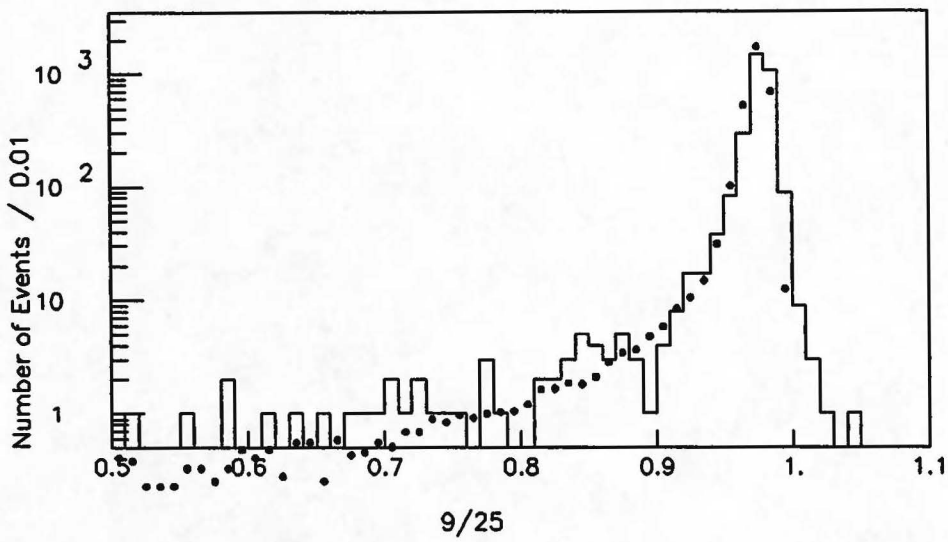

Figure 74: (3x3 energy) / (5x5 energy) for photons. (The long tail is due to nearby clusters. Solid circles are Monte Carlo.)

now be discussed, before summarizing the acceptances for all 4 modes.

9.3.1 $K_{L(S)} \rightarrow \pi^+\pi^-$ Modes

We present first some comparisons for charged mode. Figures 75 and 76 show the track illuminations at the B Bank for $K_L \rightarrow \pi^+\pi^-$ events. The dip in the middle of these plots is due to the software requirement that the tracks be outside of the holes which were cut in the Lead Curtain (re. Ke_3 rejection cut). Figure 77 shows the observed kaon energy distributions in the vacuum beam. Here the data has been weighted to eliminate the remnant 'primary' K_S component at high energies (see the discussion in Section 10.1) and the Monte Carlo is what results from using Malensek's spectrum with no alterations. The agreement here is seen to be very good for kaon energies below 120 GeV, while there is a discrepancy at higher energies. This discrepancy probably indicates a problem with the Malensek spectrum. (It was not expected that this spectrum would fit well at large energies, because it was determined from low energy data.) We have used our $K_L \rightarrow \pi^+\pi^-$ data to correct this and all further Monte Carlo plots will include this correction. The corresponding $K_S \rightarrow \pi^+\pi^-$ energy distributions (with Monte Carlo spectrum correction) are shown in Figure 78. The Z distributions for K_L and K_S decays are shown in Figures 79 and 80; the agreement is very good, and must be so for the acceptance calculations to be right.

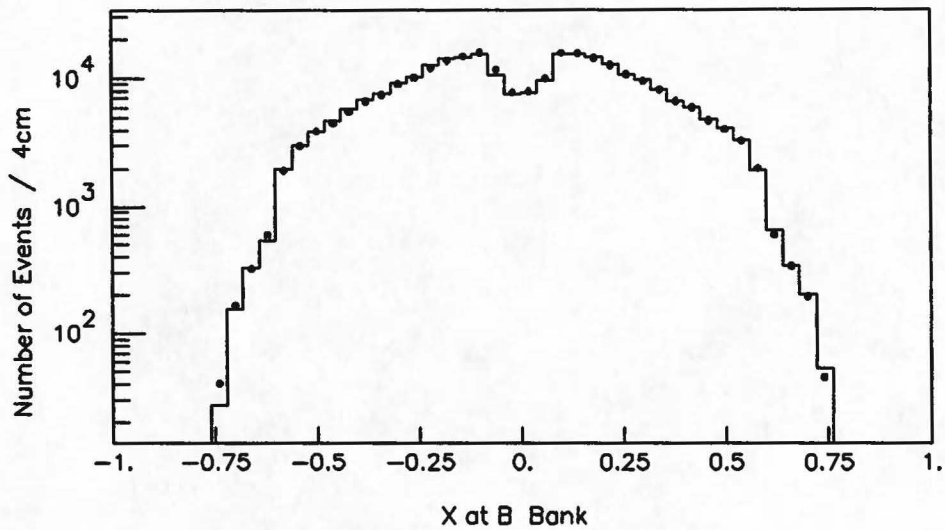

Figure 75: Illumination of π^+ and π^- at the B Bank, x view. (Solid circles are Monte Carlo.)

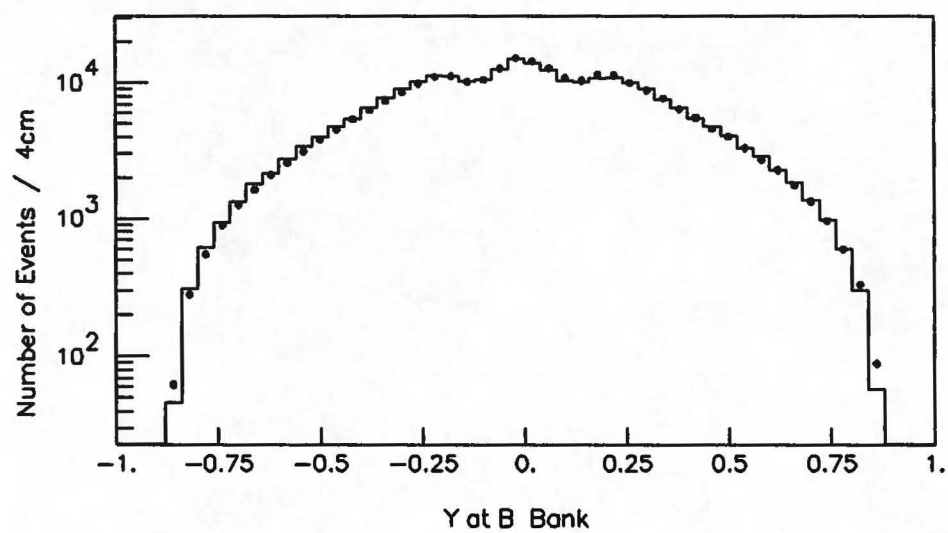

Figure 76: Illumination of π^+ and π^- at the B Bank, y view. (Solid circles are Monte Carlo.)

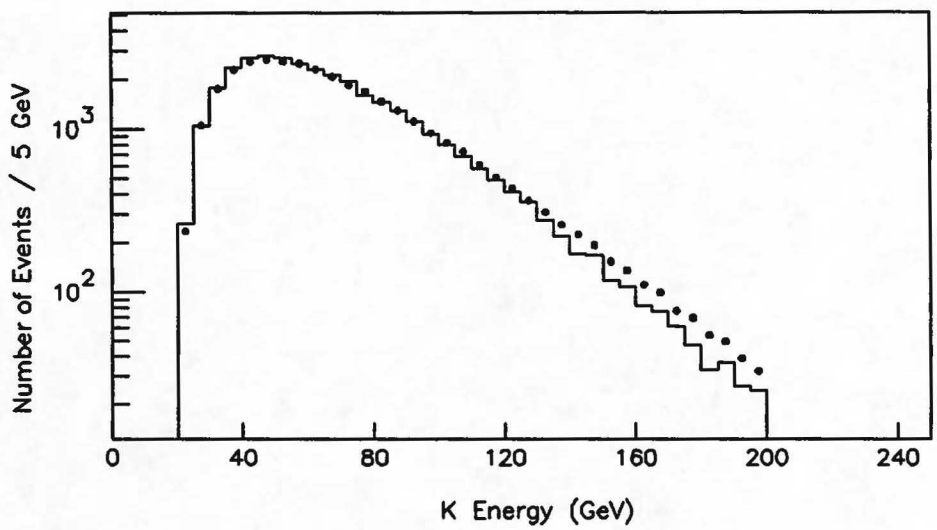

Figure 77: Kaon energy distribution for charged mode vacuum events. (Solid circles are Monte Carlo.)

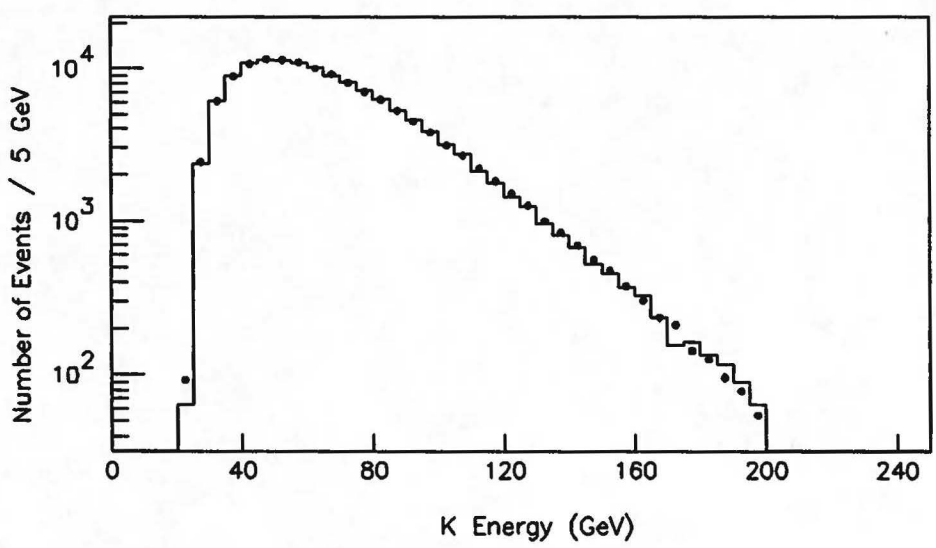

Figure 78: Kaon energy distribution for charged mode regenerator events (with correction applied to Monte Carlo spectrum. Solid circles are Monte Carlo).

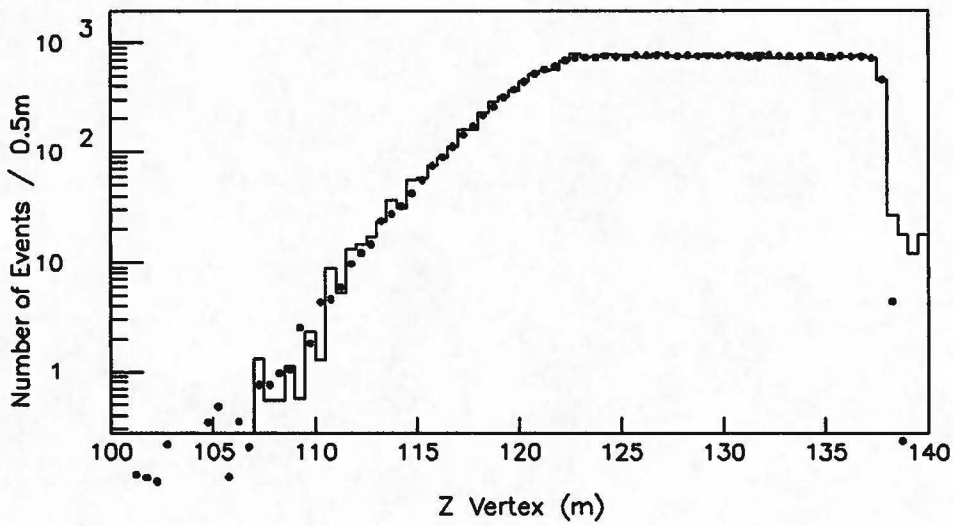

Figure 79: Longitudinal decay vertex distribution for charged mode vacuum events. (Solid circles are Monte Carlo.)

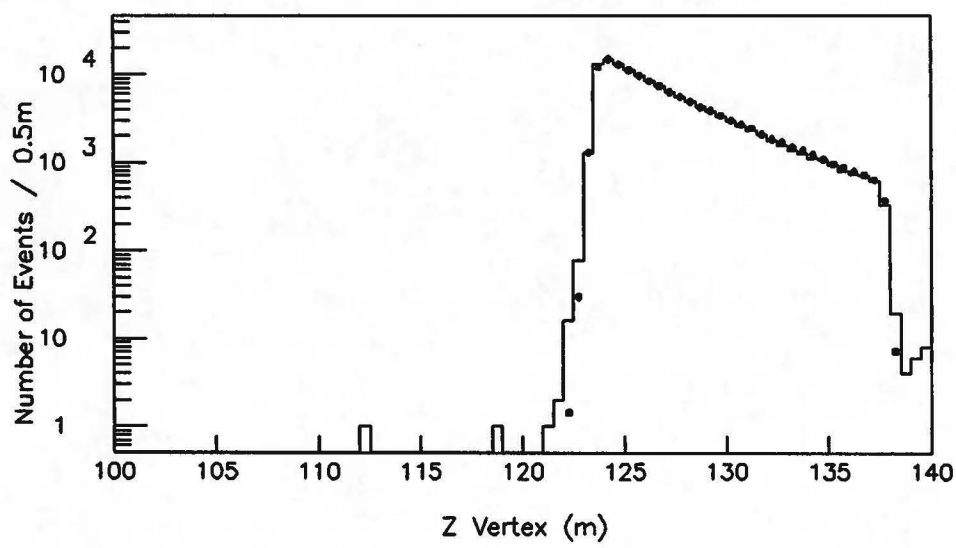

Figure 80: Longitudinal decay vertex distribution for charged mode regenerator events. (Solid circles are Monte Carlo.)

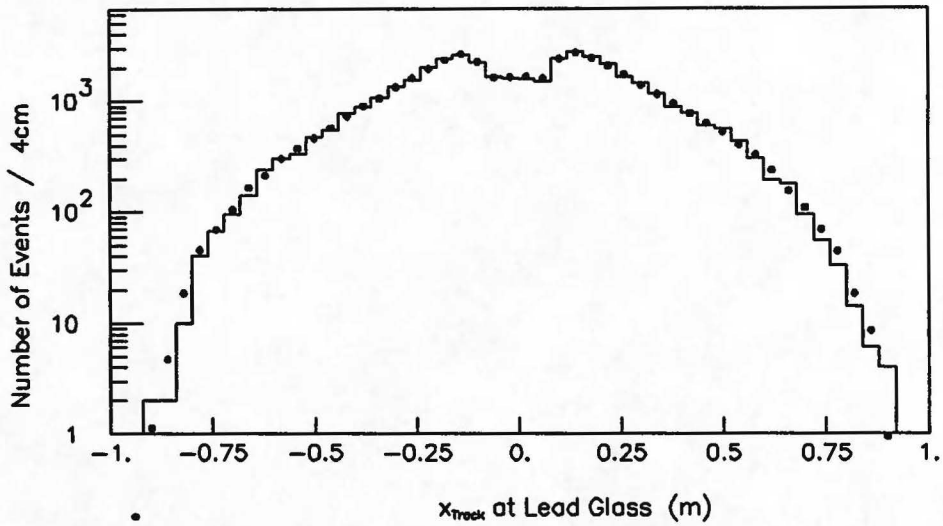

Figure 81: Illumination of electrons and positrons at the Lead Glass; x view. (Solid circles are Monte Carlo.)

9.3.2 $K_{L(S)} \to \pi^0\pi^0$ Modes

As in charged mode, many particle illumination plots were compared between Monte Carlo and data, and Figures 81–84 show the electron (and positron) and photon illuminations at the Lead Glass. Because of the complex topology of electromagnetic showers in lead glass, careful attention was paid to understanding reconstruction of events with overlapping showers and events where an electron or photon landed near an edge of the array. Figure 85 shows the distribution for Monte Carlo and data of the number of overlapping clusters (remember a cluster is a 3x3 array of blocks), while Figures 86 and 87 compare the distributions for number of clusters neighboring the beam pipes and number of clusters that are on the array's outer edge. The agreement is excellent and demonstrates that the reconstruction of events with these topologies is well understood.

The energy spectra for K_L and K_S decays are compared in Figures 88 and 89. These plots demonstrate that the charged and neutral data samples give consistent measurements of the K_L energy spectrum, and this is a good crosscheck. The Z distributions for K_L and K_S data are compared with Monte Carlo in Figures 90 and 91, and again the agreement is good.

9.3.3 $K_L \to 3\pi^0$ Mode

The neutral mode data contained over 500,000 fully reconstructed $K_L \to 3\pi^0$ events. Their analysis was identical to that for the $2\pi^0$ events, except that there

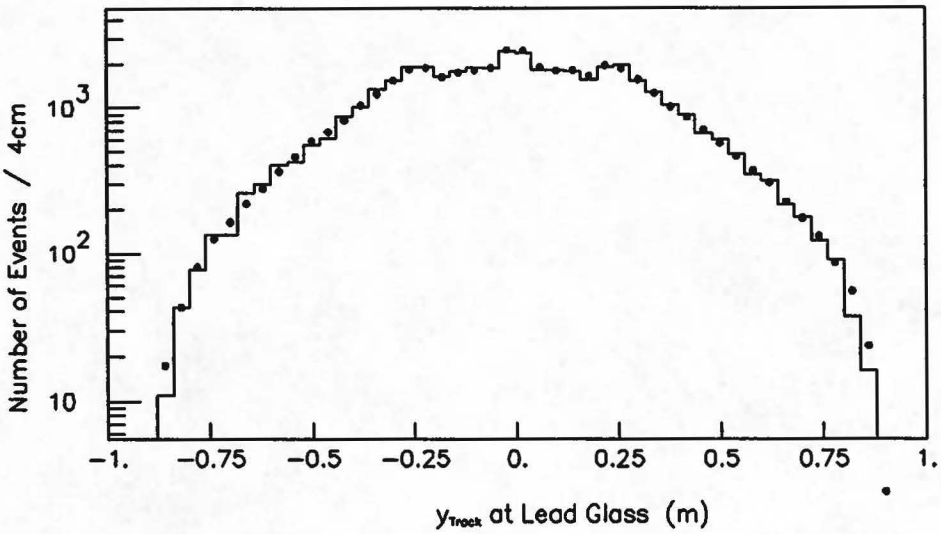

Figure 82: Illumination of electrons and positrons at the Lead Glass; y view. (Solid circles are Monte Carlo.)

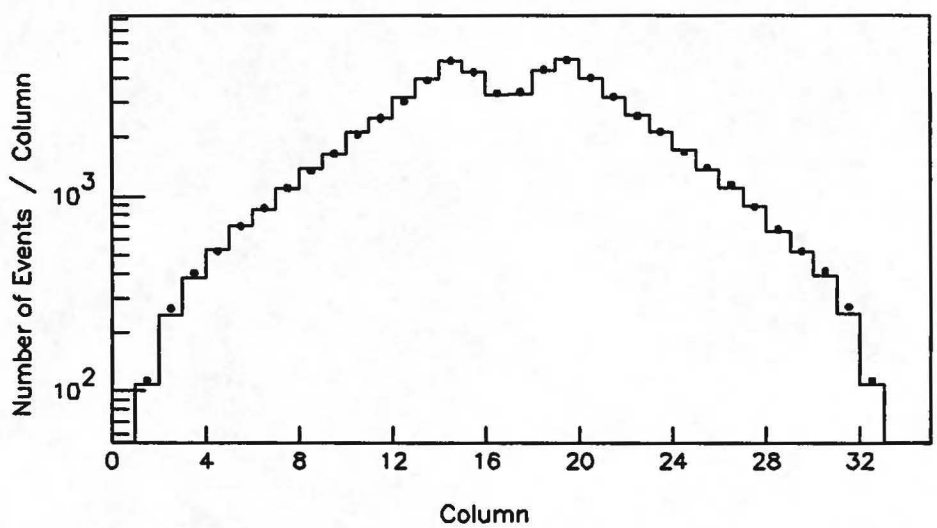

Figure 83: Illumination of photons at the Lead Glass; x view (Column corresponds to a column of Lead Glass blocks. The solid circles are Monte Carlo.)

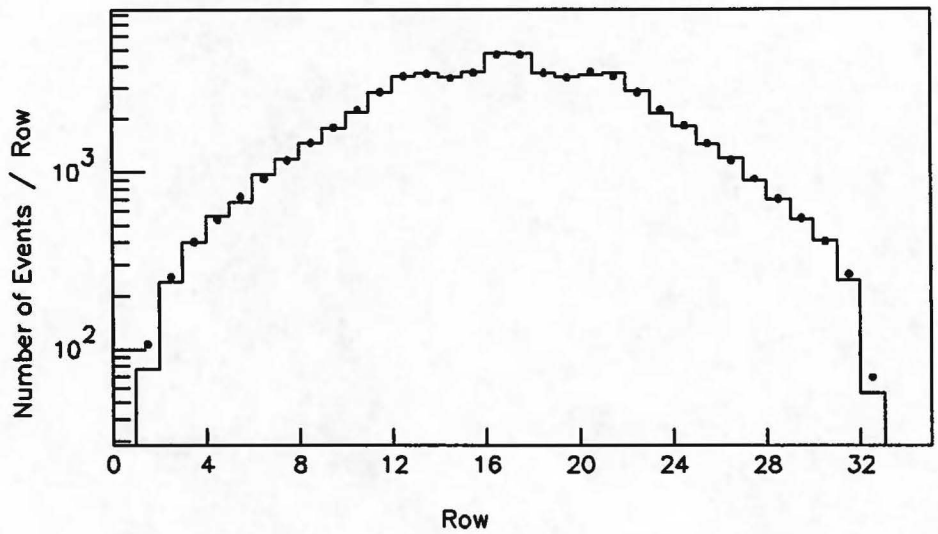

Figure 84: Illumination of photons at the Lead Glass; y view (Row corresponds to a row of Lead Glass blocks. The solid circles are Monte Carlo.)

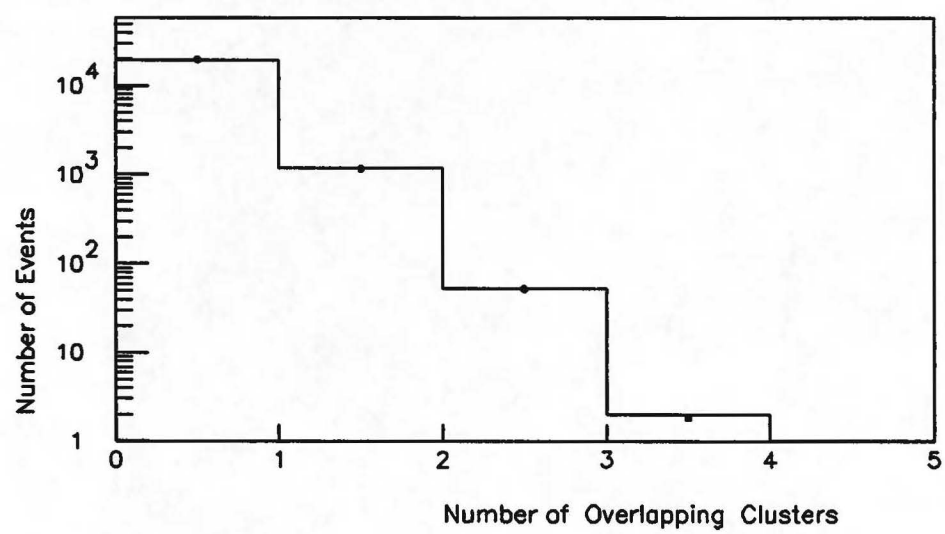

Figure 85: Distribution of number of overlapping clusters for $K_S \rightarrow 2\pi^0$ events. (Solid circles are Monte Carlo.)

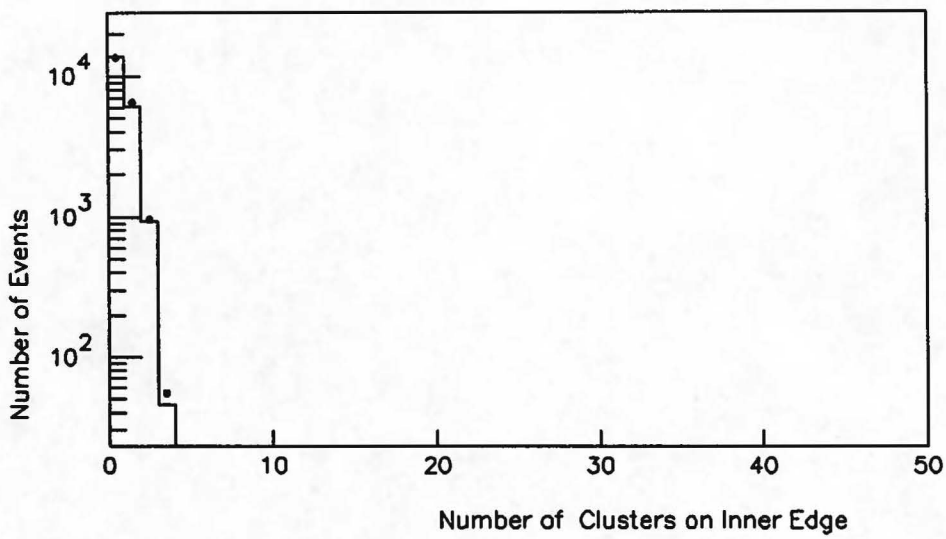

Figure 86: Distribution of number of clusters neighboring the beam pipes for $K_S \rightarrow 2\pi^0$ events. (Solid circles are Monte Carlo.)

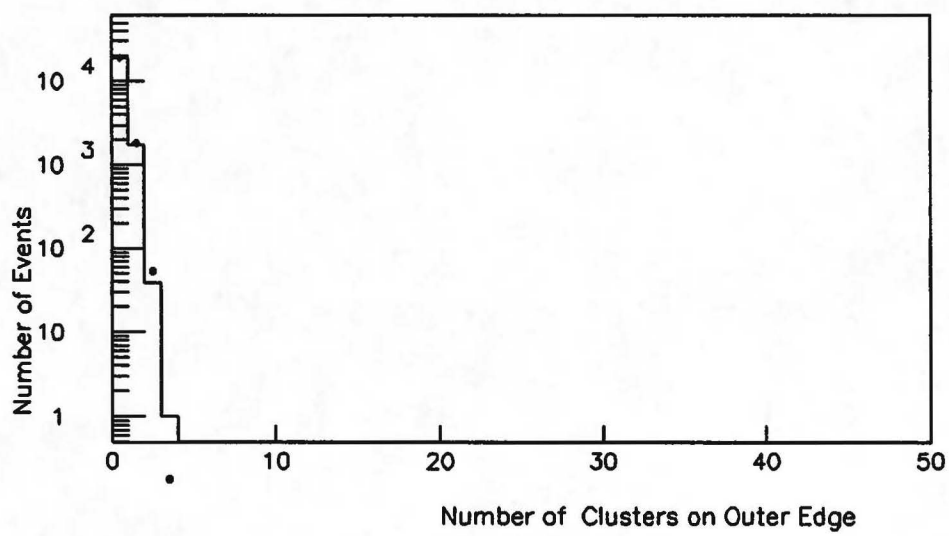

Figure 87: Distribution of number of clusters on the array's outer edge for $K_S \rightarrow 2\pi^0$ events. (Solid circles are Monte Carlo.)

were two more photons present in the Lead Glass. This sample had negligible background and proved extremely useful for checking the Monte Carlo and measuring the acceptance. Figures 92, 93, and 94 show Monte Carlo and data comparisons for $SEP2, \chi^2$ and q^2, all showing good agreement. The kaon energy spectra is shown in Figure 95 and Figures 96 and 97 show the photon and electron (and positron) energy distributions. This $K_L \rightarrow 3\pi^0$ sample provided a third independent measurement of the K_L energy spectrum, and it also gives a consistent result. The Z distribution of $K_L \rightarrow 3\pi^0$ events will be discussed in Chapter 11, where it is used to quantify our understanding of the neutral mode acceptance.

9.4 What are the Acceptances?

The acceptance in a given mode was measured as a function of P and Z in 10 GeV energy bins and 0.5m Z bins, and was defined to be

$$A(P,Z) = \frac{N_R(P,Z)}{N_G(P,Z)}$$

where

$N_R(P,Z)$ was the number of events reconstructing in bin (P,Z) passing all cuts, and

$N_G(P,Z)$ was the number of events generated in bin (P,Z) as was described in Section 9.2.

The acceptance in a given energy bin, summing over Z, was then given by

$$A(P) = \frac{\sum N_R(P,Z)}{\sum N_G(P,Z)}$$

Tables 14 and 15 give the acceptances in energy bins for the four $K \rightarrow 2\pi$ modes, indicating the range in Z used. These numbers were used to correct the observed number of events (given in Tables 18 and 19) to arrive at the decay rates.

These acceptance corrections appear to be large, but what is important is the relative acceptance of vacuum and regenerator events. So of more relevance are the ratios of the vacuum and regenerator acceptances. Even these are not a good measure of the size of the correction being applied, though, since the vacuum acceptances depend artificially on how far upstream one wants to go in generating or reconstructing events. One gets the best measure for the

Table 14: Acceptances for the $2\pi^0$ data

P (GeV)	Vacuum $110m < Z < 141m$	Regenerator $110m < Z < 141m$
40–50	0.01454	0.01602
50–60	0.03034	0.03973
60–70	0.04338	0.05791
70–80	0.05108	0.06922
80–90	0.05406	0.07241
90–100	0.05510	0.07040
100–110	0.05178	0.06609
110–120	0.04816	0.05974
120–130	0.04332	0.04992
130–140	0.04094	0.04303
140–150	0.03377	0.03572

Table 15: Acceptances for the $\pi^+\pi^-$ data

P (GeV)	Vacuum $110m < Z < 138.5m$	Vacuum $122.5m < Z < 138.5m$	Regenerator $110m < Z < 138.5m$
30–40	0.0651	0.1115	0.0883
40–50	0.1128	0.1836	0.1643
50–60	0.1478	0.2331	0.2156
60–70	0.1711	0.2616	0.2457
70–80	0.1855	0.2744	0.2591
80–90	0.1948	0.2807	0.2679
90–100	0.1951	0.2718	0.2621
100–110	0.1970	0.2647	0.2492
110–120	0.1905	0.2461	0.2374
120–130	0.1842	0.2300	0.2255
130–140	0.1703	0.2079	0.2043
140–150	0.1680	0.1987	0.1906
150–160	0.1525	0.1766	0.1801

Table 16: Ratio of vacuum and regenerator beam acceptances downstream of the Lead Mask

K Energy (GeV)	Vac Acceptance/ Reg Acceptance (Neutral Mode)	Vac Acceptance/ Reg Acceptance (Charged Mode)
30–40		1.26
40–50	1.56	1.12
50–60	1.24	1.08
60–70	1.15	1.06
70–80	1.08	1.06
80–90	1.04	1.05
90–100	1.04	1.04
100–110	0.99	1.06
110–120	0.97	1.04
120–130	1.01	1.02
130–140	1.03	1.02
140–150	0.98	1.04
150–160		0.98

size of these corrections by only considering events generated downstream of the Lead Mask. Ideally, the Lead Mask would have completely choked off decays upstream of it; in practice, about 10% of $K_L \rightarrow 2\pi^0$ and $K_L \rightarrow \pi^+\pi^-$ events are from upstream. Table 16 gives the ratio (vacuum acceptance / regenerator acceptance) when generated and reconstructed Z's were required to be downstream of 122.5m. We therefore see that the acceptance corrections are only large for the low energy bins in neutral mode. (In a high statistics experiment, it would be a good check to measure $|\epsilon'/\epsilon|$ using only neutral data above 70 GeV where the acceptance corrections are small. For the data presented in this thesis the level of statistics does not permit this as a useful check. With the large statistics of the 1987-88 run, however, this should be very useful.)

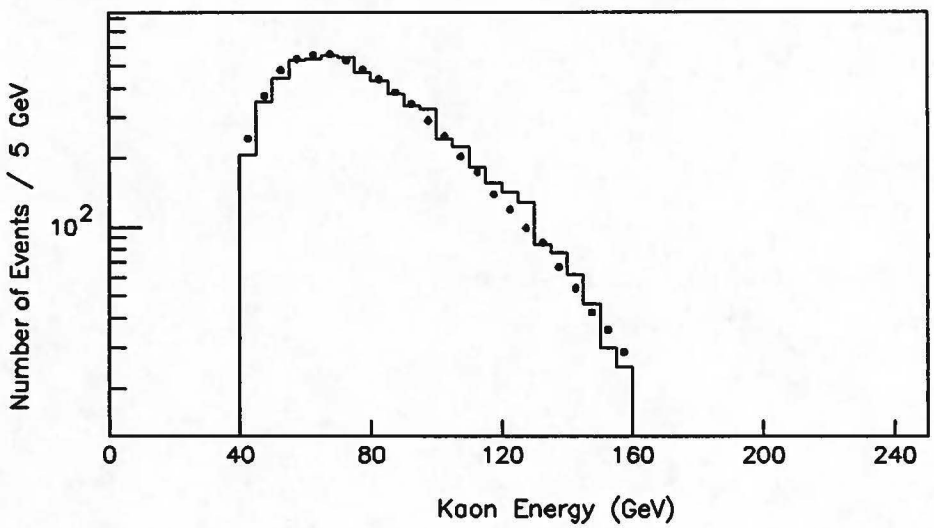

Figure 88: Kaon energy distribution for $\pi^0\pi^0$ events from the vacuum beam. (Solid circles are Monte Carlo.)

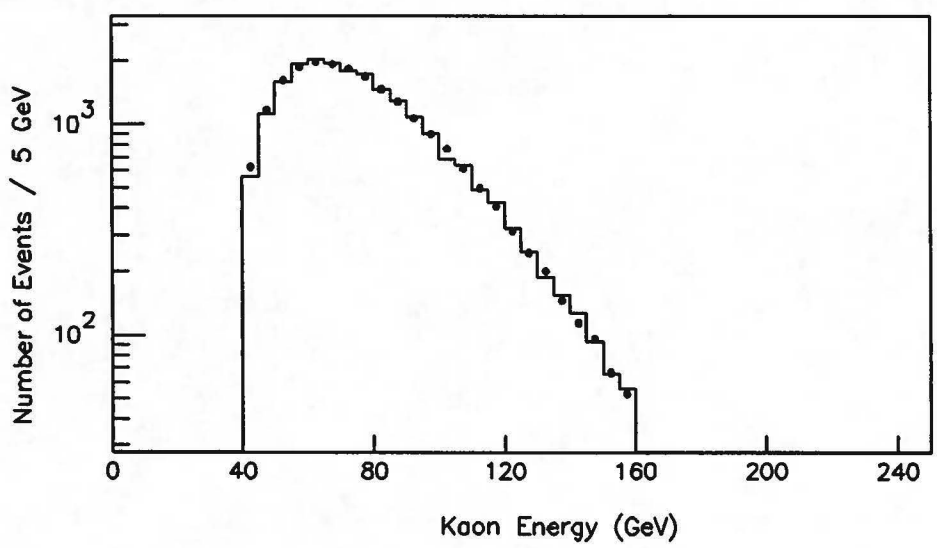

Figure 89: Kaon energy distribution for $\pi^0\pi^0$ events from the regenerator beam. (Solid circles are Monte Carlo.)

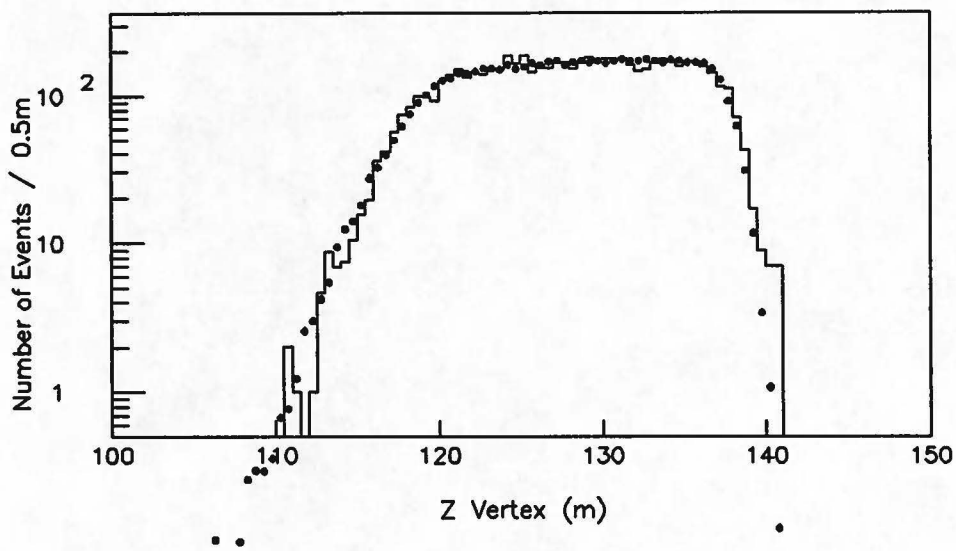

Figure 90: Longitudinal decay vertex for $\pi^0\pi^0$ events from the vacuum beam. (Solid circles are Monte Carlo.)

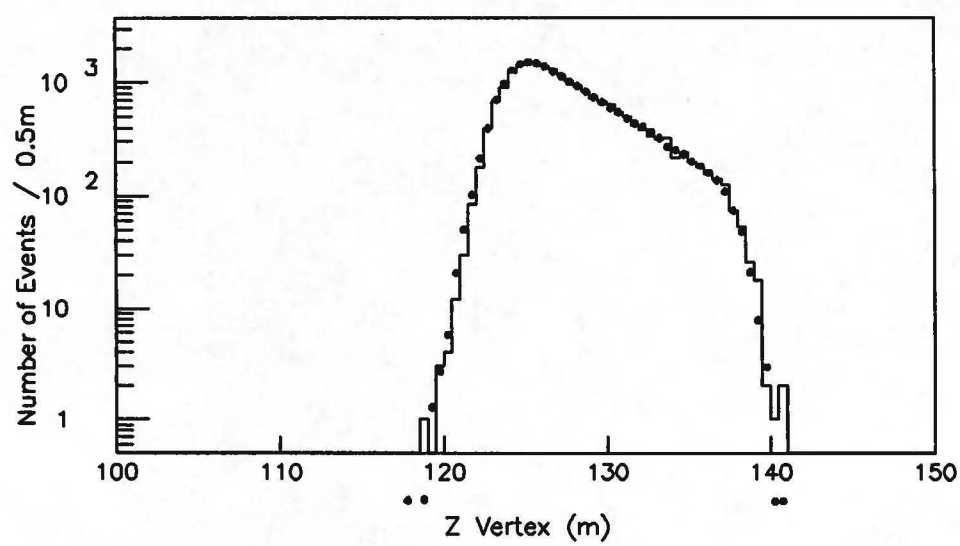

Figure 91: Longitudinal decay vertex for $\pi^0\pi^0$ events from the regenerator beam. (Solid circles are Monte Carlo.)

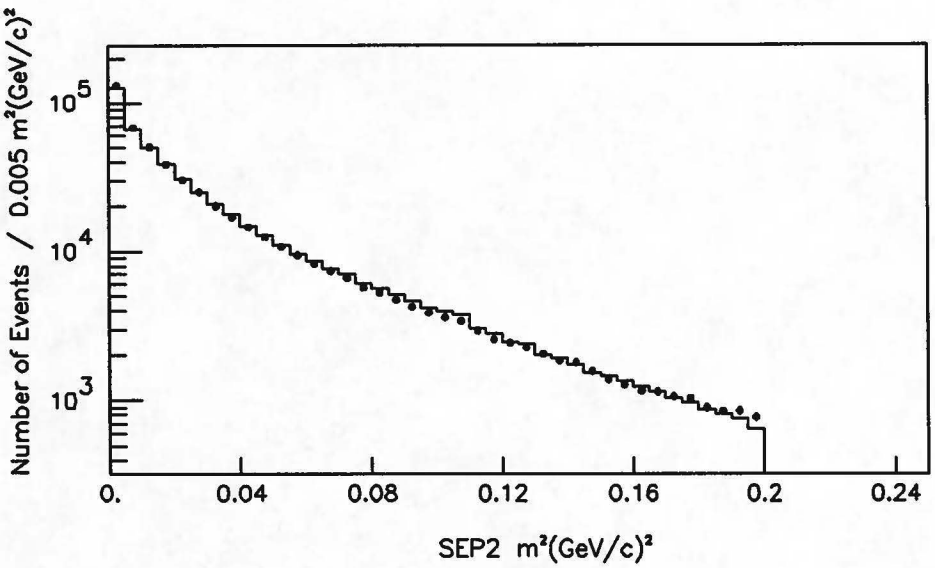

Figure 92: $SEP2$ distribution for $3\pi^0$ events. (Solid circles are Monte Carlo.)

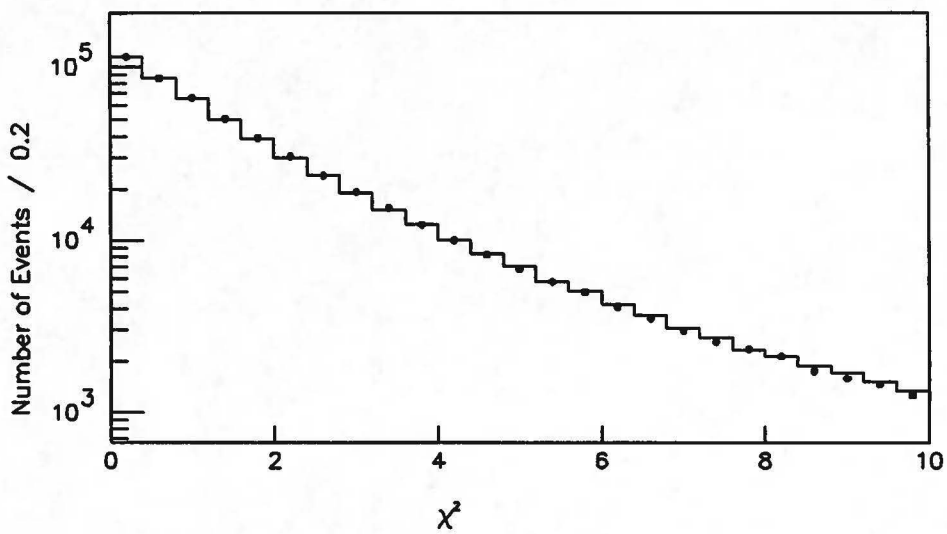

Figure 93: χ^2 distribution for $3\pi^0$ events. (Solid circles are Monte Carlo.)

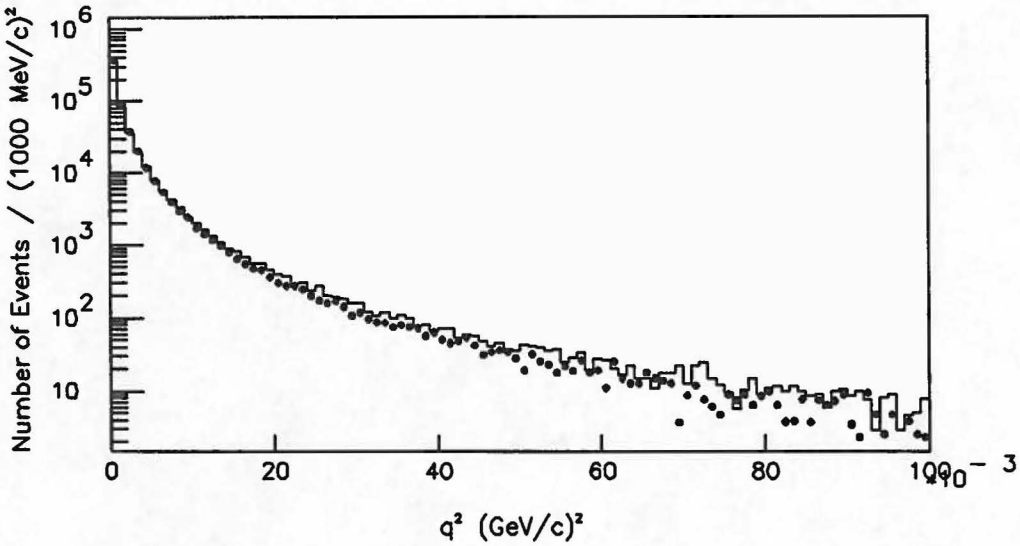

Figure 94: q^2 distribution for $3\pi^0$ events. (Solid circles are Monte Carlo.)

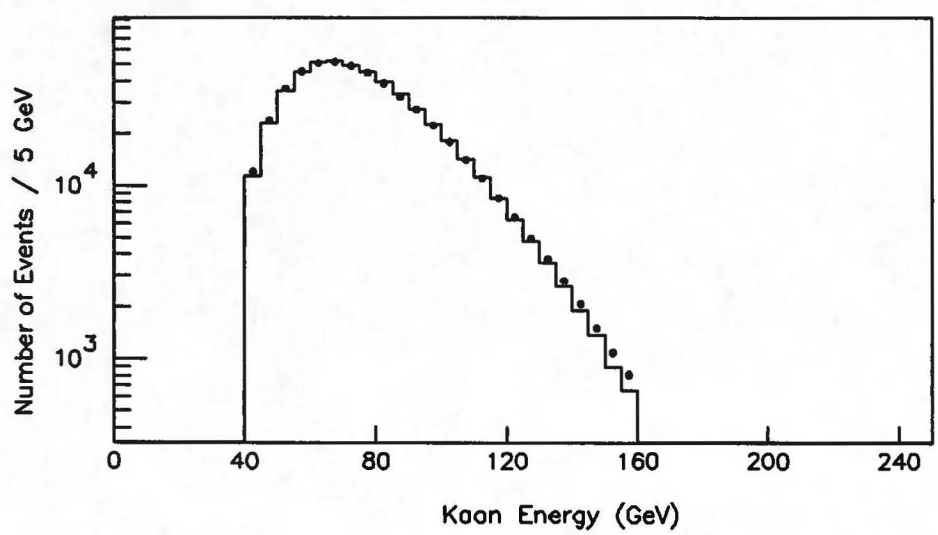

Figure 95: Kaon energy distribution for $3\pi^0$ events. (Solid circles are Monte Carlo.)

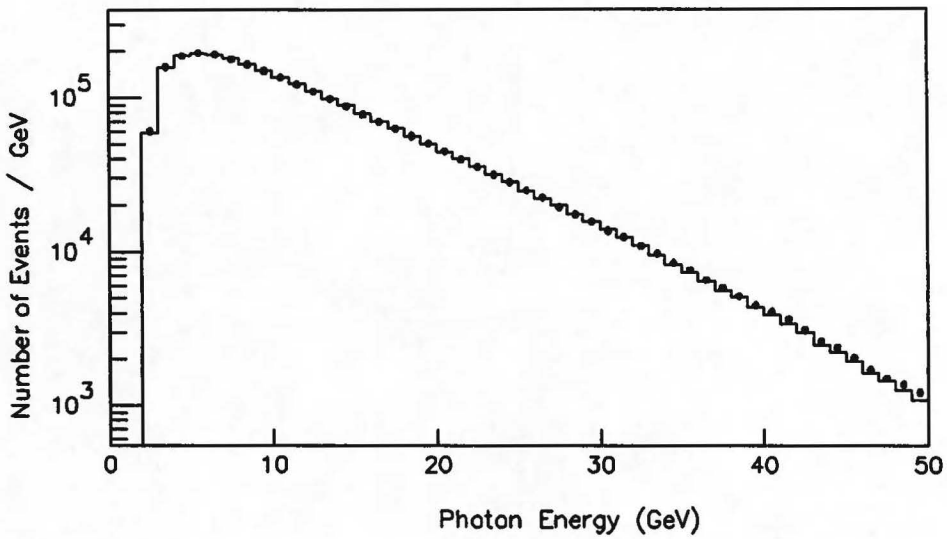

Figure 96: Energy distribution of photons for $3\pi^0$ events. (Solid circles are Monte Carlo.)

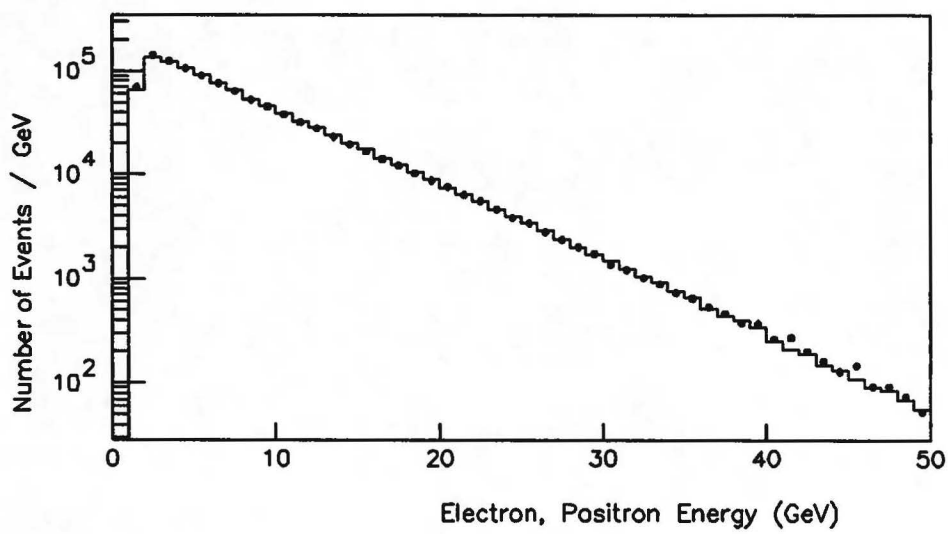

Figure 97: Energy distribution of electrons and positrons for $3\pi^0$ events. (Solid circles are Monte Carlo.)

Chapter 10

The Determination of $|\epsilon'/\epsilon|$

The ratio of the $K \to 2\pi$ rates in the vacuum and regenerator beams, when measured for both charged and neutral modes, gives a determination of $|\epsilon'/\epsilon|$. The rates are calculated by subtracting the backgrounds from the measured data samples and correcting each sample for the acceptance of the detector. In Section 2.1 an approximate relation between $|\epsilon'/\epsilon|$ and the 2π rates was given. Here we present the exact relation taking into account CP violating decays in the regenerator beam, as well as the small K_S component of the incident kaon beams at high energy and a small effect due to scattering in the Shadow Absorber. Given this, we obtain and present our result for $|\epsilon'/\epsilon|$, and we also present a measurement of the regeneration amplitude for B_4C.

10.1 Determining $|\epsilon'/\epsilon|$ from the 2π Rates

Assume first that the kaon vacuum beam and the kaon beam incident on the Regenerator are pure K_L beams (no K_S component) and that they have an identical energy distribution. Then the 2π rates (apart from a common normalization factor[1]) in the regenerator and vacuum beams at a proper time, τ, downstream of the Regenerator are given by

$$\begin{aligned}
\mathcal{R}_R(\tau)/e^{-X} &= \left|\rho e^{\nu\Gamma_S\tau} + \eta e^{-\Gamma_L\tau/2}\right|^2 \\
&= |\rho|^2 e^{-\Gamma_S\tau} + |\eta|^2 e^{-\Gamma_L\tau} + \\
&\quad 2|\rho||\eta| e^{-(\Gamma_S+\Gamma_L)\tau/2}\cos(\Delta m\tau + \Phi_\rho - \Phi_\eta) && (10.1)\\
\mathcal{R}_V(\tau) &= |\eta|^2 e^{-\Gamma_L\tau} && (10.2)
\end{aligned}$$

where

[1] For a discussion of this factor see Section 11.1.1

X is the the number of kaon interaction lengths for the Regenerator and the Shadow Absorber,

$|\rho|$ and Φ_ρ are the magnitude and phase of the regeneration amplitude,

$|\eta|$ and Φ_η are the magnitude and phase of η_{00} or η_{+-},

$\nu = i\Delta m/\Gamma_S - 1/2$,

$\Gamma_L = 1/\tau_L$ and $\Gamma_S = 1/\tau_S$ (τ_L and τ_S are the K_L and K_S proper lifetimes), and

Δm is the $K_L - K_S$ mass difference

The ratio $\mathcal{R}_R/\mathcal{R}_V$ for charged (neutral) mode determines $|\rho/\eta_{+-}|$ ($|\rho/\eta_{00}|$), and the charged and neutral ratios together give a measurement of $|\epsilon'/\epsilon|$ via

$$|\epsilon'/\epsilon| = \frac{1}{6}\left(1 - \left|\frac{\eta_{00}}{\eta_{+-}}\right|^2\right)$$

There is a correction to Equation 10.2 for high energy kaons, that results from the K_S component of the kaon beam not having completely decayed away. This experiment considered kaons with energies up to 160 GeV, for which the K_S mean lifetime is 8.6m in the lab frame. Decays as close as 110m to the production target were considered, which corresponded to 12.8 K_S lifetimes at 160 GeV. At this energy and decay point the 2π rate in the vacuum beam had a significant contribution from the K_S component of the kaon beam, and Equation 10.2 should therefore be modified to reflect this as follows,

$$\begin{aligned} \mathcal{R}_V(\tau) &= \frac{|a_S(P)e^{\nu Z/\Lambda_S} + \eta a_L(P)e^{-Z/(2\Lambda_L)}|^2}{|\eta a_L(P)e^{-Z/(2\Lambda_L)}|^2}|\eta|^2 e^{-\Gamma_L\tau} \qquad (10.3) \\ &\equiv W(P,Z)|\eta|^2 e^{-\Gamma_L\tau} \end{aligned}$$

where

P is the kaon energy,

Z is the distance from the target to the decay point,

$\Lambda_L = \gamma c\tau_L$ and $\Lambda_S = \gamma c\tau_S$ (c is the speed of light and $\gamma = P/m_K$),

$a_L(a_S)$ is the amplitude for a kaon produced at the target to be a $K_L(K_S)$, and

$W(P,Z)$ is the resulting weighting factor that reflects the 'primary' K_S component of the vacuum beam

Table 17: Weighting factor that reflects the relative contribution of the kaon beam's primary K_S component to the vacuum 2π rate

P (GeV)	Z (meters downstream of target)							
	105	110	115	120	125	130	135	140
35	1.000	1.000	1.000	1.000	1.000	1.000	1.000	1.000
45	1.000	1.000	1.000	1.000	1.000	1.000	1.000	1.000
55	1.000	1.000	1.000	1.000	1.000	1.000	1.000	1.000
65	1.000	1.000	1.000	1.000	1.000	1.000	1.000	1.000
75	1.000	1.000	1.000	1.000	1.000	1.000	1.000	1.000
85	0.998	0.999	1.000	1.000	1.000	1.000	1.000	1.000
95	0.995	0.996	0.998	0.999	1.000	1.000	1.000	1.000
105	1.002	0.995	0.994	0.995	0.997	0.998	0.999	1.000
115	1.044	1.015	1.000	0.994	0.993	0.994	0.995	0.997
125	1.146	1.082	1.040	1.013	0.999	0.993	0.991	0.992
135	1.327	1.215	1.133	1.075	1.036	1.012	0.998	0.992
145	1.597	1.424	1.294	1.196	1.122	1.069	1.033	1.010
155	1.993	1.719	1.527	1.381	1.267	1.179	1.112	1.064

To determine $a_L(P)$ and $a_S(P)$, we assumed that the states K^0 and $\overline{K^0}$ were produced independently at the target via the strong interaction. Ignoring CP violation,

$$|K^0\rangle = \frac{1}{\sqrt{2}}(|K_S\rangle + |K_L\rangle)$$
$$|\overline{K^0}\rangle = \frac{1}{\sqrt{2}}(|K_S\rangle - |K_L\rangle)$$

So for a K^0 produced at the target $a_L(P) = a_S(P) = 1/\sqrt{2}$ and for a $\overline{K^0}$, $a_L(P) = -a_S(P) = 1/\sqrt{2}$. The Malensek spectrum (described in Section 9.2) was used to determine the relative amounts of K^0 and $\overline{K^0}$ produced, and the resulting weighting factors ($W(P,Z)$) are shown in Table 17. At very high kaon energies there is also a correction to the regenerated decay distribution (Equation 10.1) due to the primary K_S component, but below 160 GeV kaon energy this is negligible.

There was a second effect modifying Equations 10.1 and 10.2 resulting from kaons scattering in the absorbers yet staying in the beams and passing all the trigger and reconstruction criteria. There is some regeneration in these absorbers (the amplitude is a few percent), but it is small and the absorbers

are far enough upstream of the Decay Region that this effect was negligible. The Shadow Absorber produced different intensities between the two beams, so that the measurement of $|\rho/\eta|$ depended on knowing the amount of attenuation of kaons in it. This factor did not affect the $|\epsilon'/\epsilon|$ calculation, however, since it was common to both charged and neutral modes. Similarly, not knowing the precise attenuation of kaons in the Regenerator did not affect the $|\epsilon'/\epsilon|$ calculation.

The most important effect of the absorbers related to the relative acceptance of scattered and unscattered kaons. Recall from Section 9.2 that a large fraction of kaons have an elastic scatter in the absorbers and that roughly 10% of fully reconstructed events passing all cuts have scattered. So while many of the scattered kaons are eliminated by the collimators, beam pipe and Lead Mask, there are a significant number that scatter yet stay in the beam. This affects the observed energy distribution of kaons, since scattered kaons with high energy are more likely to be forward in the lab frame and stay within the beam. Thus, because of the Shadow Absorber, the kaon energy spectra in the vacuum and regenerator beams are not identical. This affects the determination of $|\rho/\eta|$, but again $|\epsilon'/\epsilon|$ is not affected. A possible bias in $|\epsilon'/\epsilon|$ does arise, however, due to how cuts in charged and neutral modes affect scattered and unscattered events respectively. The only cut made distinguishing scattered kaons from unscattered ones is the q^2 cut, where q^2 measures the 'scattering' angle of kaons at the regenerator plane. Unscattered kaons have $q^2 = 0$, while kaons scattering in the Be absorbers have $< q^2 >= 120$ (MeV/c)^2 and kaons scattering in the Pb have $< q^2 >= 40$ (MeV/c)^2 (as determined by Monte Carlo for events passing all other cuts). In neutral mode where the q^2 requirement was very loose ($q^2 < 4000$ (MeV/c)^2, scattered and unscattered kaons were not distinguished. In charged mode, however, we required $q^2 < 250$ (MeV/c)^2 which had no effect on unscattered kaons, but rejected approximately 15% of kaons which scattered in Be. Less than 1% of events which pass all our cuts had a kaon which scattered in the Shadow Absorber (most of the scattered kaons which reconstructed scattered in the Pb absorber); so if the analysis had not considered the possibility of kaons scattering, an error of less than 0.15% (1% x 15%) in the double ratio,

$$\frac{(\mathcal{R}_R/\mathcal{R}_V)_{charged}}{(\mathcal{R}_R/\mathcal{R}_V)_{neutral}}$$

would have resulted, corresponding to an error of less than 0.00025 in $|\epsilon'/\epsilon|$. The effect is therefore small; it has been corrected for by simulating the scattering in the Monte Carlo, instead of correcting Equations 10.1 and 10.2.

Table 18: Event totals in each energy bin for the neutral data after background subtractions

K Energy (GeV)	Neutral Data ($110m < Z < 141m$) Vac	Reg
40–50	615.6	1820.8
50–60	1032.4	3746.1
60–70	1171.7	4198.1
70–80	1061.8	3688.6
80–90	844.3	2839.1
90–100	683.2	2036.5
100–110	477.7	1362.3
110–120	350.8	941.8
120–130	266.0	572.3
130–140	151.8	355.7
140–150	98.8	231.8

10.2 Extracting $|\epsilon'/\epsilon|$ from the Data

To extract $|\epsilon'/\epsilon|$, we have binned the data in P and Z, subtracted the backgrounds as described in Chapter 8, and weighted the vacuum events to account for the primary K_S component. The event totals after these corrections are given in Tables 18 and 19. We then calculated $\mathcal{R}_R$ and $\mathcal{R}_V$ in 10 GeV energy bins (integrating over Z), and corrected these ratios for acceptance as was described in Chapter 9. Kaon energies from 30-160 GeV in charged mode and 40-150 GeV in neutral mode were considered, and the acceptance corrected ratios were fit to the theoretical prediction given by the ratio of Equations 10.1 and 10.2 (again integrating over Z). The 3 charged mode data sets were treated independently with a Z cut of 122.5m for the first set and a Z cut of 110.0m for the other two sets, so that there were 50 data points in the fit (3 x 13 charged energy bins + 11 neutral energy bins). The input parameters to the fit are given in Table 20, and the parameters fit for were

$|\epsilon'/\epsilon|$, where $\eta_{00} = \epsilon - 2\epsilon'$ and $\eta_{+-} = \epsilon + \epsilon'$;

A, where A is the B_4C regeneration amplitude for 70 GeV kaons; and

α, where α is the power in the energy dependence of the B_4C regeneration amplitude ($f_{21} \propto P^{-\alpha}$)

Table 19: Event totals in each energy bin for charged data after background subtractions

K Energy (GeV)	Charged Data Set 3 ($110m < Z < 138.5m$)		Charged Data Set 2 ($110m < Z < 138.5m$)		Charged Data Set 1 ($122.5m < Z < 138.5m$)	
	Vac	Reg	Vac	Reg	Vac	Reg
30–40	1683.6	5851.4	1451.0	5162.5	1073.1	4030.9
40–50	2356.7	8692.8	2032.1	7608.1	1411.8	5995.0
50–60	2271.6	8657.0	2003.4	7465.5	1328.4	5972.0
60–70	2017.2	7407.7	1785.6	6542.3	1134.0	5184.4
70–80	1638.1	5927.2	1420.4	5262.2	976.9	4041.8
80–90	1324.4	4553.3	1166.0	3989.0	699.0	3075.7
90–100	1061.6	3222.3	875.4	2871.4	525.3	2292.1
100–110	788.4	2289.1	638.3	2078.7	406.5	1511.5
110–120	607.0	1561.7	474.8	1315.3	262.7	1019.9
120–130	423.2	1040.8	366.2	920.9	207.2	728.2
130–140	262.6	656.7	253.2	590.7	121.2	520.8
140–150	202.8	468.1	181.4	397.4	92.8	319.7
150–160	120.8	326.6	142.6	285.1	65.3	203.2

Table 20: Constants used in the fitting procedure

Constant	Value
Δm	0.5349 x 10^{10} $\hbar$ sec^{-1}
τ_S	0.8923 x 10^{-10} sec
τ_L	5.183 x 10^{-8}sec
ϵ	$0.002275e^{i44.6^o}$
$\Phi_{\epsilon'}$	48.6^o
Φ_ρ, B_4C	-126°
Φ_η	44.9^o
Density of B_4C	2.45 g/cm^3
Density of Pb	11.35 g/cm^3
$(f - \overline{f})/k$ for Pb	$150.7P^{-0.654}e^{-i122.2^o}$ mb
Absorption: σ_T for $^{56}B_4C$	887 mb
Absorption: σ_T for ^{207}Pb	2050 mb
Absorption: σ_T for ^{9}Be	148 mb

The result of the fit was

$$\begin{aligned} |\epsilon'/\epsilon| &= +0.0032 \pm 0.0028 \\ A &= (6.129 \pm 0.022)\text{mb} \\ \alpha &= 0.596 \pm 0.009 \end{aligned}$$

with a χ^2 of 46.8 for 47 degrees of freedom. The statistical error for $|\epsilon'/\epsilon|$ is dominated by the sample of 6800 events of $K_L \rightarrow 2\pi^0$, while the error in the power law is determined from the charged mode data. The power law is in good agreement with results from other regeneration experiments [35]. This result for $|\epsilon'/\epsilon|$ is consistent with 0 and is consistent with both the Standard Model and superweak predictions.

One can also fit for $|\epsilon'/\epsilon|$ and the regeneration amplitude in individual energy bins, and the results for this are presented in Figures 98 and 99 for energies between 40 GeV and 150 GeV. Doing a statistical averaging of these results gives $|\epsilon'/\epsilon| = 0.0031 \pm 0.0028$. This is a consistent result and does not depend on a power law assumption for the energy dependence of the regeneration amplitude. Figure 98 does show, however, that a power law fits the energy dependence very well. Finally, Figures 100 and 101 show the energy dependence of the regeneration amplitudes for B_4C as determined by charged and neutral modes independently and assuming $\epsilon' = 0$. A non-zero value for $|\epsilon'/\epsilon|$ would result in these charged and neutral amplitudes being shifted with respect to each other, but having nearly the same energy dependence. These amplitudes have been fit in the same way as that described above (but with $\epsilon' = 0$) and the fits are superimposed on the data. The results from these fits for A and α are

$$\begin{aligned} A_{+-} &= (6.108 \pm 0.022)\text{mb}, \quad \alpha_{+-} = -0.591 \pm 0.009 \\ A_{00} &= (6.202 \pm 0.057)\text{mb}, \quad \alpha_{00} = -0.644 \pm 0.027 \end{aligned}$$

The difference in amplitudes is small, signifying a small value for $|\epsilon'/\epsilon|$. There is a 1.9 standard deviation difference in the slope of the power laws for the energy dependence; this is consistent with being a statistical fluctuation, but could also signify a potential systematic problem. We must, of course, consider possible systematic errors in our measurement, and this is the subject of the next chapter.

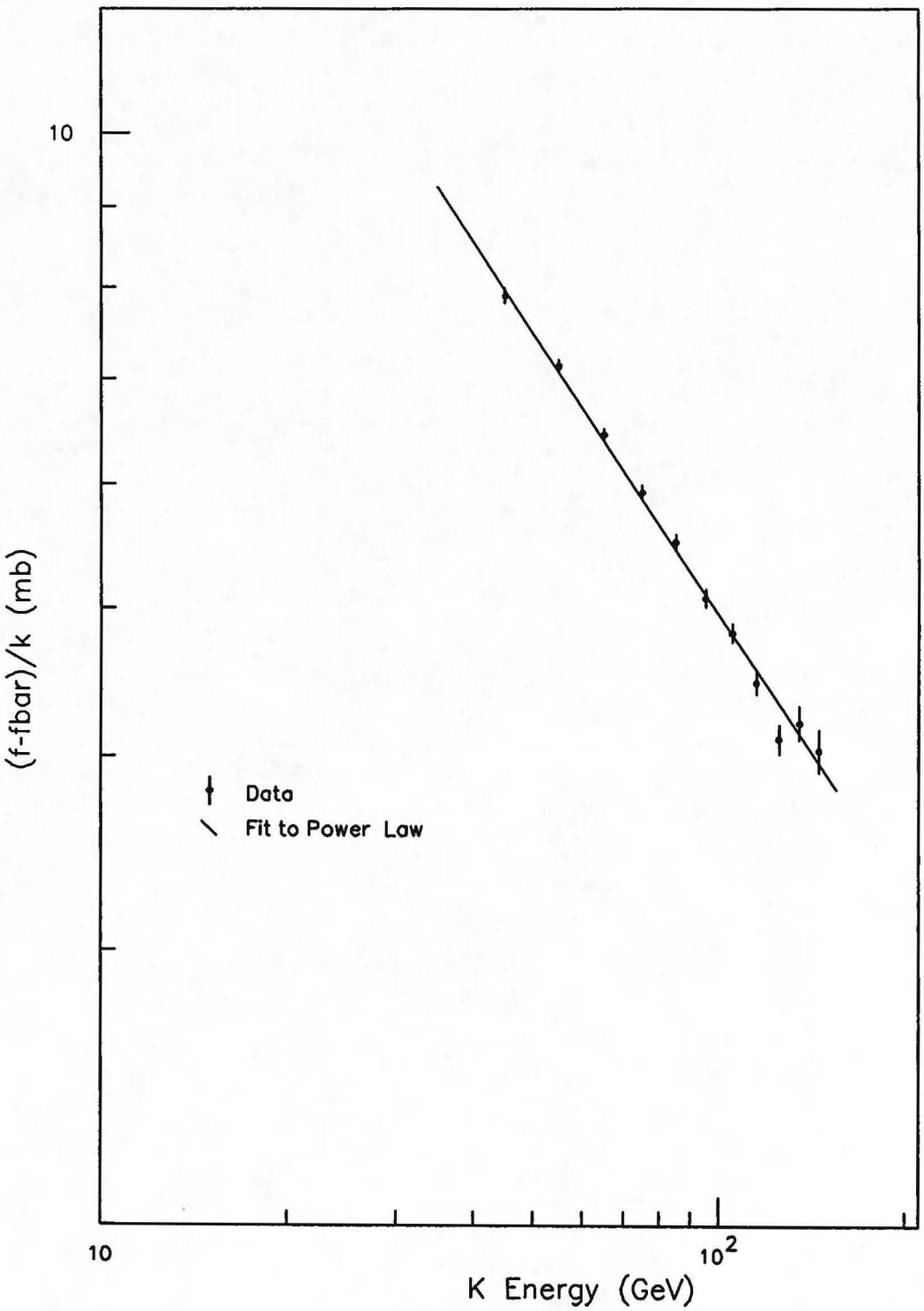

Figure 98: Energy dependence of the regeneration amplitude for B_4C

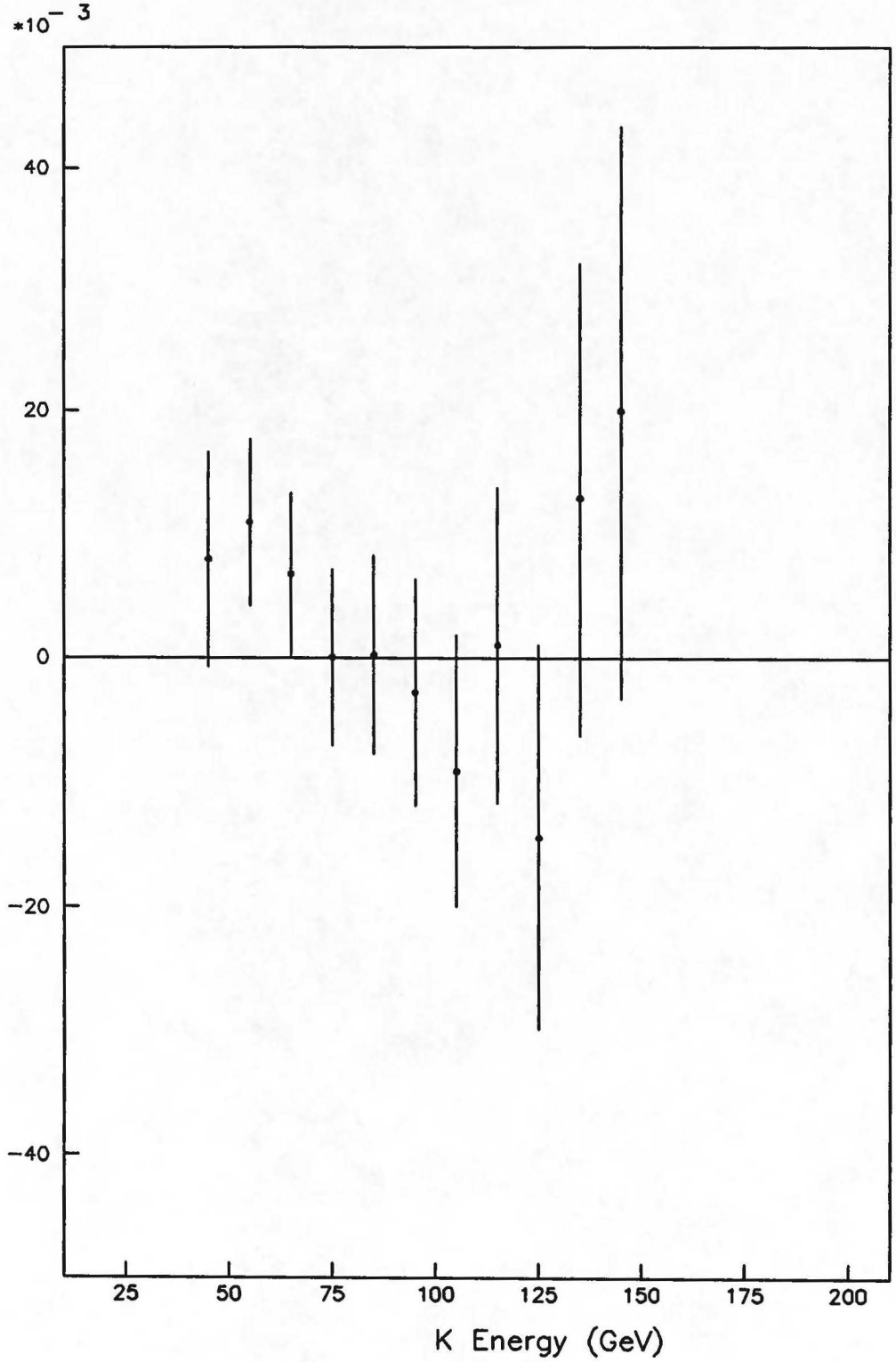

Figure 99: Energy dependence of $|\epsilon'/\epsilon|$

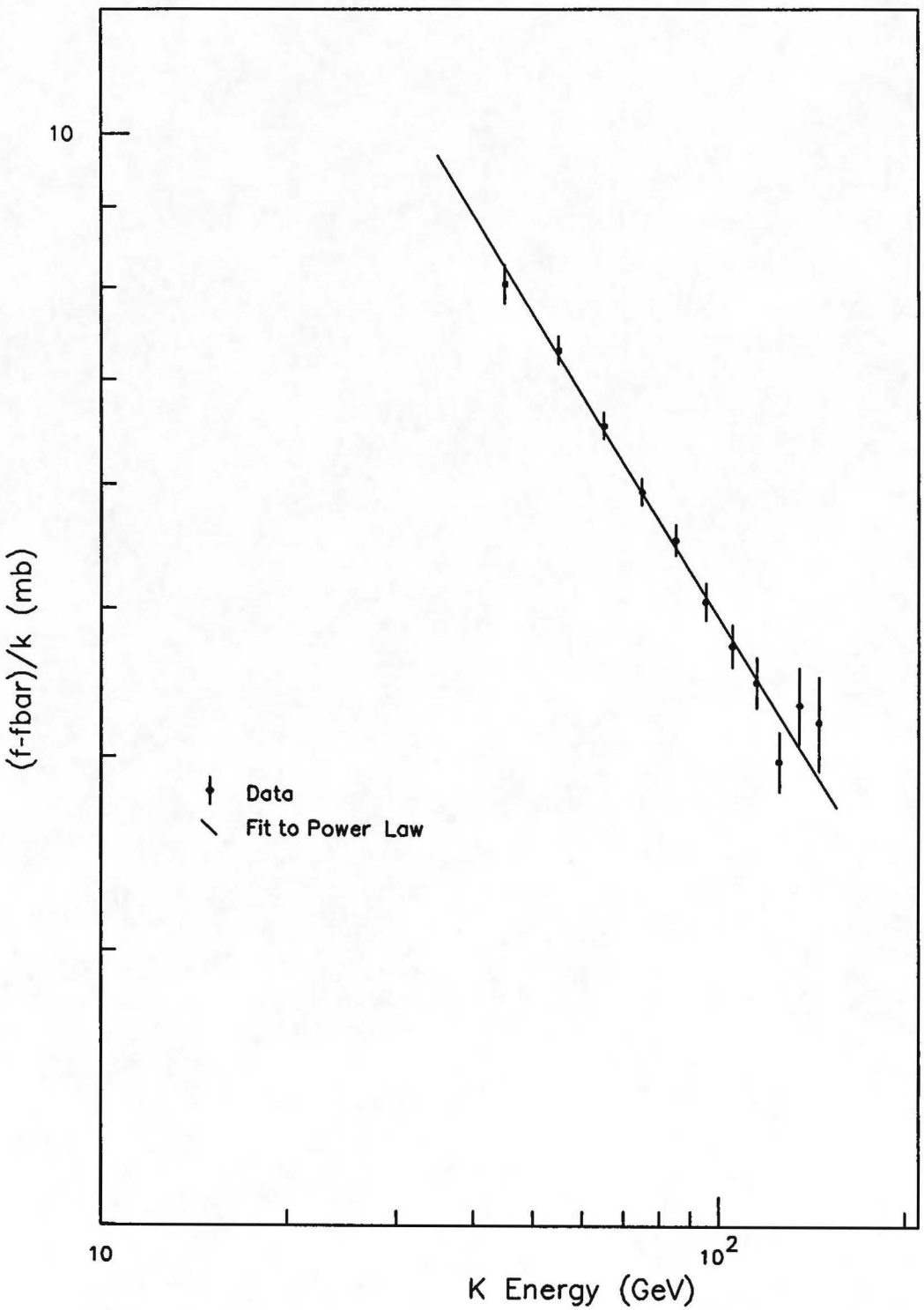

Figure 100: Energy dependence of the regeneration amplitude for B_4C as determined by neutral mode data only

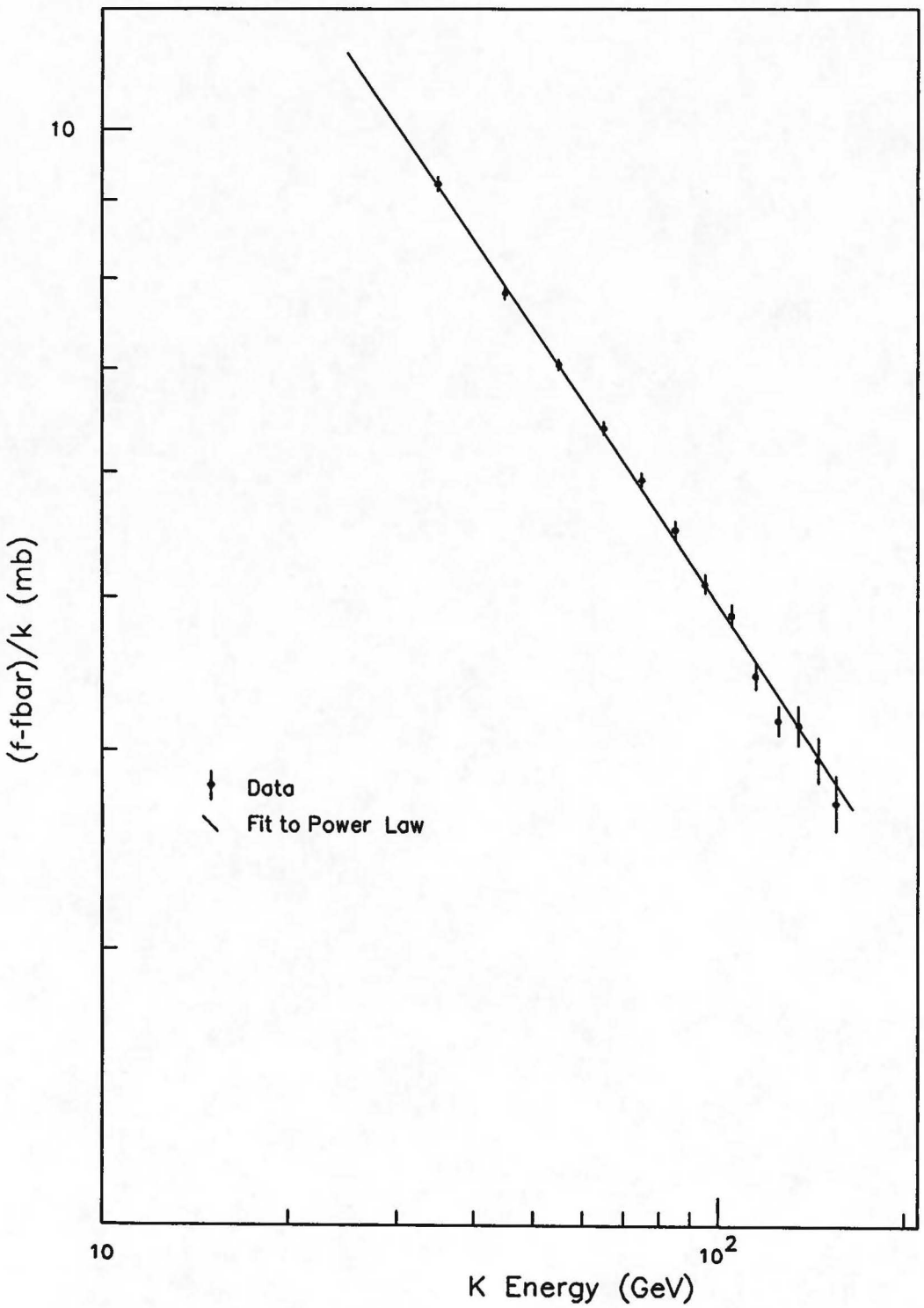

Figure 101: Energy dependence of the regeneration amplitude for B_4C as determined by charged mode data only

Table 21: Summary of results from fits for $(f - \overline{f})/k$ and $|\epsilon'/\epsilon|$

P (GeV)	$(f-\overline{f})/k$ (mb) Charged Data	$(f-\overline{f})/k$ (mb) Neutral Data	$(f-\overline{f})/k$ (mb) All 2π Data	$\lvert\epsilon'/\epsilon\rvert$ All 2π Data
30–40	9.22 ± 0.10			
40–50	7.84 ± 0.07	8.05 ± 0.23	7.91 ± 0.09	$+0.0079 \pm 0.0087$
50–60	7.05 ± 0.06	7.31 ± 0.15	7.14 ± 0.07	$+0.0109 \pm 0.0068$
60–70	6.41 ± 0.06	6.55 ± 0.13	6.46 ± 0.06	$+0.0067 \pm 0.0066$
70–80	5.94 ± 0.06	5.94 ± 0.12	5.94 ± 0.06	$+0.0000 \pm 0.0071$
80–90	5.52 ± 0.07	5.53 ± 0.13	5.52 ± 0.06	$+0.0002 \pm 0.0080$
90–100	5.10 ± 0.07	5.05 ± 0.14	5.08 ± 0.07	-0.0028 ± 0.0091
100–110	4.87 ± 0.08	4.73 ± 0.15	4.82 ± 0.07	-0.0091 ± 0.0109
110–120	4.46 ± 0.09	4.48 ± 0.17	4.47 ± 0.08	$+0.0010 \pm 0.0127$
120–130	4.18 ± 0.09	3.98 ± 0.18	4.11 ± 0.09	-0.0144 ± 0.0154
130–140	4.15 ± 0.12	4.33 ± 0.25	4.21 ± 0.11	$+0.0129 \pm 0.0192$
140–150	3.95 ± 0.13	4.22 ± 0.30	4.04 ± 0.13	$+0.0200 \pm 0.0234$
150–160	3.71 ± 0.15			

Chapter 11

Systematic Errors and Systematic Checks

The experiment we have performed to search for evidence of direct CP violation in $K \rightarrow 2\pi$ decays involved a precise measurement of the relative rates of K_L and K_S to charged and neutral pions. The signal we have looked for that would demonstrate this CP violation is the deviation of $|\eta_{00}/\eta_{+-}|^2$ from unity. This signal is not of the nature that if it exists it manifests itself in an unambiguous manner, such as the occurrence of a new decay mode or a resonance in some kinematic distribution. Instead, the signal appears as a small asymmetry in a ratio of decay rates, and the experiment that searches for this signal must necessarily be a precision experiment. A precision experiment must demonstrate a good understanding of the physics of the signal and a good understanding of effects that could simulate the signal. It is therefore necessary to have good experimental control and understanding of systematic errors. Additionally, there must be checks that the experiment was done correctly. Ideally one would 'calibrate' the experiment by making a similar measurement with a known result. For our experiment this is unfortunately not possible; we can, however, check our result by calculating it with different (ideally independent) methods, and by measuring known physics processes and getting them right. In this chapter, we discuss the sources and sizes of systematic errors, and the systematic checks that give us confidence in our measurement.

11.1 Systematic Errors

The largest sources of systematic error resulted from the background subtractions and acceptance corrections. We also considered systematic effects due to

accidentals, asymmetries between the upper and lower beams, and energy calibration. The background systematic uncertainties have been discussed earlier (see Chapter 8), so we only summarize those results here. The other sources of uncertainty we now describe in detail.

11.1.1 Uncertainties Associated with Accidentals and Differences Between the Upper and Lower Beams

We have stressed that our experiment was designed to greatly reduce systematic errors associated with having to know beam intensities, absolute reconstruction efficiencies and losses due to accidentals. The reason that these possible sources of systematic errors are negligible is because K_L and K_S decays were measured simultaneously with the same detector and because the Regenerator was alternated frequently between beams (once per minute). It is necessary, though, to demonstrate quantitatively how well this worked. Consider the neutral mode data by itself in a given (P, Z) bin,[1] and recall that Equations 10.1 and 10.2 describe the 2π rates in the regenerator and vacuum beams apart from a 'common' normalization factor.

The observed 2π events can be divided into 4 categories, where events are distinguished by being from the vacuum or regenerator beams for each of the two regenerator positions (up or down). There are four factors that affect the number of events in each category. The first is beam intensity, which is the number of kaons per spill. It can be different between upper and lower beams due to small differences in beam sizes, and we denote this by N_u or N_l. The second factor is the number of spills that occur with the Regenerator in the upper or lower positions, and this is given by S_u or S_l. The third factor is the detector livetime, which again can depend on the regenerator position. The livetime is related to the trigger rate and if more triggers come from the vacuum beam than the regenerator beam (or vice versa), the livetime will be lower when the Regenerator is in the less intense beam (more intense beam). The livetime is denoted by L_u or L_l. Lastly, the number of observed events depends on the reconstruction efficiency. This can be different between events from the upper and lower beams due to small asymmetries in geometry. It can also depend on the regenerator position due to the effect of accidentals. If accidental activity in the Lead Glass, for example, is greater around the vacuum beam then more vacuum events than regenerator events are likely to be misreconstructed and lost due to accidental activity. The reconstruction efficiency is therefore denoted by ε_{ij}, where the first index indicates which beam

[1] Here the data is binned both in momentum and in the longitudinal decay vertex, so that the geometrical acceptance is very nearly the same for both K_L and K_S decays.

(upper or lower) the decay is from and the second index indicates which beam (upper or lower) the Regenerator is in. Thus, we can write the normalization factor as follows,

$$V_u = N_u S_l L_l \varepsilon_{ul} \tag{11.1}$$
$$V_l = N_l S_u L_u \varepsilon_{lu} \tag{11.2}$$
$$R_u = N_u S_u L_u \varepsilon_{uu} \tag{11.3}$$
$$R_l = N_l S_l L_l \varepsilon_{ll} \tag{11.4}$$

where

V_u (V_l) is the normalization factor for vacuum events in the upper (lower)beam, and R_u (R_l) is the normalization factor for regenerator events in the upper (lower) beam,

N_u (N_l) is the number of kaons per spill in the upper (lower) beam,

S_u (S_l) is the number of spills with the Regenerator in the upper (lower) beam,

L_u (L_l) is the livetime of the detector with the Regenerator in the upper (lower) beam, and

ε_{ij} is the efficiency for detecting and reconstructing an event, where the first index indicates which beam the decay is from and the second index indicates which beam the Regenerator is in

Our analysis considered the ratio $\mathcal{R}_R/\mathcal{R}_V$ as given by the ratio of Equations 10.1 and 10.2, and we assumed

$$\frac{R_u + R_l}{V_u + V_l} = \frac{N_u S_u L_u \varepsilon_{uu} + N_l S_l L_l \varepsilon_{ll}}{N_u S_l L_l \varepsilon_{ul} + N_l S_u L_u \varepsilon_{lu}} = 1$$

(due to simultaneously measuring K_L and K_S and alternating the Regenerator frequently). So how good is this assumption? To address this, let us consider the quantity $(R_u R_l)/(V_u V_l)$,

$$\frac{R_u R_l}{V_u V_l} = \frac{(N_u S_u L_u \varepsilon_{uu}) \cdot (N_l S_l L_l \varepsilon_{ll})}{(N_u S_l L_l \varepsilon_{ul}) \cdot (N_l S_u L_u \varepsilon_{lu})} \tag{11.5}$$
$$= \frac{\varepsilon_{uu}\varepsilon_{ll}}{\varepsilon_{ul}\varepsilon_{lu}} \tag{11.6}$$

This ratio has the advantage that the terms involving beam intensities, number of spills, and detector livetimes cancel explicitly. Let us further consider the

nature of the reconstruction efficiency terms. These efficiencies can be split into a geometrical part, which does not depend on the regenerator position, and an accidental part, which does. We have

$$\varepsilon_{ij} = \varepsilon_i^G \varepsilon_{ij}^A$$

where we denote the geometrical efficiency by ε_u^G (ε_l^G) for a decay from the upper (lower) beam. The geometrical efficiency is equal to the reconstruction efficiency in the limit that the beam intensity goes to 0 (no accidentals, and hence $\varepsilon_{ij}^A = 1$), ie.

$$\varepsilon_i^G = \lim_{(N_i \to 0)} \varepsilon_{ij}$$

We have noted that accidentals in the Lead Glass kill approximately 10% of neutral mode events that would otherwise be accepted, this arising primarily from extra accidental clusters rather than accidentals landing on top of good clusters. There is a small spatial asymmetry in the distribution of Lead Glass clusters between K_L and K_S decays in a given (P, Z) bin and for a given regenerator position. There can also be a small spatial asymmetry in the illumination of accidentals. The net result is that these 3 factors—accidental activity, asymmetry in cluster illuminations between K_L and K_S decays, and asymmetry in the illumination of particles from accidentals can combine to bias our result. We expected this effect to be small since it results from the product of 3 small factors, but to check this we did a Monte Carlo study where we superimposed accidental events on top of $2\pi^0$ events. This study considered only accidental activity in the Lead Glass, the Glass being most sensitive to accidentals due to the long integration time (250 ns) of its signals. We considered the two regenerator positions separately and overlayed accidentals on both K_L and K_S events. We did not have a pure accidental trigger with which to do the study—instead, we used the prescaled $B \cdot MU$ muon triggers that were taken at the same time as the $2\pi^0$ data and subtracted out obvious muon clusters. The results of the study were that for the Regenerator in the lower beam we lost (0.24±0.14)% more vacuum events than regenerator events; and for the Regenerator in the upper beam we lost (0.06±0.14)% more vacuum events than regenerator events. From this, we concluded that there was no evidence for an asymmetry in accidental losses outside of statistics. Hence, no accidental correction was made and we assigned a systematic uncertainty of 0.0004 in $|\epsilon'/\epsilon|$ due to accidentals.

Our accidental study allowed us to conclude $\varepsilon_{uu}^A = \varepsilon_{lu}^A$ and $\varepsilon_{ll}^A = \varepsilon_{ul}^A$ within the systematic error quoted above. Substituting this into Equation 11.6 gives

$$\frac{R_u R_l}{V_u V_l} = \frac{(\varepsilon_u^G \varepsilon_{uu}^A) \cdot (\varepsilon_l^G \varepsilon_{ll}^A)}{(\varepsilon_u^G \varepsilon_{ul}^A) \cdot (\varepsilon_l^G \varepsilon_{lu}^A)} = 1$$

and this is independent of beam intensities, live times, detector and reconstruction efficiencies, and accidental effects. If we now decompose $\mathcal{R}_R$ and $\mathcal{R}_V$ into upper and lower beam components, we have

$$\begin{aligned} \mathcal{R}_R &= \mathcal{R}_{uR} + \mathcal{R}_{lR} \\ \mathcal{R}_V &= \mathcal{R}_{uV} + \mathcal{R}_{lV} \end{aligned}$$

We can analyze our data to fit for $(\mathcal{R}_{uR}\mathcal{R}_{lR})/(\mathcal{R}_{uV}\mathcal{R}_{lV})$ rather than $\mathcal{R}_R/\mathcal{R}_V$. The procedure is identical to that described in Section 10.2 and we found that this gives $|\epsilon'/\epsilon| = 0.0028 \pm 0.0028$. We therefore assigned a systematic uncertainty of 0.0004 in $|\epsilon'/\epsilon|$ due to differences in beam intensities, live times and efficiencies between the upper and lower beams.

11.1.2 Uncertainties Associated with Energy Calibration

Another source of systematic error arises from how well we know the energy calibration. In a (P, Z) bin analysis we effectively measure $|\epsilon'/\epsilon|$ by comparing $|\rho/\eta|^2$ for charged and neutral modes. Because $|\rho|^2 \propto P^{-1.2}$, comparing charged and neutral data at different energies induces a systematic error in $|\epsilon'/\epsilon|$. For example, suppose the energy scales were mismatched by 1%, then this would induce a bias in the rates of $(1.01)^{1.2}$ or approximately 1.2% and therefore a systematic error in $|\epsilon'/\epsilon|$ of 0.002. In a (P) bin analysis we integrate over Z with the effect that nearly all the K_S particles decay while the probability for a K_L to decay is proportional to $1/P$. Therefore in each momentum bin we effectively measure $P|\rho/\eta|^2$ and we are less sensitive to an error in the energy scale, since $P|\rho/\eta|^2 \propto P^{-0.2}$. For a momentum bin analysis a 1% error in energy scale leads to an error in $|\epsilon'/\epsilon|$ of 0.0003.

Now it is easy to know the energy scales to better than 1% in charged and neutral modes. The charged scale is known to better than 0.1% from our measurements of the K^0 and Λ masses (see Section 3.2.4). The neutral mode energy calibration was described in detail in Section 4.3 and much effort was put into determining it well. The absolute neutral energy scale is known on average to better than 0.2% from measurements of E/P for electrons, the π^0 mass, and the edges of the reconstructed Z distributions. Because of nonlinearity corrections and block to block variations in gains and nonlinearities, we have been very conservative and assigned a 0.0004 systematic uncertainty in $|\epsilon'/\epsilon|$ due to energy scale.

11.1.3 Uncertainties Associated with the Background Subtractions and Acceptance Corrections

The largest sources of systematic errors were associated with the background subtractions and acceptance corrections. A summary of the systematic errors due to the background subtractions was given in Table 12. Adding these errors in quadrature (since they are independent), gives a total uncertainty in $|\epsilon'/\epsilon|$ of 0.00066.

To check the acceptance correction in charged mode, we have calculated $|\epsilon'/\epsilon|$ by analyzing charged data in (P, Z) bins, neutral data in (P) bins and using a maximum likelihood fit so that the low statistics which occurred in some bins were treated correctly. A (P, Z) analysis has the advantage that there are no acceptance corrections and the Monte Carlo is only used to correct for resolution smearing effects between bins. In charged mode the resolution of the reconstructed kaon momentum was 0.4 GeV (rms), and the resolution of the reconstructed Z vertex was 17 cm (rms). This (P, Z) analysis used 10 GeV energy bins from 30-160 GeV and 1.5m Z bins from $Z = 124$m to $Z = 137.5$m. The size of the resolution smearing effect was only 0.0008 in $|\epsilon'/\epsilon|$, where this was determined by calculating $|\epsilon'/\epsilon|$ with and without the Monte Carlo determined smearing correction. The smearing was therefore small (and well understood) and this fitting procedure gave $|\epsilon'/\epsilon| = +0.0036 \pm 0.0029$, and the result was independent of knowing the charged mode acceptance. From this study and from others where we varied the bin sizes in the (P, Z) analysis and varied the Z ranges in the (P) analysis, we assigned a systematic uncertainty of 0.0005 due to charged mode acceptance (no changes larger than this were seen).

In neutral mode it is tempting to also try a (P, Z) analysis, but there one encounters many more difficulties than in charged mode. The resolution is much worse—1.4 GeV (rms) in P and 1.1m (rms) in Z so that the smearing effects are large. Additionally, an energy scale error of 0.2% would shift the Z vertex by 10cm (10cm=0.2% x 50m; 50m is the average distance from the Lead Glass to the decay region), and this would induce an error in $|\epsilon'/\epsilon|$ on the order of 0.002 primarily from using an incorrect proper time in the K_S distribution. We therefore decided it was very difficult to do a (P, Z) neutral analysis (with a small enough systematic error) that would provide a meaningful check.

The method chosen to check and quantify our understanding of the neutral mode acceptance correction was to study in detail the Z distributions of data and Monte Carlo events. From the $2\pi^0$ modes there were not enough statistics in the data to provide a meaningful check. All we could conclude there was that for the 6800 $K_L \rightarrow 2\pi^0$ events, the data and Monte Carlo were consistent;

however, we would not be able to discern a systematic problem at the level of a 0.002 contribution to $|\epsilon'/\epsilon|$. (Remember the statistical uncertainty is 0.0028.) We did, however, have a sample of over 500,000 $K_L \rightarrow 3\pi^0$ events and it was with this sample that we quantified our understanding of the validity of the acceptance correction.

We demonstrated qualitative agreement between Monte Carlo and data for $K_L \rightarrow 3\pi^0$ events in Chapter 9. Here we wish to look quantitatively at the agreement of the Z distributions. Figures 102–105 show the Monte Carlo and data comparisons in several energy bins, where a total sample of 400,000 $K_L \rightarrow 3\pi^0$ Monte Carlo events has been generated. Taking the ratio of data to Monte Carlo and plotting this, yields the distributions shown in Figures 106–109. These ratio plots should be flat as a function of Z and if they are not, this reflects the Z-dependence to an acceptance error. For example, if the data to Monte Carlo ratio changes by 10% over 20m, then there is an acceptance error of 0.5% /m. So if the K_L and K_S distributions were different by an effective Z distance of 2m, an error of 1% in the relative acceptance determinations would result, corresponding to an 0.0017 error in $|\epsilon'/\epsilon|$. The ratio plots in Figures 106–109 have been fit to straight lines and Figure 110 plots the fitted line slopes in each energy bin, where the slopes have been normalized to correspond to an acceptance error per meter. As can be seen from Figures 102–110, the Monte Carlo and data are in good agreement and the acceptance errors are small. If we assume that Figure 110 does in fact correspond to the acceptance error per meter for the $2\pi^0$ data, then we can fold this into the observed $2\pi^0$ Z distributions for K_L and K_S and determine the resulting change in $|\epsilon'/\epsilon|$. We have done this and we find that this causes a change of -0.00047 in $|\epsilon'/\epsilon|$.

There are two criticisms one can make of this method for checking the acceptance correction. First, the check is done using $3\pi^0$ data rather than $2\pi^0$ data, which is what determines $|\epsilon'/\epsilon|$. However, the detector and decay particles are the same for these and so if we get the $3\pi^0$ acceptance correct, we make the reasonable claim that we also get the $2\pi^0$ acceptance correct at the same level. In fact, any acceptance error that exists is likely to be greater in $3\pi^0$ data than in $2\pi^0$ data, since the $3\pi^0$ acceptance changes more rapidly as a function of Z. The second criticism is that an acceptance error may not be linear in Z. In particular, the acceptance in the vacuum beam extends upstream of the Regenerator and is 'choked off' in that region by the Lead Mask, which is not an aperture for the regenerator beam. To address this, we have considered how well we understand the Lead Mask aperture. In part, we know it is understood well because the Z distributions in $K_L \rightarrow 3\pi^0$ and $K_L \rightarrow \pi^+\pi^-$ agree well between Monte Carlo and data upstream of the Lead

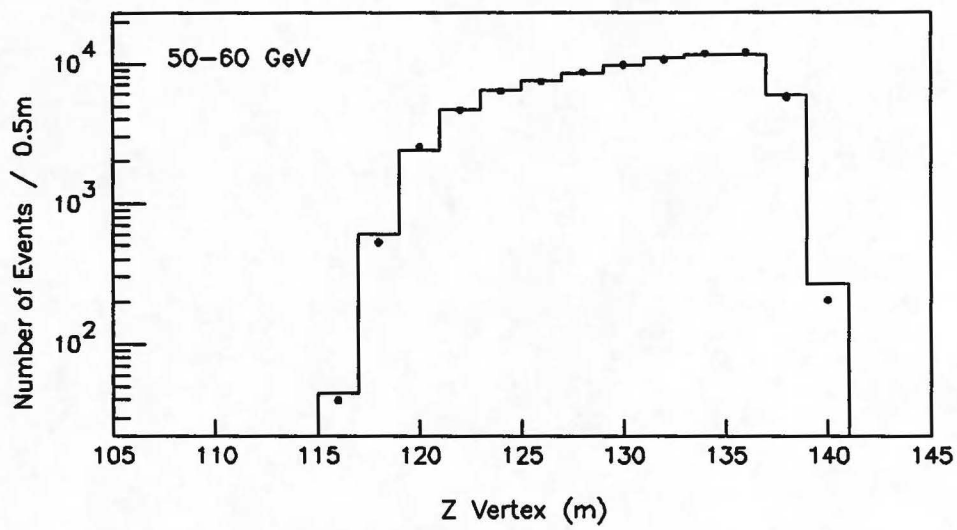

Figure 102: The longitudinal decay vertex distribution for $K_L \rightarrow 3\pi^0$ events for kaon energies between 50 and 60 GeV. (The solid circles are Monte Carlo.)

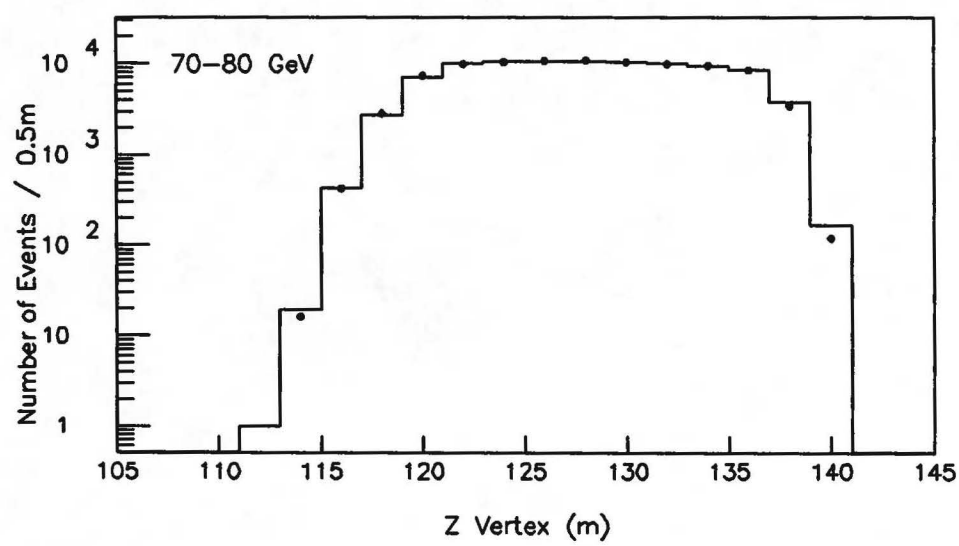

Figure 103: The same plot as 102 for kaon energies between 70 and 80 GeV.

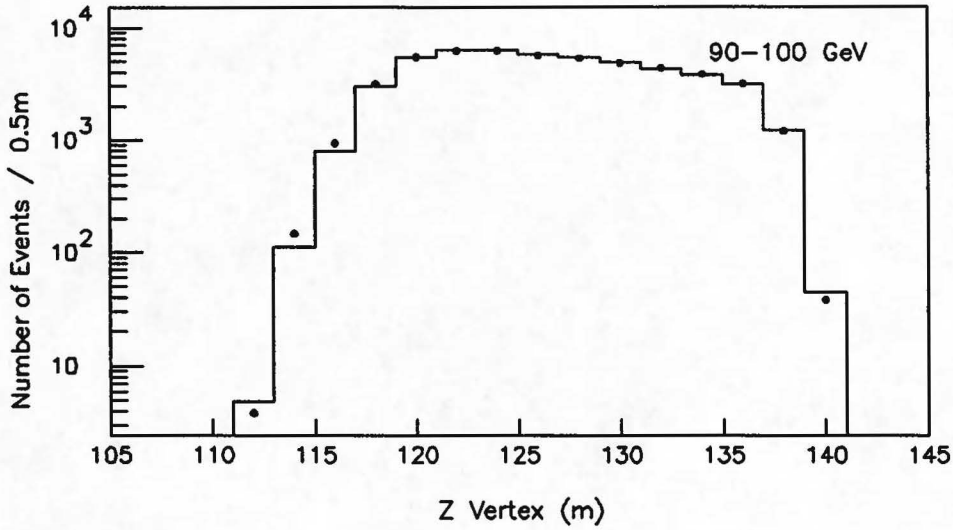

Figure 104: The same plot as 102 for kaon energies between 90 and 100 GeV.

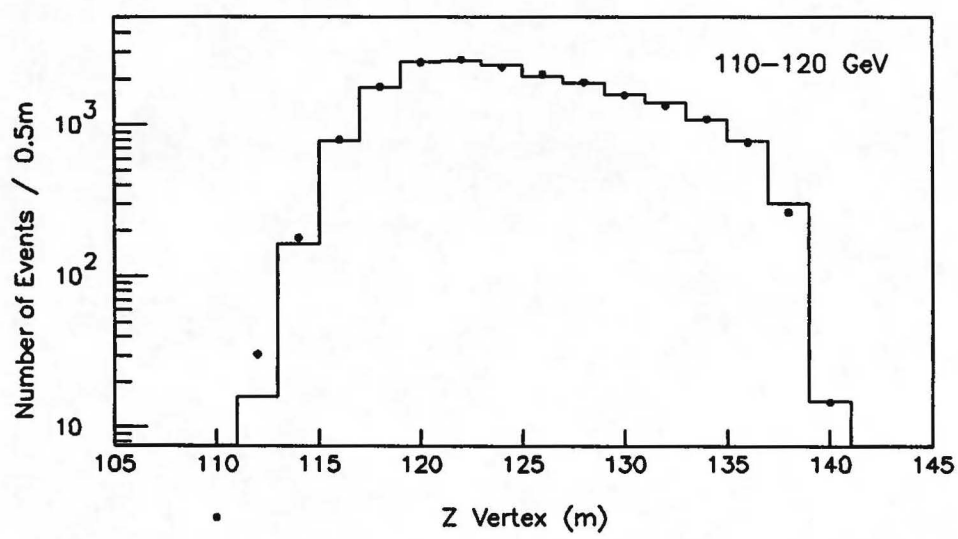

Figure 105: The same plot as 102 for kaon energies between 110 and 120 GeV.

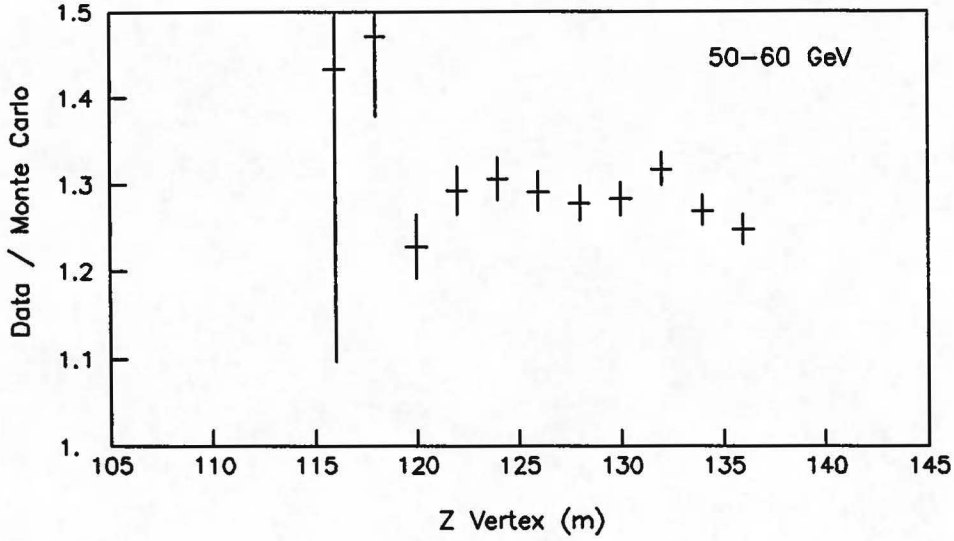

Figure 106: The ratio of data to Monte Carlo from Figure 102.

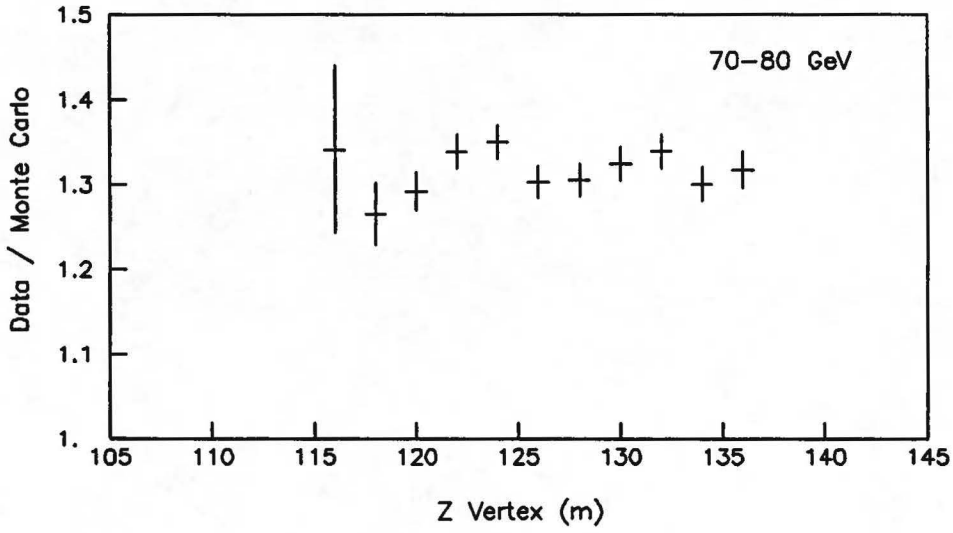

Figure 107: The ratio of data to Monte Carlo from Figure 103.

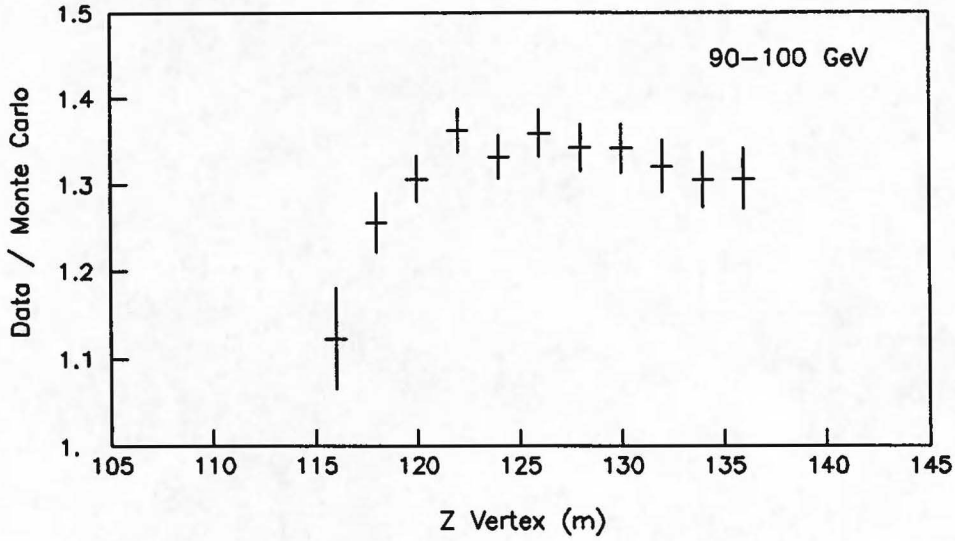

Figure 108: The ratio of data to Monte Carlo from Figure 104.

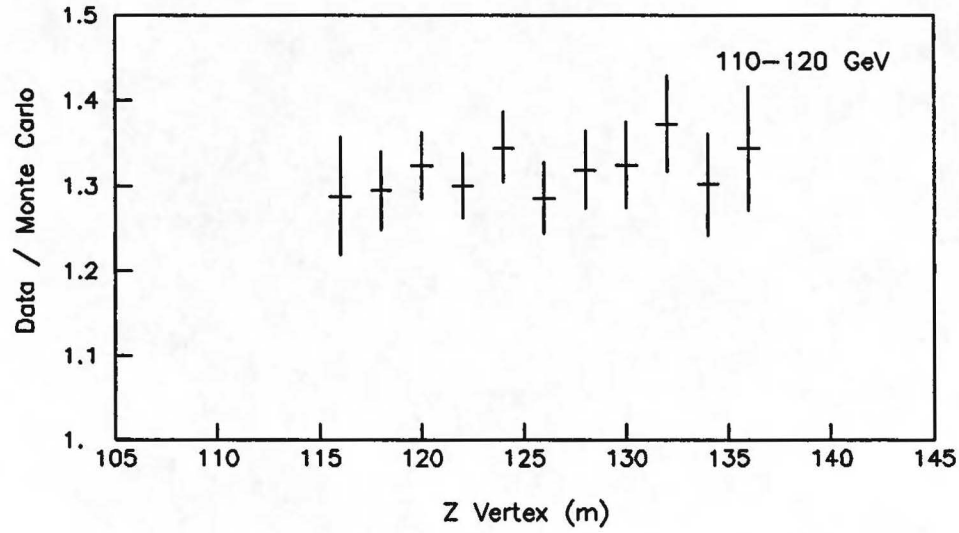

Figure 109: The ratio of data to Monte Carlo from Figure 105.

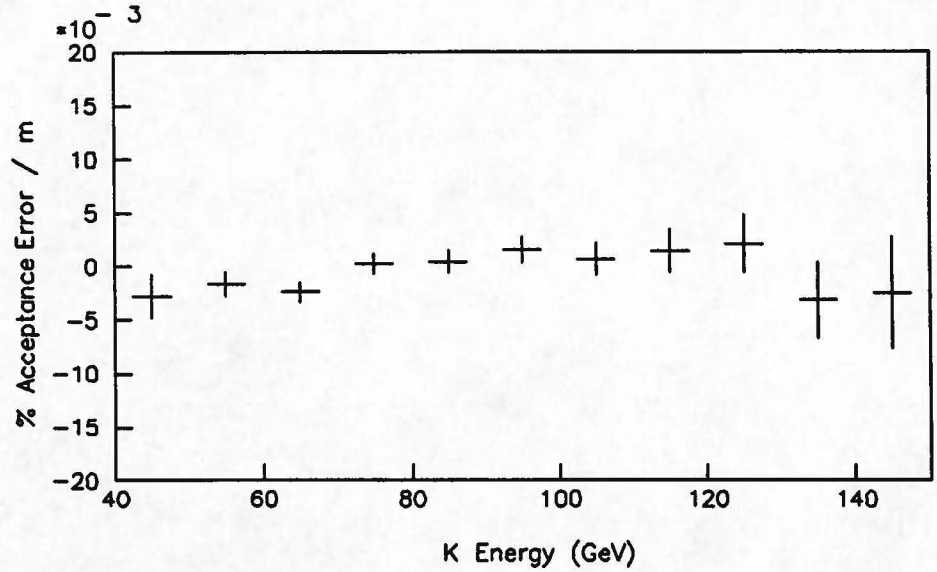

Figure 110: Energy dependence to the effective acceptance error per meter as determined from straight line fits to plots in Figures 106–109

Mask. Additionally, we have studied the acceptance as a function of beam shape (the way in which the Lead Mask affects the acceptance is correlated with the beam shape) and observed changes in $|\epsilon'/\epsilon|$ no larger than 0.0005 for reasonable changes to the beam shape. We have also cut the vacuum data at different Z locations from 115m to 121m and we see no changes in $|\epsilon'/\epsilon|$ larger than 0.0007. From these studies and from the agreement between Monte Carlo and data for $K_L \rightarrow 3\pi^0$ events, we have determined the systematic uncertainty in $|\epsilon'/\epsilon|$ due to the neutral mode acceptance correction to be 0.0007.

Table 22 summarizes the systematic errors from accidentals, upper/lower beam differences, energy scale, charged mode acceptance and neutral mode acceptance. These errors are independent and so we add them in quadrature to yield a total systematic error of 0.0012.

11.2 Systematic Checks

We have now determined the systematic uncertainty in our result, but we should ask what were the systematic checks present in the data. A number of these have already been discussed. The first and very important check was the agreement between Monte Carlo and data in many modes and in many quantities. This provided the check that we understood our detector and the physics of our signal—recall, for example, that we were required to understand

Table 22: Summary of systematic uncertainties

Source	Systematic Uncertainty in $\lvert\epsilon'/\epsilon\rvert$
Backgrounds	0.00066
Accidentals and beam differences	0.0004
Neutral mode energy calibration	0.0004
Charged mode acceptance	0.0005
Neutral mode acceptance	0.0007
Total	0.0012

scattering in the absorbers and primary K_S contamination from the target. In particular, it was an important check that we understood the kaon energy spectrum and measured consistent results for it in the $K_L \to \pi^+\pi^-$, $K_L \to 2\pi^0$, and $K_L \to 3\pi^0$ modes. We made independent measurements of the B_4C regeneration amplitude in charged and neutral modes and found consistent results for the energy dependence to this amplitude.

We have done a (P, Z) analysis in charged mode, thereby eliminating the charged acceptance correction, and achieved a consistent result. Lastly, we have analyzed the neutral mode data making some changes to the normal cuts so as to probe effects that were important in our measurement. We tried eliminating the fusion cut for photon clusters to probe our understanding of the $K_L \to 3\pi^0$ background contamination, where the dominant uncertainty was due to the relative contribution of background events with 0, 1 and 2 fusions. Without this fusion cut the background went from 1.56% to 2.34%, and we found a change of 0.0001 in $|\epsilon'/\epsilon|$. It was important to understand well the acceptance around the holes in the Lead Glass and we analyzed the data requiring reconstructed y positions of photon clusters to be more than 2cm outside of the CA region—this resulted in a change in $|\epsilon'/\epsilon|$ of +0.0006. We tried requiring individual track momenta to be greater than 1.5 GeV/c (we worried about the acceptance of low energy tracks) and found this changed $|\epsilon'/\epsilon|$ by -0.0001. Finally, we tried artificially changing the energy scale in neutral mode by 1% to verify the calculation of this effect as outlined in the previous section, and found this changed $|\epsilon'/\epsilon|$ by 0.0006. All these changes were small and therefore provided an additional check that our result was unbiased.

Chapter 12

Conclusions

This experiment has studied CP violation in the 2π decay modes of neutral kaons, and has measured [1]

$$|\epsilon'/\epsilon| = [3.2 \pm 2.8(\text{stat}) \pm 1.2(\text{syst})] \cdot 10^{-3}$$

Adding the statistical and systematic errors in quadrature then gives $|\epsilon'/\epsilon| = (3.2 \pm 3.0) \cdot 10^{-3}$. The dominant source of statistical error is due to the 6800 $K_L \rightarrow 2\pi^0$ events observed, while the dominant systematic uncertainties arise from understanding of the neutral mode acceptance corrections and from estimation of the neutral mode background subtractions. We thus find no significant evidence for direct CP violation. The result is consistent with recent Standard Model calculations that give $0.001 < |\epsilon'/\epsilon| < 0.01$. At the same time, the superweak model which predicts $\epsilon' = 0$ is still viable.

Our measurement is the most precise determination of $|\epsilon'/\epsilon|$ except for a very recent result from the NA31 group at CERN which gives $|\epsilon'/\epsilon| = (3.3 \pm 1.1) \cdot 10^{-3}$ [37]; Figure 111 summarizes the experimental measurements that have been made and the range of values one expects in the Standard Model. The CERN result is the only measurement yielding a significant departure of $|\epsilon'/\epsilon|$ from 0, and if correct would demonstrate that direct CP violation exists. The 1987–88 run of our FNAL experiment and a 1988 run of the CERN experiment should each produce new measurements of $|\epsilon'/\epsilon|$ with better than 0.001 precision in the next one or two years and thus be able to establish the direct CP violation mechanism if $|\epsilon'/\epsilon|$ is greater than about 0.002. The experimental techniques used by the two experiments are significantly different and have different sources of systematic uncertainty. This is beneficial because of the difficulty of these experiments, and in particular because a very careful understanding of systematic effects must be achieved.

[1] This result has recently been published; see reference [36].

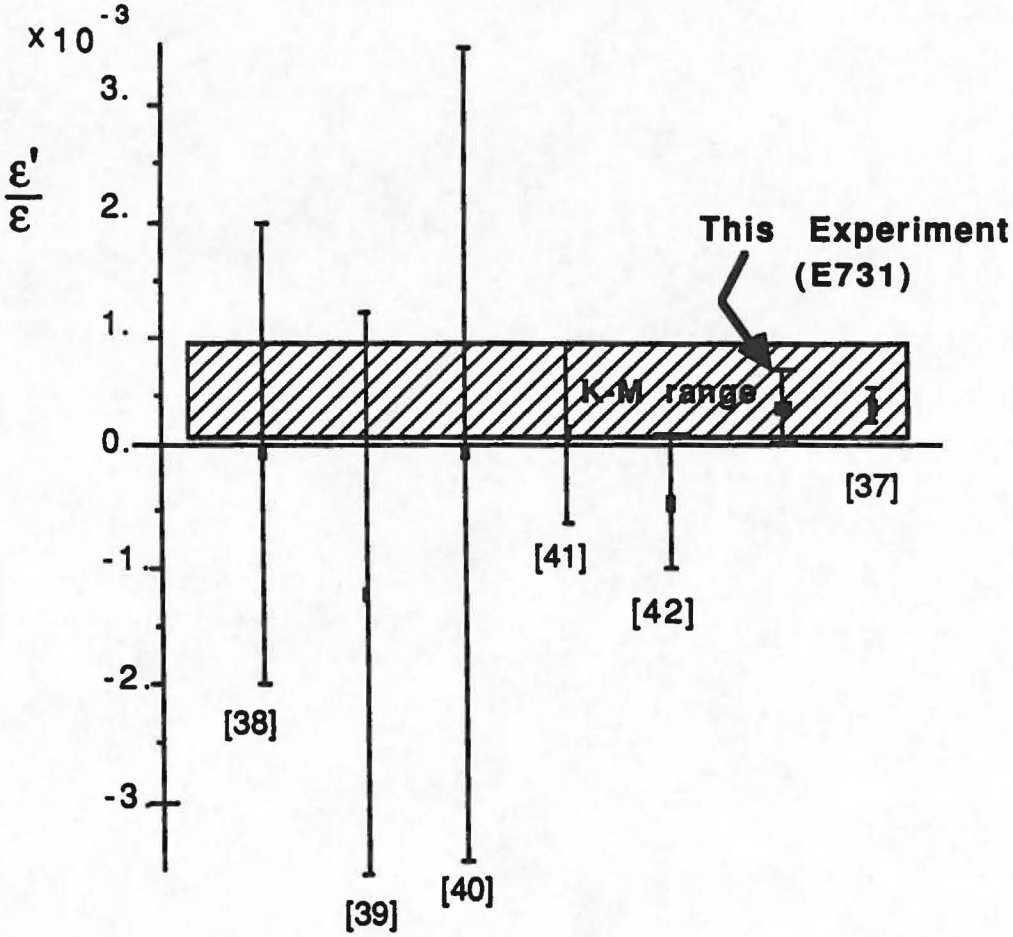

Figure 111: Measurements of $|\epsilon'/\epsilon|$

The CERN experiment uses a single beam, detects charged and neutral kaon decays simultaneously and uses no regenerator. The experiment is run in two modes, one for K_L and one for K_S. Their decay region is 50m long; for the K_S mode the target station is moved through the decay region so that the observed decay distribution is made to simulate a flat distribution very similar to that from the K_L mode of running. This has the advantage that acceptance corrections between the K_L and K_S modes are small. The detector consists of a liquid argon electromagnetic calorimeter, two MWPC's for tracking charged pions and a hadron calorimeter for energy measurements of the charged pions. There is no magnet, so the energy resolution for the π^+ and π^- is poor; very stringent requirements are therefore used offline to distinguish signal from background in the $\pi^+\pi^-$ mode. Because K_L and K_S decays are not observed simultaneously, this experiment must have very stable detector and beam performance and be able to measure and monitor these well. The K_L and K_S modes have different beam intensities and different kaon momenta spectra, and these effects have to be well understood. Because the momenta spectra are different, the absolute energy scales for both charged and neutral modes also have to be known well.

From our second data run at FNAL, greater than 200,000 $K_L \rightarrow 2\pi^0$ decays are expected in the event sample and substantially more in the other 2π decay modes. The large increase in statistics over the 1985 run resulted from improvements to the trigger and data acquisition and longer running time. Additionally, it was realized that for very high statistics it was necessary to accept events with no photon conversions at the HDRA, and the running conditions were optimized for this. The unconverted sample gives more than a factor of four increase in yield over the converted sample, but gives up the directional information provided by the electron-positron pair, which was very useful in reducing backgrounds. Studies have indicated, however, that (new) cuts requiring the center of energy at the Lead Glass to be within the beams and understanding of the backgrounds will be adequate to achieve the required low systematic uncertainties. It will also be necessary to understand the Lead Glass energy calibration to better than 0.1%, since the downstream end of the Decay Region for neutral mode will no longer be defined by hardware at the HDRA. A software cut, which is sensitive to energy scale, will therefore have to be made.

If $|\epsilon'/\epsilon|$ is smaller than 0.002, it is unlikely that the FNAL or CERN experiments will be able to convincingly establish (at a 3σ level) a direct CP violation signal, even if they were to obtain significantly more data. In this scenario, new experimental techniques or significant detector improvements would be required. For the Fermilab experiment, a significant reduction of systematic

uncertainties could be achieved by improving resolution in the neutral mode to a level comparable to that of the charged mode. Such an improvement would greatly reduce backgrounds and would enable a P and Z bin analysis, similar to that done for charged mode, thereby eliminating acceptance corrections. Improving the resolution would require the Lead Glass array to be replaced with a superior electromagnetic calorimeter. BaF crystals, for example, have recently shown much promise due to their good energy resolution, fast signal characteristics, and good radiation hardness [43]. Conceivably, they or some new type of crystal may be very useful for future precision $|\epsilon'/\epsilon|$ experiments.

In the coming years, one also hopes to observe CP violation in heavy quark systems.[2] Similar phenomenology exists for neutral D and B mesons, as for kaons, though there are no corresponding long- and short-lived states (due to the large number of decay modes available). CP violating rate asymmetries will in general arise in a decay process when there are two or more paths to a particular final state and there are physical relative phases between the amplitudes for the different decay paths. Recently reported observations of $B^0 - \overline{B^0}$ mixing from Argus [46], and also evidence for mixing from UA1 [47], have stimulated interest in CP violation with B's, and there is much interest in future B factories that could produce the estimated 10^7–10^8 B's (based on predictions within the K–M framework) required to observe significant CP violating signals. The reported mixing results also put strong constraints on parameters in the K–M model. In particular, they imply that U_{td} is non-zero and that the top quark mass should be greater than 50 GeV/c^2 [46].

Theoretical calculations of ϵ and ϵ' have been significantly improved recently and it is possible that reliable estimates of $|\epsilon'/\epsilon|$ with 0.001 precision, comparable to that of the experiments, will exist soon. (As discussed in Chapter 1, such an estimate has already been put forth by Buras and Gérard [21]) The Standard Model will soon undergo strong tests to accommodate experimental determinations of ϵ, ϵ', the b lifetime, $\Gamma(b \to u)/\Gamma(b \to c)$, and $B^0 - \overline{B^0}$ mixing. If the top quark is found, its mass will also severely constrain the theoretical calculations. To date, the Standard Model has worked well and is not in conflict with any experimental data. But there are good reasons, coming from unified gauge theories, to believe that new physics must exist and there is hope that this will impact such quantities as ϵ and ϵ'.

Symmetries appear to be fundamental with regard to the nature of the uni-

[2] For recent reviews of prospects for observing CP violation in the B system, see references [44] and [45].

verse. Clearly, they have been fundamental in our attempts at understanding it. The laws of conservation of energy, momentum and electric charge all arise from symmetries, while in gauge theories the symmetries of local gauge invariance lead to interactions. It is vital that the nature and role of the discrete symmetries C, P, and T be understood in a unified theory of interactions. While CP violation is phenomenologically understood in the Standard Model, it appears only as a parameter in the theory and it appears in a similar manner as the quark masses and quark mixing angles. The origin of all these remains a mystery and it will take much experimental input to unravel this mystery. This experiment has been part of the attempt to do that.

Appendix

Regeneration

A regenerator was used to produce a secondary K_S beam from an incident K_L beam for this experiment. This method produced a very clean beam with much less contamination of lambdas and neutrons than if a primary beam had been used. It also enabled the double beam technique of having side by side beams of K_L and K_S, which allowed simultaneous measurement of the K_L and K_S decay rates.

Regeneration of K_S from a K_L beam arises due to different scattering amplitudes of K^0 and $\overline{K^0}$. Consider the scattering processes, at momentum transfer q, of $K^0X \rightarrow K^0X$ with amplitude $f(q^2)/k$ and $\overline{K^0}X \rightarrow \overline{K^0}X$ with amplitude $\overline{f}(q^2)/k$. If one then calculates the amplitude for the process $K_LX \rightarrow K_{\text{out}}X$, one finds

$$\begin{aligned} |K_{\text{out}}> \;&\propto\; \left(\frac{f(q^2)+\overline{f}(q^2)}{2k}\right)|K_L> + \left(\frac{f(q^2)-\overline{f}(q^2)}{2k}\right)|K_S> \\ &\equiv\; \frac{f_{22}(q^2)}{k}|K_L> + \frac{f_{21}(q^2)}{k}|K_S> \end{aligned}$$

The first term represents elastic scattering, while the second term describes the regeneration phenomenon.

A.1 Coherent Regeneration

The regeneration amplitude per scattering center in the forward direction ($q^2 = 0$) is called coherent regeneration and is given by:[1]

$$\rho(0) = 2\pi i \frac{f_{21}(0)}{k}$$

[1]Coherent regeneration was first described quantitatively by Case and Good [48].

For a macroscopic target, the coherent regeneration amplitude is given by integrating this over all scattering centers. Doing this, one finds (dropping the q^2 dependence)

$$\rho = 2\pi i \frac{f_{21}}{k} N \delta(L)$$
$$\delta(L) = \Lambda_S \frac{1 - e^{-\nu L/\Lambda_S}}{\nu}$$

where

N is the density of scattering centers,

L is the length of the regenerator,

$\nu = i\Delta m/\Gamma_S - 1/2$,

$\Gamma_S = \hbar/\tau_S$,

$\Lambda_S = c\tau_S$,

Δm is the K_L–K_S mass difference, and

τ_S is the K_S lifetime

The regeneration amplitude, ρ, for the regenerator in this experiment is approximately 4% for 70 GeV kaons. The amplitude f_{21}/k is dominated by ω exchange and is predicted by Regge theory [49] to have a power law dependence on energy with constant phase:

$$f_{21}/k \propto P^{-n} e^{i\Phi}$$

Further, the phase and power law are related by $\Phi = -\frac{\pi}{2}(2 - n)$.

Including contributions from CP-violating decays, the 2π rate downstream of a regenerator from coherent K_L and K_S is given by:

$$R(\tau) = \left|\rho e^{\nu \Gamma_S \tau} + \eta e^{-\Gamma_L \tau/2}\right|^2 e^{-L/\Lambda}$$

where

τ is the proper time, and

Λ is the interaction length of kaons in the regenerator

A.2 Diffractive and Inelastic Regeneration

Diffractive Regeneration corresponds to K_S production at a finite momentum transfer q. Including elastic scattering effects in addition to diffractive regeneration, the 2π diffractive rate downstream of the regenerator is given by: [50]

$$\frac{\mathrm{d}R_{\mathrm{diff}}(q^2)}{\mathrm{d}q^2} = \pi N L e^{-L/\Lambda} \cdot \left| \left(\frac{f_{21}(q^2)}{k} + \rho \frac{f_{22}(q^2)}{k} \right) e^{\nu \Gamma_S \tau} + \frac{f_{22}(q^2)}{k} \eta e^{-\Gamma_L \tau/2} \right|^2 \quad (A.1)$$

The first term comes from diffractive regeneration; the second term is from coherent regeneration accompanied by an elastic scatter; and the third term is from an elastic scatter followed by a CP-violating decay. These three effects add coherently because the scattering centers and scattering angles are the same. It turns out that for a two interaction length regenerator, the first two terms largely cancel. This is fortunate, because this is also the length that maximizes the coherent signal. Thus, the regenerator was chosen to be two interaction lengths long. For this length, the coherent signal is further optimized by choosing a regenerator with low atomic number and so Carbon is a good choice. B_4C was chosen for the actual material because it is denser than Carbon, and there were space limitations in the regenerator design.

Inelastic regeneration results from a K_L scattering with an individual nucleon inside the nucleus and regenerating a K_S with momentum transfer q. The nucleus breaks apart and extra particles are produced. The q^2 dependence to this resembles scattering from a single nucleon, and is approximately e^{-6q^2} [50]. Figure 112 depicts schematically the q^2 dependence of the 2π rate downstream of a regenerator and the regions of importance for the coherent, diffractive and inelastic signals.

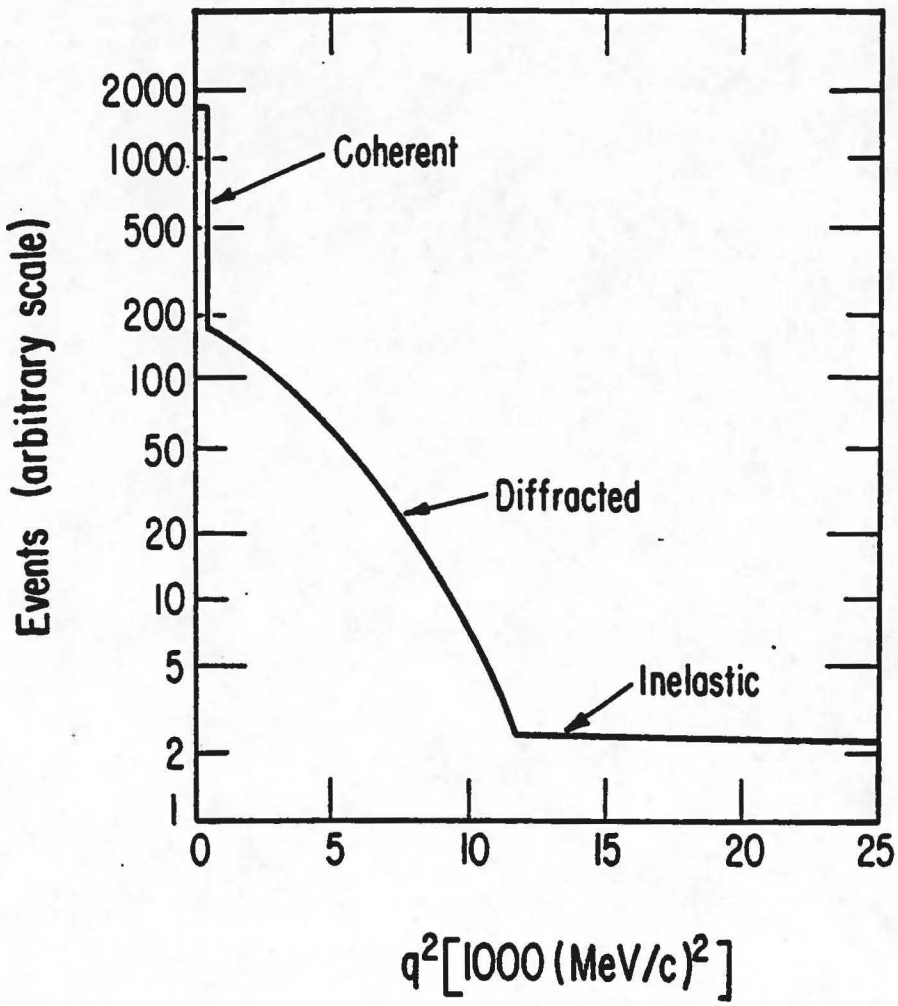

Figure 112: Schematic representation of the q^2 dependence to the 2π rate downstream of a regenerator.

Bibliography

[1] J. H. Christenson, J. W. Cronin, V. L. Fitch, and R. Turlay, Phys. Rev. Lett. **13**, 138 (1964).

[2] C. Quigg, Gauge Theories of the Strong, Weak, and Electromagnetic Interactions (Benjamin/Cummings, Reading, MA,1983).

[3] E. Noether, Nachr. Kgl. Ges. Wiss. Göttingen, 235 (1918).

[4] T. D. Lee and C. N. Yang, Phys. Rev. **104**, 254 (1956).

[5] C. S. Wu, E. Ambler, R. W. Hayward, D. D. Hoppes, and R. P. Hudson, Phys. Rev. **105**, 1413 (1957).

[6] R. G. Sachs, The Physics of Time Reversal (The University of Chicago Press, Chicago 1987).

[7] W. Pauli in Neils Bohr and the development of physics, edited by W. Pauli (McGraw-Hill, New York, 1955).

[8] Review of Particle Properties, Phys. Lett. B **170** (1986).

[9] L. Wolfenstein, Ann. Rev. Nucl. Sci. **36**, 137 (1986).

[10] J. W. Cronin, Acta Phys. Pol. B **15**, 419 (1984).

[11] V. V. Barmin et al., Nucl. Phys. B **247**, 293 (1984).

[12] E. D. Commins and P. H. Bucksbaum, Weak interactions of leptons and quarks (Cambridge University Press, Cambridge 1983).

[13] K. Kleinknecht, Ann. Rev. Nucl. Sci. **26**, 1 (1976).

[14] V. Weisskopf, E. P. Wigner, Z. Phys. **63**, 54 (1930).

[15] T. J. Devlin and J. O. Dickey, Rev. Mod. Phys. **51**, 237 (1979).

[16] V. L. Fitch, R. F. Roth, J. S. Russ, and W. Vernon, Phys. Rev. Lett. **15**, 73 (1965).

[17] I. J. R. Aitchison and A. J. G. Hey, Gauge Theories in Particle Physics (Adam Hilger, Bristol 1982).

[18] M. Kobayashi and K. Maskawa, Prog. Theor. Phys. **49**, 652 (1973).

[19] W. Schmidt-Parzefall in Proceedings of the International Symposium on Lepton and Photon Interactions at High Energies, Hamburg, West Germany, 1987 (to be published).

[20] J. F. Donoghue et al., Phys. Rep. **131**, 1 (1986).

[21] A. J. Buras and J.-M. Gérard, Phys. Lett. B **203**, 272 (1988).

[22] J. Gasser and H. Leutwyler, Phys. Rep. **87**, 77 (1982).

[23] L. Wolfenstein, Phys. Rev. Lett. **13**, 569 (1964).

[24] I. S. Altarev et al., JETP Lett. **44**, 460 (1986).

[25] H.–Y. Cheng, Phys. Rep. **158**,1 (1988).

[26] A symmetry mechanism giving $\theta = 0$ was first put forth by Peccei and Quinn; see R. D. Peccei and H. R. Quinn, Phys. Rev. Lett. **38**,1440 (1977). Weinberg and Wilczek have pointed out that this would result in a new physical particle, the axion; see S. Weinberg, Phys. Rev. Lett. **40**, 223 (1978) and F. Wilczek, Phys. Rev. Lett. **40** 279 (1978).

[27] R. H. Bernstein Ph. D. Thesis, University of Chicago 1984 (unpublished).

[28] W. R. Lewis, Notes on Soldering (Tin Research Institute, Greenford, Middlesex, England 1964).

[29] E. Longo and I. Sestilli, Nucl. Inst. and Meth. **128**, 283 (1975).

[30] H. Yamamoto, internal E731 memo (1986).

[31] A. J. Malensek, FN-341 (1981).

[32] H. W. Atherton et al., CERN 80:07 (1980).

[33] A. Schiz et al., Phys. Rev. D **21**, 3010 (1980).

[34] H. A. Bethe and W. Heitler, Proc. R. Soc A **146**, 83 (1934). See also Y.-S. Tsai, Rev. Mod. Phys. **46**, 815 (1974), and Y.-S. Tsai, Rev. Mod. Phys. **49**, 421 (1977).

[35] A. Gsponer et al. Phys. Rev. Lett. **42**, 13 (1979); J. Roehrig et al., Phys. Rev. Lett. **38**, 1116 (1977).

[36] M. Woods et al., Phys. Rev. Lett. **60**, 1695 (1988).

[37] H. Burkhardt et al., CERN preprint CERN-EP/88-47 (1988).

[38] M. Banner et al., Phys. Lett. **13**, 569 (1964).

[39] M. Holder et al., Phys. Lett. B **40**, 141 (1972).

[40] J. H. Christenson et al., Phys. Rev. Lett. **43**, 1209 (1979).

[41] J. K. Black et al. Phys. Rev. Lett. **54**, 1628 (1985).

[42] R. H. Bernstein et al., Phys. Rev. Lett. **54**, 1631 (1985).

[43] E. Lorenz. et al., Nucl. Inst. and Meth. A **249**, 235 (1986); S. Majewski and D. Anderson, Nucl. Inst. and Meth. A **241**, 76 (1985); D. F. Anderson et al., Nucl. Inst. and Meth. A **228**, 33 (1984).

[44] F. J. Gilman, SLAC–PUB–4508 (1987).

[45] I. I. Bigi and A. I. Sanda, Nucl. Phys. B **281**, 41 (1987).

[46] H. Albrecht et al., Phys. Lett. B **192**, 245 (1987).

[47] C. Albajar et al., Phys. Lett. B **186**, 247 (1987).

[48] Case, Phys. Rev. **103**, 1449 (1956); Good, Phys. Rev. **106**, 591 (1957).

[49] For a discussion of scattering and Regge theory, see V. D. Barger and D. B. Cline, Phenomenological Theories of High Energy Scattering (W. A. Benjamin, New York 1969); R. J. Eden, High Energy Collisions of Elementary Particles (Cambridge University Press, Cambridge 1967). For Regge theory applied to kaon regeneration and a discussion of ω exchange, see F. Gilman, Phys. Rev. **171**, 1453 (1968).

[50] W. Molzon, Ph. D. Thesis, University of Chicago 1979 (unpublished).